Università degli Studi di Trieste

XXV Ciclo del Dottorato di Ricerca in

Geofisica della Litosfera e Geodinamica

The geodynamics of the Mediterranean in the framework of the global asymmetric Earth: evidences from seismological and geophysical methods

Settore scientifico-disciplinare: GEO 10

Dottorando:

dott. Enrico Brandmayr

Coordinatore:

Chiar.mo Prof. Peter Suhadolc

Supervisore di Tesi:

Il.mo Chiar.mo Prof. Giuliano Francesco Panza

Anno Accademico 2011-2012

to my Mother, in loving memory.

Contents

Riassunto

La tesi presenta l'estensione ed il raffinamento del modello cellulare tridimensionale della crosta e del mantello superiore dell'area centrale mediterranea e propone una interpretazione geodinamica del suddetto modello nel contesto della asimmetria globale della tettonica delle placche. Il modello cellulare è espresso in termini di velocità delle onde di taglio (V_S) e di spessore e densità degli strati, fino ad una profondità di 350 chilometri. Tali proprietà caratterizzanti gli strati sono ottenute mediante avanzate tecniche di inversione non lineare, quali l'inversione con il metodo *hedgehog* di curve di dispersione delle velocità di gruppo e di fase per la determinazione delle V_S e l'inversione non lineare di dati gravimetrici mediante il metodo $GRAV3D$. Il metodo *hedgehog* consente la definizione di un insieme di modelli strutturali senza fare ricorso ad alcun modello a priori, considerando la V_S e lo spessore degli strati come variabili indipendenti. Data la ben nota non unicità del problema inverso, la soluzione rappresentativa di ogni cella è determinata per mezzo dell'applicazione di algoritmi di ottimizzazione ed è inoltre validata alla luce di dati geologici, geofisici e petrologici indipendenti, in particolare la distribuzione della sismicità, sia passata, ottenuta dai bollettini internazionali, sia presente, ottenuta mediante inversione non lineare dei meccanismi focali. Le proprietà delle sorgenti sismiche sono state studiate utilizzando la metodologia $INPAR$ per l'inversione di forme d'onda complete di periodo relativamente corto (fino a 10 s), che permette la determinazione realistica del tensore momento sismico in particolare per eventi poco profondi. Questa metodologia si rivela particolarmente utile nelle aree caratterizzate da eventi di moderata magnitudo, dove le tecniche globali standard non possono in genere venire applicate. Il metodo $INPAR$ fornisce inoltre risultati attendibili anche quando sono disponibili soltanto pochi segnali registrati da un numero limitato di stazioni. L'inversione gravimetrica è stata vincolata alla geometria degli strati definita dal modello V_S ottenuto dai dati sismologici. Ai dati gravimetrici di input è applicato un rumore gaussiano con ampiezza di 1,5 $mGal$. Al fine di non imporre a priori l'esistenza di decrementi della densità al crescere della profondità, il modello di densità di riferimento utilizzato come input dell'inversione consiste, per tutte le celle, in un modello di densità crescente o costante

con la profondità, che soddisfa, entro i valori di incertezza, la relazione di Nafe-Drake. Le anomalie ottenute dal processo di inversione gravimetrica vengono poi trasformate in valori assoluti di densità riferiti al modello di riferimento. Il modello tridimensionale così ottenuto, analizzato e discusso lungo sezioni perpendicolari ai complessi orogenetici dell'area di studio (Appennini, Alpi, Dinaridi) conferma l'esistenza di profonde asimmetrie strutturali tra le subduzioni est e ovest-vergenti e la presenza di litosfera sottile nell'area estensiva del bacino Tirrenico, che sovrasta una zona a bassa velocità (LVZ) indicativa della presenza di vaste aree magmatiche o di fusione parziale, probabile sede di un flusso del mantello verso est. Tale flusso è possibile causa dell'asimmetria riscontrata tra la subduzione appenninica, quasi verticale, e la subduzione alpina e dinarica, caratterizzata da un basso angolo di immersione. Ulteriore ed inaspettata caratteristica del modello è rappresentata dal fatto che la litosfera in subduzione risulta essere meno densa del mantello circostante. Tale risultato apre la strada a nuove interpretazioni riguardo alla dinamica delle zone di subduzione, che nella sua descrizione ortodossa vede come fattore determinante il fenomeno dello *slab pull*. La tesi si articola in un capitolo introduttivo iniziale dove viene esposta l'ipotesi della asimmetria della tettonica delle placche, con particolare riferimento alle evidenze in area mediterranea, mentre nei capitoli successivi vengono presentati i risultati del modello in V_S e densità ottenuto a differenti scale risolutive. Tali risultati sono poi discussi, con l'ausilio di sezioni interpretative lungo profili significativi, alla luce di evidenze indipendenti con l'intento di delineare un quadro geodinamico coerente dell'area di studio. In Appendice, unitamente alla presentazione dei risultati tabulati, sono approfondite alcune tematiche particolari.

Summary

This thesis presents the extension and refinement of the 3D cellular model of the crust and upper mantle of the central Mediterranean and offers a geodynamic interpretation of the obtained model in the framework of the global asymmetry of plate tectonics. The cellular model is expressed in terms of shear waves velocity (V_S), thickness and density of the layers, to a depth of 350 kilometers. These physical properties are obtained by means of advanced non-linear inversion techniques, such as the *hedgehog* inversion method of group and phase velocity dispersion curves for the determination of V_S and the non-linear inversion of gravity data by means of the method $GRAV3D$. The *hedgehog* method allows the definition of a set of structural models without resorting to any a priori model, considering the V_S and the thickness of the layers as independent variables. Given the well-known non-uniqueness of the inverse problem, the representative solution of each cell is determined through the application of optimization algorithms and is also validated with the use of independent geological, geophysical and petrological data, e.g. the distribution of historical and recent seismicity, obtained from international bulletins and by non-linear inversion of focal mechanisms. The properties of the seismic sources have been studied using the $INPAR$ methodology for the inversion of complete waveforms at relatively short period (as short as 10 s), that allows the determination of the realistic seismic moment tensor in particular for shallow events. This methodology is very useful in areas of moderate magnitude events, where generally the global standard techniques can not be applied. The $INPAR$ method also provides reliable results even using few signals recorded by a limited number of stations. The gravimetric inversion has been constrained to the geometry of the layers defined by the V_S model obtained from the inversion of seismological data. A Gaussian noise with an amplitude of 1.5 $mGal$ has been applied to the gravimetric data input. In order not to impose a priori the existence of the density decreases with increasing depth, the reference density model used in the inversion consists, for all the cells, in a model of increasing or at least constant density with depth, which satisfies, within the range of uncertainty, the Nafe-Drake relation. The density anomalies obtained by the gravimetric inversion

process are then transformed into absolute values relative to the reference model. The three-dimensional model thus obtained, analysed and discussed along selected sections perpendicular to the orogenic complexes of the study area (Apennines, Alps, Dinarides) confirms the existence of deep structural asymmetries between E- and W-directed subductions and the presence of a thin lithosphere in the extensional area of the Tyrrhenian basin, which overlies a low velocity zone (LVZ) indicative of the presence of large amount of magma or partial melting, where an eastward mantle flow is likely present. This flow possibly causes the asymmetry found between the almost vertical Apenninic subduction and the Alpine-Dinaric subduction, which is in turn characterized by a low dip angle. Further and unexpected feature of the model is the fact that the subducting lithosphere turns out to be less dense than the surrounding mantle. This result opens the way to new interpretations in subductions dynamics, which in its common description relies on the *slab pull* phenomenon as a first order acting force. The thesis consists of an introduction where the hypothesis of the global asymmetry of plate tectonics is addressed, with particular attention to the Mediterranean context, while in the Chapters 2, 3 and 4 are presented the V_S and density models obtained at different resolution scales. These results are then discussed in the Chapter 5, with the aid of interpretive sections along significant profiles, in the light of the validation though independent data, aiming to establish a coherent geodynamic picture of the study area. In the Appendixes, together with the presentation of the tabulated results, some particular topics are discussed.

Chapter 1

Introduction

1.1 The asymmetric Earth

Plate tectonics is the theory explaining the evolution of the outermost and brittle shell of the Earth, fragmented in several different pieces moving relative to each other and relative to the underlying mantle. This movement controls not only the present structure of the Earth lithosphere and the seismic phenomena in it but also the structure of the deeper layers of the upper mantle. Although this theory is today widely accepted since it is corroborated by several geological, geophysical and geodetic evidences, there is not general consensus on the driving mechanisms that cause the plate's motion. It is still debated whether plates and subducted slabs drive mantle flow from above (Elsasser, 1969; Hager and O'Connell, 1979, 1981) or whether the plates are passive passengers that simply record the surface motions of deep mantle convection (Tackley, 1998, 2006; Phillips and Bunge, 2005; Nakagawa et al., 2008). Labrosse and Jaupart (2007) stated that the main driving force is related to the thermal cooling of the Earth, that is basically non directional (i.e. spherically symmetric). Two different reference frameworks are generally used to represent absolute plate motion: the hotspots reference framework, which is based on the assumption that hotspots are fixed with respect to the mesosphere and to one another; the mean-lithosphere reference framework, which is based on the no-net-rotation condition (NNR; Solomon and Sleep, 1974) and it assumes a uniform coupling between lithosphere and asthenosphere, hypothesis which is contradicted by an increasing number of seismological proofs and laboratory experiments. In the deep hotspots reference framework the plates show an average westward motion with respect to the underlying mantle which turns into a complete westward polarization in the shallow hotspots reference framework (Cuffaro and Doglioni, 2007), that is usually referred to as *westward drift* of the lithosphere. The westward

motion persists even if the plate's motion is calculated with respect to Antarctica plate (Le Pichon 1968; Knopoff and Leeds 1972). There are two competing hypotheses about the kinematics and the mechanism driving the W-ward rotation of the lithosphere relative to the mantle. Hypothesis A states that lateral viscosity and density variations in the mantle can be the primary sources of the net rotation, and the net rotation is only a mean rotation mainly generated by the stronger pull of slabs surrounding the western Pacific. Consequently the faster W-ward velocity of the Pacific plate dominates the global kinematics of plates, giving a W-ward residual to the whole lithosphere (e.g., Ricard et al., 1991; O'Connell et al, 1991). The alternative is hypothesis B, where the net rotation is interpreted as a result of rotational drag on the lithosphere due to the tides affecting both the fluid and solid Earth (e.g., Bostrom, 1971; Knopoff and Leeds, 1972; Nelson and Temple, 1972; Moore, 1973). According to hypothesis B, the motion of the lithosphere to the *west* is driven by the concurrent action of Earth's rotation, tidal despinning and mantle convection (e.g., Doglioni et al., 2005; Crespi et al., 2007; Cuffaro and Doglioni, 2007; Riguzzi et al., 2010). The amount of the net-rotation of the lithosphere with respect to the mantle is controlled by the viscosity contrast in the upper asthenosphere, which lateral variations determine the plate interactions (Doglioni et al., 2011). Crespi et al. (2007) introduced the concept of tectonic mainstream based on geological evidences and consistently with geodetic data under three different hypotheses regarding the Pacific hotspot source depths. This lead to the definition of the Tectonic Equator, which is the great circle depicting the flow line approximating the path of the westward mainstream of the lithosphere with respect to the mantle, i.e. the line along which plates move over the Earth's surface with the fastest mean angular velocity toward the west relative to the mantle. Its latitude range is about the same of the Moon maximum declination range ($\pm 28^{\circ}$) during the nutation period ($\approx 18.6\ yr$), this evidence supporting a role of Moon's tidal drag in plates motion. The global mainstream and related geographically polarized asymmetries are confirmed by several independent geological and geophysical signatures. Doglioni et al. (2003) observed a topographic asymmetry of the rift flanks, which eastern side has a general higher elevation of 200-300 meters with respect to the western side, both in oceanic and in continental lithosphere, even thousands of kilometres far from the ridge. (e.g. under Arabia and Africa). Similar asymmetry is observed between W-directed and E-directed subduction zones: the former present, for example, steeper slabs and lower topographic elevation of the accretionary prism with respect to the latter (Isacks and Barazangi, 1977; Doglioni et al., 2007).

A global reconstruction of the seismic shear wave anisotropy in the astheno-

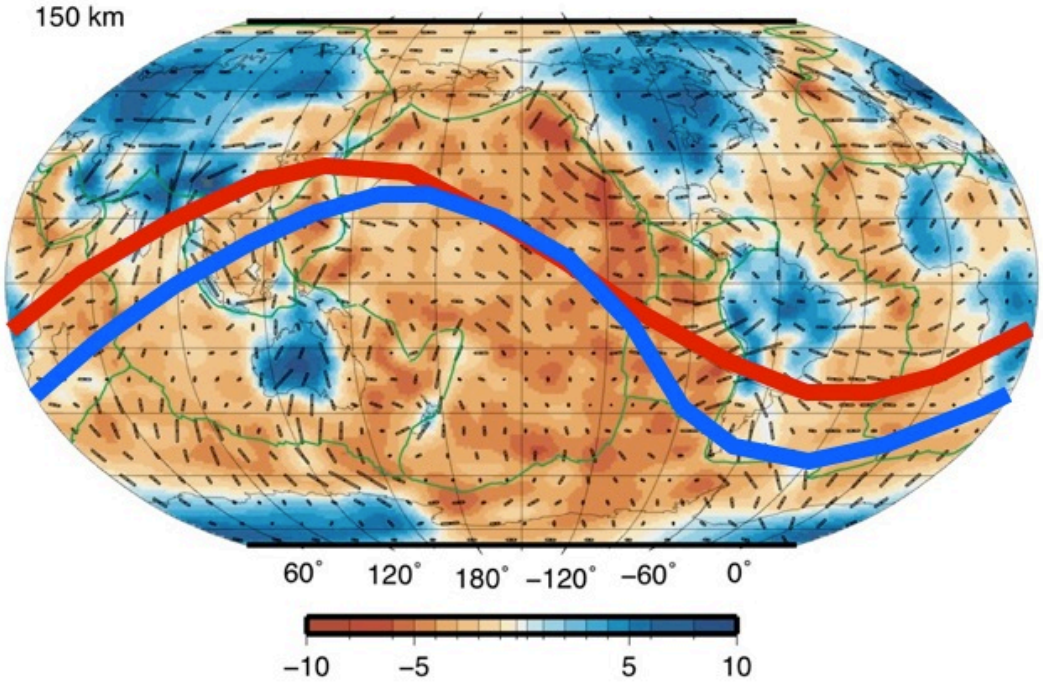

Figure 1.1: Global reconstruction of the seismic shear wave anisotropy (bars) and V_S model (color scale) from Debayle et al. (2005) at 150 km of depth. Path of the Tectonic Equator (red line, Crespi et al. 2007) and of the perturbed Tectonic Equator (blue line, Panza et al. 2010), the latter representing the perturbation of the former along a global seismic low velocity zone in the upper asthenosphere.

sphere (Montagner et al. 2003; Debayle et al., 2005) fits quite well the flow of plates motion, apart along subduction zones where the shear wave splitting anisotropy shows orthogonal trend compatible with the re-orientation of a flow encroaching an obstacle (Figure 1.1). More recently, Panza et al. (2010) observed asymmetric seismic structure through tomographic modelling of the ridge zones, whose western flank has a faster lithosphere and a slower asthenosphere relative to the eastern or north-eastern flank, with a stronger shear wave velocity contrast between lithosphere and asthenosphere in the western limb of the rift with respect to the eastern one.

1.2 The geodynamics of the Mediterranean in the asymmetric Earth perspective

The geodynamics of the Mediterranean has been controlled by the Mesozoic Tethyan rifting and the main Cenozoic subduction zones, the Alps-Betics, the Apennines-Maghrebides, and the Dinarides-Hellenides-Taurides. Closely related to the Mediter-

ranean geodynamics are the Carpathian subduction and the Pyrenees. The Mediterranean orogens show two distinct signatures, which are similar to those occurring on opposite sides of the Pacific Ocean. High morphological and structural elevations, double vergence, thick crust, involvement of deep crustal rocks, and shallow foredeeps characterize E- or NE-directed subduction zones (Alps-Betics and Dinarides-Hellenides-Taurides). Conversely, low morphological and structural elevations, single vergence, thin crust, involvement of shallow rocks, deep foredeeps, and a widely developed back-arc basin characterize the W-directed subduction zones of the Apennines and Carpathians. This asymmetry can be ascribed to the *westward* drift of the lithosphere relative to the mantle (Carminati and Doglioni, 2004). The Permian-Mesozoic rifting developed separating Europe and Africa, and possibly some smaller intervening microplates. Toward the east, at the same time, the Cinmerian NE-directed subduction zone was operating in the eastern Mediterranean-area. The rifting in the Mediterranean evolved on a lithosphere previously thickened by the Paleozoic orogens. The stretching of the lithosphere locally evolved to oceanization in some areas of the Mediterranean (Ligure-Piemontese, Valais, Pennidic zone, eastern Mediterranean), and generated articulated continent-ocean transitions (i.e., passive continental margins) with undulated shapes. During the early Cretaceous the Alpine subduction initiated to transfer some oceanic basins underneath the Adriatic-African plates. Collision possibly started during the Eocene. At a later stage, possibly during the Eocene-Oligocene, the opposite Apennines subduction initiated along the retrobelt of the Alps where oceanic or thinned continental lithosphere was present. The Alpine and Apennines orogens involved the passive margin sequences into their accretionary prisms. Most of the oceanic lithosphere was consumed into subduction, and only some small fragments of oceanic suites have been sandwiched into the belts. The oceanic crust formed during the expansion was almost totally assimilated in the subduction and dragged deep in the mantle, although it is possible to see its fragments involved in collision and visible in Western Alps and NW-Apennines as ophiolites. The crust involved in the collisional process got thicker and thicker, uplifting for isostatic adjustment, so starting the Alpine orogenic process. The deformation in the Alps started first involving the Adriatic margin (African promontory). The European continental margin and the related sedimentary prism deformed last, thrusting over the European foreland to complete the generation of the Alpine orogen. At the same time there were other active subductions, like the NE-directed subduction of the Adriatic plate below Eurasia (along the Dinarides), and the W-directed subduction below the Apennines. In this belt, the slab retreat generated a different style of orogen, with a rather lateral growth, lower topography, shallower decollement

and deeper foredeep. In the hanging wall of the Apennines slab a back-arc basin opened to form the present western Mediterranean basins. During the back-arc rifting, since about 20 Ma, a fragment of the European margin detached from the continent and, counter-clockwise rotating by about 60°, moved south-eastward the Sardinia-Corsica block to its present position (Figure 1.2). Behind this movement the crust thinned, forming the Algerian-Provencal oceanic basin. Then, since about 15 Ma, to the east of the Sardinia-Corsica block, a new tensional process caused the opening of the Tyrrhenian oceanic basin (Gueguen et al. 1997; Carminati et al., 2004). These rotations and expansions modified and completed the structure of the Apennines chain. Evidences of these process are the Calabrian-Peloritan arc's reliefs, whose *Alpine* rocks represent a relict of alpine chain, *boudinated* and dragged inside the accretionary prism of the Apennines during the eastward migration of the subduction hinge. The rifting accompanied the eastward retreat of the Apenninic subduction zone, and the slab retreat kinematically requires a contemporaneous eastward mantle flow, regardless this is the cause or a consequence of the retreat (Doglioni et al., 1999). Therefore, the Mediterranean mantle recorded this long history with relevant anisotropies. Despite the numerous proofs confirming this reconstruction coming from different branches of geoscience, some of which will be dealt with in the present work, the debate about the geodynamic evolution of the Mediterranean area is still open. The advantage of joining geophysical models with geological and petrological data in order to understand the complex evolution of Italic region has been discussed in Panza et al. (2007a): the study describes, for the first time, a very shallow crust-mantle transition and a very low S-wave velocity (V_S) just below it, in correspondence of the submarine volcanic bodies (Magnaghi and Vavilov) indicating the presence of high amounts of magma. Panza et al. (2007b) integrated crustal geological and geophysical constraints with the V_S models along the TRANSMED III geotraverse. As a result, a new model of the mantle flow in a back-arc setting, which reveals an easterly rising low-velocity zone (LVZ) in the active part of the Tyrrhenian basin, is obtained. An upper mantle circulation in the Western Mediterranean, mostly easterly directed, affects the boundary between upper asthenosphere and lower asthenosphere, which undulates between about 180 km and 280 km. An explanation for the detected shallow and very low velocity mantle in the non-volcanic part of the Tyrrhenian region is presented in Frezzotti et al. (2009). These anomalous layers are explained by the melting of sediments and/or continental crust of the subducted Adriatic-Ionian (African) lid at temperatures above 1100°C and pressure greater than 4 GPa (130 km). The resulting low fractions of carbonate-rich melts have low density and viscosity and can migrate upward forming a carbonated partially molten CO_2-rich mantle in the

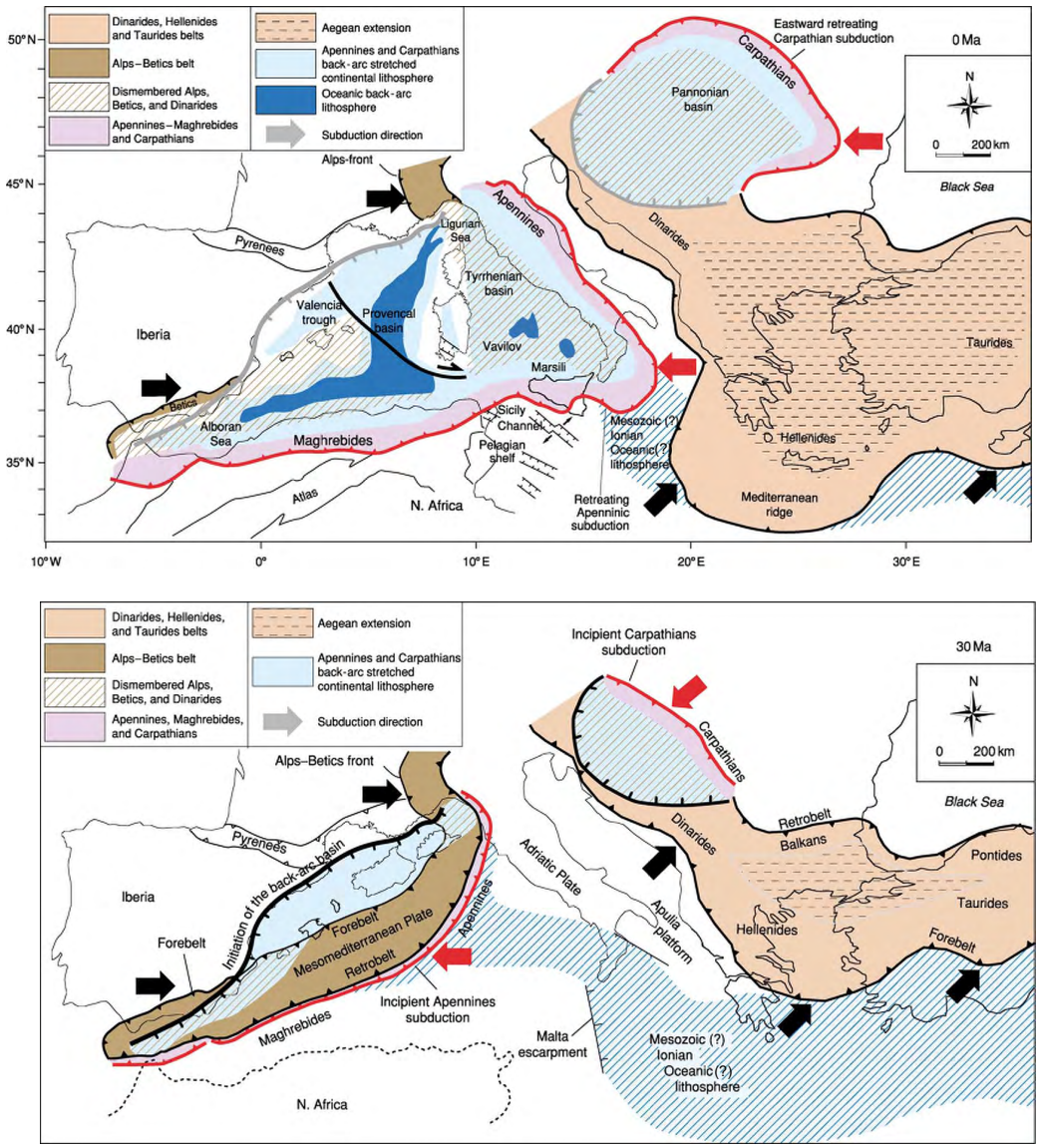

Figure 1.2: Two snapshots of the geodynamic history of the Mediterranean basin. Top: present geodynamic framework, with four subduction (the W-directed Apennines-Maghrebides; the W-directed Carpathians; the NE-directed Dinarides-Hellenides-Taurides; and the SE-directed Alps. Bottom: paleogeodynamics at about 30 Ma. The locations of the subduction zones were controlled by the Mesozoic palaeogeography. The Alps Betics formed along the south E-dipping subduction of Europe and Iberia underneath the Adriatic and Mesomediterranean plates. The Apennines developed along the Alps Betics retrobelt to the east, in which oceanic or thinned pre-existing continental lithosphere was present. Similarly, the Carpathians started to develop along the Dinarides retrobelt (i.e. the Balkans). Note the Sardinia-Corsica Block, not yet migrated in the present day position (modified after Carminati and Doglioni, 2004).

depth range from 130 km to 60 km. Carbonate-rich melts upwelling to depth less than 60-70 km induce massive outgassing of CO_2, that can migrate and be accumulated beneath the Moho and within the lower crust. Brandmayr et al. (2010) contributed to the debate on the geodynamical evolution of the Italic region with

an improvement of the existing cellular model of the lithosphere-asthenosphere system of the area. The V_S-depth model discussed in the following chapters represents a further optimization of previous models constrained with independent studies concerning Moho depth (Dezes and Ziegler, 2001; Grad and Tiira, 2008; Tesauro et al., 2008), seismicity-depth distribution (ISC, 2007) and P-wave velocity (V_P) tomographic data (Piromallo and Morelli, 2003). The layering of each representative cellular model is used as fixed (a priori) information to obtain a 3D density model by means of linear inversion of gravimetric data (ISPRA, ENI, OGS, 2009). The results, discussed in Chapter 5, reveal some unexpected features of the mantle in subduction zones: in particular, no evidence of negative buoyancy of the subducting slabs with respect to the surrounding mantle is found. This finding agrees with recent xenolites studies (Kelly et al., 2003) as well with the $LLAMA$ model proposed by Anderson (2010). Therefore the common concept of *slab pull*, usually evoked as leading force in subduction dynamics, but criticized in some detail by Doglioni et al. (2007), is hardly in agreement with our results.

1.3 Mantle nomenclature

Following Gutenberg (1959), the mantle region above $\approx 220\ km$ of depth is called *region B*. At 220 km of depth $PREM$ model (Dziwonski and Anderson, 1981) defines a prominent discontinuity in seismic velocity. *Region B* roughly represent the upper boundary layer of the mantle, and contains the more loosely defined lithosphere and the seismologically defined lid. Although they are very different concepts, many authors (following McKenzie and Bickle, 1988) often equate lid, lithosphere and thermal boundary layer. The lithosphere is the strong layer, for geological loads, and as measured from flexural studies is about half the thickness of the lid. Originally a rheological concept, the lid assumed various connotations in petrology, including implications about isotope composition, temperature gradient, melting point, seismic velocity and thermal conductivity (Anderson, 2010). According to recent modelling (Schuberth et al., 2009) asthenosphere should be homogeneous and isothermal. As the lithosphere, the asthenosphere has been petrologically defined through major element, trace elements and isotope composition. Seismology detects the high velocity lid and low velocity zone (LVZ). The lid and the LVZ are different from the lithosphere and asthenosphere concepts, respectively, although the lid-LVZ interface (i.e. the region of sharp drop of seismic velocity) is often called lithosphere-asthenosphere boundary (LAB), even if LVZ (V_P between 7.9 km/s and 8.6 km/s; V_S between 4.0 km/s and 4.4 km/s; density

between 3.1 g/cm^3 and 3.5 g/cm^3) may of course overlap with the asthenosphere, but, in general, is nor homogeneous nor isothermal. Nevertheless the term lithosphere is sometimes used in literature referring to seismic lid, that is a high seismic velocity ($V_S \geq 4.35\ km/s$, $V_P \geq 7.5\ km/s$, density $\geq 3.0\ g/cm^3$) thermal boundary layer comprising both crustal material and refractory peridotite. The soft mantle lid is a layer of lithospheric mantle material with anomalous behaviour and low seismicity, found right below the Moho discontinuity; this material is partially melt, with low V_S and relatively high density values. The origin of this high-percentage melt layer's has not to be limited nor directly bound to subduction areas (V_P between 6.9 km/s and 8.2 km/s; $V_S \leq 4.35\ km/s$; density between 3.0 g/cm^3 and 3.3 g/cm^3). The mantle wedge is the portion of mantle material found between a subducting slab and the overriding lithosphere where plastic deformation occurs; in absence of this geo-dynamic setting, mantle material with similar physical behaviour has been simply described as $soft\ mantle$. In this region, according to Van Keken (2003), hydrothermal uprising flow causes partial melting of subducting slab material due to dehydration. The term *lithospheric roots* is widely used in literature and will be used in the following, but should be intended as structural term without implications on geochemical composition and thermal gradient.

Chapter 2

Structural models of the crust and the upper mantle

2.1 Introduction

Seismic tomography represents one of the most powerful tools to investigate the seismic structure of the mantle, and thus has been widely used both on a global and on a regional scale to infer geodynamic conclusions. Besides the inherent limits of the tomography methods, the most important being the resolution, which vary for different methods, and the reference model choice in case of relative tomography, there are some common assumptions and widely popular practices which have great potential for misleading Earth scientists who are not seismologists and, even those who are, but are unfamiliar with the shortcomings of the particular experiment or issue. The common assumption is that seismic velocities are a mantle thermometer, which is a very simplistic assumption since seismic velocities depend on composition and phase as well. Thus it is simplistic to interpret low velocities as hot material and high velocities as cold. The popular practice is to show selected colored 2D sections across the mantle with color scales going from red (for low velocities or negative velocity anomalies) to blue (for high velocity or positive velocity anomalies), saturated at different values, aiming to enhance low or high velocity features according to desired object of the imaging (a plume or a slab). Many examples are given by Anderson (http://www.mantleplumes.org/TomographyProblems.html) and I will not go further in detail. The data on which these pictures rely are usually more rough, present more or less wide uncertainties depending on resolution and deserve major appraisal, possibly through independent data, before any sound interpretation can be made. Finally this will be done with the help of cross sections or cartoons, as I

will do in Chapter 5, but relying on the data from which the interpretation comes from. In this chapter the results are presented of the non linear inversion of surface wave dispersion data on cells sized $1° \times 1°$ covering the study area (Figure 2.1).

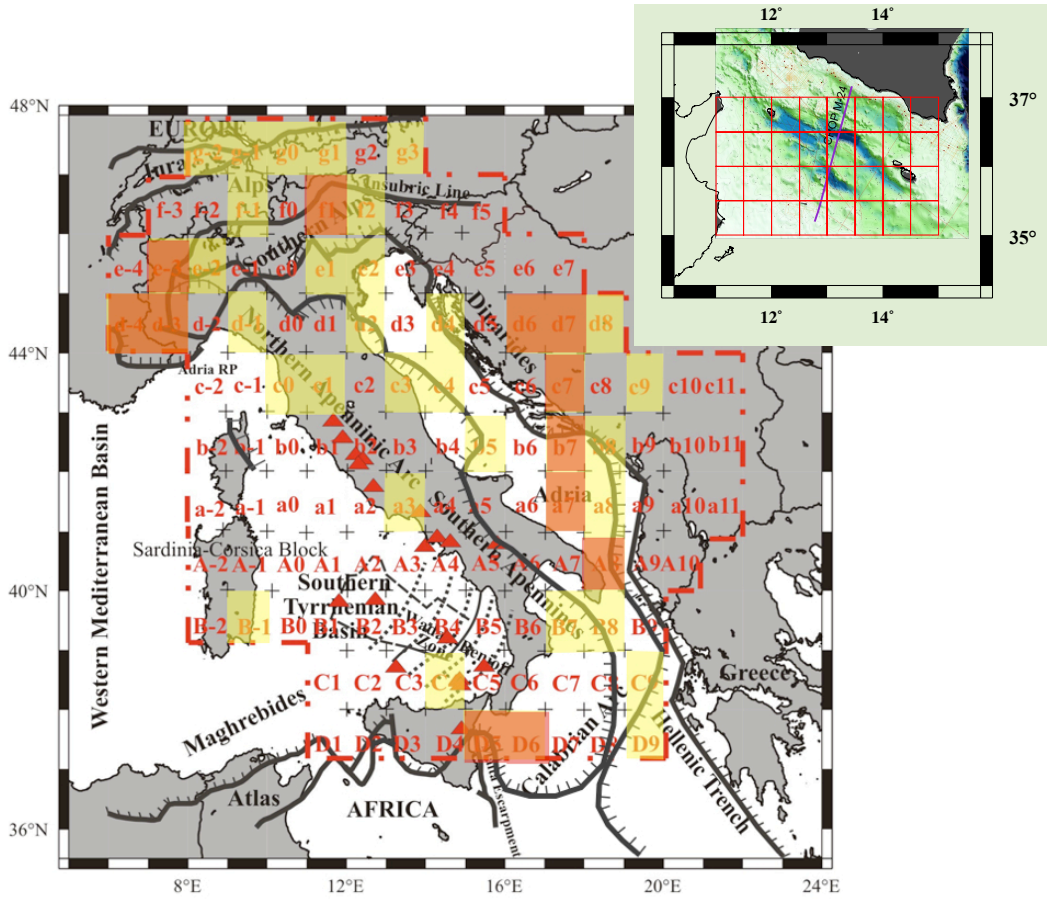

Figure 2.1: Map of the study area modelled by $1° \times 1°$ cells, with main tectonic lineaments. The representative solution in each cell has been chosen by hierarchical application of the optimization algorithms. The cells in which the final GFO solution is different from both GSO and LSO solutions (yellow) and from LSO solution only (orange) are shown. Inset: the Sicily Channel area modelled at variable resolution according to bathymetric survey and CROP M24 seismic profile data (purple line).

For each cell the representative model, chosen by mean of optimization algorithms and appraised with independent geophysical data, is shown. The ensemble of the selected cellular models outcomes in a smooth 3D model of the study area enlightening the major structural features of the crust and the upper mantle and allowing, besides density model presented in Chapter 3, a deep insight in the geodynamical evolution of the area.

2.2 The inverse problem

Physical theories allow us to make predictions: given a complete description of a physical system, we can predict the outcome of some measurements. This problem of predicting the result of measurements is called the forward problem, that is the use of the discovered physical laws allowing us, for given values of the model parameters, to make predictions on the results of measurements on some observable parameters. In the inverse problem, the aim is to reconstruct the model from a set of measurements. In the ideal case, an exact theory exists that prescribes how the data should be transformed in order to reproduce the model. The mathematical conditions for a problem to be well-posed are the existence, uniqueness and smoothness of the solution, the latter meaning that the solution depends continuously on the data. This means that the model has infinitely many degrees of freedom. However, in a realistic experiment the amount of data that can be used for the determination of the model is usually finite. A simple count of variables shows that the data cannot carry sufficient information to determine the model uniquely. In the context of linear inverse problems this point has been raised by Backus and Gilbert (1967, 1968) and more recently by Parker (1994). This issue is equally relevant for nonlinear inverse problems. The model obtained from the inversion of the data is therefore not necessarily equal to the true model that one seeks. For realistic problems, inversion really consists of two steps. Let the true model be denoted by m and the data by d. From the data d one reconstructs an estimated model me, this is called the estimation problem. Apart from estimating a model me that is consistent with the data, one also needs to investigate what relation the estimated model me bears to the true model m. In the appraisal problem one determines what properties of the true model are recovered by the estimated model and what errors are attached to it. Therefore $inversion = estimation + appraisal$. It does not make much sense to make a physical interpretation of a model without acknowledging the effect of errors and limited resolution in the model (Trampert, 1998). The determination of the physical structure of the Earth interior is usually accomplished through inversion methods: modeling the density from gravity data is a linear inverse problem, while determining shear waves velocity-depth distribution from surface waves phase and group velocity dispersion curves, as well the determination of the focal mechanism of a seismic event form the observed seismograms, are severely non-linear inverse problems. We will see in the following how the non-uniqueness and, definitely, the ill-posedness of the inverse problems addressed in this work are treated, for example using optimization algorithms in order to *restore* the smoothness mathematical condition and to face the non-uniqueness of

the solutions and through imposing proper additional constraint in order to make the estimated model as close as possible to the true model, or, at least, as useful as possible for geological interpretations.

2.3 Method and data

2.3.1 Surface wave dispersion data and tomography

The available surface wave dispersion data are used in the present work to investigate the V_S structure in the study area. These data are compiled from previous studies (Panza and Pontevivo, 2004; Pontevivo and Panza, 2006; Panza et al. 2007a) that apply in the sequence the following methods: (a) frequency-time analysis, FTAN (Levshin et al. 1989 and references therein), measure of group-velocity dispersion curves of the fundamental mode of Rayleigh waves; (b) two-dimensional tomography (Yanovskaya, 2001, and references therein) to map the distribution of group and phase velocities of Rayleigh waves, discretized on a grid $1^\circ \times 1^\circ$ to compile the cellular dispersion curves. The FTAN is an interactive group velocity - period filtering method that uses multiple narrow-band Gaussian filters and maps the waveform record in a two-dimensional domain: time (group velocity) - frequency (periods). The measurement of group velocity of Rayleigh and/or Love waves is performed on the envelope of the surface-wave train and can be robustly measured across a broad period band, from fractions of seconds to hundreds of seconds (e.g. Chimera et al. 2003; Guidarelli et al. 2006). Seismic records from national and international seismic networks are analysed by FTAN to study the velocity structure in the broad Mediterranean region. The information about the hypocenters of the events (location, depth, and origin time) is collected from NEIC (2003) or ISC (2007). The length of most of the epicenter-to-station paths considered does not exceed 3000 km in order to have, as much as possible, reliable measurements of group velocity at short and intermediate periods. After group-velocity measurements, all the curves are linearly interpolated and sampled at the set of predefined periods. The group-velocity measurements available in literature have been considered, in addition. The penetration depth of our dataset is increased (Knopoff and Panza, 1977; Panza, 1981) considering published phase-velocity measurements for Rayleigh waves that span over the period range from about 15 - 20 s to about 150 s. The two-dimensional tomography based on the Backus-Gilbert method is used to determine the local values of the group and/or phase velocities for a set of periods, mapping the horizontal (at a specific period) and vertical (at a specific grid knot) variations in the Earth's structure. From these

tomographic maps local values of group and phase velocities are calculated on a predetermined grid of $1^\circ \times 1^\circ$, for a properly chosen set of periods, in the ranges from 5 s to 80 s for group velocities and from 15 s to 150 s for phase velocities. The choice of the set of periods is based on the vertical resolving power of the available data, as determined by the partial derivatives of dispersion values (group and phase velocities) with respect to the structural parameters (Panza, 1981). The lateral resolution of the tomographic maps is defined as the average size, L, of the equivalent smoothing area and its elongation (Yanovskaya, 1997) and hence it is not necessary to perform checkerboard or similar tests. Checkerboard test is a widely used technique for estimating the resolving capabilities of a teleseismic tomography data set is to create a synthetic data set of travel time residuals for a checkerboard wave speed structure (horizontally alternating blocks of high and low wave speed). However, all damped teleseismic models have resolution kernels (equivalent to a column of the resolution matrix or the result for a synthetic model containing a single anomalous block) that oscillate along the horizontal direction. Because of the shape of such resolution kernels, teleseismic tomography is highly compatible with horizontal checkerboard structures. Thus, checkerboard tests are the most optimistic possible evaluation of resolution. Actual resolution is inevitably worse, often much worse, for real Earth structures (Foulger et al., in press). The local dispersion curves are assembled at each grid knot from the tomographic maps. The average size L and its stretching is used as a criterion for the assemblage of the local dispersion curves. At each period, the group and/or phase velocity value is included in the dispersion curve if L is less than some limits: for group velocity L_{max} is 300 km at the period of 5 s and it increases to 600 km at 80 s; for phase velocity L_{max} is 500 km at the period of 15 s and it reaches a value of 800 km at 80 s; the stretching of the averaging area of all considered values is less than 1.6. Hence the local dispersion curves have a different period range and take into account only the dispersion values sufficiently well resolved. Each cellular dispersion curve is calculated as the average of the local curves at the four corners of the cell. The single point error for each value at a given period is estimated as the average of the measurement error at this period and the standard deviation of the dispersion values at the four corners. If, at a given period, the cell is crossed by few wave paths, and, according to the Lmax criterion, the dispersion value at a corner of the cell is not available, the value of the single point error is doubled. The value of group velocity at 80 s is calculated as an average between our tomography results and the global data from the study of Ritzwoller and Levshin (1998). The single point error for group velocity at this period is estimated as the r.m.s. of the errors of our data and those of the global data set. The r.m.s. for the whole dispersion

curves (group or phase velocity) are routinely estimated as 60-70% of the average of the single point errors of the specific cellular curve (Panza 1981; Panza et al. 2007a). The assembled cellular dispersion curves span over a varying period range according to the available reliable data.

2.3.2 The non-linear inversion

The non-linear *hedgehog* inversion method is applied to obtain the V_S models for cells sized $1^\circ \times 1^\circ$ in the study area using the compiled cellular dispersion curves. To solve the inverse problem, the structural model of each cell has to be replaced by a finite number of numerical parameters, and, in the elastic approximation, it is divided into a stack of homogeneous isotropic layers. The method is a trial-and-error optimized Monte Carlo search and the layer parameters (thickness, V_P, V_S, and density) can be defined as independent, dependent or fixed. For each independent parameter the value is searched during the inversion (in our case V_S and thickness). A dependent parameters is linked through a formal relationship to some independent parameter (V_P in our case). A fixed parameter is held constant during the inversion according to independent geophysical evidences (V_P/V_S ratio and density in our case). The number of independent parameters has to be optimized as they have not to be too many in order to be easily interpreted and not be too small in order not loose information really contained in the inverted data. For each dispersion curve, digitized at N points, the parameter's steps δP_j (where j is the number of parameters, equal to 10 in our case) are defined following Knopoff and Panza (1977) and Panza (1981) and they are minima subject to the condition:

$$\left(\frac{1}{N} \sum_{j=1}^{N} \left(\frac{\partial V(T)}{\partial P_j} \right)^2 \cdot \sigma(T)^{-2} \right)^{1/2} \tag{2.1}$$

where $V(T_i)$ is group or phase velocity at period T_i, and, $\sigma(T_i)$ is the relevant standard deviation. The uncertainties of the accepted model are defined as $\pm$ half of the relevant parameter's step. The group and phase velocities of the Rayleigh waves (fundamental mode) are computed for each tested structural model. The model is accepted if the difference between the computed and measured values at each period are less than the single point error at the relevant period and if the r.m.s. values for the whole group and phase velocity curves are less than the given limits. The structure is parameterized taking into account the resolving power of the data and a priori geophysical information. The resolving power of dispersion measurements is only indirectly connected with the lateral variations of the structural models and identical dispersion properties do not necessarily correspond to equal structures.

A priori independent information about the crustal parameters of each defined cell can be introduced in the inversion procedure to improve the resolving power of the tomographic data (Panza and Pontevivo, 2004; Pontevivo and Panza, 2006). Similar conclusion is reached by Peter at al. (2008): in the absence of an accurate crustal model, the retrieved upper mantle structure is dubious down to about 200 km of depth. Accordingly with the values of the partial derivatives of the group and phase velocities for Rayleigh waves with respect to structural parameters (Urban et al., 1993), the assembled cellular dispersion data in the period ranges from 5 s to 150 s for group velocity and from 15 s to 150 s for phase velocity allows us to obtain reliable velocity structure in the depth range from 3 km - 13 km to about 350 km. In each cell, the Earth structure is modelled by 19 layers down to the depth of about 600 km: the uppermost five layers have properties fixed a priori, using independent literature information specific for each cell; the following five layers have variable V_S, V_P, thicknesses; in the eleventh layer V_P, V_S, and density are fixed while the thickness varies in such a way that the whole stack of eleven layers has a total thickness, H, equal to 350 km; below 350 km of depth there are eight layers, of Poissonian material, with constant properties common to all cells. The structure below 350 km is taken from the average model for the whole Mediterranean, EurID database, of Du et al. (1998). The EurID database is based upon existing geological and geophysical literature, it incorporates topographic and bathymetric features and it has been proven to be well consistent with several broad-band waveforms. The use of global models, e.g. ak135 (Kennett et al., 1995), for the structure below 350 km does not introduce any significant difference in the calculated dispersion curves up to 150 s (Raykova and Panza, 2010), thus does not affect our inversion results. In each cell, the thickness of the fixed uppermost crustal structure depends on the lower limit of the period range of the cellular dispersion curves, and varies from about 3 km to 13 km. When the cell is located in a sea region, the thickness of the water layer is defined as a weighted average of the bathymetry and topography (on-line data from NGDC, 2003) inside the area of the cell. The thickness of the sediments is defined in a similar way from the map of Gennesseaux et al. (1998) or from the data given by Laske and Masters (1997). The structural data available from seismic, geophysical and geological studies in the region are used to fix the properties of the remaining upper crustal layers. The same information is considered in the parameterization of the five layers used to model the depth range from 3 km - 13 km to 350 km. Eleven parameters (Pj, j=1,10 and P0) are used to define these five layers: five for the shear-wave velocity in each layer, five for the thickness of each layer, and P0 for the V_P/V_S ratio. The independent available geophysical information is used to define, as a rule, the

following ranges for the inverted parameters: (1) Moho depth; (2) V_S in the crust ($V_S \leq 4.0$ km/s); (3) V_S in the mantle layers (4.0 km/s $\leq V_S \leq$ 4.85 km/s); (4) the total thickness of the parameterized structure ($\leq$350 km, the maximal depth of relevant penetration of our data). The V_S ranges for crust and mantle represent globally valid rules that may not be satisfied in some specific complex cases. In the Alps, for example, the maximum V_S in the crust is set to 4.15 km/s according with reported velocities for some crustal minerals (Anderson, 2007) and in the upper mantle beneath the Tyrrhenian Sea, where high percentage of melting is present (Panza et al., 2007a) low mantle velocities ($V_S \leq 4.0$ km/s) are allowed.

2.3.3 Optimization algorithms

The non-linear inversion is multi-valued and a set of models is obtained as the solution for each cell. In order to summarize and define the geological meaning of the results, it is necessary to identify a representative model, with its uncertainties, for each cell. An optimized smoothing method, which follows the Occam's razor principle, is used to define the representative model for each cell with a formalized criterion. This method avoids as much as possible the introduction of artificial discontinuities in V_S models at the borders between neighbouring cells and keeps the 3D structure as homogeneous as possible by minimizing the lateral velocity gradient. In this way, the dependence of the final model from the predefined grid is minimized. The method represents the models as velocity vectors with equal size (250 layers) for all sets of cellular solutions. The distance (divergence) d between two models (velocity vectors) w and v is defined as the standard Euclidean norm between two vectors:

$$\|w - v\| = \sqrt{\sum_{i=1}^{n} (w_i - v_i)^2} \tag{2.2}$$

where w_i and v_i are the S-wave velocities in the i_{th} layer and n is the number of layers in the models. To take into account the contribution of the i_{th} layer thickness, each velocity value has been weighted with the ratio given by the correspondent layer thickness, h, over the total thickness of the structure, i.e. in the i_{th} layer the weighted velocity (v_{w_i}) is:

$$v_{w_i} = v_i \cdot \frac{h_i}{H} \tag{2.3}$$

Three quite different criteria for optimization have been developed, that lead to the minimization of the lateral velocity gradient for the whole domain, or, in

other words, to the smoothing of the shape of the global solution in all the study area Ω as much as possible. The definitions of the criteria are as follows.

I Local Smoothness Optimization (LSO): the optimized local solution of the inverse problem is the one that is searched for, cell by cell, considering only the neighbours of the selected cell and fixing the solution as the one which minimizes the norm between such neighbours.

II Global Smoothness Optimization (GSO): the optimized global solution of the inverse problem with respect to the smoothness criterion is the one with minimum norm in-between all the members of the subset $\Gamma(\Omega)$.

III Global Flatness Optimization (GFO): the optimized global solution of the inverse problem with respect to the flatness criterion is the one with minimum global norm in-between the set of global combinations $G(\Omega)$.

The LSO follows the principle of minimal divergence in the models. The search starts from the cell where the average dispersion of the cellular models is minimal, i.e. the accepted solutions in this cell are the densest in the parameter space and therefore the potential systematic bias introduced by the choice is minimized. The LSO fixes as the representative solution of the processed cell $\delta_{i,j}$ the cellular model that minimizes the norm between neighbour cells $\delta_{i\pm1,j\pm1}$ (i.e. cells with one side in common). Once a solution is chosen in the running cell, it is fixed and the search continues by applying the procedure to one of the neighbouring cells, not yet processed, and with the smallest average dispersion of the cellular models. The LSO follows the direction of *maximum stability* in the progressive choice of the representative solution of the cells until the whole investigation domain is explored. The GSO is based on the idea of close neighbours (local smoothness) extended, in a way, to the whole study domain. The method consists of two general steps. The first step extracts a suitable subset $\Gamma(\Omega)$ from $G(\Omega)$, namely the global combination u belongs to $\Gamma(\Omega)$ if and only if:

$$\|u_{i,j} - u_{i\pm1,j\pm1}\| = \min\Big(\|u_{i,j} - \tilde{u}\|\Big) \tag{2.4}$$

where $\tilde{u} \in \delta_{i\pm1,j\pm1}$. In other words $\Gamma(\Omega)$ contains all global combinations with close neighbouring components. Then we select as the best solution in $G(\Omega)$, with respect to the smoothness criteria, the member of $\Gamma(\Omega)$ with least global norm, i.e. we apply the flatness criterion to $\Gamma(\Omega)$ and not to the entire $G(\Omega)$. The GFO is based on the concept of maximum flatness among all the domain Ω. It records, by iterative steps, for every row starting from the right border of the domain Ω, each

combination of solutions in the processing row which has minimal norm with the combinations in the previous processed row. Then, in the last step, GFO selects the combinations which have the minimal global norm, with respect to flatness criterion, among the global set $G(\Omega)$. Due to different way of action and computing time necessary to perform GFO and GSO, the three smoothing algorithms should be applied hierarchically: first LSO and GSO, which are the fastest methods acting on the smoothing criterion basis, are performed. The application of these two methods allows to preserve some local features which may be flattened by GFO, according to its acting criterion. Then, in order to reduce the dependence from the starting cell that affects LSO, the common solution to LSO and GSO are selected and fixed during the GFO run (Figure 2.1). This sequential execution of the smoothing algorithms reduces the computing time and concentrates the effort on that portion of Ω in which the solutions chosen by LSO and GSO differ. Since the non-linear inversion and its smoothing optimization guarantee only the mathematical validity of the solution of the inverse problem, the optimization procedure can be repeated whenever necessary, including additional geophysical constrains, such as Moho depth, seismic energy distribution versus depth, presented magmatism, heat flow, etc., until the appraisal of the selected models against well-known and constrained structural features gives an agreement comparable with the model's uncertainties. The resulting three-dimensional V_S structure of the study region is assembled as a juxtaposition of the selected representative one-dimensional cellular models. The steps used in the parameterization of the non-linear inversion obey to the condition (2.1) therefore they can be used to define the uncertainties of each cellular model (Panza et al., 2007a). The representative cellular solution gives, for each inverted layer, the preferred value of V_S and thickness with uncertainties equal, as a rule, to $\pm 1/2$ of the relevant parameter (V_S or thickness) step. The a priori information is taken into account when the uncertainties of the representative solution are specified. Therefore, the variability range of the inverted parameters can turn out to be smaller than the step used in the inversion and the exact value given by the representative solution does not necessarily fall in the middle of its uncertainty range.

2.3.4 Independent geophysical constraints

The obtained representative cellular models are appraised and constrained using independent studies concerning Moho depth (Dezes and Ziegler, 2001; Grad et al., 2008; Tesauro, 2008), seismicity-depth distribution (ISC, 2007), V_P tomographic data (Piromallo and Morelli, 2005) and other independent information as the heat

flow (Hurting et. al, 1991; Della Vedova et al., 2001) and gravimetric anomaly (ISPRA, ENI, OGS, 2009). The data from Dezes and Ziegler (2001), Tesauro et al. (2008), and Grad et al. (2009) are used to define the range of Moho depth for each cell. The Moho depth, with its uncertainties, is compared for each cellular model with the depth range derived from the literature. Where the value indicated by our models is out of the range additional constraints are used. The depth distribution of seismicity is used as an additional criterion for the appraisal of the cellular models. The revised ISC (2007) catalogue for the period 1904-June 2005 is used and for each cell we compute several histograms, grouping hypocentres in depth intervals. The depth grouping considers the uncertainties of the hypocentre's depth calculation: 4 km for the crustal seismicity and 10 km for the mantle seismicity. The computed histograms are the following: (a) distribution of the logarithm of earthquake's number per depth intervals ($\log N$-h): (b) distribution of the logarithm of total energy released by the earthquakes per depth intervals ($\log E$-h); (c) distribution of the logarithm of product of energy released by the earthquakes per depth intervals ($\log \Pi E$-h). Each of these three depth distributions is generated for two selections of the events: all events in the considered catalogue and all events with depth not fixed during hypocenter calculations in order to reduce the influence of *standard* (i.e. fixed) depths, as 33 km, in the histogram construction. The $\log N$-h distribution gives an estimation of the material fragility in the relevant depth interval: high earthquake's frequency is related to more brittleness materials. Similar distributions are used in the studies of Meletti and Valensise (2004) and Ponomarev (2007) but this kind of earthquake frequency distribution does not evidence the presence of strong single events. The $\log E$-h distribution valuates the strangeness of the material in the relevant depth interval: high energy release is relevant to high energy accumulation in strong materials. This kind of seismic energy distribution is used by Panza et al. (2007a) but some strong badly located events can bias the results. The $\log \Pi E$-h distribution gives an integral characteristic of the seismicity in the relevant depth interval, since the product of energy is proportional to the number of earthquakes and relevant energy release. Let we consider two events in one depth interval, with energy release of E_1 and E_2 respectively and $E_1 = aE_2$. The $\log \Pi E$ for this interval is following:

$$\log E_1 \cdot E_2 = \log E_1 + \log E_2 = \log aE_2 + \log E_2 = \log a + 2 \log E_2 \qquad (2.5)$$

The seismicity distribution presented in such way is used by Panza and Raykova (2008) to define the Moho depth in the Italic region. The $\log N$-h distribution is

calculated using all events from ISC catalogue (with and without depth estimated). For energy calculation ($\log E$-h and $\log \Pi E$-h) the relation of Richter (1958) $\log E = 1.5M_S + 11.4$ is used considering all events from ISC catalogue with indicated magnitude. The value of M_S is either directly taken from the ISC catalogue or computed from currently available relationships between M_S and other magnitudes (Peishan and Haitong, 1989; Gasperini, 2002; Panza and Raykova, 2008). The information about heat flow (Hurting et. al, 1991; Della Vedova et al., 2001) is used to define the nature of some relatively shallow layers (down to about 80 km of depth). A high heat flow likely indicates the presence of magma reservoirs with low V_S at shallow depths. A low heat flow usually requests cold mantle (relatively high V_S) and thick crust. The V_P tomographic data of Piromallo and Morelli (2003) are used to reduce the uncertainty range of our V_S models in the construction of the cellular database.

2.3.5 Cellular database

A cell-by-cell database has been compiled to complete the obtained results with some independent data (V_P, attenuation and density) to create an easier way to access the data. All collected information for each cell is stored in a table. The V_P data are taken from Piromallo and Morelli (2003) where a P-wave tomography study of the whole Mediterranean region is provided on a grid of 50 km in both horizontal and vertical directions down to a depth of 1000 km. The V_P data are given in a coordinate system which is rotated with respect to the geographical one. The prime meridian in the rotated system is the $10°W$, while the *rotated equator* is the great circle crossing the prime meridian at $45°N$. To complete our database, the V_P data are averaged to obtain a single set of V_P values for each of our $1° \times 1°$ cells. The averaged data are interpolated linearly to obtain the value of V_P at the centre of each layer of our cellular structures. The V_P data are considered only for the mantle layers down to a depth of 350 km, as the considered P-wave tomography poorly resolves the upper crustal structure. The calculated V_P value for each layer in our cellular models permits to reduce the uncertainty ranges of V_S, in the mantle, as far as the V_P/V_S ratio in the mantle is kept as close as possible to 1.82 (Kennet et al., 1995). The database is completed with S-wave attenuation (Q_S) data given in recent studies of Martinez et al. (2009, 2010) for the Mediterranean at latitude less than $45°N$. Using averaging and linear interpolation, the value of Q_S is calculated for the centre of each layer in our cellular solutions. The Q_S data for the rest of the cells are taken from Craglietto et al. (1989). The values of P-wave attenuation (Q_P) has been derived using the relation $Q_P = 2.2Q_S$ (Anderson, 2007). All V_P

and V_S values are rounded to 0.05 km/s, according to the precision of our modelled data.

2.4 Results with $1^\circ \times 1^\circ$ resolution

Starting from the north-western margin of the study region we face a prominent crustal thickening from cell g-2, with a low V_S crust of 19 km depth lying on a 30 km thick soft mantle lid (V_S about 4.30 km/s) to cell g-1, where a fast crust (V_S about 4.10 km/s) extends down to 44 km of depth. Here the underlying mantle is characterized by a 50 km thick lid (V_S about 4.55 km/s), lying above a LVZ layer extended from 90 to about 200 km depth (V_S about 4.45 km/s) (Figure 2.2). In cells g0 and g1 an about 30 km thick crust (V_S about 3.70 km/s) lies above lid layers (V_S about 4.50 km/s) extended down to about 200 km and 143 km of depth respectively. No LVZ is detected in cell g0, possibly indicating the presence of lithospheric roots, while a layer with V_S of 4.25-4.50 km/s is detected in cell g1 down to about 200 km of depth.

To the east, in cells g2 and g3, the crust is about 35 km thick. The underlying mantle is characterized in both cells by fast lid layers (V_S about 4.55 km/s) down to a depth of about 235 and 330 km respectively, while no LVZ is detected on the bottom, possibly indicating lithospheric roots. The cells f-3, f-2 and f-1 (Figure 2.2) are characterized by a crust gradually thinning eastward from 43 to 39 km of thickness. The underlying mantle is characterized by a lid layer (V_S about 4.50 km/s) thickening to the east and extending down to about 80-90 km of depth, where a LVZ layer is present top is present (V_S about 4.40 km/s), extending down to about 150-190 km of depth. In cells f0 and f1 a crust of about 30 km thickness lies on a lithospheric mantle respectively extended down to about 140 km (V_S about 4.50-4.60 km/s). In cell f1 a soft mantle lid is found just bellow the crust (45 km thickness V_S lower than 4.35 km/s). At the bottom of the lid the LVZ is clearly marked by a layer with V_S about 4.25 km/s extending down to about 210 km of depth. In cells f2, f3 and f4 (Eastern Alps) the crust gradually thickens eastward from about 30 to 40 km (Figure 2.3). The underlying mantle is characterized by velocities gradually increasing (from V_S about 4.35 to 4.60 km/s) down to 250-280 km of depth. The same mantle velocity structure characterizes the cell f5, where the crust is thinner (25 km) than in cell f4.

In the Western Alps, cell e-4 is characterized by a crust of about 30 km thickness, lying on two lid layers of increasing velocity (V_S about 4.45 and 4.60 km/s) extended down to a depth of about 170 km, where the LVZ top is located (V_S

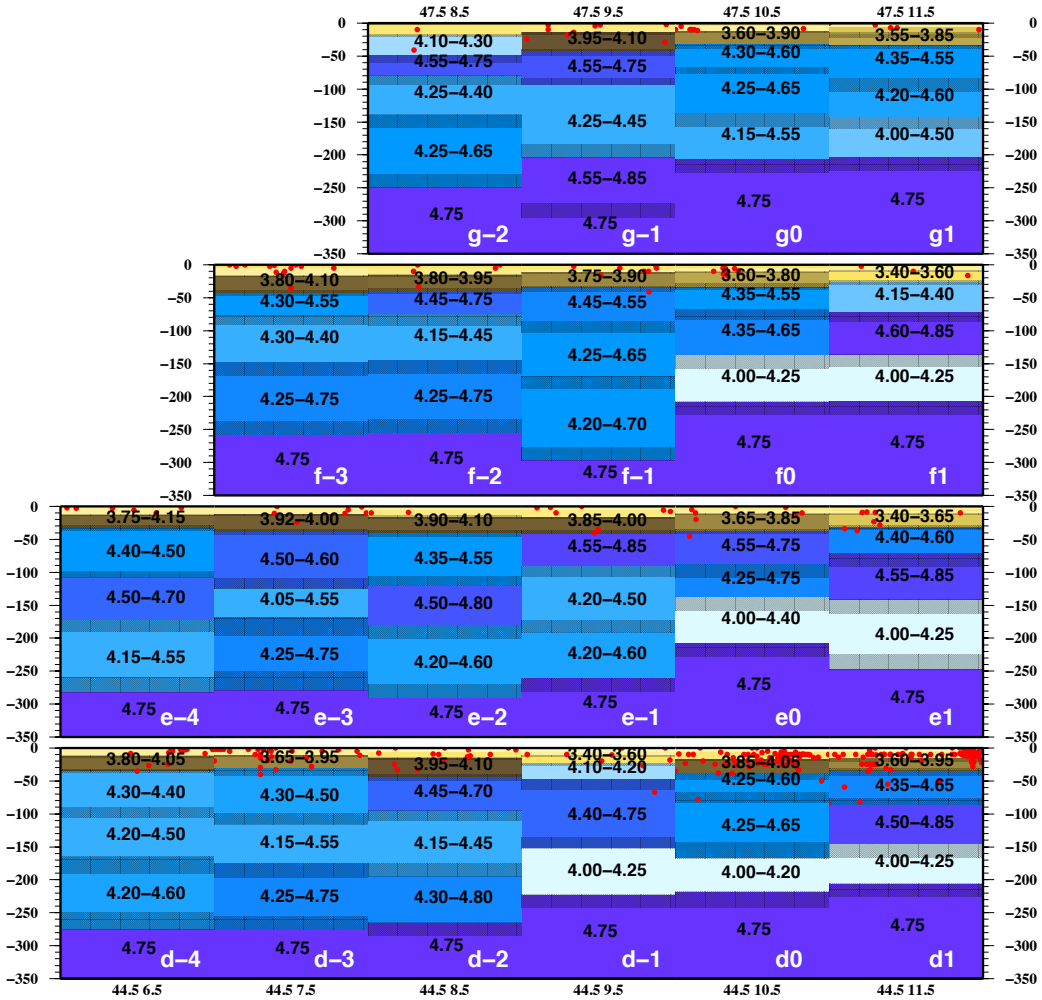

Figure 2.2: Cellular structural model extended down to 350 km depth for the NW Alps area. Yellow to brown colors represent crustal layers, blue to violet colors indicate mantle layers. Red dots denote all seismic events collected by ISC with magnitude ≥ 3 (1904-2006). For each layer V_S variability range is reported. For the sake of clarity, in the uppermost crustal layers the values of V_S are omitted. The uncertainty on thickness is represented by texture. All the values are given in Appendix D.

about 4.35-4.55 km/s). To the east, cells e-3, e-2 and e-1 (Figure 2.2), are characterized by a crust thick about 40 km, lying on a lid extended down to about 250-290 km of depth, with V_S about 4.50- 4.60 km/s. No LVZ is detected below the lid, clearly indicating the presence of lithospheric roots (Panza and Muller, 1980). Cell e0 presents a crust of about 40 km thickness lying on two layers of lithospheric mantle extended down to about 140 km depth (V_S about 4.65 and 4.50 km/s). At this depth a marked LVZ is detected (V_S about 4.20 km/s). Cells e1, e2 and e3 present a crust of increasing thickness from about 30 to 45 km depth. The underlying mantle is characterized by lid layers extended to about 140 km of depth in cell e1 (V_S from about 4.55 km/s), about 100-110 km of depth in cell e2

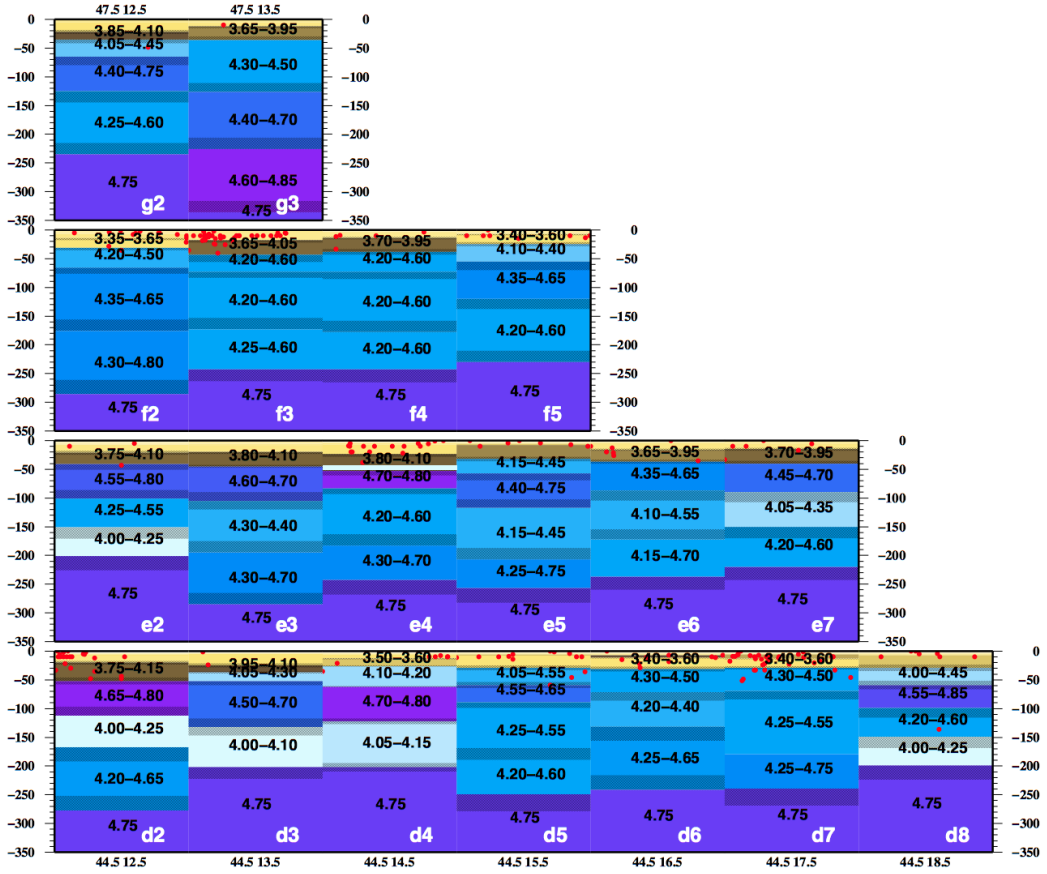

Figure 2.3: Cellular structural model extended down to 350 km depth for the NE Alps area. Yellow to brown colors represent crustal layers, blue to violet colors indicate mantle layers. Red dots denote all seismic events collected by ISC with magnitude ≥ 3 (1904-2006). For each layer V_S variability range is reported. For the sake of clarity, in the uppermost crustal layers the values of V_S are omitted. The uncertainty on thickness is represented by texture. All the values are given in Appendix D.

and e3 (V_S about 4.55 and 4.60 km/s respectively). At these depths the LVZ top is detected (V_S about 4.20 km/s in cells e1 and e2, 4.35 km/s in cell e3). In cell e4 we find a crust of about 39 km thickness lying on a soft mantle layer (V_S about 4.20 km/s) extended down to about 53 km depth (Figure 2.3). Here a fast lid extends down to about 90 km (V_S about 4.80 km/s). At this depth the LVZ is detected, with a layer that extends down to about 180 km (V_S about 4.40-4.50 km/s). Cells e5 and e6 are characterized by a crust of about 35 km thickness lying on a lid (V_S about 4.45) extended to about 110 and 170 km of depth respectively. At this depth an LVZ layer is likely present in cell e5, while this is not well defined in cell e6, where a V_S of about 4.55 km/s is present down to about 235 km of depth. Cell e7 is characterized by a crust of about 40 km thickness, below which a lid layer (V_S 4.45-4.55 km/s) extends down to about 90 km of depth, where a marked LVZ is found (V_S 4.20-4.35 km/s). In the Western Alps, cell d-4 and d-3 (Figure

2.2) present a crust of about 35 and 31 km thickness respectively. The underlying mantle is characterized by lid layers with V_S increasing down to a depth of about 275 km (V_S from about 4.35 to 4.70 km/s). No LVZ is detected in both cells, possibly indicating the presence of lithospheric roots. Cell d-2 present a crust of about 45 km of thickness, lying on a lid layer extended down to about 95 km of depth (V_S 4.45 km/s). At this depth the LVZ top is detected (V_S 4.30-4.45 km/s). Cell d-1 present a thin crust of about 23 km of thickness, lying on a soft mantle lid (V_S about 4.20 km/s) layer extended down to about 48 km of depth. Here a lid layer is present (V_S about 4.45 km/s) down to about 150 km of depth, where a marked LVZ is detected (V_S about 4.25 km/s). To the east, approaching the Apennines collisional front, cells d0, d1, and d2 are characterized by a thickening crust, ranging from about 36 to 52 km of thickness. The underlying mantle is characterized by lid layers extending down to about 150 km in cells d0 and d1 (V_S about 4.45 and 4.55 km/s respectively) and down to a depth of about 110 in cell d2 (V_S about 4.65 km/s). Below, a well marked LVZ (V_S about 4.20 km/s) extends down to depths of about 210-220 in cells d0 and d1 and 165 km in cell d2. The cells d3 and d4 (Figure 2.3) are characterized by a crust of about 37 and 65 km of thickness respectively, lying on a soft mantle lid extended down to about 60 km (V_S about 4.30 and 4.20 km/s respectively). Below a lid of about 60 km thickness (V_S about 4.50 and 4.5 km/s respectively) extends down to about 130 km depth, where a well marked LVZ layer (V_S about 4.10 km/s) is present down to a depth of about 200 km. Cells d5, d6 and d7 present an about 30 km thick crust. The underlying mantle presents lid layers with increasing velocity in cell d5 and d6 (V_S from about 4.40 to 4.55 km/s) extending down to about 70-90 km depth respectively. At this depth an LVZ layer is detected in cells d5 and d6 (V_S about 4.50 and 4.40 km/s respectively), while in cell d7 a LVZ is not clearly present. In cell d8 the crust is about 29 km, lying on lid layers with increasing velocity (V_S from about 4.40 to 4.60 km/s) down to a depth of about 150 km. Below a well marked LVZ (V_S of about 4.25 km/s) extends down to about 200 km of depth. In cell d9 the crust is about 37 km, lying on lid layers with increasing velocity (V_S from about 4.40 to 4.60 km/s) down to a depth of about 250 km, while a LVZ layer in not clearly detected. In cell c-2 and c-1 (Figure 2.4), Ligurian Sea, the crust is respectively about 16 and 29 km thick. In the former a soft mantle layer extends for 15 km below the crust (V_S about 4.10 km/s), lying on a lid extended down to a depth of about 116 km (V_S about 4.45 km/s). In the latter the lid starts below the Moho down to about 99 km depth (V_S about 4.40 km/s). At these depths a LVZ layer is likely detected (V_S about 4.20-4.40 km/s).

Cell c0 is characterized by a crust of about 28 km of thickness, lying on a

Figure 2.4: Cellular structural model extended down to 350 km depth for the northern Tyrrhenian and Apennines area. Yellow to brown colors represent crustal layers, blue to violet colors indicate mantle layers. Red dots denote all seismic events collected by ISC with magnitude ≥ 3 (1904-2006). For each layer V_S variability range is reported. For the sake of clarity, in the uppermost crustal layers the values of V_S are omitted. The uncertainty on thickness is represented by texture. All the values are given in Appendix D.

slightly increasing velocity mantle (V_S from about 4.35 to 4.60 km/s), extended down to a depth of about 300 km. The crust in cell c1 is about 33 km thick overlying a mantle lid (V_S about 4.50 km/s) extended down to about 173 km of depth. Below a LVZ layer is clearly marked (V_S about 4.20 km/s), and extends down to about 223 km of depth. In cells c2 and c3 the crust is thick about 37 to 43 km respectively. The underlying mantle is characterized by lid layers (V_S about 4.60 and 4.50 km/s respectively) extending down to about 220 and 143 km respectively, below which, in cell c3, a LVZ layer is detected (V_S about 4.20 km/s). In cell c4, offshore Adriatic sea, the crust is about 30 km of thickness and lies on two lid layers (V_S about 4.45 km/s) extended down to about 140 km of depth. Below this depth a LVZ layer (V_S about 4.20 km/s) is present extending down to about 190 km of depth. The cells c5, c6 and c7 (Figure 2.5) are characterized by a crust of about 35 km thickness.

The underlying mantle presents an almost constant velocity sequence down to about 230 km (V_S about 4.40 km/s) in cells c5 and c6, while in cell c7 an about 60 km thick lid (V_S about 4.50 km/s) extends below the Moho down to about 90 km depth, where the top of the LVZ is likely present (V_S 4.30-4.45 km/s). Cells c8

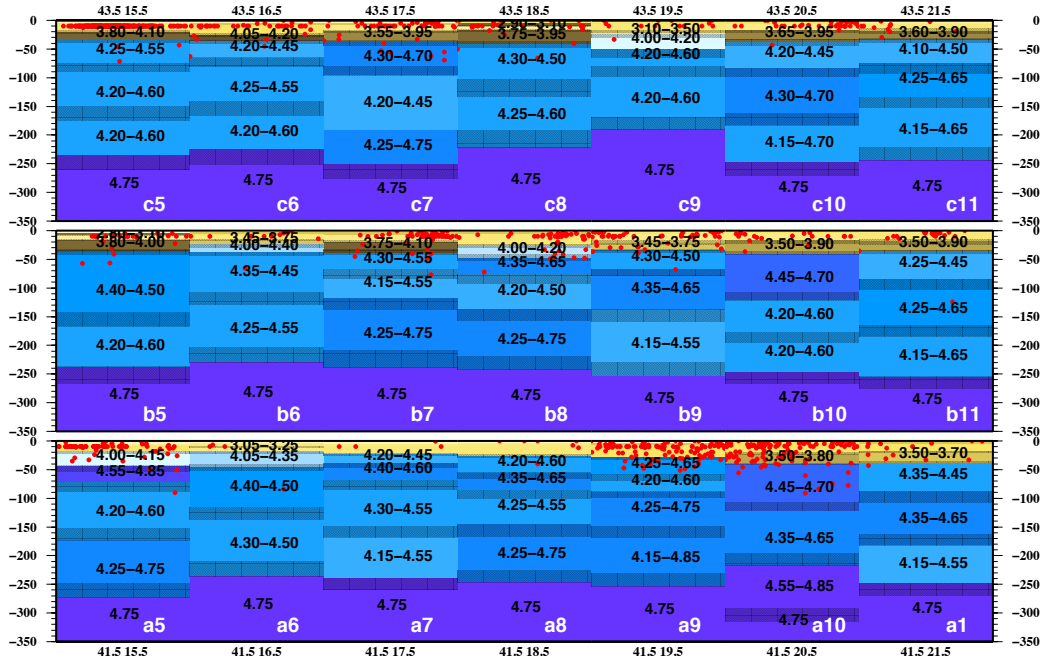

Figure 2.5: Cellular structural model extended down to 350 km depth for the central Adria and Dinarides area. Yellow to brown colors represent crustal layers, blue to violet colors indicate mantle layers. Red dots denote all seismic events collected by ISC with magnitude ≥ 3 (1904-2006). For each layer V_S variability range is reported. For the sake of clarity, in the uppermost crustal layers the values of V_S are omitted. The uncertainty on thickness is represented by texture. All the values are given in Appendix D.

and c9 present a crust of 42 and 25 km of thickness respectively. The underlying mantle is characterized in cell c8 by lid layers with increasing velocity (V_S from about 4.40 km/s to 4.55 km/s) extended down to about 220 km of depth, while in cell c9 a soft mantle layer (V_S about 4.10 km/s) 25 km thick is present just below the crust. Cells c10 and c11 present a crust of about 38 and 35 km respectively. The underlying mantle in both cells is characterized by lid layers with increasing V_S from about 4.35 to 4.70 km/s down to a depth of about 245 km, while the LVZ is not clearly detected in both cells. Cell b-2 (Figure 2.4), in north-eastern Corsica, is characterized by a thin crust (about 14 km) lying on a soft mantle layer of about 15 km thickness. Below a lid layer (V_S about 4.40 km/s) extends down to a depth of about 94 km, where the LVZ top is well marked by a V_S of about 4.15-4.35 km/s. Cell b-1 presents a crust of about 18 km of thickness that lies on a soft mantle layer (V_S about 4.25 km/s) extended down to about 50 km depth. Here a lid layer (V_S about 4.35 km/s) extends down to about 73 km of depth, followed by a LVZ of about 60 km thickness (V_S about 4.30 km/s). In cell b0 the crust is about 18 km thick and lies on soft mantle layers (V_S 4.10-4.35 km/s) extending down to about 165 km of depth. In cell b1 a 23 km thick crust lies on

soft mantle layers (V_S 4.20-4.40 km/s) extending down to about 180 km of depth. In cell b2 the crust is about 33 km thick and lies on a 55 km thick soft mantle layer (V_S about 4.35 km/s). Below two layers of slightly increasing velocity follow (V_S about 4.40 and 4.60 km/s respectively) down to a depth of about 280 km. In cells b3 and b4 the crust is about 35 and 41 km of thickness respectively. The underlying mantle in cell b3 is characterized by a lid layer (V_S about 4.40 km/s) extending down to a depth of about 95 km, below which a LVZ is present (V_S about 4.35 km/s), while in cell b4 lid layers of increasing velocity (V_S from 4.40 to 4.75 km/s) extend down to about 280 km of depth and no LVZ is detected. To the east, offshore Adriatic Sea, cell b5 (Figure 2.5) present an about 37 km thick crust. The underlying mantle in cell b5 is characterized by a lid layer (V_S about 4.50 km/s) down to a depth of about 160 km, where the top of a LVZ layer is likely detected (V_S about 4.40 km/s) that is extending down to about 240 km depth. In cell b6 a thin crust (about 25 km) overlies a soft mantle layer (V_S about 4.20 km/s) that extends below the Moho for 14 km of thickness. Below a lid layer (V_S about 4.40 km/s) extends down to a depth of about 110 km, where the LVZ top is likely detected (V_S about 4.40 km/s). In cell b7 an about 38 km thick crust lies on lid layers (V_S about 4.50 km/s) extending down to about 118 km of depth. Here the top of the LVZ is likely detected (V_S about 4.40 km/s). In cells b8 and b9 the crust is about 27 and 33 km thick respectively. The underlying mantle in cell b8 is characterized by a soft mantle layer (V_S about 4.20 km/s) of about 20 km of thickness just below the Moho, followed by a lid layer (V_S about 4.50 km/s) extending down to about 80 km of depth, where the top of the LVZ is detected (V_S about 4.35 km/s). In cell b9 two lid layers (V_S about 4.50 km/s) extend down to about 140 km of depth, where the LVZ is likely detected (V_S 4.35-4.55 km/s). In cells b10 and b11 the crust is about 42 and 35 km thick respectively. In cell b10 a lid layer (V_S about 4.60 km/s) extends down to about 122 km of depth, where the LVZ top (V_S 4.40-4.55 km/s) is detected. In cell b11 a gradually increasing velocity mantle (V_S from 4.45 to 4.55 km/s) extends down to about 185 km of depth, where the LVZ top is likely detected (V_S 4.40-4.65 km/s). Cell a-2 (Figure 2.4), in south-western Corsica, presents a crust of about 16 km of thickness lying on a lid layer (V_S about 4.40 km/s) that extends down to about 63 km of depth. Below, a well marked LVZ (V_S about 4.20 km/s) of 50 km of thickness is present. Cell a-1 present crust of about 18 km of thickness, lying on soft mantle layers (V_S from 4.15 to 4.35 km/s) extending down to about 170 km of depth. In cell a0, offshore Tyrrhenian, a crust of about 31 km of thickness lies on a thin lid layer (V_S about 4.55 km/s) extended down to about 40 km of depth, where the LVZ top is well marked (V_S about 4.20 km/s). In cell a1 a very thin crust (about 6 km)

lies on a thin fast lid (V_S about 4.75 km/s) extended down to about 11 km depth. Below, very soft mantle layers (V_S from 3.75 to 4.20 km/s) extend down to about 130 km of depth. In cell a2 a crust of about 25 km of thickness lies on a thin very soft mantle layer (V_S about 3.95 km/s) that reaches the depth of about 35 km. A fast lid layer (V_S about 4.60 km/s) follows, extending down to about 50 km depth, where the LVZ top is well marked (V_S about 4.15 km/s). The structure in this cell is appraised by means of the seismicity-depth distribution analysis and gravimetric inversion, and it is yet discussed in details in Panza et al (2007a) and Panza and Raykova (2008). Cell a3 presents an about 21 km thick crust lying on soft mantle layers (V_S about 4.30 km/s) that extend down to about 160 km of depth. In cell a4 an about 40 km thick crust lies on a lid layer (V_S about 4.45 km/s) that extends down to about 150 km of depth, while the LVZ is not clearly detected in this cell. In cell a5 (Figure 2.5) the crust is about 18 km thick and it lies on a soft mantle layer (V_S about 4.10 km/s) extending down to about 43 km of depth and followed by a lid layer (V_S about 4.55 km/s) about 30 km thick. At 73 km of depth the LVZ top is likely present (V_S about 4.40 km/s). To the east, offshore Adriatic Sea, cells a6, a7 and a8 present a gently eastward thickening crust (from about 20 to 26 km). In cell a6 and a7 the crust lies on a soft mantle layer (V_S about 4.20 km/s) of about 26 and 15 km of thickness respectively, below which a lid layer (V_S 4.45 km/s) extends down to about 120 and 69 km of depth respectively, where the LVZ top is likely located (V_S 4.35-4.50 km/s). In cell a8 the crust lies directly on two lid layers (V_S about 4.40 km/s) extending down to about 86 km of depth, where the LVZ top is likely located (V_S 4.40 km/s). In cells a9 and a10, across Dinarides, an eastward thickening crust (from about 29 to 42 km) lies on lid layers (V_S about 4.55 km/s) extending down to about 89 and 122 km of depth respectively, where the top of the LVZ is likely located (V_S about 4.50 km/s). In cell a11 an about 38 km thick crust lies on lid layers with increasing velocity (V_S from about 4.40 to 4.55 km/s) that extend down to about 248 km of depth, while the top of the LVZ not clearly detected. In cell A-2 (Figure 2.6), north-western Sardinia, an about 16 km thick crust lies on a 8 km thick fast lid (V_S about 4.75 km/s). Below another lid layer (V_S about 4.30 km/s) extends down to about 70 km depth, where a marked LVZ layer starts (V_S about 4.25 km/s), reaching the depth of about 160 km. Cells A-1, A0 and A1 are characterized by an about 20 km thick crust, lying on a lid layer (V_S about 4.40 km/s) that extends down to about 60-70 km depth, where a LVZ layer of about 80 km thickness in cells A-1 and A0 and 30 km of thickness in cell A1 is present (V_S about 4.30 in cells A-1 and A0 and 4.10 km/s in cell A1). In cell A2 an about 26 km thick crust lies directly on soft mantle layers (V_S about 4.20 km/s), that extends down to about 100 km depth. In cell A3 a thin crust

(about 6 km) overlies an about 8 km thick lid (V_S about 4.40 km/s) which lies on very soft mantle layers (V_S from 3.50 to 4.15 km/s) extended down to about 61 km of depth.

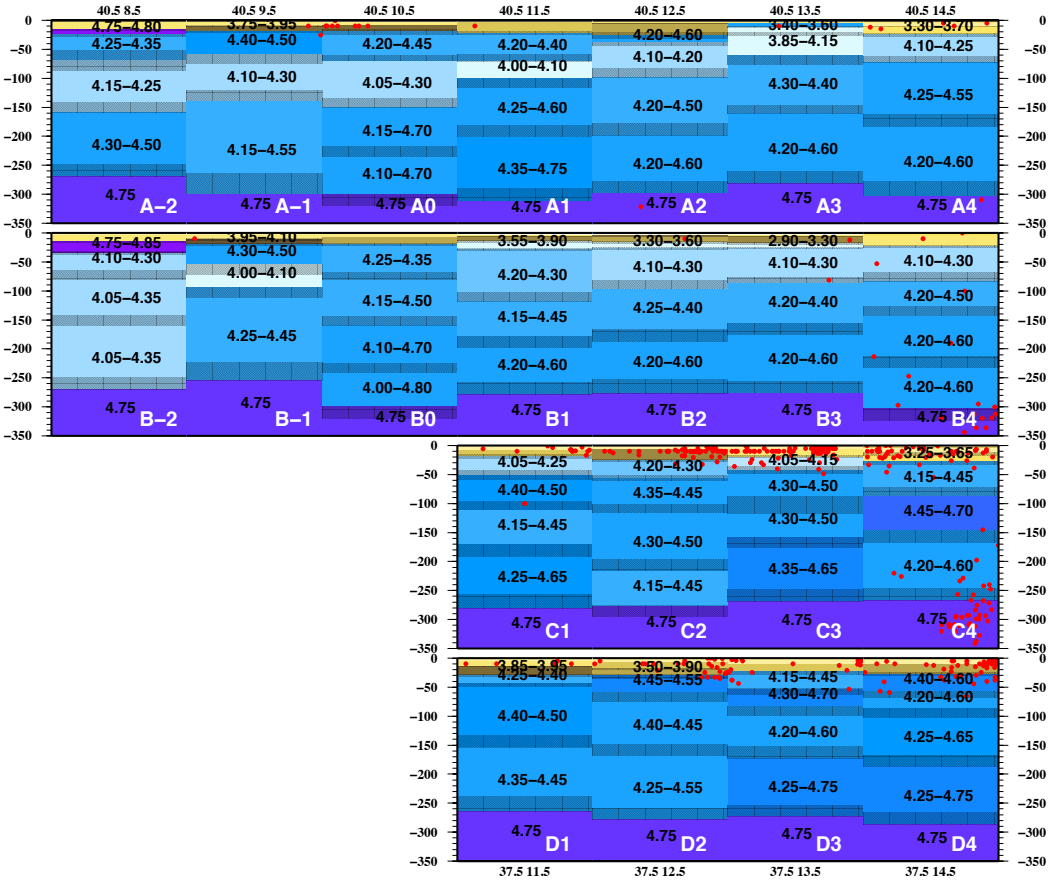

Figure 2.6: Cellular structural model extended down to 350 km depth for the southern Tyrrhenian area. Yellow to brown colors represent crustal layers, blue to violet colors indicate mantle layers. Red dots denote all seismic events collected by ISC with magnitude ≥ 3 (1904-2006). For each layer V_S variability range is reported. For the sake of clarity, in the uppermost crustal layers the values of V_S are omitted. The uncertainty on thickness is represented by texture. All the values are given in Appendix D.

In cell A4 an about 23 km thick crust lies on a soft mantle layer (V_S about 4.25 km/s) that extends down to about 73 km depth. Below two faster layers (V_S about 4.50 km/s) extend down to about 300 km depth. In cells A5 and A6 (Figure 2.7), across Southern Apennines, an eastward thickening crust (about 21 km thick in A5 and 36 km thick in A6) overlies a soft mantle layer with velocities 4.25-4.35 km/s and thickness about 50 km in A5 and 13 km in A6.

A high velocity westward thickening lid (V_S about 4.65 km/s) is extended down to about 80-100 km of depth, where the top of the LVZ is detected (V_S about 4.45 km/s). In cell A7 a 40 km thick crust overlies a lid layer (V_S about 4.55 km/s) that extends down to about 90 km of depth. Below a LVZ layer (V_S about 4.45

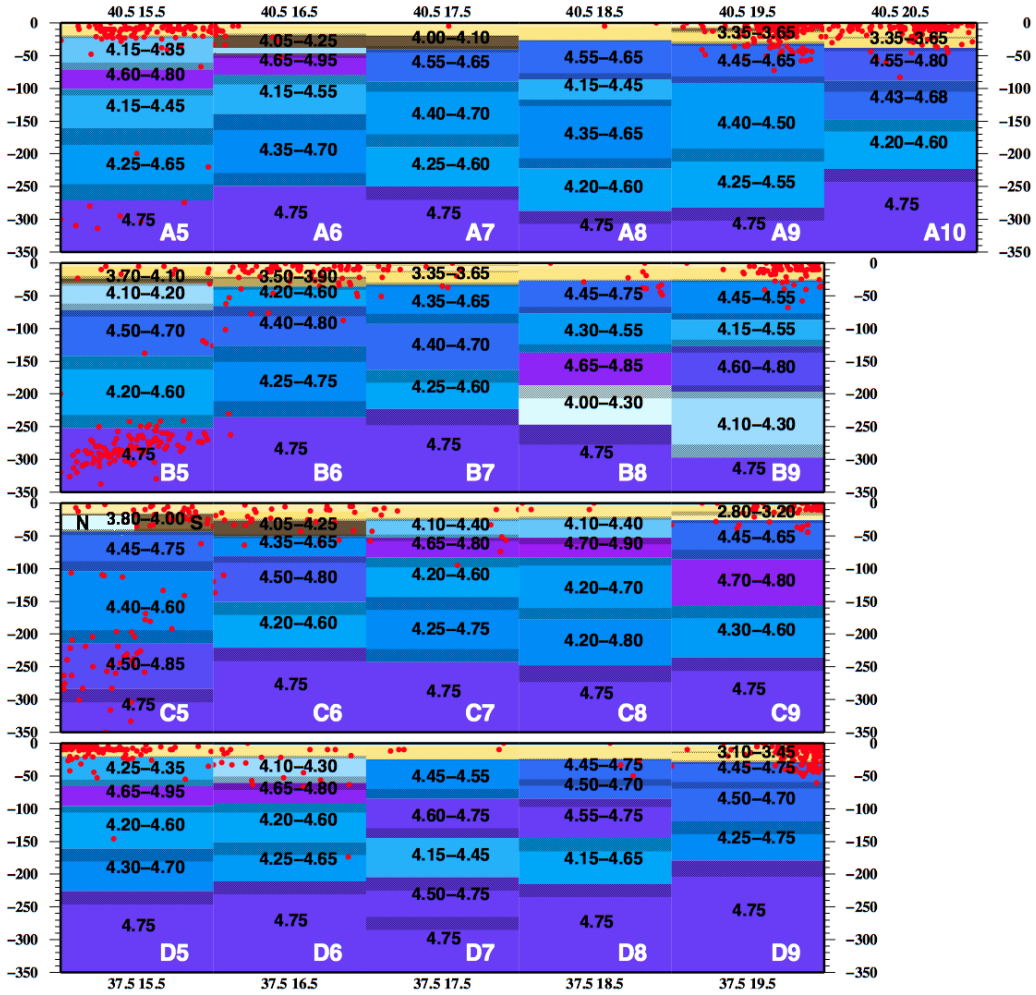

Figure 2.7: Cellular structural model extended down to 350 km depth for the Ionian area. Yellow to brown colors represent crustal layers, blue to violet colors indicate mantle layers. Red dots denote all seismic events collected by ISC with magnitude ≥ 3 (1904-2006). For each layer V_S variability range is reported. For the sake of clarity, in the uppermost crustal layers the values of V_S are omitted. The uncertainty on thickness is represented by texture. All the values are given in Appendix D.

km/s) extends down to about 190 km of depth. Across Dinarides, in cells A8, A9 and A10, an eastward thickening crust (from about 27 to 38 km, Figure 2.8) lies on lid layers (V_S about 4.55 km/s) that extends down to about 90 km of depth.

Below, the LVZ is detected, markedly in cell A8 (V_S about 4.30, about 4.45 km/s in cells A9 and A10). In cell B-2 (Figure 2.6), south-western Sardinia, an about 15 km thick crust lies on a fast lid layer (V_S about 4.75 km/s) that extends down to about 35 km of depth. Here a LVZ layer (V_S about 4.30 km/s) extends down to about 270 km of depth. Cell B-1 has an about 19 km thick crust that overlies a lid (V_S about 4.40 km/s) with thickness of about 35 km. Below a marked LVZ layer (V_S about 4.10 km/s) extends down to about 94 km of depth, followed

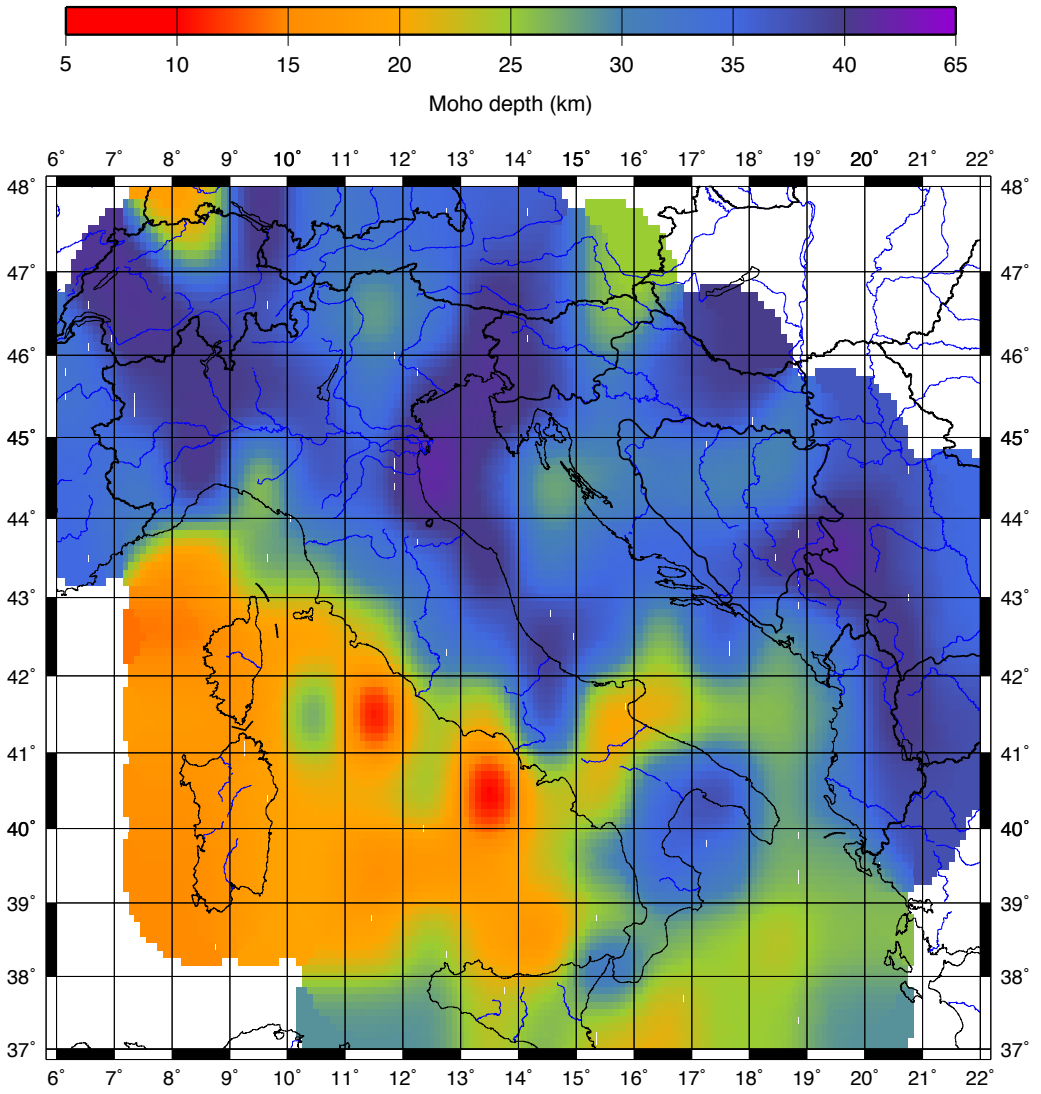

Figure 2.8: Moho depth determined by V_S model.

by a layer with V_S about 4.35 km/s about 160 km thick. Cell B0 has a crust of about 20 km of thickness, overlying two soft mantle layers with rather constant V_S (4.30-4.40 km/s) down to about 160 km of depth. In cells B1, B2 and B3 a relatively thin crust (15, 16 and 18 km respectively) lies on a very soft mantle (V_S about 3.85, 3.60 and 3.30 km/s respectively) of about 12 km of thickness. The V_S in the underlying mantle layers is about 4.30 to 4.45 km/s, down to about 150-180 km of depth. Offshore Calabria, in cell B4, an about 23 km thick crust lies on a soft mantle layer (V_S about 4.30 km/s) that extends down to about 83 km of depth. Below slightly increasing velocity layers (V_S from about 4.50 to 4.60 km/s) extend down to about 300 km of depth. In cell B5 (Figure 2.7) an about 32 km thick crust lies on a soft mantle layer (V_S about 4.20 km/s) extended down to

about 72 km of depth. Below two lid layers (V_S about 4.50 km/s) extend down to about 250 km of depth, while the LVZ is not clearly detected. Across Calabria, in cells B6 and B7 a crust of about 36 km and 33 km of thickness respectively overlies lid layers (V_S about 4.50 km/s) that extend down to about 230 km of depth, while the LVZ is not clearly detected. Offshore Ionian Sea, in cells B8 and B9 an about 27 km thick crust is present, lying on a lid layer (V_S about 4.45 km/s) extended down to about 77 km of depth (Figure 2.9). Below, a LVZ layer is likely present (V_S about 4.45 and 4.35 km/s respectively) down to a depth of about 130 km.

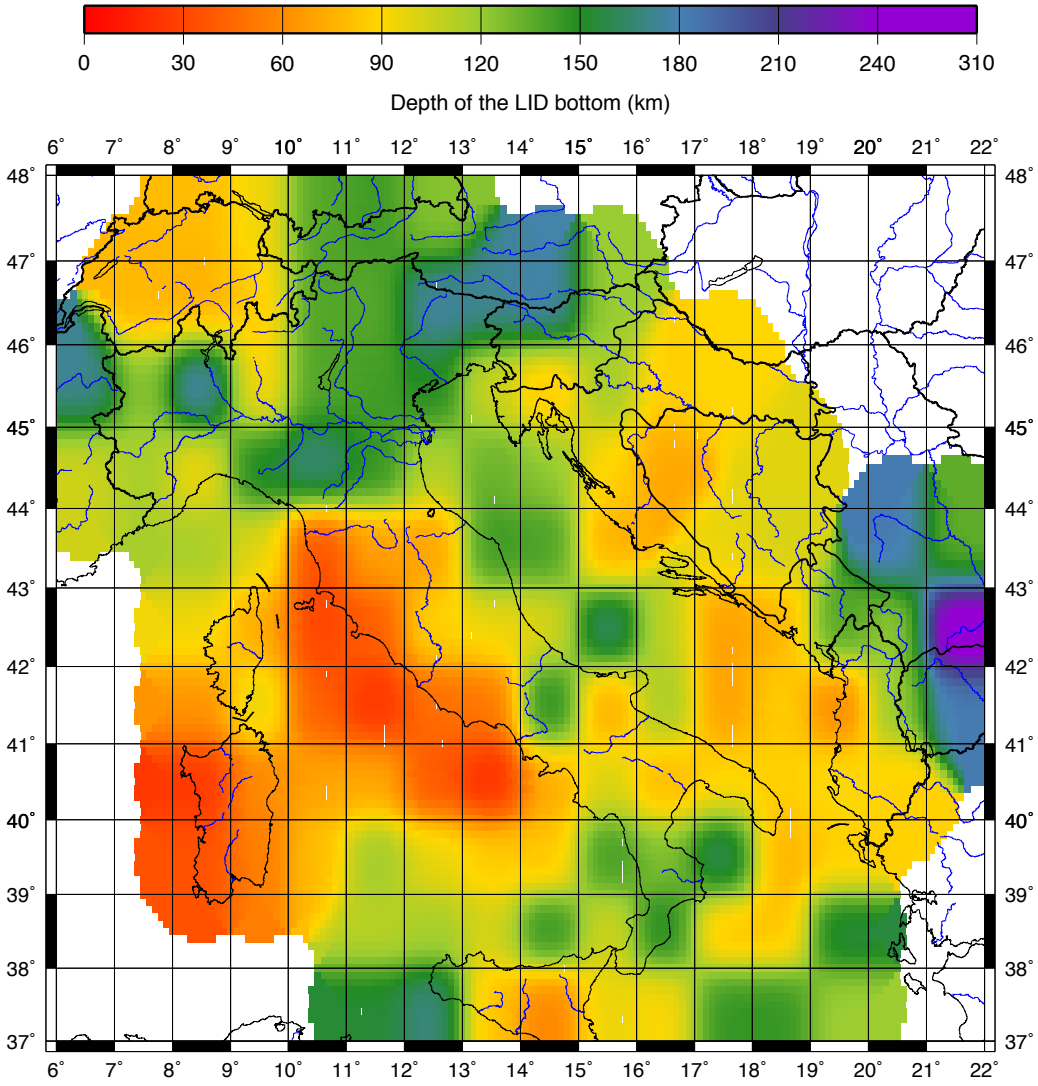

Figure 2.9: Depth of the LID bottom determined by V_S model.

Offshore Sicily, in cells C1 and C2 (Figure 2.6) a crust about 19 and 26 km thick respectively overlies a soft mantle layer (V_S about 4.25 km/s). Below a lid layer (V_S about 4.40 km/s) extends down to about 100 km depth, where the LVZ top

is likely located (V_S about 4.40 km/s). In cells C3 and C4 a crust of about 19 and 15 km of thickness respectively lies on a soft mantle layer (V_S 4.10 and 3.65 km/s respectively) extended down to 30-40 km of depth. The underlying mantle layers present slightly increasing V_S (from 4.30 to 4.65 km/s) down to the depth of about 265 km. Toward Calabria, the V_S structure of cell C5 (Figure 2.7) is appraised with the distribution of the seismicity with depth. The crust in the northern part of the cell is about 17 km thick and lies over a soft mantle layer (V_S about 4.00 km/s and thickness of 27 km), followed by lid layers (V_S about 4.55 km/s) extended down to about 280 km of depth. The crust in southern part of the cell is about 44 km thick and lies on seismic lid layers (V_S about 4.55 km/s) that extend down to about 280 km of depth. In cell C6 an about 51 km thick crust lies on lid layers (V_S about 4.50 km/s) extending down to about 221 km of depth. Offshore Ionian Sea, cells C7 and C8 present a crust of about 25 and 23 km of thickness respectively lying on a two lid layers (V_S about 4.40 and 4.65 km/s respectively) extended down to about 83 km of depth. Below the LVZ layer is likely located (V_S about 4.40 and 4.45 km/s respectively). Toward Hellenides, in cell C9 a crust of about 26 km of thickness lies on lid layers (V_S 4.45 and 4.70 km/s) that extend down to about 156 km, where the top of the LVZ is detected (V_S about 4.45-4.60 km/s). In cell D1 (Figure 2.6), in the Sicily Strait, an about 29 km thick crust lies on a soft mantle layer (V_S about 4.25 km/s) that extends down to about 44 km of depth. Below a lid layer (V_S about 4.40 km/s) possibly extends down to 154 km of depth, where the top of the LVZ is likely detected (V_S about 4.40 km/s). In cells D2 and D3 the crust is about 29 and 23 km thick respectively and lies on lid layers (V_S about 4.45 km/s) that extend down to about 60 and 80 km of depth respectively, where the LVZ top is likely located (V_S about 4.40 km/s). In cell D4 an about 27 km thick crust lies on two lid layers (V_S about 4.50 and 4.40 km/s) extended down to about 87 km. The LVZ layer is not clearly detected, possibly represented by a V_S about 4.45 km/s layer between 87 and 170 km of depth. In cells D5 and D6 (Figure 2.7), offshore Eastern Sicily, a 21 km thick crust lies on a soft mantle layer (V_S about 4.35 and 4.30 km/s respectively) that extends down to about 60 km depth. Below a fast lid (V_S about 4.65 km/s) layer of about 30 km thickness extends down to about 90 km depth, where the LVZ top is detected (V_S about 4.40 km/s). Toward Hellenic Trench, in cells D7, D8 and D9 a gently thickening crust (from about 25 to 29 km) lies on two lid layers (V_S about 4.50 and 4.60 km/s in cell D7, 4.45 and 4.50 km/s in cell D8 and D9) that extends down to about 150-180 km depth, thickening to the east. At this depth the LVZ top is likely detected (V_S about 4.45, 4.50 km/s and 4.50 km/s respectively).

2.5 The Sicily Channel, an example of variable lateral resolution

The structural model for the Sicily Channel area (see inset in Figure 2.1) was obtained by non-linear inversion of the dispersion curves by using the "hedgehog" method at a variable resolutions (from $1° \times 1°$ to $0.5° \times 0.5°$). The representative solution for each cell has been selected with the usual optimization method and appraised with independent data. The data used in the definition of the surface structure (first 6 km of depth) are derived from seismic profiles and crustal magnetic and gravimetric modelling (Lodolo et al., 2012). Where allowed by the data, the structure has been defined on cells of $0.5° \times 0.5°$: it is the case of the cells E2-II and E3-IV (Figure 2.10), along the profile CROP-M24, where are located magmatic bodies protruding from the seabed or buried beneath the sedimentary layer.

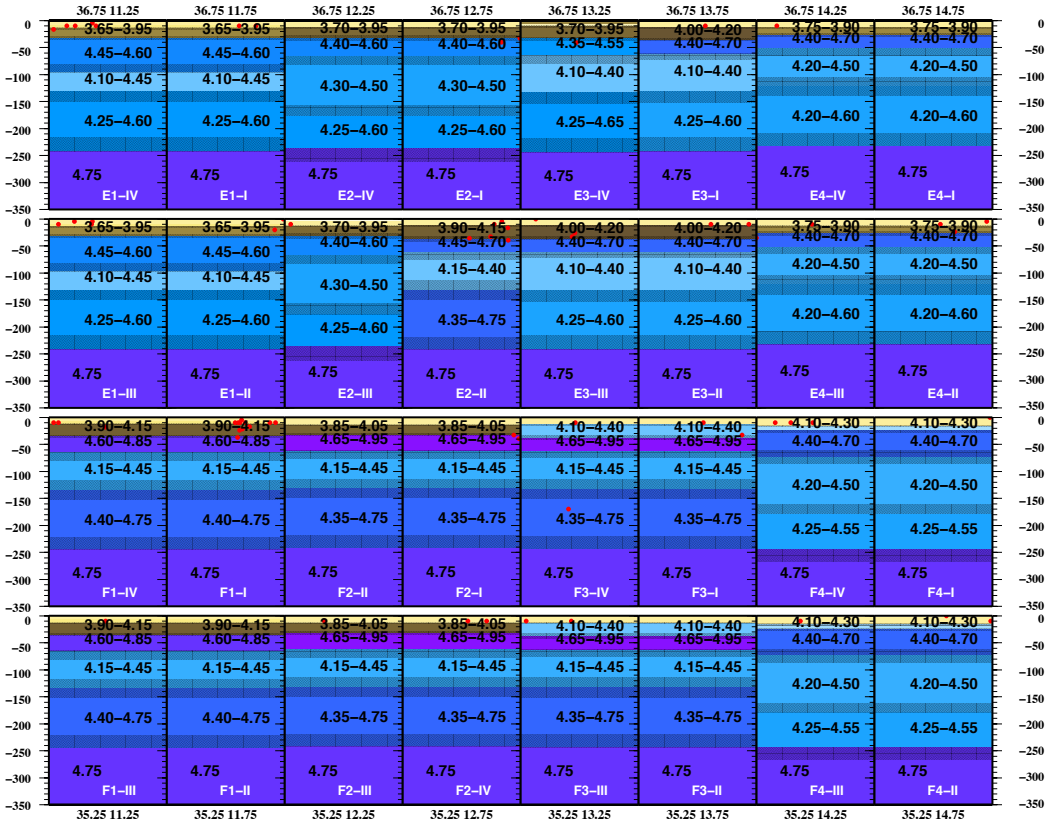

Figure 2.10: Cellular structural model at variable resolution ($1° \times 1°$ and $0.5° \times 0.5°$) for the Sicily Channel (see inset in fig. 2.1) extended down to 350 km depth. Yellow to brown colors represent crustal layers, blue to violet colors indicate mantle layers. Red dots denote all seismic events collected by ISC with magnitude ≥ 3 (1904-2011). For each layer V_S variability range is reported. For the sake of clarity, in the uppermost crustal layers the values of V_S are omitted. The uncertainty on thickness is represented by texture.

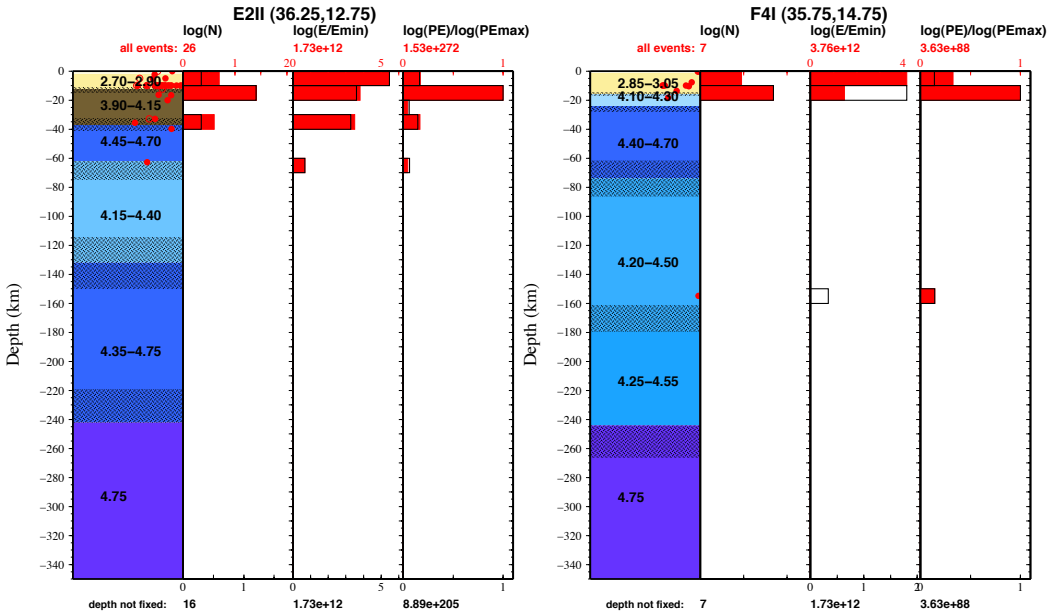

Figure 2.11: Cell E2 II (left) and F4 I (right): model and seismicity. The cellular V_S structure of the cells and distributions of seismicity. The model is plotted on the leftmost graph (a). The V_S ranges of variability in km/s are printed on each layer and the hatched rectangles outline the ranges of variability of the layer's thickness. The values of V_S in the uppermost crustal layers are omitted for the sake of clarity. The hypocentres with depth and magnitude type specified in ISC catalogue are denoted by dots. The hypocentres without magnitude values in ISC catalogue are denoted by circles. (b) $\log N$-h, distribution of the number of earthquakes with respect to depth obtained by grouping hypocentres in 10-km intervals. (c) $\log E$-h, distribution of the normalized logarithm of seismic energy for 10-km-thick depth intervals. (d) $\log \Pi E$-h, distribution of the normalized logarithm of product of seismic energy for 10-km-thick depth intervals. The filled red bars histograms represent the computation that used all earthquakes from the revised ISC catalogue for period 1904-2011. The black line histograms represent the computation that used earthquakes which hypocentre's depth is not fixed a priori in the ISC catalogue. The normalizing values of energy's logarithm $\log E_{min}$ and product of energy's logarithm $\log \Pi E_{max}$ are given on the horizontal axes of the relevant graphs.

The crustal thickness varies between 15 and 25 km, with thickening towards W-SW. The crustal seismicity is rare and the events have magnitude generally lower than 4, concentrated in the central sector, at the edge of the Pantelleria graben and in correspondence of volcanic bodies (Figure 2.11). The mantle seismicity is characterized only by sporadic hypocenters in the sub-crustal fast lid. The lid thickness varies between 50 km and 100 km, with a tendency to thickening at the western edge of the study area. In the south-east is present a layer of sub-crustal soft aseismic mantle with V_S about 4.20 km/s and thickness of about 15-20 km, overlying a high velocity lid ($V_S \approx 4.80$ km/s, Figure 2.11). This seismic velocity heterogeneity in the mantle, not found in the western and north-east parts of the study area, are probably witnessing differences in the developmental stage of the Linosa graben with respect to the Pantelleria and Malta graben. The determination

of the structural models and the analysis of seismicity in the Sicilian Channel are part of the Project of Scientific and Technological Cooperation between Italy and Israel *The Sicily Channel: a morphological and tectonic environment unique in the Mediterranean. A top-to-bottom study approach.*

2.6 The major recent seismic events in Italy

In the previous paragraphs has been discussed the wide use of seismicity distribution with depth in order to appraise the V_S model, in particular to better define the Moho depth where this discontinuity is not clearly defined by the model itself. A more detailed information about seismicity can be obtained by means of moment tensor inversion and it's useful to constrain the local stress field and thus to corroborate geodynamics interpretation. The moment tensors of the major recent seismic events ($M_w \geq 4.8$ occurred in Italy since 1997) have been retrieved by means of the non linear method named $INPAR$ (Šílený et al., 1992). $INPAR$ is a powerful inversion method that allows the use of relatively short period (as short as 10 s) waveforms. A very limited number of stations can be used to retrieve a stable source mechanism, thus $INPAR$ is particularly suitable for regions with a sparse seismic network. The confidence level of the retrieved source parameters is estimated through a genetic algorithm (Šílený, 1998). The methodology of $INPAR$ inversion is addressed in Appendix A, in which the seismic sequence that affected Emilia in 2012 is discussed in details. In Figure 2.12 the best double couple fault plane solutions of the events listed in Table 2.1 are shown. The events are plotted with different colours according to the depth of the source. The largest number of events affected central Apennines, that were hit by two major seismic sequences in the considered time period: Umbria-Marche sequence (1997) and L'Aquila sequence (2009). Most of the events in this area take place in the crust (≤ 35 km of depth) and show a normal fault mechanism, in accordance with the extensional tectonics on-going in central Apennines. Besides normal faulting a relevant number of strike-slip events are present, likely representing zones of accommodation of different extensional stress rates through the Apennines chain. However some intra-slab thrust seismicity is likely present (event 4, table 2.1) in the depth range 11-35 km.

A more complex seismic pattern characterizes the northern part of the Apennines and the related Po Plain foredeep, where a major seismic sequence hit in 2012. Normal faulting prevails in the inner front, as shown by Pondrelli et al. (2006) in their review of the CMT and RCMT Italian dataset. Conversely, thrust

to strike-slip faulting is dominant in the external front and on the buried faults below the Po Plain. Some lower crust earthquakes show a clear strike-slip mechanism, probably generated by buried faults located at the salient-recess interfaces (Cuffaro et al., 2010). Relevant intermediate (36 - 100 km) seismicity is also present in the northernmost part of the Apennines chain, both on the inner and the external front. North-eastern Alps show limited seismicity in the considered period, and the observed shallow thrust to strike-slip mechanism are fairly in agreement with the compressional tectonics of the area. Also southern Italy presented limited seismic activity in the time period and magnitude range considered, mostly concentrated along the Calabrian arc and the Tyrrhenian margin, with some minor events in the Ustica volcanic area. On the inner front of the Calabrian arc, as shown in Figures 2.6 and 2.7, the seismicity is distributed across all the subducting slab till 350 km of depth. A seismic sequence is actually active in the Pollino massif, with low magnitude events occurring since two years and a moderate magnitude (M_w 5.1), very shallow normal fault event occurred on October 25^{th}, 2012 near Mormanno.

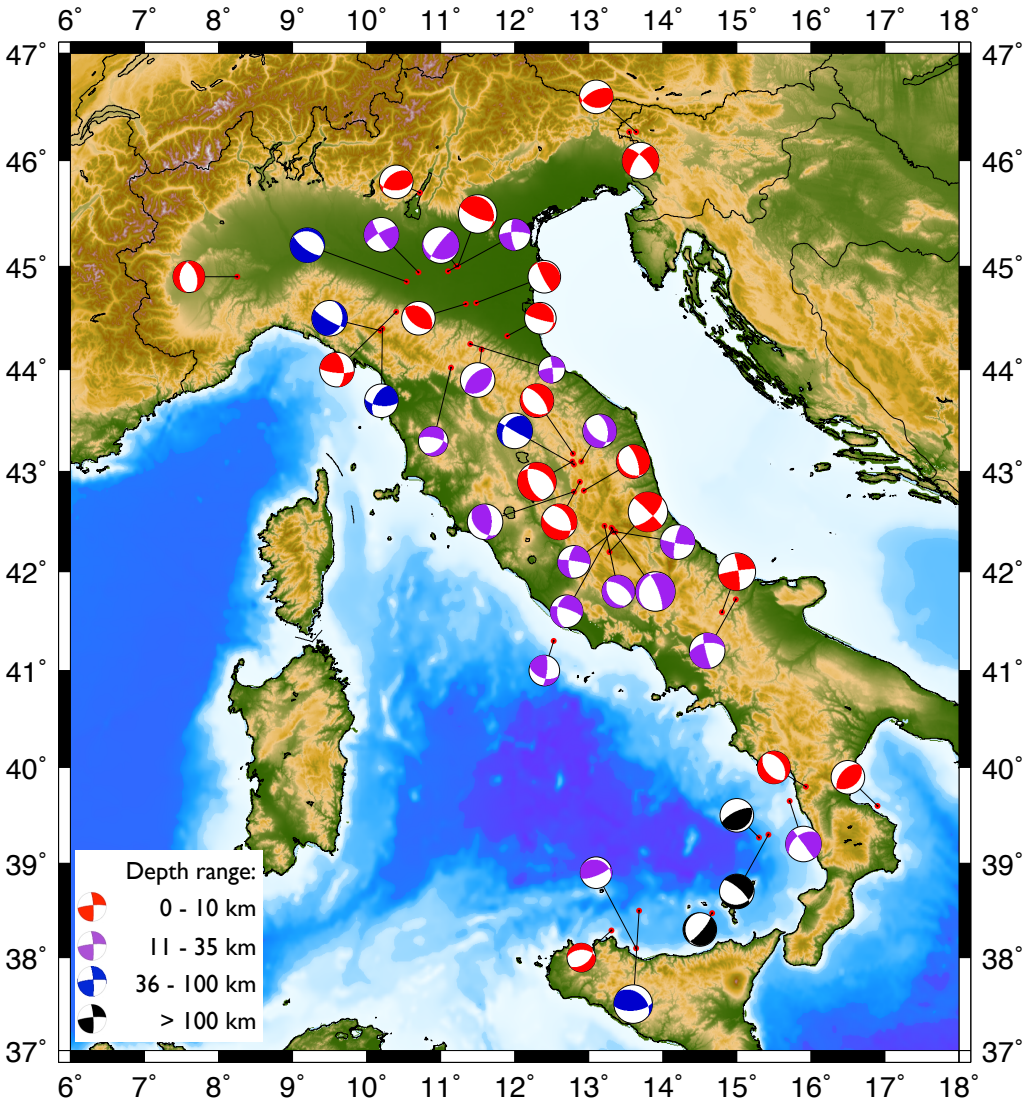

Figure 2.12: Fault plane solution of the major events ($M_w \geq 4.8$) that affected Italy since 1997 (listed in Table 2.1). Different colors represent different source depth intervals.

Event ID N.	Date(dd/mm/yyyy)	Time (hh.mm.ss)	Lat (deg)	Lon (deg)	Depth (km)	M_w	Nodal Planes (strike, dip, rake) (deg)
1	26/09/1997	00.33.12	42.90±.2	12.88±.2	3±3	5.6	333 42 -57 / 112 56 -116
2	26/09/1997	09.40.27	43.10±.1	12.78±.2	6±2	6.0	299 42 -123 / 160 56 -64
3	03/10/1997	08.55.21	43.10±.1	12.90±.2	20±1	5.2	353 51 -56 / 126 50 -124
4	06/10/1997	23.24.52	43.06±.1	12.80±.1	27±1	5.5	135 41 52 / 1 59 118
5	12/10/1997	11.08.36	42.81±.1	12.93±.1	5±2	5.2	342 70 -78 / 131 23 -119
6	26/03/1997	16.26.11	43.07±.1	12.80±.1	50±20	5.5	120 89 127 / 211 37 1
7	03/04/1998	07.26.37	43.18±.1	12.79±.1	10±1	5.2	320 65 -86 / 130 25 -99
8	12/04/1998	10.55.32	46.27±.1	13.55±.1	10±4	5.7	216 67 -20 / 314 72 -156
9	18/05/1998	17.19.05	39.27±.1	15.30±.2	278±1	5.3	50 20 77 / 244 71 95
10	09/09/1998	11.27.59	39.65±.1	15.71±.2	20±10	5.6	233 44 -1 / 324 89 -134
11	10/05/2000	15.09.01	44.33±.1	11.90±.2	8±7	4.9	106 82 75 / 350 17 153
12	21/08/2000	17.14.31	44.90±.1	8.25±.1	7±1	5.0	343 50 -105 / 187 42 -73
13	17/04/2002	06.42.54	39.60±.2	16.90±.3	10±3	5.2	54 39 101 / 219 52 81
14	06/09/2002	01.21.29	38.50±.1	13.68±.1	40±1	6.0	85 62 65 / 310 37 129
15	27/09/2002	06.10.45	38.10±.1	13.64±.2	21±6	5.0	68 75 73 / 298 23 138
16	31/10/2002	10.32.59	41.59±.1	14.80±.2	7±1	5.8	261 85 173 / 352 83 5
17	01/11/2002	16.52.10	41.72±.1	14.99±.2	15±10	5.6	262 54 -171 / 167 82 -37
18	14/09/2003	21.42.52	44.20±.2	11.55±.1	32±1	5.4	227 56 89 / 49 34 91
19	05/05/2004	13.39.44	38.47±.1	14.67±.1	230±20	5.2	182 15 -128 / 41 78 -81
20	12/07/2004	13.04.07	46.27±.1	13.64±.1	7±1	5.3	101 36 122 / 243 60 69
21	24/11/2004	22.59.40	45.70±.2	10.72±.1	10±3	5.2	231 47 64 / 87 49 115
22	22/08/2005	12.02.09	41.30±.4	12.53±.1	12±4	4.8	6 76 137 / 109 48 19
23	01/03/08	07.43.16	44.02±.1	11.14±.1	11±4	4.6	38 40 -147 / 281 69 -55
24	01/03/2008	08.43.51	44.25±.1	11.40±.1	12±1	4.2	263 78 175 / 354 85 12
25	17/12/2008	21.57.47	39.30±.1	15.43±.2	221±11	5.4	81 26 -138 / 312 73 -70
26	23/12/2008	15.24.26	44.56±.1	10.40±.2	8±3	5.4	355 57 163 / 95 76 34
27	23/12/2008	21.58.30	44.40±.2	10.21±.1	40±1	5.2	207 54 33 / 96 64 139
28	06/04/2009	01.32.41	42.20±.4	13.28±.1	4±2	6.2	46 64 -177 / 315 87 -26
29	06/04/2009	23.15.42	42.40±.1	13.33±.1	13±1	5.1	186 64 -5 / 278 85 -154
30	07/04/2009	17.47.43	42.44±.1	13.31±.2	35±3	6.1	205 19 -46 / 340 77 -103
31	09/04/2009	00.53.06	42.40±.1	13.36±.1	14±4	5.4	191 78 7 / 100 84 167
32	09/04/2009	19.38.22	42.43±.2	13.32±.1	12±3	5.1	185 42 -18 / 289 78 -130
33	13/04/2009	21.14.30	42.46±.1	13.21±.1	13±2	5.1	146 36 -72 / 305 56 -102
34	25/01/2012	08.06.37	44.85±.1	10.54±.1	45±2	5.4	92 74 -94 / 286 17 -77
35	27/01/2012	14.53.14	44.38±.1	10.19±.1	61±1	5.5	120 79 -117 / 10 29 -23
36	13/04/2012	06.21.33	38.29±.1	13.31±.1	5±1	4.5	268 46 -64 / 53 49 -114
37	20/05/2012	02.03.53	45.00±.1	11.23±.1	6±1	6.0	114 72 78 / 328 21 123
38	20/05/2012	03.02.50	44.64±.1	11.34±.1	2±1	5.2	128 54 89 / 309 36 91
39	20/05/2012	13.18.02	44.65±.1	11.48±.1	4±1	5.1	153 82 98 / 294 11 51
40	29/05/2012	07.00.03	45.00±.3	11.21±.1	24±14	5.7	107 26 158 / 217 81 66
41	29/05/2012	10.55.57	44.94±.1	10.70±.1	20±1	5.4	148 81 167 / 240 77 9
42	03/06/2012	19.20.43	44.95±.1	11.10±.2	17±1	4.9	269 75 -162 / 174 73 -16
43	25/10/2012	23.05.26	39.80±.1	15.93±.1	2±1	5.1	326 42 -85 / 139 48 -95

Table 2.1: Source parameters of major recent seismic events ($M_w \geq 4.8$) retrieved by INPAR inversion. The events from 1997 to 2005 are compiled from Guidarelli and Panza (2006).

Chapter 3

3D density model of the crust and the upper mantle

3.1 Introduction

As has been stressed in Chapter 2, the complexity of the Earth structure and the epistemic limit in its study which is mainly related to the very limited capability of direct measurement of its physical properties, suggest a wide multidisciplinary approach in order to constrain geophysical modelling with independent geophysical data from different fields. The measurement of the gravimetric field, which is a physical property of the Earth itself, can be very useful, if properly constrained by independent data (as a rule seismological ones), to investigate the properties of the crust and the upper mantle, possibly helping to sort about the withstanding issues of geodynamics. Mainly two approaches are used in gravity data modelling: forward modelling and inverse modelling. The first involves the generation of an Earth structure (crust or crust and mantle), which can then be modified until a satisfactory fit to observed gravity data is achieved. Its key advantage is that the geometry of the model can be controlled, while the drawback is that the changes in the model are user-driven, therefore been subjected to errors and misinterpretations by the modeller. Several methods have been developed, the least-structure approach is the most used being the most simple (sensu Occam). The least-structure approach anyway suffers of the oversimplification derived by assuming crust and mantle to be mainly laterally homogenous. Inverse modelling has the advantage that most of the work is done by the computer, thus avoiding subjective interpreter bias, although significant decision must still be made to drive inversion to believable results (Aitken et al., 2012). Among the different methods for inverse density modelling there is the 3D gravity modelling on cuboidal cells (Li and Oldenburg, 1998), which

is presented in this work and described in the following section. This method was extensively applied to upper crustal modelling, while applications to whole crust and upper mantle are relatively few (Welford et al., 2010; Brandmayr et al. 2011). A pioneering work in density modelling of the upper mantle in the study region was performed by Marson et al. (1995) along transects around the Tyrrhenian rim, constructed within the geometrical constraints imposed by the results of the interpretation of aeromagnetic, seismic and seismological data. Iterative forward modelling along several profiles crossing the Italian region was later performed by Farina (2006). The density was iteratively modified within the error band of the Nafe-Drake relation until a misfit ≤ 30 $mGal$ was achieved between the modelled and the observed gravity anomaly. Very recently, Tondi et al. (2012) obtained a 3D density model of the crust and upper mantle for the European region based on V_S-density coupling relations according to two different studies (Birch, 1964; Karato and Karki, 2001).

3.2 Method and data

The layering of each representative cellular model obtained by means of *hedgehog* inversion is used here as fixed (a priori) information to obtain a 3D density model by means of linear inversion of gravimetric data, using the inversion software GRAV3D developed by the University of British Columbia-Geophysical Inversion facility (Li and Oldenburg, 1998). The starting density model is an upgrading of that given by Farina (2006) along a set of 2D profiles in the Italic region and surroundings, therefore density is increasing, or at most constant, with increasing depth always satisfying, with the error bars, the Nafe-Drake relation. Given that the vertical component of the gravity field at the i_{th} observation location r_i is:

$$F_z(\mathbf{r}_i) = \gamma \int_V \rho(\mathbf{r}) \frac{z - z_i}{|\mathbf{r} - \mathbf{r}_i|^3} dV \tag{3.1}$$

where $\rho(r)$ is the anomalous mass distribution and γ is Newton's gravitational constant, the goal is to recover the density ρ directly from the observed gravity data F_z. Let the data misfit be given by:

$$\phi_d = \|W_d(\mathbf{d} - \mathbf{d}^{obs})\|^2 \tag{3.2}$$

where $dobs = (F_{z_1}, ..., F_{z_N})^T$ is the data vector, d is the predicted data, $W_d = diag\frac{1}{\sigma_1}, ..., \frac{1}{\sigma_N}$ and σ_i is the error standard deviation associated with the i_{th} datum. An acceptable model is one which makes ϕ_d sufficiently small. There are generally

infinitely many models that reduce the misfit to the desired value, thus the inverse problem is formulated as an optimization problem where the following objective function of the density model is minimized, subject to the constraints that the data is reproduced within a given error tolerance:

$$\begin{aligned}\phi_m(\rho) = a_s \int_V w_s w^2(z)(\rho-\rho_0)^2 dV + a_x \int_V w_x \left(\frac{\partial w(z)(\rho-\rho_0)}{\partial x}\right)^2 dV \\ + a_y \int_V w_y \left(\frac{\partial w(z)(\rho-\rho_0)}{\partial y}\right)^2 dV + a_z \int_V w_z \left(\frac{\partial w(z)(\rho-\rho_0)}{\partial z}\right)^2 dV\end{aligned} \tag{3.3}$$

where the functions w_s, w_x, w_y, and w_z are spatially dependent, whereas s, X, Y, and Z are coefficients which affect the relative importance of the different components of the objective function. The greater the ratio X/s the smoother the recovered model is along that axis direction. The objective function defined by eq. (3.3) has the flexibility to allow many different models to be constructed. The relative closeness of the final model to the starting model at any location is controlled by the function w_s. The weighting functions w_x, w_y, and w_z can be designed to enhance or attenuate structures in various regions in the model domain. The function $w(z)$ in eq. (3.3) is a depth weighting that depends upon the model discretization and observation location and it has the general form:

$$w(z) = (z - z_0)^{\frac{\beta}{2}} \tag{3.4}$$

where β is usually taken equal to 2 and z_0 is defined by the mesh. The weighting function is used to counteract the decay of the kernel function with depth, since gravimetric data has no inherent depth resolution and so the anomalies tend to concentrate in the shallower structures. It is assumed that the data are contaminated by Gaussian noise with zero mean. The inverse problem is solved by finding a density that minimizes equation (3.2) and misfits the data within the noise level. Since the density contrast is limited to a small range for any practical problems, and often there are well-defined bounds on the density contrast based on other geological information, it is possible to impose constraints to restrict the solution to lie between a lower and upper bound. Between the user-controlled parameters of the inversion, there are the number of gravimetric observations for each cell and the closeness to the reference density model. Our choice is to use a large number of observations and to relax the closeness condition. The data used for the inversion are a subset of those used to produce the Digital Gravity Maps of Italy (ISPRA, ENI, OGS, 2009). A Gaussian noise with amplitude of 1.5 *mGal* has been added

to the gravity anomaly data. The gravimetric input is defined on a mesh of 32×22 sub-cells (each $0.5° \times 0.5°$) along the x (longitude) and y (latitude) directions, thus for each cell of the seismological model four gravimetric observations are inverted. The density is thus retrieved after several iterations for each of the 12 layers, which thickness is fixed according to the V_S model layering. The final density-depth distribution for each cell is defined as the average of the values in the sub-cells. Since the observed and inverted data are Bouguer anomalies, in the water layer, when present, the Bouguer density has been used and allowed to vary only within a very limited range of density (-0.01, +0.01 g/cm^3), i.e. practically fixed.

3.3 Results

A prominent negative gravimetric anomaly characterizes the Alpine collisional belt and the northern Apennines, together with the western sector of the Po Plain (Figure 3.1).

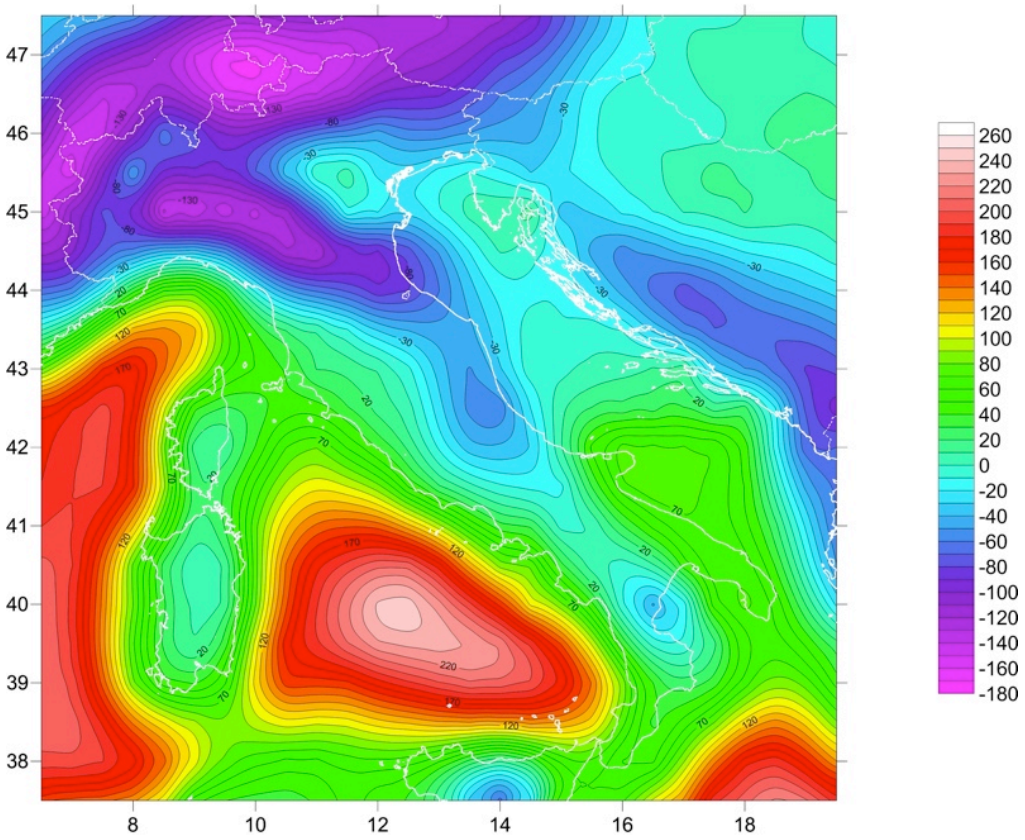

Figure 3.1: Observed gravity anomaly ($mGal$) in the study area (ISPRA, ENI, OGS, 2009)

Less marked negative anomaly is found in the northern sector of Dinarides, with

respect to the southern one, in southern Apennines and Sicily. Positive anomalies generally characterize the oceanic crust and lithosphere in Gulf of Lyon and Tyrrhenian basin, where the positive anomaly reaches its maximum (up to 240 $mGal$) in the active volcanic zone, south of $41°N$, and it is elongated in the opening direction of the basin, i.e. south-east. Similarly, strong positive anomalies characterize the southern Ionian basin (up to 220 $mGal$), even if its continental or oceanic origin is still matter of debate. The differences between the observed and predicted anomaly values show a Gaussian behaviour with a standard deviation of 1.8 $mGal$, consistent with the quality and level of the noise. The largest residuals between observed and predicted anomaly are found on the margin of the study area and they could be partially due to border effect (Figure 3.2). Relative large residuals found in western Alps, central sector of Po Plain (up to 4.5 $mGal$) and Tyrrhenian basin (up to 6 $mGal$) could be due to geometrical complexities of the lithospheric structure not present in the model.

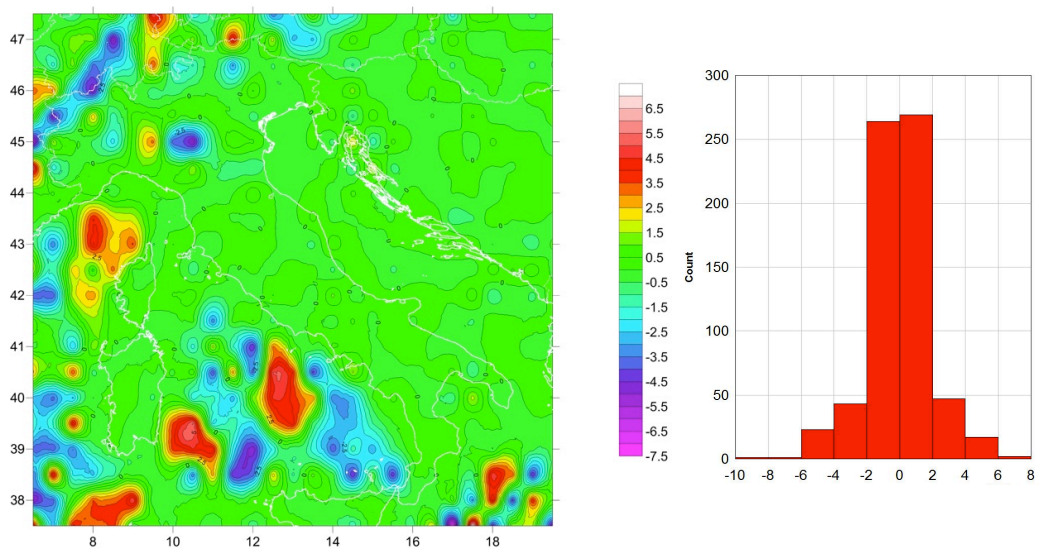

Figure 3.2: Left: residual of model to observed gravity anomaly in the study area. Right: density model uncertainties histogram of the differences between observed and model predicted gravimetric anomalies. The maximum value is 8 $mGal$, consistent with the quality and the noise level of the data.

The obtained density model is, fixed the geometry of the layers, the one between several possible models, which best fits the observed gravity data, within the experimental error. Considering a density value of 3.0 g/cm^3 as the conventional threshold between crust and mantle material, we can map the Moho depth inferred from the density model and compare it with the Moho depth inferred from the V_S model (Figure 3.3).

There is a general agreement between the two models, while in some controver-

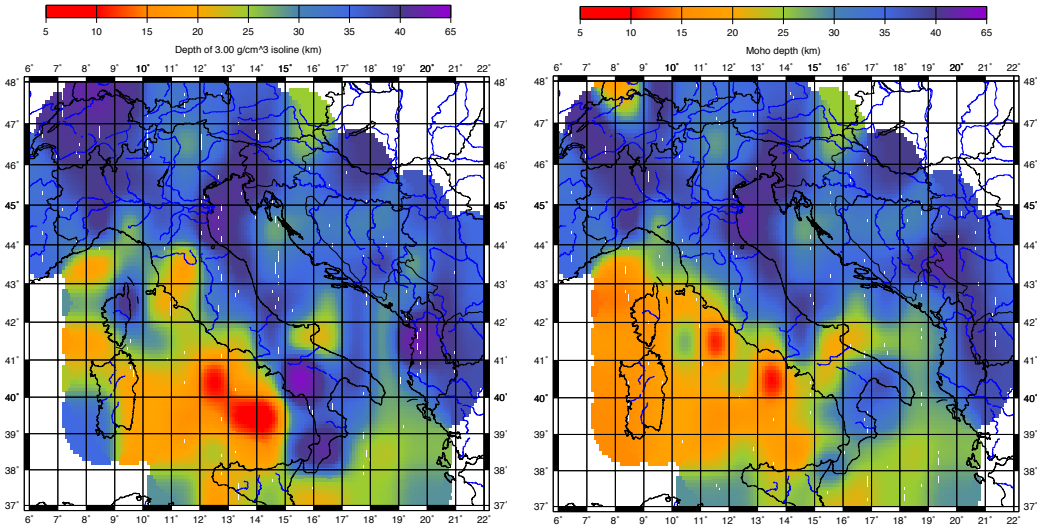

Figure 3.3: Depth of the 3.0 g/cm^3 isosurface obtained by gravity modelling (left) compared to Moho depth inferred from the V_S model (right).

sial cases the density value helps to better define the crust mantle transition where unusual high velocities in the lower crust (4.15-4.20 km/s) are present. Discrepancies still remain in about 10% of the cells (Figure 3.4) across the study area and may be due to 1) poorly resolved thickness of the lower crust layer and therefore of the crust-mantle transition defined by the seismological model, which constrains the geometrical structure of the density model; 2) anomalous properties of the lower crust layer or of the uppermost mantle layer, which need to be constrained by additional (i.e. petrological) local information.

For example, in cell A2 a crustal layer of V_S about 3.65 km/s from 6 to 26 km of depth has a density value of about 3.03 g/cm^3. The thickness of this crustal layer is probably overestimated, since from independent data Moho depth is about 16 km in this cell. In cell A3, a 5 km thick anomalous mantle layer (V_S about 4.20 km/s, density 2.95 g/cm^3) is found just below the seismological Moho (6 km of depth). In cell A5, across southern Apennines, an anomalous mantle layer (V_S 4.35 km/s, density 2.97 g/cm^3) extends for a 50 km thick just below the Moho, that is located at 21 km of depth according to the V_S model. In cell g-2, western Alps, an anomalous mantle layer (V_S 4.30 km/s, density 2.99 g/cm^3) is found just below the Moho, from 19 km to 49 km of depth. These formal discrepancies can be nevertheless reconciled with the anomalous properties of these mantle layers, in particular in the Tyrrhenian basin, where the presence of very soft mantle layers with significant percentage of magma and melt fraction is well known. Thus gravity modelling is an useful tool to image reliably the crust-mantle transition if constrained by seismological data and if gravity inversion is applied

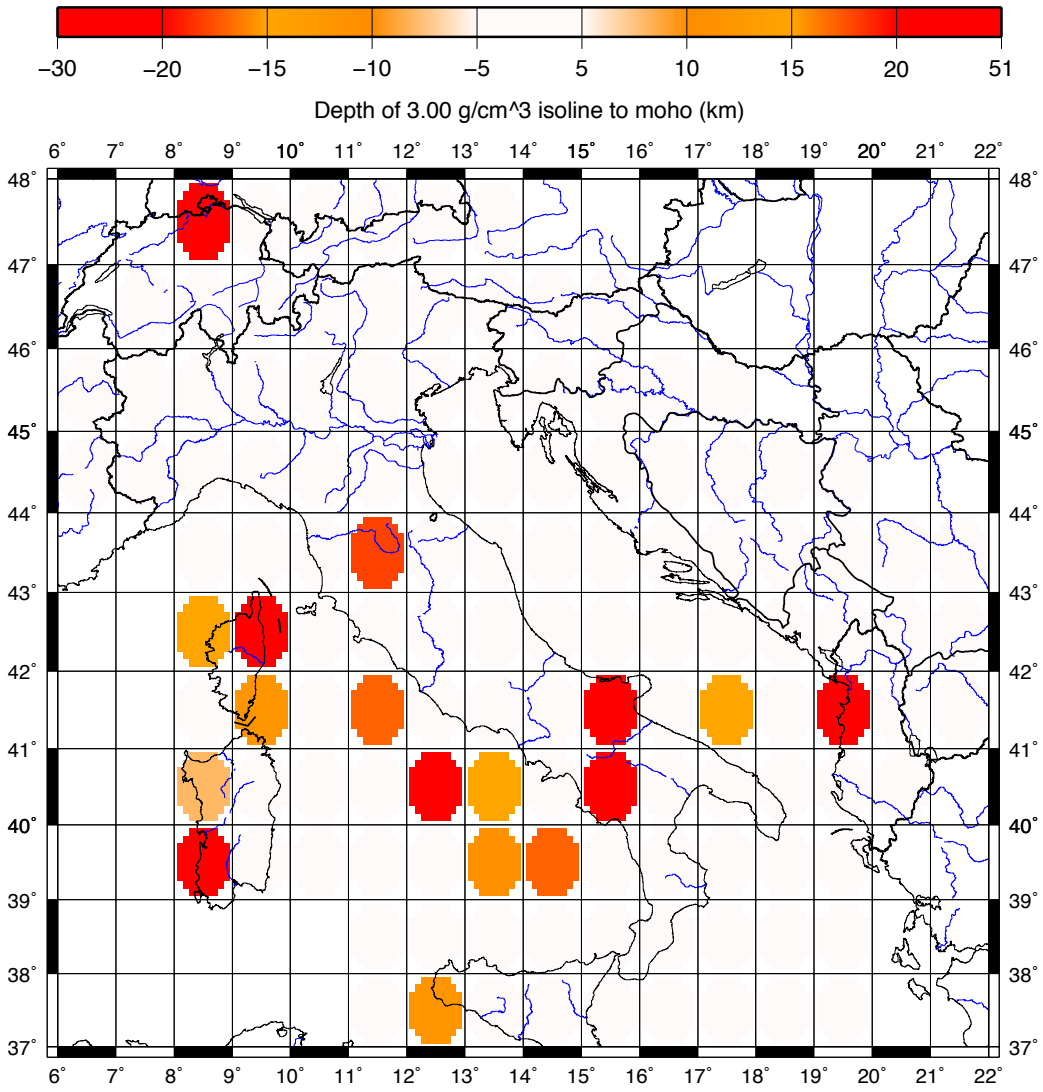

Figure 3.4: Difference between Moho depth inferred from VS model and depth of the 3.0 g/cm^3 isosurface obtained by gravity modelling.

to upper mantle layers as well, as recently stressed by Aitken et al. (2012). The model reveals significant lateral heterogeneities in mantle density distribution with depth. Local density inversion is found in cells g-1 (at 204 km of depth), g0 (at 137 km of depth) and e1 (at 142 km of depth). The depth of the 3.2 g/cm^3 topography is widely variable (Figure 3.5): it ranges from 80 km to 180 km beneath Sardinia-Corsica block, Sicily and southern Apennines; from 180 km to 260 km beneath Hellenides and external front of Dinarides, and, locally, in Western and Eastern Alps; it is shallower, ranging from 30 km to 80 km beneath the Po Plain, Central Alps, Adria, northern Apennines and Tyrrhenian basin.

Despite a clear pattern is not defined by its topography, it is nevertheless evident that the 3.2 g/cm^3 isosurface is depressed, with respect to neighbouring mantle,

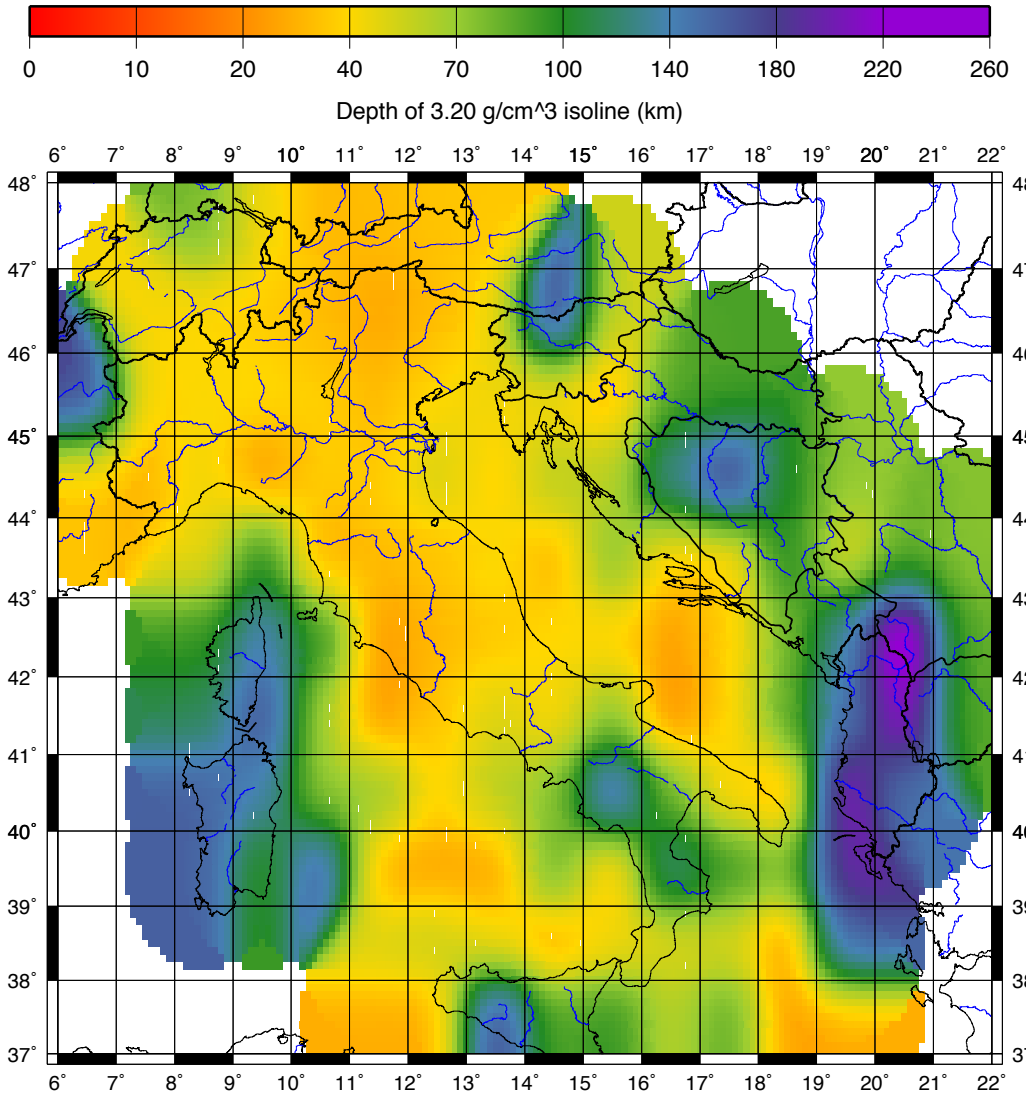

Figure 3.5: Depth of the 3.2 g/cm^3 isosurface obtained by gravity modelling.

at least in the southern Apennines and Dinarides-Hellenides subduction zones. A more clear-cut image is given by mapping the 3.3 g/cm^3 isosurface topography (Figure 3.6): this turns out to be even more variable than the 3.2 g/cm^3 isosurface and clearly depressed across all the subductions zones.

It ranges from 180 km to 310 km across the Alpine belt, Dinarides, Hellenides, Apennines, western sector of Po Plain, Sardinia-Corsica block and Sicily. Few exceptions are locally found in northern Alps and in northern Dinarides, where the depth ranges from 32 km in cell g0, where a prominent density inversion is found at 137 km of depth (3.25 g/cm^3) to 79 km in cell g-2. The depth of the 3.3. g/cm^3 isosurface is shallower beneath the eastern Po Plain, Adria, Tuscany, Tyrrhenian basin and south-eastern Ionian sea, ranging from 30 km to 90 km. Thus we can

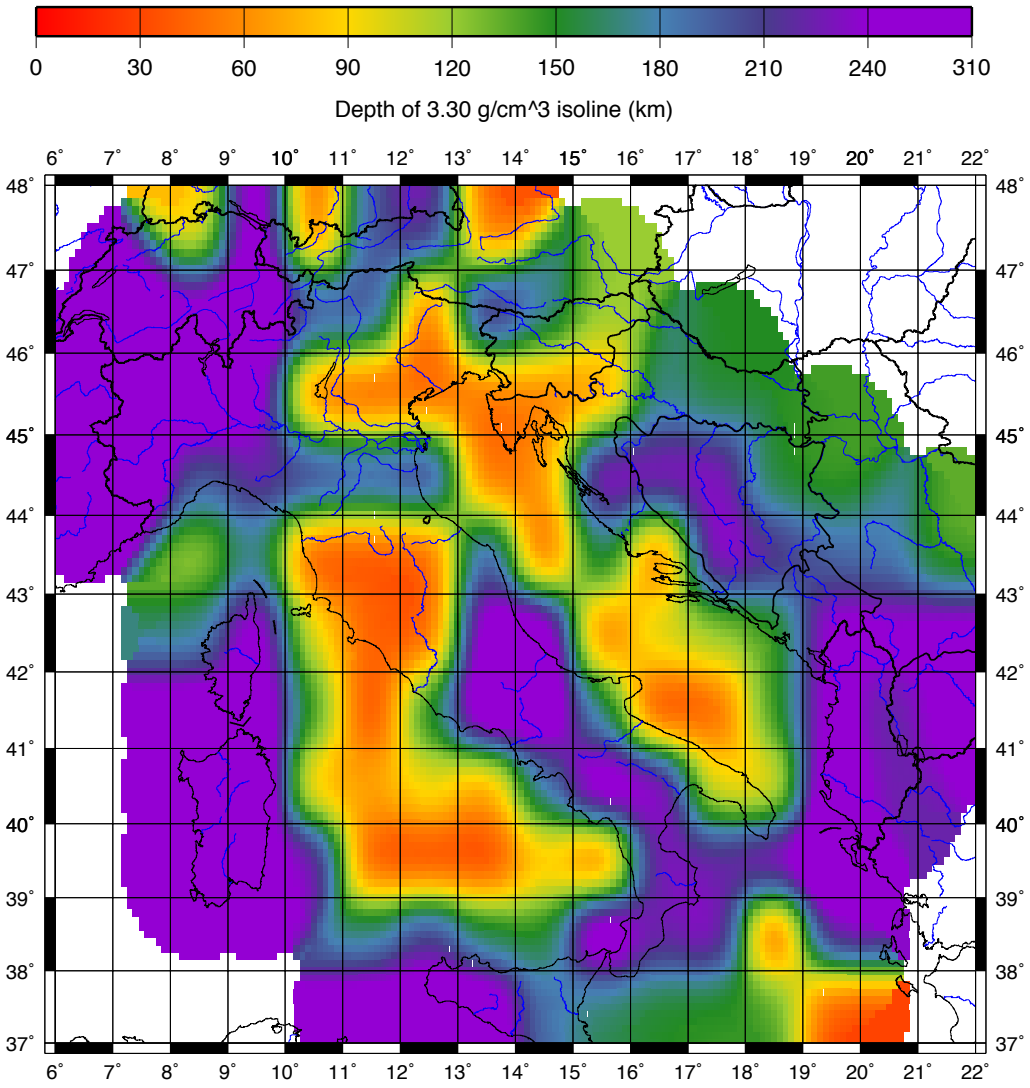

Figure 3.6: Depth of the 3.3 g/cm^3 isosurface obtained by gravity modelling.

summarize that mantle densities are generally high ($\geq$ 3.3 g/cm^3) beneath southern Tyrrhenian basin, Adria and western sector of the Po Plain, while are relatively low ($\leq$ 3.3 g/cm^3) beneath Alps, Apennines, Sardinia-Corsica block and Dinarides, i.e. mantle density is not higher in subduction zones than in the ambient mantle, despite of what is generally assumed. This is a robust feature of the model and it persists regardless of the orientation or type (i.e. Alps or Apennines) of collision/subduction. Western Alps and Sardinia-Corsica block present a common distribution of density with depth, with a relative low-density mantle with respect to surroundings (3.3 g/cm^3 at about 230-250 km). This similarity may be due to their common origin, since Sardinia-Corsica block is a fragment of the European Plate (Lustrino et al., 2009 and references therein). On the contrary, a density

higher than the surroundings is found in the LVZ, with the 3.3 g/cm^3 density reaching depths of about 70 km, in particular in the active part of the Tyrrhenian basin (south of the $41°N$ parallel) where the asthenosphere is very shallow. Similarly, high density mantle is found beneath eastern Po Plain and northern Adriatic. The north-south asymmetry observed in the mantle velocities of the Tyrrhenian basin persists in the density model, with mantle densities which are lower in the northern part of the basin than in the southern one, the axis of symmetry being the $41°N$ parallel. Therefore higher densities in the mantle seem to be strictly related to the eastward flow itself and to its ascent beneath the back-arc basin.

Chapter 4

3D model of the crust and the upper mantle beneath the Alps at $0.5^\circ \times 0.5^\circ$

4.1 Introduction

In the present chapter are described the result of the refinement of the cellular model to a resolution of $0.5^\circ \times 0.5^\circ$ for the Alpine region. The possibility to improve the resolution of the model when suitable data for the more surficial upper crust are available has been already addressed in Chapter 2. Is well known, in fact, that the inversion is strongly influenced by the definition (fixed a priori) of the properties of the most superficial layers, whose thickness, in the study area, is variable between 4 and 7 km. Earlier examples of 2D models at a scale of 0.5° are shown in Farina (2006) and Brandmayr et al. (2010) where the information obtained from seismic reflection profiles CROP-ECORS, EGT and TRANSALP is used to define a priori the uppermost (fixed) part of the cellular models.

Here the non-linear inversion of dispersion data of surface waves is performed for a set of 104 cells sized $0.5^\circ \times 0.5^\circ$ (Figure 4.1). Optimization is performed following the hierarchical scheme applied for the $1^\circ \times 1^\circ$ model, fixing the existing model solution at the boundary of the study area to avoid any border effect (nested model). The obtained model is appraised, as usual, with independent geophysical constraints and seismicity. The geometry of the V_S model is used to constrain the 3D gravity inversion. The cellular database is given in Appendix E.

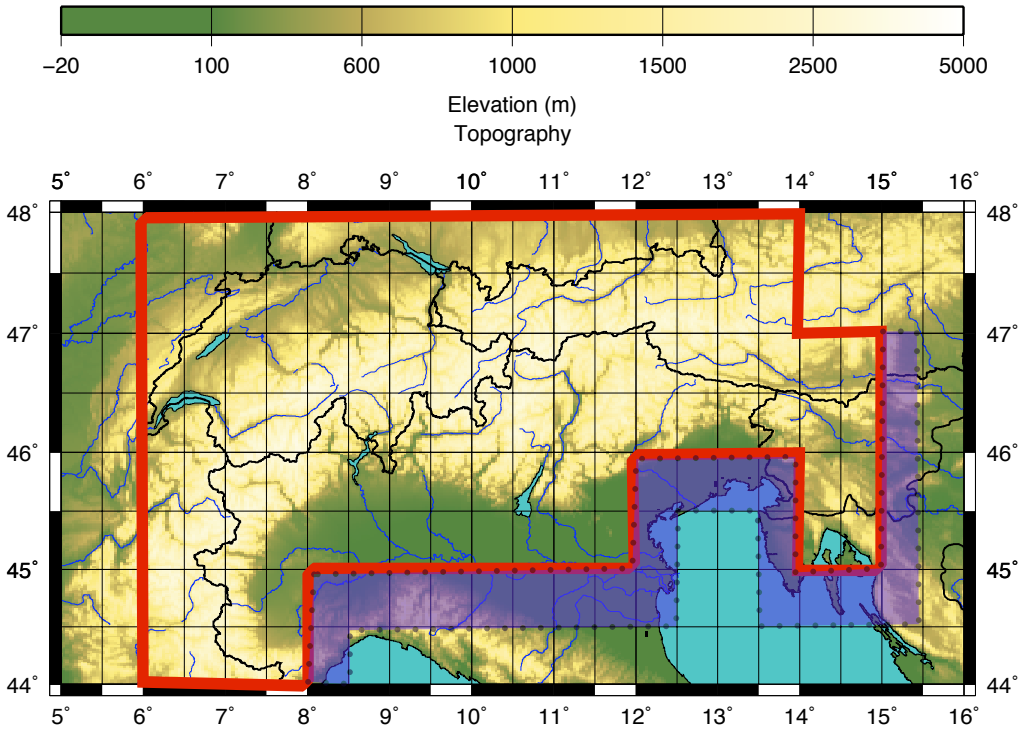

Figure 4.1: Study area of the model at 0.5° × 0.5°. Blue band is fixed in the optimization according to the 1° × 1° model.

4.2 Method and data

The most comprehensive database of surficial information for the study area is the project EuCrust 07 (Tesauro et al., 2008). The database has been used to define in particular the physical properties (V_S and density) and the thickness of the sedimentary cover (Figure 4.2), as well as the depth of the discontinuity between upper crust and lower crust (Conrad discontinuity), and the average seismic velocity of the upper crust. The Moho depth map was also used as a guide to the parameterization of the inverted layers (generally the first two inverted layers belong to the crust). Additional constraints about seismic velocities along specific profiles were taken from Cassinis (2006), Grad et al. (2008) and Šumanovac et al. (2009). In those cells where the information in the literature was not sufficient to refine the fixed surface layers, it was assumed the parameterization of the adjacent cell most similar for geomorphology and tectonic setting (actually it is the case of 27 cells out of the 104). The parameterization of the inverted layers was assumed equal to that of the pre-existing 1° × 1° model, with the sole exception of the redefinition of the thicknesses of the crustal layers, accordingly to the local depth of the Moho. The maximum number of accepted solutions has been limited to 15, with

the dual purpose to make it as close as possible to the mathematical requirement of the inversion (the number of solution is of the order of the number of inverted parameters, in this case 11) and to optimize the computation time.

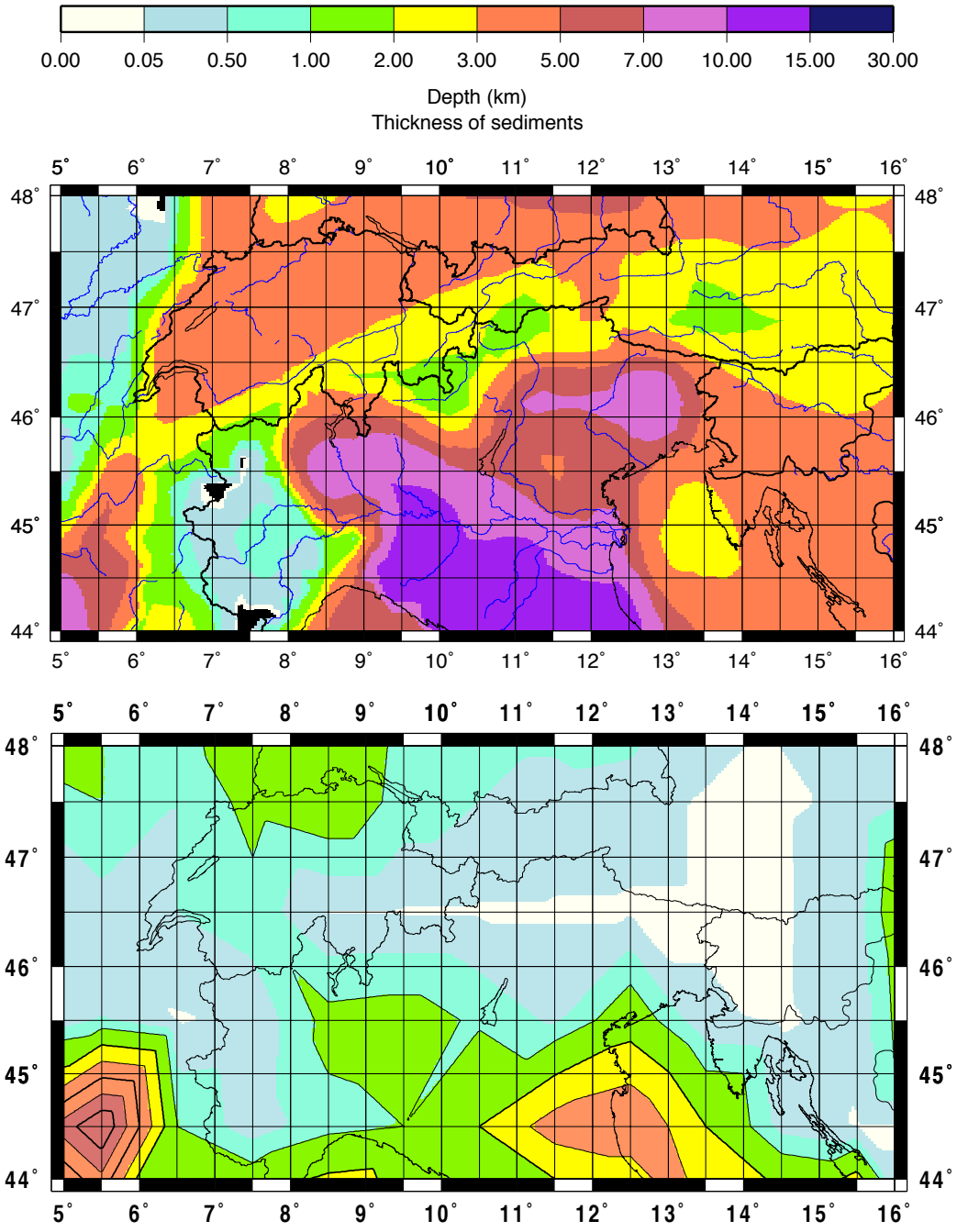

Figure 4.2: Top: thickness of the sedimentary cover according to Tesauro et al. (2008) used in the definition of the surficial properties of the refined model. Bottom: thickness of the sedimentary cover according to Laske and Masters (1997), used in the definition of the $1° \times 1°$ model.

The optimization was carried out according to the hierarchy diagram of the

algorithms defined in Brandmayr et al. (2010). As a further constraint, performing the optimization, the solutions of the cells on the border of the study area have been fixed according to the $1° \times 1°$ model.

4.3 Results

The three-dimensional model obtained, while confirming the general structural features of the model to the scale $1° \times 1°$, shows the extreme importance of the best possible definition of the fixed surface layers. Now it is possible to appreciate not only the extreme variability of the crustal thickness in the Alps and the Po Plain but also the heterogeneity in the mantle at the Alpine, subalpine, Apennines and Dinaric collisional areas.

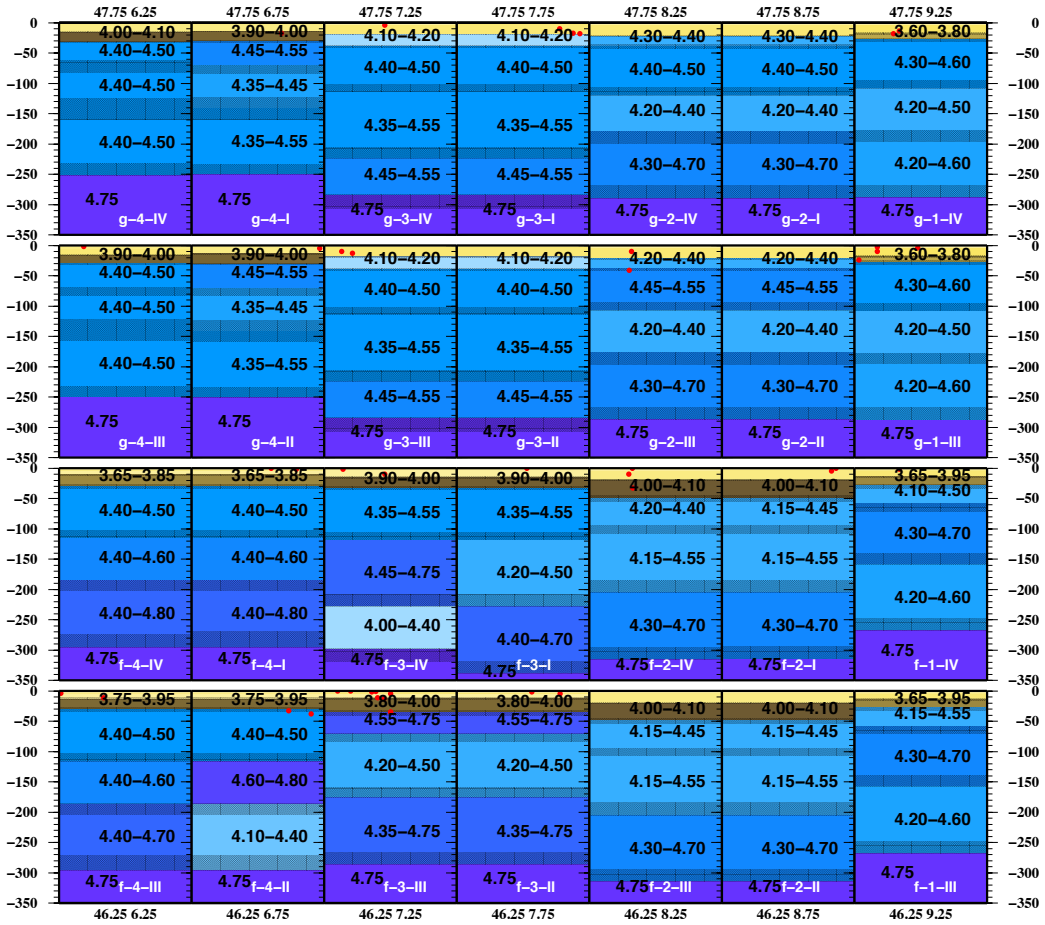

Figure 4.3: Cellular structural model extended down to 350 *km* depth for the NW Alps area. Yellow to brown colors represent crustal layers, blue to violet colors indicate mantle layers. Red dots denote all seismic events collected by ISC with magnitude ≥ 3 (1904-2006). For each layer V_S variability range is reported. For the sake of clarity, in the uppermost crustal layers the values of V_S are omitted. The uncertainty on thickness is represented by texture. All the values are given in Appendix E.

The crust presents an average thickness of 30-35 km in Jura sector, western Alps, central calcareous Alps and central Po Plain sector (Figure 4.3). Crustal thickness of more than 40 km is locally found in western Alps (cells d-4 II and e-2 III, Figure 4.4) across central sector of southern Alps (cell e0 IV) and, generally, in Eastern Alps and eastern sector of Southern Alps (cell e1 I).

Figure 4.4: Cellular structural model extended down to 350 km depth for the SW Alps area. Yellow to brown colors represent crustal layers, blue to violet colors indicate mantle layers. Red dots denote all seismic events collected by ISC with magnitude ≥ 3 (1904-2006). For each layer V_S variability range is reported. For the sake of clarity, in the uppermost crustal layers the values of V_S are omitted. The uncertainty on thickness is represented by texture. All the values are given in Appendix E.

The crust is about 25 km thick in cells g0 I, II, III, IV (Figure 4.5), across northern Calcareous Alps and in the northern sector of Dinarides and Quarnaro Gulf (cells e4 II and e4 III).

A crust of about 15-20 km thickness is found in western Molasse basin, eastern Jura sector (cells g-2 and f-2, Figure 4.3), Ivrea Zone (cell e-2 IV, Figure 4.4) and western sector of the Po Plain (e-3 II and d-3 I). V_S in the lower crust generally ranges from 3.55 km/s to 3.85 km/s. High velocity lower crust (3.90-4.15 km/s)

Figure 4.5: Cellular structural model extended down to 350 km depth for the northern Central Alps area. Yellow to brown colors represent crustal layers, blue to violet colors indicate mantle layers. Red dots denote all seismic events collected by ISC with magnitude ≥ 3 (1904-2006). For each layer V_S variability range is reported. For the sake of clarity, in the uppermost crustal layers the values of V_S are omitted. The uncertainty on thickness is represented by texture. All the values are given in Appendix E.

is found in Jura sector and Helvetic Nappes, western Po Basin (cell e-2 III, Figure 4.4), Tauern and eastern Northern Calcareous Alps (cells g2, g3) and Eastern Alps (cells f3 II, III, IV and f4 III, Figure 4.7). Values as high as 4.15 km/s for the crustal V_S (usually assumed $\leq$ 4.10 km/s according to Anderson, 2007) are compatible with metamorphism including amphibolites-facies, widespread across Northern Calcareous Alps and Eastern Alps (Handy et al., 2010).

The mantle is characterized by a thick lid ($\geq$ 160 km) across the Alps, locally thicker than 200 km in Jura sector and Helvetic Nappes, Southern Alps and western Po Plain (cells e-2 I, e-2 III, f-2 II, Figures 4.3 and 4.4), Eastern Alps (f2 IV, f3

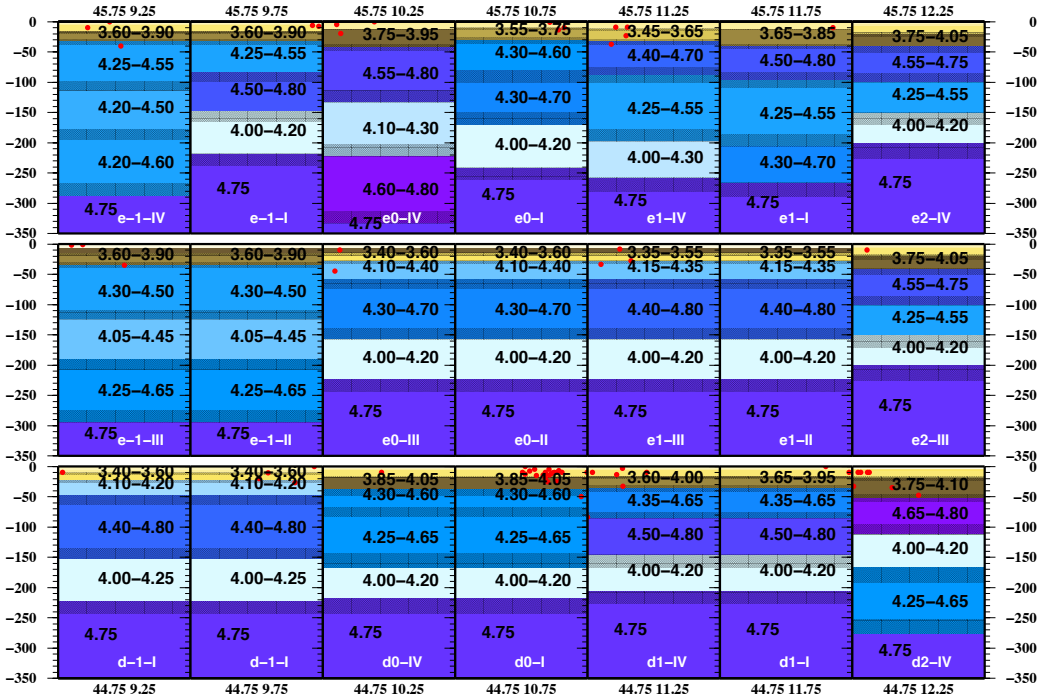

Figure 4.6: Cellular structural model extended down to 350 km depth for the southern Central Alps area. Yellow to brown colors represent crustal layers, blue to violet colors indicate mantle layers. Red dots denote all seismic events collected by ISC with magnitude ≥ 3 (1904-2006). For each layer V_S variability range is reported. For the sake of clarity, in the uppermost crustal layers the values of V_S are omitted. The uncertainty on thickness is represented by texture. All the values are given in Appendix E.

II and f4 III, Figure 4.7), where the thickness of the lid is compatible with the presence of lithospheric roots. Average thickness is in the range between 100 km and 150 km beneath Po Plain, Adria and Molasse basin.

A lid about 90-110 km thick characterizes the Ligurian Alps (cells d-3 II, III and d-2 II, III). Less than 90 km thick lid is found beneath Istria (cell e4 III, Figure 4.8), central Molasse (cells g-1 I and g0 IV) and northern Jura sector (cells g-4 I, IV). Relatively thin lid (about 100 km of thickness) characterizes Ivrea and Sesia zones, in Western Alps (cells e-3 I and e-2 IV, Figures 4.4 and 4.11). As for the $1° \times 1°$ model, the density model resulting from 3D gravimetric inversion can be used to appraise the Moho depth. If we consider the depth of 3.0 g/cm^3 isosurface, conventionally assumed as the transition density value between crust and mantle, we can see that its distribution mimics fairly well the Moho depth obtained by seismological model (Figure 4.9). Only 7 cells out of 104 present a formal discrepancy between the depth of the 3.0 g/cm^3 isosurface and the Moho depth (Figure 4.10), but in 6 of them this discrepancy can be reconciled by means of a geological less restrictive interpretation. In particular, in cell e1 I a lower crust

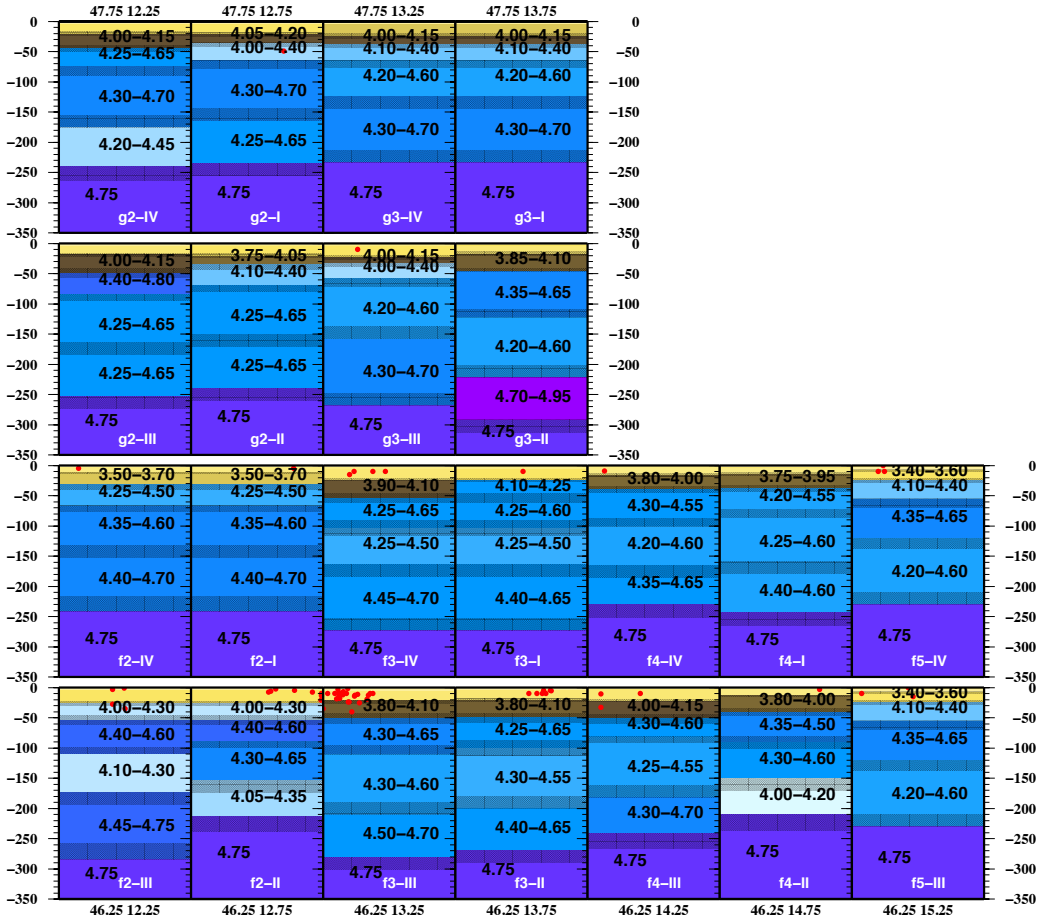

Figure 4.7: Cellular structural model extended down to 350 km depth for the NE Alps area. Yellow to brown colors represent crustal layers, blue to violet colors indicate mantle layers. Red dots denote all seismic events collected by ISC with magnitude ≥ 3 (1904-2006). For each layer V_S variability range is reported. For the sake of clarity, in the uppermost crustal layers the values of V_S are omitted. The uncertainty on thickness is represented by texture. All the values are given in Appendix E.

($V_S \approx 3.75\ km/s$) layer 28 km thick (from 13 to 41 km of depth) is probably not well resolved and causes the overestimation of the crustal thickness (about 30-35 km according to Tesauro et al., 2009) while its density resulting from gravity inversion is of about 3.12 g/cm^3 and it indicates the presence of mantle material. In cells f3 I and f3 IV the lower crust layers ($V_S \approx 4.10\ km/s$, 30 km of thickness) have a density of 3.00 and 3.01 g/cm^3 respectively, that can be considered acceptable for metamorphic crust, therefore the discrepancy is only formal and not geological.

In cells g-2 I, II, III, IV, where an anomalous mantle layer (V_S 4.20-4.25 km/s, about 15 km of thickness) just below the Moho has a density (2.97-2.99 g/cm^3) conventionally crustal, but geologically compatible with a soft mantle layer. Such small departures from conventionally defined crust-mantle density transition are not surprising in very active tectonic areas.

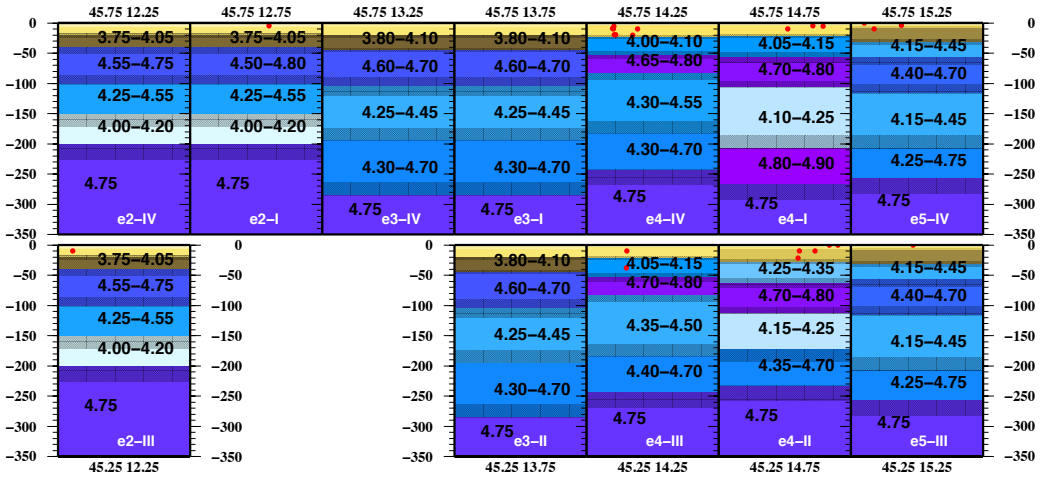

Figure 4.8: Cellular structural model extended down to 350 km depth for the SE Alps area. Yellow to brown colors represent crustal layers, blue to violet colors indicate mantle layers. Red dots denote all seismic events collected by ISC with magnitude ≥ 3 (1904-2006). For each layer V_S variability range is reported. For the sake of clarity, in the uppermost crustal layers the values of V_S are omitted. The uncertainty on thickness is represented by texture. All the values are given in Appendix E.

In order to investigate lateral density heterogeneities in the mantle, the plot of the 3.20 g/cm^3 (Figure 4.12) and 3.30 g/cm^3 (Figure 4.13) topography is used.

With respect to the $1° \times 1°$ model, the shape of the 3.2 g/cm^3 isosurface delineates more clearly the alpine subduction, where the isosurface is depressed with respect to the neighbouring mantle. It ranges from 100 km to 220 km in western Alps, eastern Alps and northern Dinarides, while it ranges from 60 to 90 km in central Alps. It ranges from 30 to 60 km of depth beneath eastern Po Plain, Molasse Basin, western Jura and, locally, beneath western Po Plain and eastern Alps. The depth of the 3.30 g/cm^3 isosurface is even more clear: it ranges from 170 km to 310 km beneath all alpine front, in Southern Alps and western Po Plain, while it is rather shallow (from 30 to 90 km of depth) beneath eastern Po Plain and Adria, central Molasse Basin (cells g0 I, IV) and western Jura sector. Intermediate depth (90-120 km) is found beneath Sesia and Ivrea zones (cells e-2 IV and e-3 I), Ligurian Alps (cell d-3 II) and, locally, in easter Northern Calcareous Alps (cells g3 II and 4). Therefore the refined model confirms the evidence that subducting slabs are not denser then surrounding mantle, but they are even lighter.

With respect to the $1° \times 1°$ model, the shape of the 3.2 g/cm^3 isosurface delineates more clearly the alpine subduction, where the isosurface is depressed with respect to the neighbouring mantle. It ranges from 100 km to 220 km in western Alps, eastern Alps and northern Dinarides, while it ranges from 60 to 90 km in central Alps. It ranges from 30 to 60 km of depth beneath eastern Po Plain, Mo-

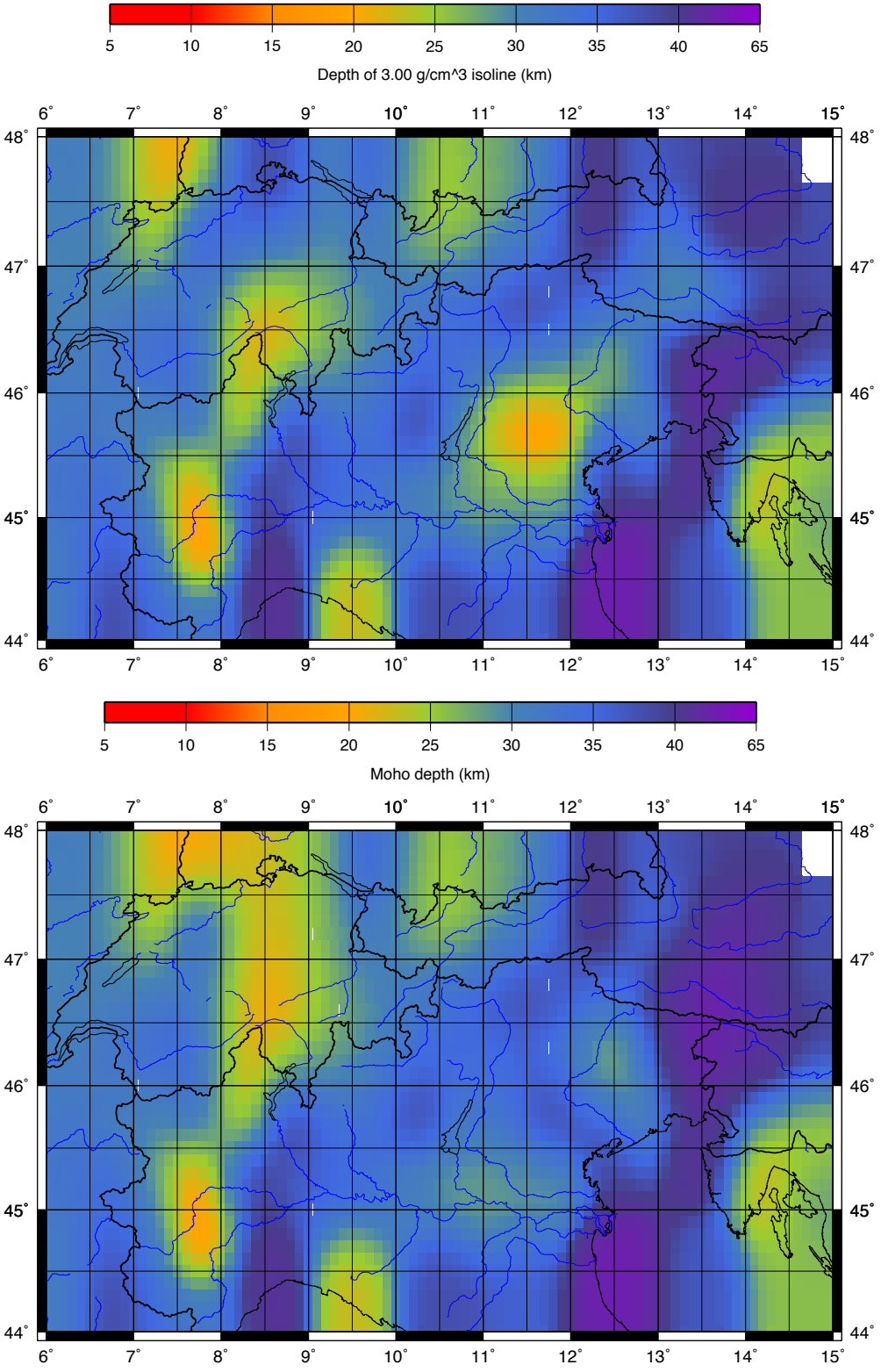

Figure 4.9: Top: depth of the 3.00 g/cm^3 isosurface determined by density model. Bottom: Moho depth determined by V_S model.

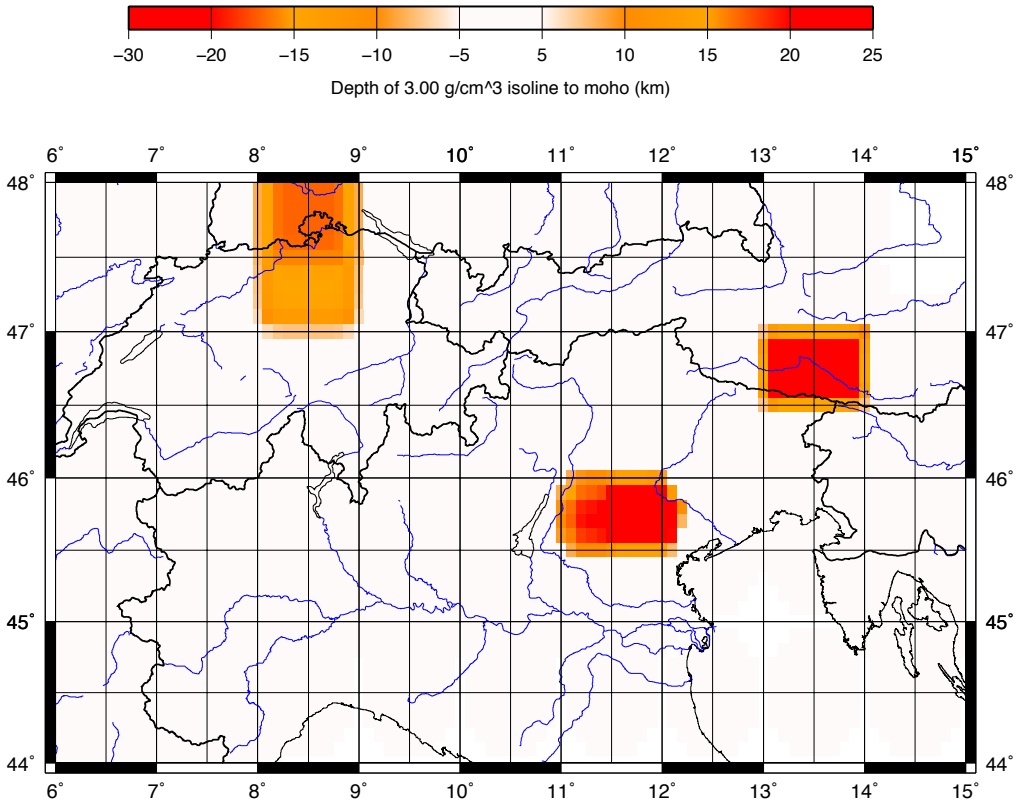

Figure 4.10: Difference between the depth of the 3.00 g/cm^3 isosurface determined by density model and the Moho depth determined by V_S model.

lasse Basin, western Jura and, locally, beneath western Po Plain and eastern Alps. The depth of the 3.30 g/cm^3 isosurface is even more clear: it ranges from 170 km to 310 km beneath all alpine front, in Southern Alps and western Po Plain, while it is rather shallow (from 30 to 90 km of depth) beneath eastern Po Plain and Adria, central Molasse Basin (cells g0 I, IV) and western Jura sector. Intermediate depth (90-120 km) is found beneath Sesia and Ivrea zones (cells e-2 IV and e-3 I), Ligurian Alps (cell d-3 II) and, locally, in easter Northern Calcareous Alps (cells g3 II and 4). Therefore the refined model confirms the evidence that subducting slabs are not denser then surrounding mantle, but they are even lighter.

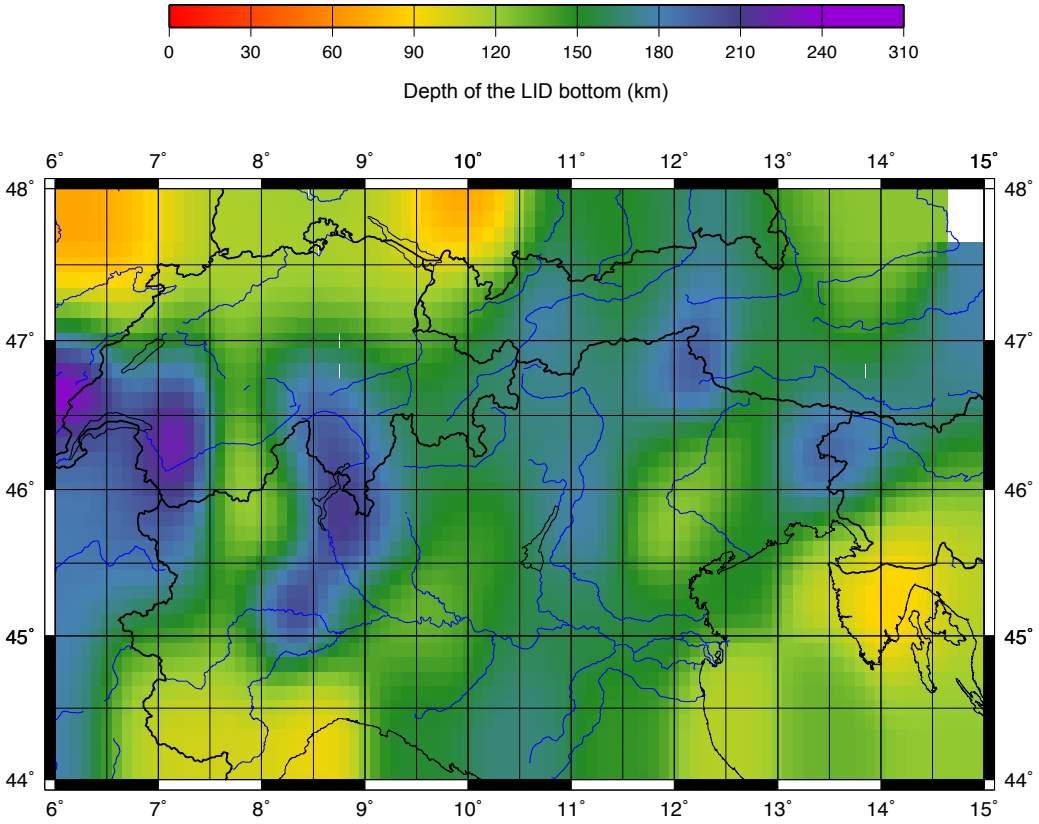

Figure 4.11: Depth of the LID bottom determined by V_S model.

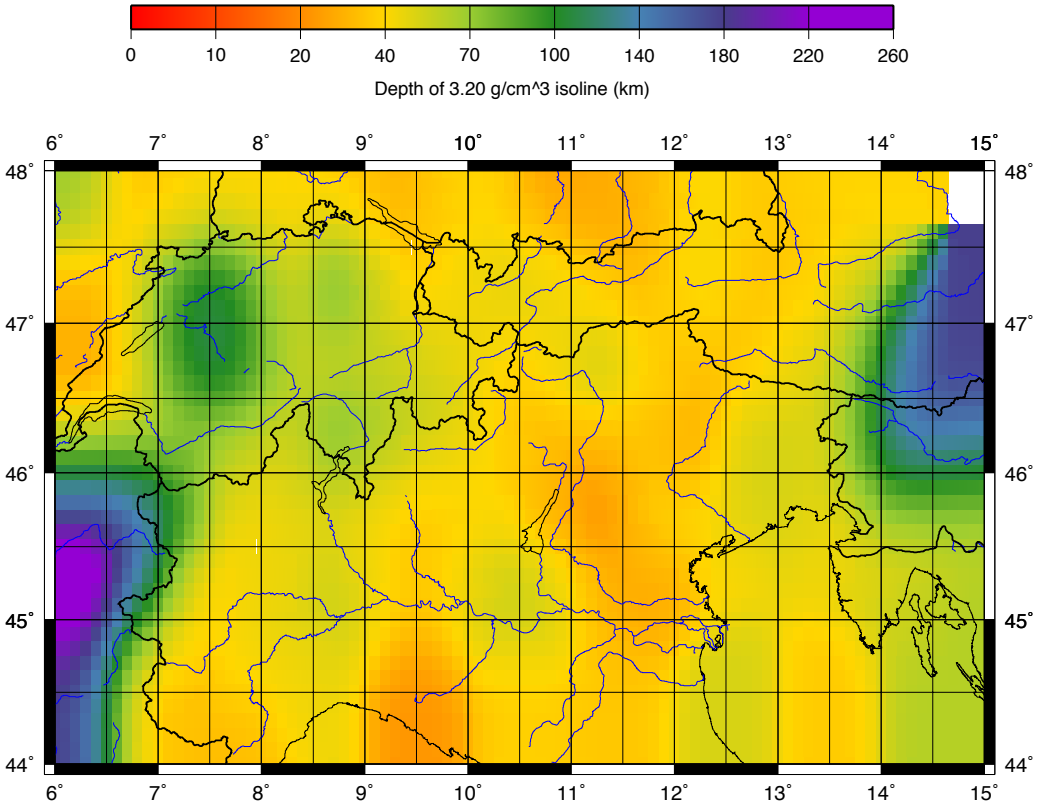

Figure 4.12: Depth of the 3.20 g/cm^3 isosurface determined by density model.

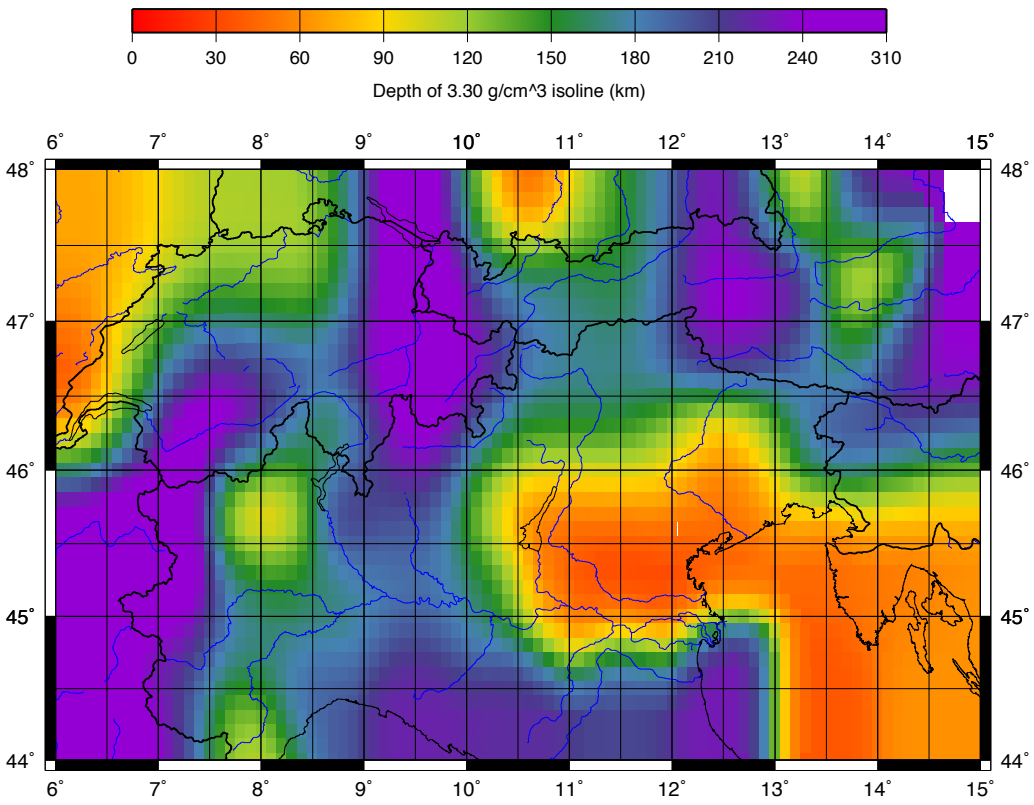

Figure 4.13: Depth of the 3.30 g/cm^3 isosurface determined by density model.

Chapter 5

Discussion and geodynamic interpretation

5.1 General discussion of the appraised model

The structural models are appraised with respect to independent information as, for instance, Moho boundary depth (Dezes et Ziegler, 2001; Tesauro et al., 2008; Grad et al., 2008). In more than half of the cells in the study area the Moho depth is in accordance with the average value reported in the literature. Considering the Moho depth uncertainties of our models and Moho depth range from the literature, the agreement rises to about 90%. The main differences are observed in cells where a steep gradient (delineating the Moho) is present (i.e. collisional or subduction zones and oceanic-continental boundaries). The crustal structure of these cells is discussed below. Some of the cells that have Moho depth in disagreement with independent studies can be considered as influenced by border effect, i.e. the cells are at the border of the study area and could not be constrained well by the optimization algorithms. In these cells we select among the cellular set of solutions one that has crustal thickness in agreement with the values in the literature, if such solutions exist. This is the case for cells e7, c10, b10 and D4. The selected models correlate well with the observed seismicity-depth distribution. Cell B-2 is on the border of the study area and present a crust thinner than the values reported in the literature, but among the set of solutions for both cells there is no model that has values for the Moho depth closer to the published ones. We consider our model for cell B-2 more realistic, and therefore preferable, since the obtained V_S models are derived from surface wave data with good coverage, especially in Sardinia region and we do not know other more detailed study of the Sardinian crustal structure.

In cells A-2, A-1 and A5 the Moho depth is shallower than the values reported

in the literature, but the obtained values are well correlated with the interpretative section across these cells given in a previous study (Panza et al., 2007b). In cell d4 a crust (25-27 km) thinner than that reported in literature (30-42 km depth) is modelled but a recent study of Sumanovac et al. (2009) indicate a crust less than 30 km thick in the Quarnaro Gulf. The cellular seismicity deeper than 20 km is almost absent. The underlying soft mantle layer ($V_S \approx 4.10$ km/s) has thickness of about 34 km and reaches 60 km of depth. The observed heat flow in this cell is low, about 50 mW/m^2 (Della Vedova et al., 2001). The selected model for cell a-1 has thin, about 16 km, crust that overlies a soft mantle layer with $V_S \approx 4.15$ km/s that reaches the depth of 28 km. The cellular seismicity is weak and the heat flow values do not exceed 70 mW/m^2. In cell a1 the Moho is observed at about 6 km of depth. The crust overlies a LID layer with V_S of 4.70-4.80 km/s that reaches the depth of about 10 km. The underlying 10 km thick soft mantle lid, with V_S of 3.65-3.85 km/s, is the most probable source of the observed high heat flow (150 mW/m^2). In cell A3 the crust reaches the depth of about 6 km and overlies a layer with V_S 4.20-4.60 km/s that reaches 11 km of depth. The underlying layers have $V_S \approx 3.50$ km/s and ≈ 4.00 km/s and thickness ≈ 10 km and ≈ 40 km, respectively therefore they can be interpreted as soft mantle, in fair accordance with the observed high heat flow ($\approx$150 mW/m^2). Alternatively we could interpret the 5 km thick layer with V_S between 4.20 km/s and 4.40 km/s as an Ultra High Pressure (UHP) metamorphosed crust with high percentage of coesite ($V_S \approx 4.60$ km/s and density of about 2.9 g/cm^3, according to Anderson 2007) and locate the Moho depth at about 20 km (as discussed in Panza et al., 2007a) but this second interpretation is not supported by the seismicity-depth distribution that is consistent with a depth of ≈ 11 km. In cell A7 a layer with $V_S \approx 4.10$ km/s extends to a depth of 35-45 km and depicts a crust relatively thicker with respect to the crustal depth values found in the literature (30 - 36 km). Nevertheless our interpretation fits well the low heat flow ($\leq$ 40 mW/m^2) that is observed in the area and with the weak seismicity in the cell, that reaches a depth of ≈ 35 km. In cell c6, a relative high V_S layer (4.05-4.20 km/s) extending between 26 km and 36 km of depth is considered as crustal according to the average crustal depth values reported in literature (32 - 43 km) and to density modelling (2.75 g/cm^3). In cell a5, the 18-22 km thick crust is thinner than the published values (29 - 38 km). It lies on a soft mantle layer (4.00 - 4.10 km/s, about 3.2 g/cm^3 of density) that reaches ≈ 45 km of depth. Similarly the cell a6 (offshore Apulia) presents a thinner crust (about 20 km) than the published values (27 - 38 km), which lies on a soft mantle layer with $V_S \approx$ 4.05-4.35 (density ≈ 3.32 g/cm^3) that extends to ≈ 45 km of depth. The observed seismicity in this layer is weak and heat flow is ≤ 65 mW/m^2.

The structural model we propose, i.e. a relative thin crust lying on a soft mantle layer, is in fairly good agreement with the presence of ancient (62-56 Ma) volcanic activity in the area, as indicated by intrusive mafic alkaline rocks outcropping in the northern Gargano peninsula (Carminati et al., 2010). In the cell a2, under Albani hills and the Tyrrhenian offshore, where the heat flow reaches 150 mW/m^2, the definition of Moho is difficult using V_S alone. The Moho can be located at ≈ 25 km of depth if, according to the seismicity-depth distribution (discussed in details in Panza et al., 2007a; Panza and Raykova, 2008), the 29 km thick layer with V_S in the range 3.90-3.95 km/s is split in two parts: 19 km thick crustal layer on top of a 10 km thick mantle layer. The results of density modelling, performed with this split layer, are fairly in accordance with this choice, and give values of 2.89 g/cm^3 and 3.03 g/cm^3, respectively for the crust and mantle layer. Similarly in cell e4 below about 23 km of depth, the 30 km thick layer with V_S about 4.00 km/s, considering the seismicity distribution that is concentrated in the uppermost 40 km (Panza et al., 2007a), can be split in two parts: a 17 km thick crustal layer on top of a 13 km thick soft mantle layer. The density modelling, performed with the split layer, gives respectively 2.95 g/cm^3 and 3.25 g/cm^3 for the crust and mantle portion of the layer, thus supporting our interpretation. The Moho depth defined in this way in the cells a2 and e4 is in fair agreement with published data. Similar procedure has been applied to cell A6. The values for the crustal thickness range from 32 km to 39 km and the heat flow ranges from 30 mW/m^2 to 90 mW/m^2. In the obtained V_S model an upper crustal layer with V_S of about 3.10 km/s reaches the depth of 19 km. In the underlying 30 km thick layer V_S varies from 4.05 km/s to 4.25 km/s. Below this layer a high velocity lid (V_S 4.65-4.80 km/s) reaches the top of the asthenosphere at about 80 km of depth. The depth distribution of the observed seismicity is analysed and the computed histograms are shown in Figure 5.1. The obtained V_S model down to the depth of 60 km is presented in Fig. 5.1a. The location of the earthquakes with magnitude specified by ISC catalogue are noted by red dots, while the events without magnitude indication are noted by red circles. The seismicity-depth distribution is presented in several histograms: logN-h distribution (Fig. 5.1b), $\log E$-h distribution (Fig. 5.1c), and $\log PiE$-h distribution (Fig. 5.1d).

All the three kinds of seismicity-depth distributions are calculated for two selections of events: all events from ISC catalogue (red histograms, related red-color annotations and writes on the top of the Figs 5.1b, c, and d) and events with depth not fixed a priori in the computation of the hypocentre (black-line histograms, related black-color annotations and writes on the bottom of the Figs 5.1b, c, and d). The Nmax in Fig. 5.1b gives the maximal number of the earthquakes in 4

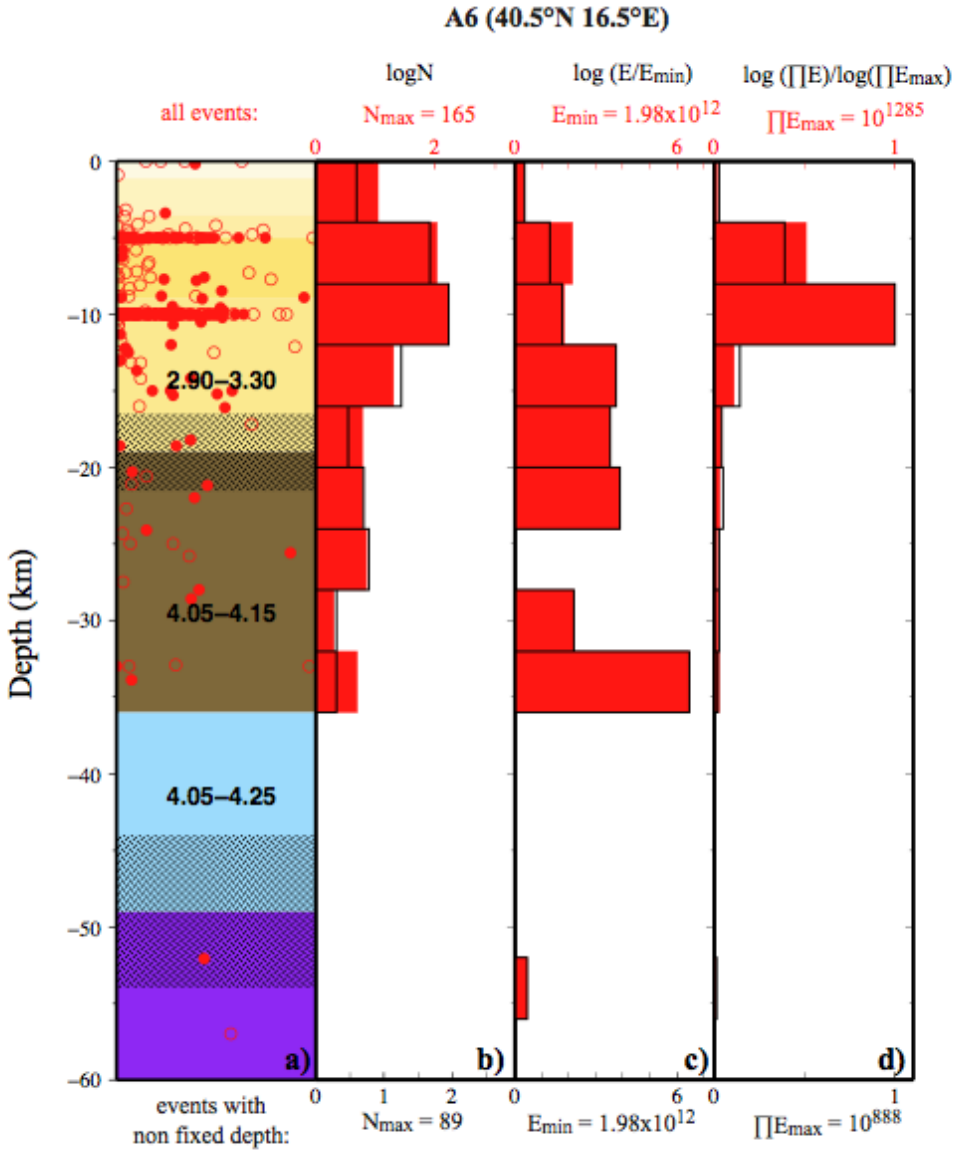

Figure 5.1: The cellular V_S structure of cell A6 and distributions of seismicity. The model is plotted on the leftmost graph (a). The V_S ranges of variability in km/s are printed on each layer and the hatched rectangles outline the ranges of variability of the layer's thickness. The values of V_S in the uppermost crustal layers are omitted for the sake of clarity. The hypocentres with depth and magnitude type specified in ISC catalogue are denoted by dots. The hypocentres without magnitude values in ISC catalogue are denoted by circles. (b) $\log N$-h, distribution of the number of earthquakes with respect to depth obtained by grouping hypocentres in 4-km intervals. (c) $\log E$-h, distribution of the normalized logarithm of seismic energy for 4-km-thick depth intervals. (d) $\log \Pi E$-h, distribution of the normalized logarithm of product of seismic energy for 4-km-thick depth intervals. The filled red bars histograms represent the computation that used all earthquakes from the revised ISC (2007) catalogue for period 1904-June 2005. The black line histograms represent the computation that used earthquakes which hypocentre's depth is not fixed a priori in the ISC catalogue. The normalizing values of energy's logarithm logEmin and product of energy's logarithm $\log \Pi E_{max}$ are given on the horizontal axes of the relevant graphs.

km thick depth intervals. The Emin in Fig. 5.1c means minimal sum of energy in the depth intervals, that is greater than 0 and that is used as the normalization factor in $\log \Pi E$-h calculation. The ΠE_{max} in Fig. 5.1d denotes the maximum of the energy product in the depth intervals, that is greater than 0 and that is used as the normalization factor in $\log E$-h calculation. Analysing the seismicity-depth distributions the clear ending of the seismicity at about 36 km is observed and thus we fix the Moho at this depth. So the lower crust (17 km thick) with V_S in the range 4.05-4.15 km/s is followed by 13 km thick soft mantle layer with V_S in the range 4.05-4.25 km/s. The presence of this shallow, thin, and soft mantle layer can be related to the elevated local heat flow data (up to 90 mW/m^2). The density modelling gives for the lower crustal layer a value of 2.72 g/cm^3, while the soft mantle layer has a density of 3.09 g/cm^3. The V_S models of the cells where the intensive deep mantle seismicity is observed are correlated with computed seismicity-depth distribution. Very intensive deep seismicity is observed in cell C5 (Figure 5.2) (area of Stromboli and Messina strait to Southern Calabria) down to the depth of about 400 km. The unconstrained V_S model selected by LSO is not consistent with the observed seismicity and independent data about the presence of a subducting slab (Panza et al. 2007a). Thus among the set of solutions for this cell only these consistent with the seismicity are considered and LSO is performed again keeping fixed the solutions in the neighbouring cells. The selected model is further analysed considering the seismicity in the northern and in the southern half of the cell separately (Panza et al. 2007a, Panza and Raykova, 2008).

The comparison between the unconstrained solution and the selected representative cellular model and their correlation with the seismicity distributions is shown in Figure 5.2a,b. The unconstrained solution is not consistent with the observed seismicity and known structural features in the region, while the constrained solution shown in Fig. 5.2b correlates very well with the seismicity-depth distributions ($\log N$-h shown in Fig. 5.2c; $\log E$-h shown in Fig 5.2d, $\log \Pi E$-h shown in Fig. 5.2e; the symbols used are the same as in Fig. 5.1). It is difficult to define the nature of the crust in the selected V_S model as a layer with V_S in the range 3.8-4.0 km/s that reaches a depth of about 44 km overlies high velocity mantle material. The analysis of the seismic energy distribution (details given in Panza et al., 2007a; Panza and Raykova, 2008) leads to two distinct interpretations for this two-faced (Janus) crust/mantle layer. Considering only the hypocentres at sea (northern half of the cell), this layer is totally aseismic and therefore it is assigned to the mantle, and the crust in this half of the cell has an average thickness of 17 km. On the other hand, considering only the hypocenters in the continental southern half of

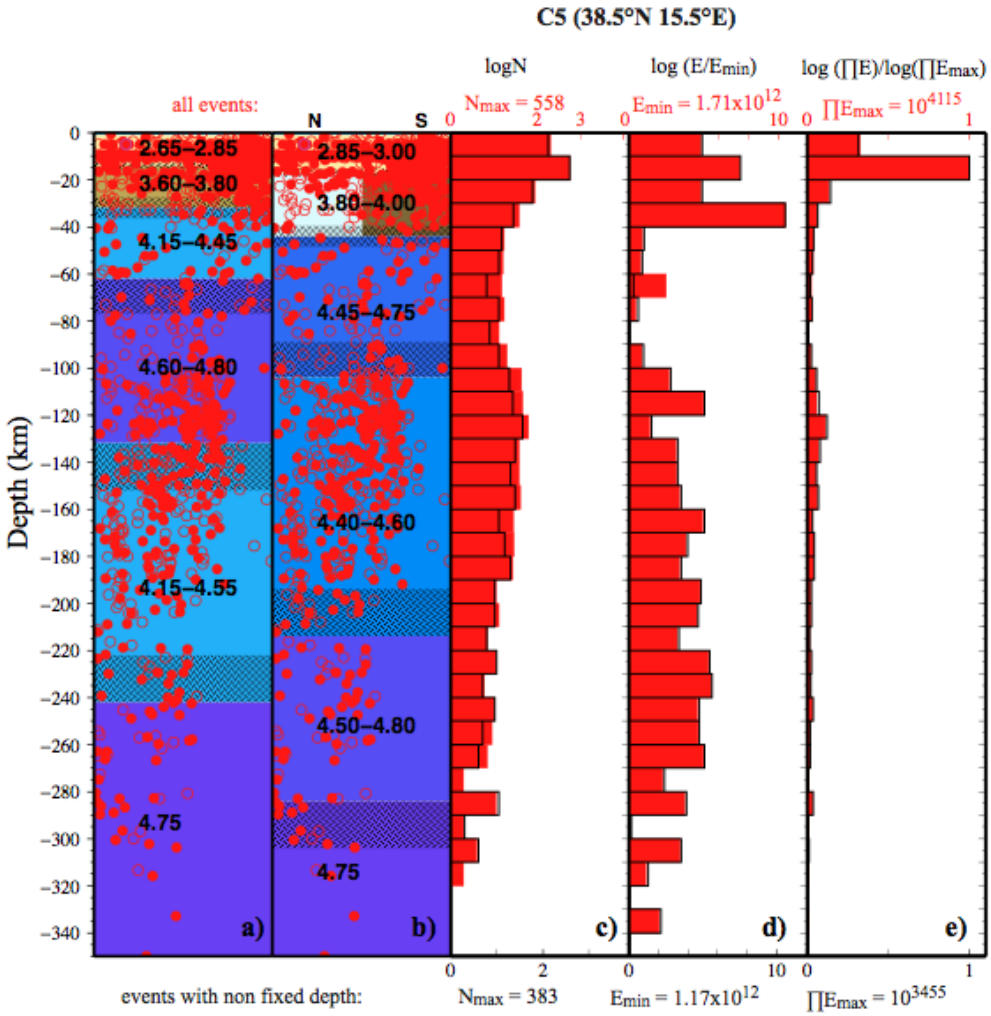

Figure 5.2: The cellular V_S structure in cell C5 and related seismicity distribution obtained grouping hypocentres in 10 km intervals: (a) the unconstrained model selected by the optimization algorithm; (b) the representative cellular model; (c) $\log N - h$; (d) $\log E - h$; (e) $\log \Pi E - h$. The symbols used are the same as in Fig. 5.1.

the cell, the *Janus* layer is seismically very active and therefore it is assigned to the brittle continental crust, which, thus, turns out to be $\approx$ 44 km thick. The modelling results confirm and better delineate some general well-known features as the presence of deep lithospheric roots in western Alps (Panza et Mueller, 1979; Dal Piaz, 1997; Farafonova et al., 2007) down to 180-200 km of depth (cells e-4, f-4, e-2 and f-2), while lithospheric roots are likely absent in northern Jura sector (cell g-4) and central sector of Northern Calcareous Alps (g-1 and g-0), where the lid thickness is about 90 km. Lithospheric roots are also detected in the eastern Alps and south-Alpine sector, across the Insubric line (cells f1, f2 and f3), where the lid extends down to 180-210 km depth, indicating a N- or NE-dipping with respect to

the lid in cells e1, e2, e3. In the central and eastern Po Valley the lid thickness ranges between 110 km and 140 km, with a prominent LVZ ($V_S \approx 4.00$ km/s) at the top of the asthenosphere below the Adria Plate (cells e0, e1, d0-d4). A lid about 90-100 km thick characterizes Ligurian Alps (cells d-3 and d-2) and Istria (e3-II and f4-III), possibly indicating the presence of a mantle wedge. The refined model obtained for the Alpine region at a scale of $0.5° \times 0.5°$ confirms the general features described in Chapter 2 and 3 and it evidences some small scale details. In particular, a relative shallower crust (about 20 km of thickness) is found in the Ivrea zone and beneath Lanzo and Dora Maira domains (cells e-2 IV, e-3 II, d-3 I), with respect to the neighbouring zones, where crustal thickness ranges from 30 km to 40 km. This observation is confirmed by the density model: the 3.0 g/cm^3 isosurface is located at the same depth. The lid thickness mimics the crustal thickness, being significantly shallower beneath Ivrea, Lanzo and Dora Maira (90-130 km) with respect to neighbouring zones (165 -210 km). This area where shallow crust and lid are observed fairly agrees with the distribution of Alpine Tethys remnants (Handy et al., 2010). The structural model obtained in the western Alps is fairly in agreement also with the V_P model proposed by Di Stefano et al. (2009) which has a comparable resolution to our $0.5° \times 0.5°$ model at least in the first 60 km of depth. Their finding of an high velocity lower crust (V_P 7.1-7.2 km/s), N-NE directed finger in western Alps is substantially confirmed by our V_S model and testifies the high-grade metamorphism, basic and ultra-basic rocks involved in the exhumation of the Adriatic plate mantle. In the Ivrea zone, Di Stefano et al. (2009) detect a prominent negative V_P anomaly just below a thinned crust, that fairly agrees with the soft mantle layer (V_S about 4.25 km/s) modeled in cells e-3 II and e-2 IV between about 20 and 40 km of depth. Adriatic plate lid generally presents higher V_S and thus is more rigid than the European plate lid. This result is in agreement with the V_P model of Di Stefano et al. (2009) and supports the possible lateral fragmentation of the plate and the formation of slab windows where asthenospheric material flows. In northeastern Italy our model fairly agrees with double verging collision between European and Adriatic plate, evidencing a variable Moho depth across the Alps, and thus supporting different shortening rates between northern and southern Alps (Brückl et al., 2010). Soft mantle layers just below the Moho are found below Engadine and Dolomites, in accordance with independent V_P model. In northeastern Italy the Adriatic plate is undergoing three different collisional process, being subducted N-ward beneath the Alps, NE-ward beneath Dinarides and SW-ward beneath Apennines. The main geodynamical features of the Apennines and Tyrrhenian basin are well delineated by the model, as the presence of relatively high-velocity bodies along the Apennines indicating the subduction of the Adria

lithosphere (Panza et al., 2007b), and the shallow crust-mantle transition beneath the Tyrrhenian Sea, with extended soft mantle layers ($V_S \leq 4\ km/s$) just below the Moho indicating high percentage of melts and magmas (Panza et al., 2007a). In general, the shallow asthenosphere beneath the Tyrrhenian supports the extension process in act following the eastward migration of Apenninic subduction (Gueguen et al., 1997; Doglioni et al., 1999), as a result of the global westward motion of the lithosphere with respect to the underlying mantle (Panza et al., 2010; Riguzzi et al., 2010). The active part of the Tyrrhenian basin (cells a0, a1, a2, A0, A1, A2, A3, B-2, B-1) is characterized by an eastward emerging LVZ from a depth of about 150 km to 30 km. The considerable thickness of the LVZ may be explained (Frezzotti et al., 2009) not only by the presence of a wide front of basaltic magma, but more likely by the simultaneous presence of small fractions of volatile elements (e.g. CO_2). This hypothesis supports CO_2 non-volcanic emissions extended from the Tyrrhenian coast to the Apennines, in the zone of relatively low heat flow as recently confirmed by means of isotopic composition analysis of CO_2 by Giustini et al. (2013), who estimated between 24 and 42% the mantle derived CO_2 beneath not only the peri-Tyrrhenian sector but also beneath pre-Apennines and Apennines belts. We therefore interpret the central Tyrrhenian LVZ as induced by the presence of carbonate-rich melts. In this picture the bottom of the LVZ at depth of 130-150 km likely represents the bottom of partially molten mantle, while its upper margin, at about 30 km depth, likely represents the upper limit of melt's ascent. To the east the LVZ vanishes in cell B5 (Paola basin), where a tick lid (V_S about 4.50 km/s) between 70 km and 150 km of depth likely represents the subducting Ionian slab (Panza et al., 2003) as also indicated by deep seismicity. Evidences of subducting slab are clear along all Calabrian Arc (cells C5, C6 and B6). The Hellenic subduction is well delineated (cells A10, B9 and C9) by an eastward thickening lid. In cell B9 a lithospheric doubling is present: a lithospheric layer extends down to about 90 km of depth, lying on an asthenospheric layer (V_S about 4.35 km/s), below which we find another high-velocity (lithospheric) layer with $V_S \approx 4.60\ km/s$, which extends down to about 200 km of depth, where a LVZ starts. The arc-shaped Ionian-Adria lithosphere supports a strong connection between Hellenic subduction and Ionian-Tyrrhenic subduction, possibly endorsing an upduction-subduction counterflow mechanism in the upper mantle (Doglioni et al., 2007; Scalera, 2007). In fact, regardless if we assume the shallow or the deep hotspot reference frame, both Africa and Anatolian-Aegean plates move westward with respect to the underlying mantle, the latter moving faster. Thus, assuming fixed the mantle, the slabs of E-NE directed subduction zones, like the Adria/Ionian plate, are actually upducting, i.e. escaping from the

mantle (Figure 5.3).

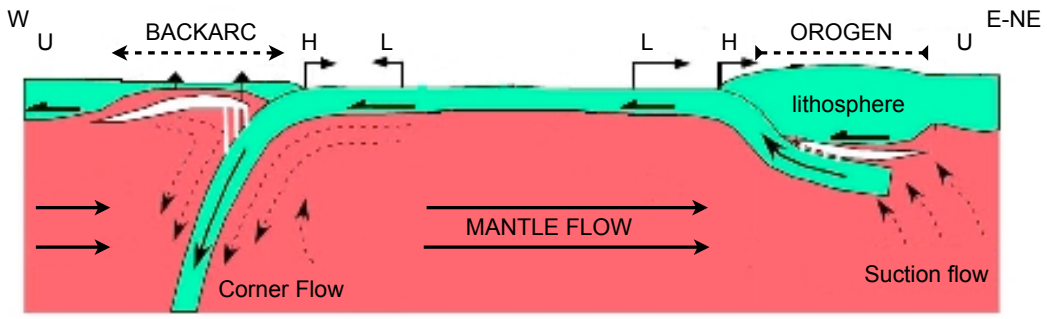

Figure 5.3: Simplified cartoon of the upduction in the Hellenides, modified after Doglioni et al., (2009). The arrows representing the motion of the subduction hinge (H) and of the lower plate (L) are referred to the upper plate (U) and not to the mantle. Ionian and Aegean plates are both moving west with respect to the mantle, but Ionian plate moves faster than Aegean plate, this resembling subduction and causing the shortening below Hellenic orogen (Doglioni et al., 2007). Ionian plate is at the same time undergoing to subduction below Calabria, with backarc spreading in the upper plate. The E-direct mantle flow with respect to the lithosphere is perturbed by 2^{nd} order turbulent effects such corner flow and suction flow.

This kinematic explanation is in natural agreement with the westward drift of the lithosphere with respect to the mantle, and it is corroborated by the evidence that Adria/Ionian plate is not undergoing any rifting process, while some rifting process would be naturally required if the Adria/Ionian lithosphere undergoes two subductions in opposite directions (i.e. W-directed Apenninic subduction and E-directed Dinaric-Hellenic subduction). This dynamic setting may involve suction of deep and fertile mantle material by the upducting slab that is imaged as an high-velocity body by seismic tomography, as recently evidenced by El Gabry et al. (2012) in the Aegean region.

5.2 Discussion of selected cross sections

Some of interpretative profiles are developed starting from seismic reflection experiments (e.g. CROP-ECORS and TRANSALP), other starting from geological sketches. The location of the sections is shown in Figure 5.4. Velocity features of most of the sections can be summarized as follows: high velocity lid characterizes subducting slabs ($V_S \geq 4.5\ km/s$); the bottom of the lid is generally marked by a velocity inversion, or at least by a null gradient, with V_S lower than 4.4 km/s; very low mantle velocities (soft mantle lid, V_S even lower than 3.6 km/s) are found in the active part of the Tyrrhenian basin, in agreement with a high percentage of melts and magmas (Panza et al., 2007a).

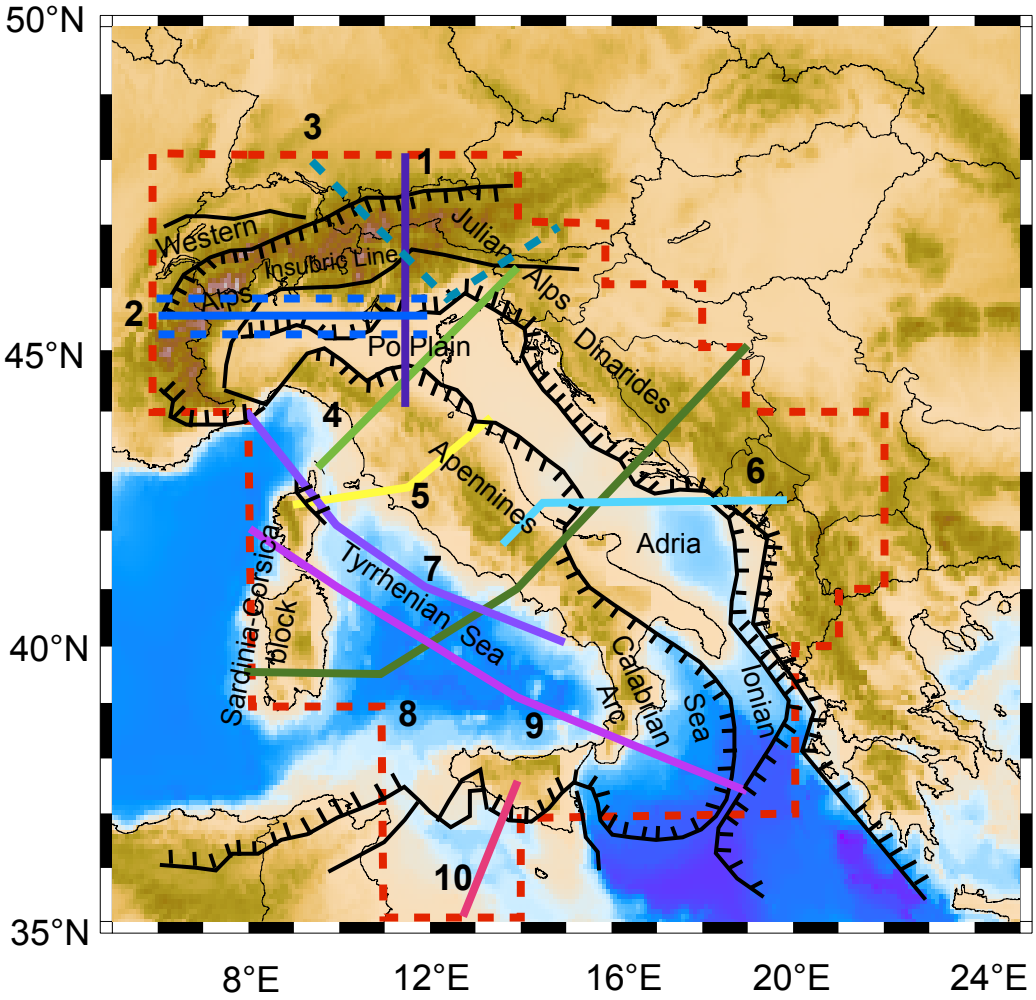

Figure 5.4: Map of the study area enclosed by the dashed bold line showing the geographical location of the considered sections. The cellular grid is omitted for seek of clarity. Main tectonic lineaments are shown, comb lines indicate compressive fronts and single lines indicate transfer zones. The sections are numbered as follow: 1) Transalp (Fig. 5.5); 2) Ecors (Fig. 5.6); 2a,b) Ecors0.5 (Fig. 5.7); 3) Alps3D (Fig. 5.8); 4) Adria43-46 (Fig. 5.9); 5) Crop03 (Fig. 5.10); 6) Adria42 (Fig. 5.11); 7) Tyrrhenian I (Fig. 5.12); 8) Sardinia-Balkans (Fig. 5.13); 9) Tyrrhenian II (Fig. 5.14); 10) CropM24 (Fig. 5.15).

In the density model, a dominant feature in all the sections, is that the subducting slabs are not denser than the ambient mantle, but they are slightly lighter. This feature persists, regardless of the orientation or type (i.e. Alps or Apennines) of collision/subduction.

The collisional process is evinced along the Transalp profile (Figure 5.5), across central Alps. This section is extended till the Apennines in order to depict a complete cross-section of the Po Plain. We note the very low angle double vergence of the European and Adriatic lid, the latter subducting southward beneath the Apennines, as supported by significant shallow and intermediate depth seismicity. The Adriatic lid appears to be faster than the European one. A soft mantle layer

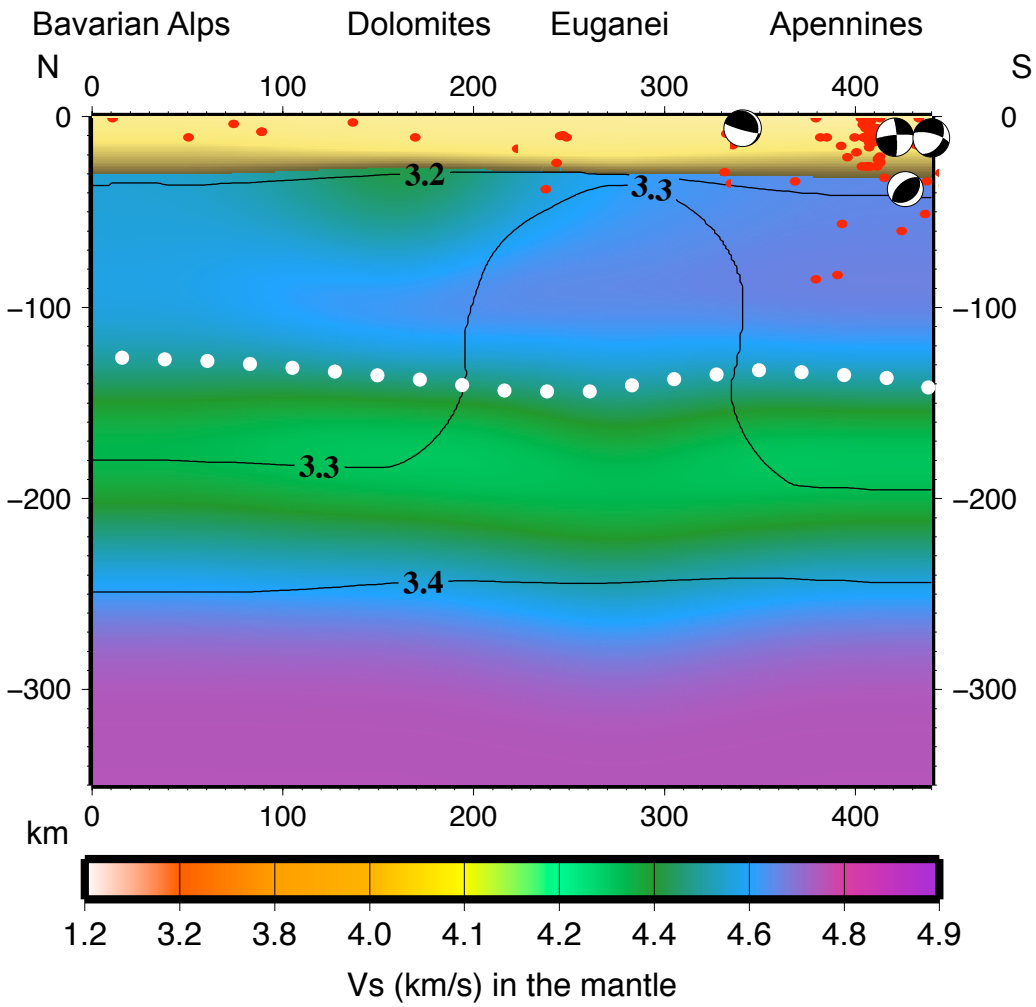

Figure 5.5: V_S and density model along a N-S profile from Bavarian Alps to Northern Apennines. V_S distribution is given by the color scale while continuous contour lines refer to density (g/cm^3). Seismicity (red dots) and focal mechanisms of major events (*beach balls* plotted in map view) are shown as well. Dotted white lines delineate the lid-LVZ margin. The low-angle subduction of the European plate below the Adriatic plate is fairly well evidenced by gently N-S dipping high velocity lid and in accordance with scarce shallow seismicity and almost absent intermediate depth seismicity, as seen in Ecors section. A relatively low velocity lid is found beneath Dolomites, just below the Moho. The bottom of the lid is found at about 120-140 km of depth and overlies a well marked LVZ in the asthenosphere. In the southernmost part of the section Apennines subduction is delineated by high seismicity that reaches intermediate depth. The prominent high-density body, as shallow as 40 km of depth, below Venetian plain, may be a signature of the Euganei Hills magmatic activity.

is found beneath Dolomites and it extends from the Moho down to about 60 km of depth. At a depth ranging from 120 to 150 km a marked LVZ is found. The section ECORS, in the Western Alps, has been extended to the east till the Adriatic coast. Major elements enlightened are the European-Adriatic plates collisional process in the Western Alps, with a thick lid subducting eastward. The presence of lithospheric roots is speculated in cell e-2 and e-1 (Milan), where an almost

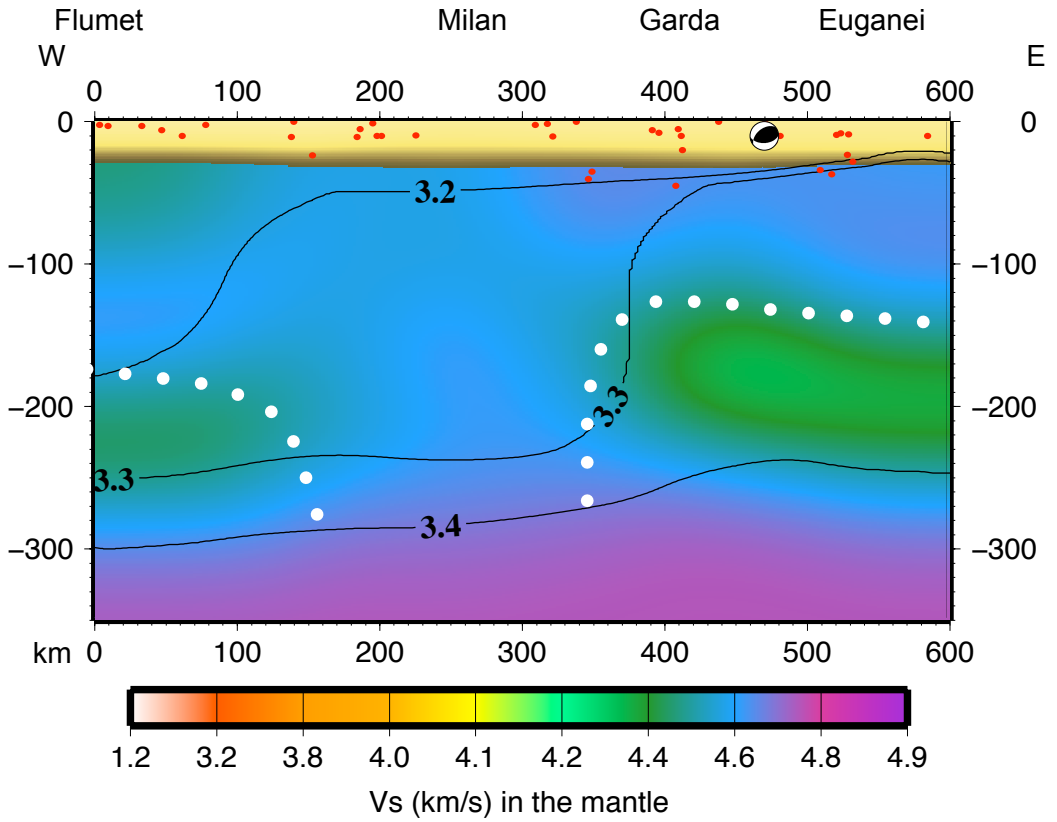

Figure 5.6: V_S and density model along a W-E profile from Flumet (western Alps) to Euganei Hills. The labelling is the same of Figure 5.5. Striking feature of the section is the subduction of the European plate below the Adriatic plate, with deep *lithospheric roots* below Milan, represented by high velocity lid, well in agreement with what shown by Mueller and Panza (1986). In contrast to Apennines subduction, no intermediate depth seismicity is observed in western Alps. To the West the LVZ is found at a depth of about 180 km. To the East, a prominent LVZ marks the Euganei Hills magmatic zone below a depth of about 130 km. The subducting lid is characterized by negative density anomaly, while a positive density anomaly is seen beneath Euganei Hills, as shallow as 30 km.

constant V_S sequence (V_S about 4.60 km/s) extends till about 280 km of depth. In cell e0 a LVZ (V_S about 4.00 km/s) is clearly seen beneath the Garda zone at depth between 180 and 260 km, fairly in accordance with the high heat flux and volcanism of Euganei hills (Figure 5.6). A more detailed picture is obtained by the model with a resolution of 0.5° × 0.5°, with small scale features visible both in the crust and in the mantle. In particular the refined ECORS profile is shown in Figure 5.7, with two W-E sections along latitude 45.75°N (a) and 45.25°N (b), respectively. Both northern (a) and southern section (b) show a thinned crust in the Ivrea and Lanzo zone respectively, lying on a SW-NE trending soft mantle mainly aseismic layer, in accordance with the V_P model obtained by Di Stefano et al. (2009) for the same area.

The lid extends down to 90-100 km of depth in the northern section (Figure

5.7a), while it is slightly ticker (about 130 km) in the Lanzo zone (Figure 5.7b). Thus the Adriatic plate indented beneath western Alps in the Ivrea-Verbano zone bended to the south beneath the Apennines and possibly broke-up undergoing torsion. Deep lithospheric roots are found both to the west (Sesia) and to the east (Bergamo and southern Alps). In both sections a prominent LVZ with relative high density ($\geq 3.3\ g/cm^3$) is seen below the eastern Po Plain and Euganei hills, while the subducting lid is generally lighter ($\leq 3.2\ g/cm^3$).

The Adriatic plate is involved in three distinct tectonic processes: the N-directed collision with the European plate, the SW- or W-directed subduction beneath Apennines and NE-directed subduction beneath Dinarides. In northeastern Italy, Alps and Dinarides developed, overlapping and cross-cutting each other, during the Cenozoic (Cuffaro et al., 2010). In fact Julian Alps and Koralpe, across Insubric Line (Figure 5.8) represent the overlapping zone of Alps with Dinarides. The subduction beneath Apennines is well modelled by the Adriatic Moho deepening and by a lid with V_S about 4.50-4.70 km/s that reaches a depth of about 160 km beneath the north-eastern Apennines (Figure 5.9).

The Apenninic subduction is clearly steeper than the NE-directed Julian Alps subduction, as confirmed by the space distribution of significant seismicity, reaching the depth of about 90 km beneath Apennines. A marked LVZ extends beneath the Adriatic lid (V_S about 4.30 km/s), while the mantle velocity is relatively higher in the western flank of the subduction (V_S about 4.40 km/s). The density model shows higher density in the LVZ with respect to the subducting lid. Although in the northern Adriatic three distinct subduction zones coexist, (i.e. the Alpine, Apenninic and Dinaric) the Apenninic subduction seems to have a dominant role, due to its present eastward migration, as marked by high seismicity and by the thickening toward NE of the Pliocene-Pleistocene sediments (Cuffaro et al. 2009). The eastward migration of the Apenninic subduction likely causes loss of lithospheric material that should be replaced by uprising asthenospheric material (Doglioni et al., 1999). This is clearly evinced along the Crop03 profile (Figure 5.10a), where the Tyrrhenian LVZ rises up to 30 km of depth, much shallower than the Adriatic LVZ, which is observed below about 120 km of depth. The shallow Tyrrhenian LVZ feeds the Tuscan volcanism, as also marked by the high heat flow (Hurting et al., 1991). The very steep shape of the subucting slab is even more clear if we consider the shear modulus (μ) obtained from V_S and density values (Figure 5.10b).

The two-opposite-side undergoing subduction processes of Adriatic plate under the Apennines and Dinarides are clearly distinguishable in Figure 5.11, which is a cross section of the Adriatic at about $42°N$ latitude. In this section, as in

section Crop03, the Apennines slab is marked by a high-velocity almost vertical body, with some intermediate depth seismicity reaching about 60 km of depth. To the West, the low velocity at a depth of about 50 km to 100 km, just above the sinking slab, is probably related to mantle wedge dynamics (e.g. dehydration). To the east, a relative low velocity, mainly aseismic, mantle lid extends for about 100 km just beneath the Adriatic crust. In the easternmost portion of the section an eastward thickening lid is well marked by high velocity and intense intermediate depth seismicity, in fair agreement with a low angle Dinaric slab. Prominent negative density anomalies characterize both the Apennines and Dinarides at a depth between 100 km and 200 km, while high-density mantle material seems to be related to the Adriatic plate, both in the lid and in the asthenospheric LVZ. According to Cuffaro et al. (2009), the Dinarides are older than Apennines, but they were downward tilted by the eastward migration of the Apennines subduction hinge. Therefore the Dinaric foredeep is thinner, being eroded and subsided.

The section in Figures 5.12 samples the Tyrrhenian Sea along its supposed direction of opening. It is well known that the Tyrrhenian sea started opening about 15 Ma, as the result of backarc expansion (Scandone, 1980; Gueguen et al, 1997 and reference therein) process induced by the eastward migration of the Apenninic subduction (Royden et al, 1987; Doglioni et al, 1991), which took place in the late Oligocene on the pre-existing alpine-betic orogen. The Tyrrhenian Sea is still opening with age of the newly formed oceanic lithosphere decreasing from west to east. This process was likely inhomogeneous and asymmetric. Clear evidence of this are the numerous *boudins* disseminated in the basin at different scales. A *boudin* is a continental isolated block, common at the mesoscale, as the product of extension of a competent layer (i.e. with high resistance to deformation and loss of thickness) within a less competent matrix (Ramsay and Huber, 1983, and reference therein). The *boudins* are bounded by thinned areas (necks) where material with lower viscosity flows. The distance between *boudins* is in the order of the original lithospheric thickness, ranging from 100 km to 400 km as argued in Guegen et al. (1997). The most prominent one is the Sardinia-Corsica block (cells a-2, A-1, B-1), where the lithosphere preserves its original thickness (about 80-90 km), which represent a fragment of the Betic foreland. To the east a thin neck extends with a lithospheric thickness of about 25-30 km (Magnaghi basin) down to cell A2, where an intra-Tyrrhenian *boudin* is located, likely representing a fragment of the hinterland of the previous Alpine-Betic orogen. Generally the crustal thickness mimics the lithospheric thickness, being about 20-25 km beneath *boudins*, and 10-15 km and even less beneath necks. Another intra-Tyrrhenian *boudin* is seen in cell a0, with a thin neck that separates it from cell A2. The

mantle beneath the lid is clearly characterized by a LVZ emerging south-eastward from about 100 km of depth, beneath Ligurian Sea and northern Corsica, to about 30 km in the Ischia volcanic zone. The northern part of the basin is characterized by a relatively low-density mantle, in contrast with the southern active part, where density increases, as seen in other sections. Density is relatively low again east of Ischia, in the vicinity of Apennines subduction.

A clear picture of the main geological and tectonic features of the central Mediterranean is given by the profile shown in Figure 5.13: 1) the southernmost part of the Corsica-Sardinia block characterized by scarce seismicity and rather low velocities in the lid, down to about 70 km of depth; 2) the active part of Tyrrhenian basin, characterized by an asthenospheric LVZ emerging eastward from 70 km of depth in the western part of the basin to 30 km of depth below Ischia and well visible lithospheric *boudinage*; 3) the westward dipping Apennines, characterized by high seismicity even at intermediate depth and high velocities; 4) a relatively low velocity and mostly aseismic lid beneath the Adriatic sea (as in section Adria42); 5) eastward dipping Dinaric slab, characterized by relatively high velocity and intermediate depth seismicity. Relatively low-density mantle is seen beneath Corsica-Sardinia block, Apennines and Dinarides, while a prominent positive density anomaly is found below Tyrrhenian and Adriatic seas.

In Figure 5.14, a NW-SE trending profile from Corsica to Ionian Sea, the outstanding feature is the high velocity body representing subducting lid beneath the Calabrian Arc, seismically active at all depths. To the west, the active part of the Tyrrhenian is marked by a lid about 60-70 km thick, with some very low velocity soft mantle lid beneath volcanic areas. Lid is slightly thicker beneath Sardinia-Corsica block and reaches about 90 km of thickness. To the east of the Calabrian Arc, the Ionian lid is about 130 km thick, and the underlying mantle is relatively faster than the Tyrrhenian one. Generally, the mantle velocity is higher in the Ionian plate than in the Tyrrhenian basin. A prominent negative density anomaly characterizes the subducting slab and the Sardinia-Corsica block, while a positive anomaly characterizes both the active Tyrrhenian, with a 3.3 g/cm^3 density at about 60-70 km of depth, and the Ionian mantle, with a 3.3 g/cm^3 density reaching about 80 km of depth and a 3.4 g/cm^3 density at about 170 km of depth. Asymmetry between west-directed (Apennines) and east-directed (Alps, Dinarides) subductions is a robust feature of the model: low angle subduction is seen in western Alps, along section Ecors and in Julian Alps and Dinarides. Very low angle collision process ($\leq 7^\circ$) is found in Eastern Alps, along section Transalp. Subduction below Apennines is steeper than below Alps and Dinarides in all analysed sections. This feature is much more clear-cut in a section where the distribution of

the shear modulus (μ) is shown; as a rule, in the Alpine and Adriatic sections, the dotted white line corresponds to the isoline of 65 GPa. The asymmetric feature, as well the eastward emerging LVZ in the Tyrrhenian asthenosphere is in agreement with an east directed mantle flow (Doglioni et al., 1999). In all the sections but one, the velocity in the mantle on the west side of Apennines is lower than in the east side, both in the Ionian plate and in the Adriatic plate, mainly in the depth range from 100 km to 200 km (asthenosphere) where the eastward flow can reach its maximum. The exception is given by section Adria43-46, across northern Apennines, where a marked LVZ is found below and to the north-east of the slab ($V_S \approx$ 4.2 km/s), while mantle velocities on the western flank are ≈ 4.35 km/s. Similarly, asymmetric features in the velocity model can be observed between northern and southern Tyrrhenian basin, with a longitudinal axis roughly corresponding to the $41°N$ parallel. The southern (active) part of the basin is generally characterized by mantle velocities which are lower than those in its northern part; this difference can be attributed to several causes, e.g. different extension rates, difference in the intensity of mantle flow, presence of lithospheric fragments, metamorphism and/or compositional differences. The north-south asymmetry observed in the mantle velocities of the Tyrrhenian basin persists in the density model, with lower mantle densities in the northern part of the basin than in the southern, the axis of symmetry being the $41°N$ parallel. Therefore higher densities in the mantle seem to be strictly related to the eastward flow itself and to its ascent beneath the back-arc basin. Western Alps and Sardinia-Corsica block present a common distribution of density with depth, with a relative low-density mantle with respect to surroundings (3.3 g/cm^3 at about 230-250 km). This similarity may be due to their common origin, since Sardinia-Corsica block is a fragment of the European Plate (Lustrino et al., 2009 and references therein). On the contrary, a density higher than the surroundings is found in the LVZ, with the 3.3 g/cm^3 density reaching depths of about 70 km, in particular in the active part of the Tyrrhenian basin where the asthenosphere is very shallow. Similarly, high density mantle is found beneath Po Plain and northern Adriatic. All these findings suggest a deep source of denser material that, in spite of depressurization, persists to be denser than ambient mantle, instead of a top source of colder (and denser) material, that, in spite of increasing temperature and ambient pressure, persists to be denser. Therefore, the common concept of ‚Äúslab pull‚Äù usually evoked to be one of the leading forces in subduction dynamics, is hard to be endorsed in this context, being no evidence of negative buoyancy of the slab itself with respect to the ambient mantle. In the Sicily Channel the lid thickness varies between 50 km and 100 km, thickening in the south-western part of the study area (Pelagian platform). The lid below the

Pelagian platform presents higher V_S with respect to the lid below Linosa graben (LG) and Malta graben (MG). Below Sicily, the lid extends down to about 80 km of depth and is marked by intermediate depth seismicity, almost absent in the Sicily Channel (Figure 5.15). A marked LVZ is present at about 100 km of depth below MG, emerging northward. The mantle heterogeneities found in the south-eastern part of the study area likely indicate a difference in the evolutional stage of the Linosa graben with respect to the Pantelleria and Malta graben.

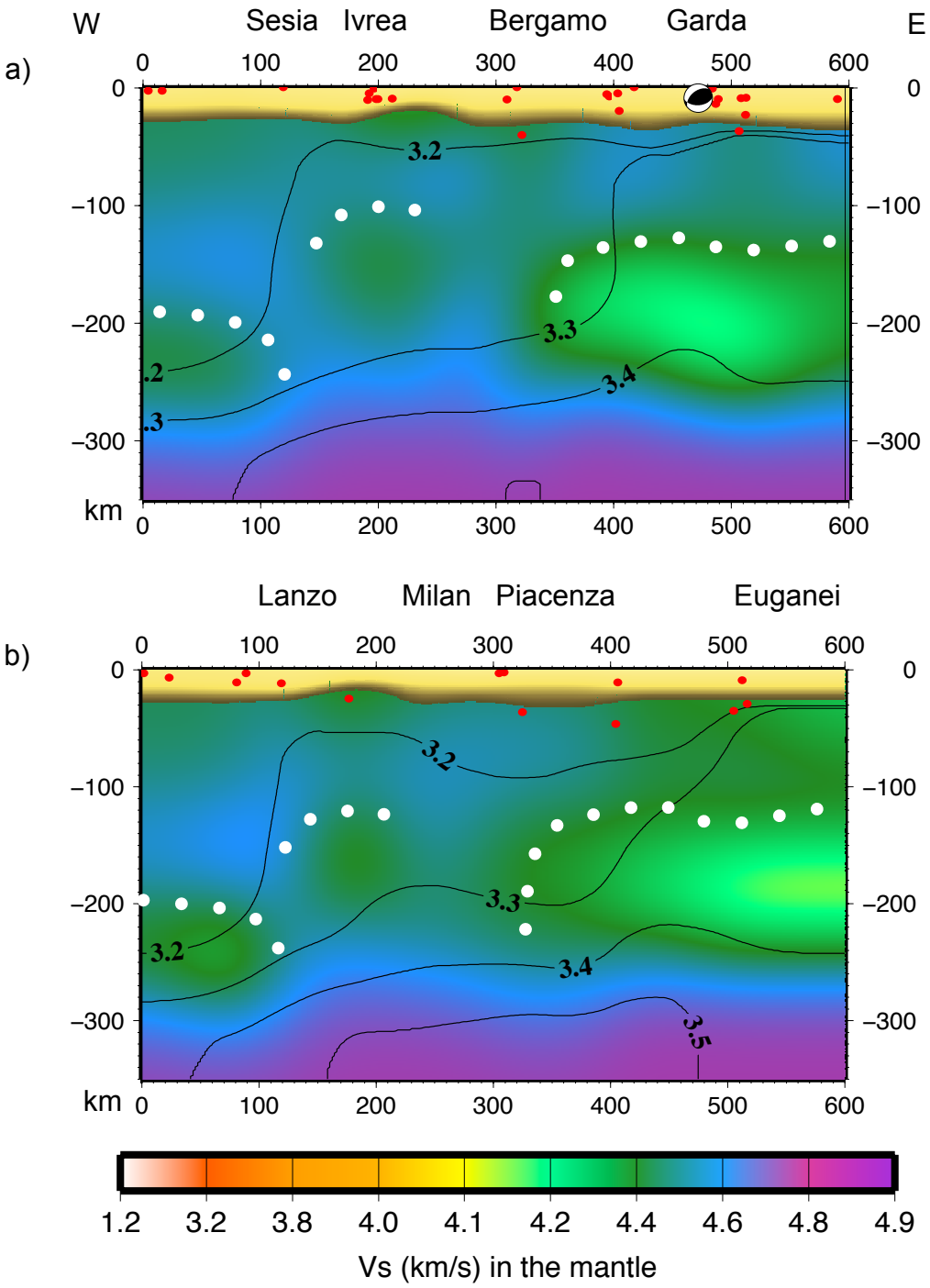

Figure 5.7: V_S and density model along a W-E profile along latitude $45.75°N$ (a) and along latitude $45.25°N$ (b), obtained from the $0.5° \times 0.5°$ model presented in Chapter 4. The labelling is the same of Figure 5.5. The general features described in Figure 5.5 are confirmed, but a more complex mantle structure is evinced in the Sesia-Ivrea and Lanzo zone, where a thinner lid is found with respect to the neighbouring areas, where deep lithospheric roots are present. The crust thickness mimics the lid thickness, being significantly thinner below Ivrea and Lanzo zones, confirming the results of Di Stefano et al. (2009). The density values are similar to those presented in Fig. 5.5, with the exception of relative higher densities below 300 km of depth in the southern section (b).

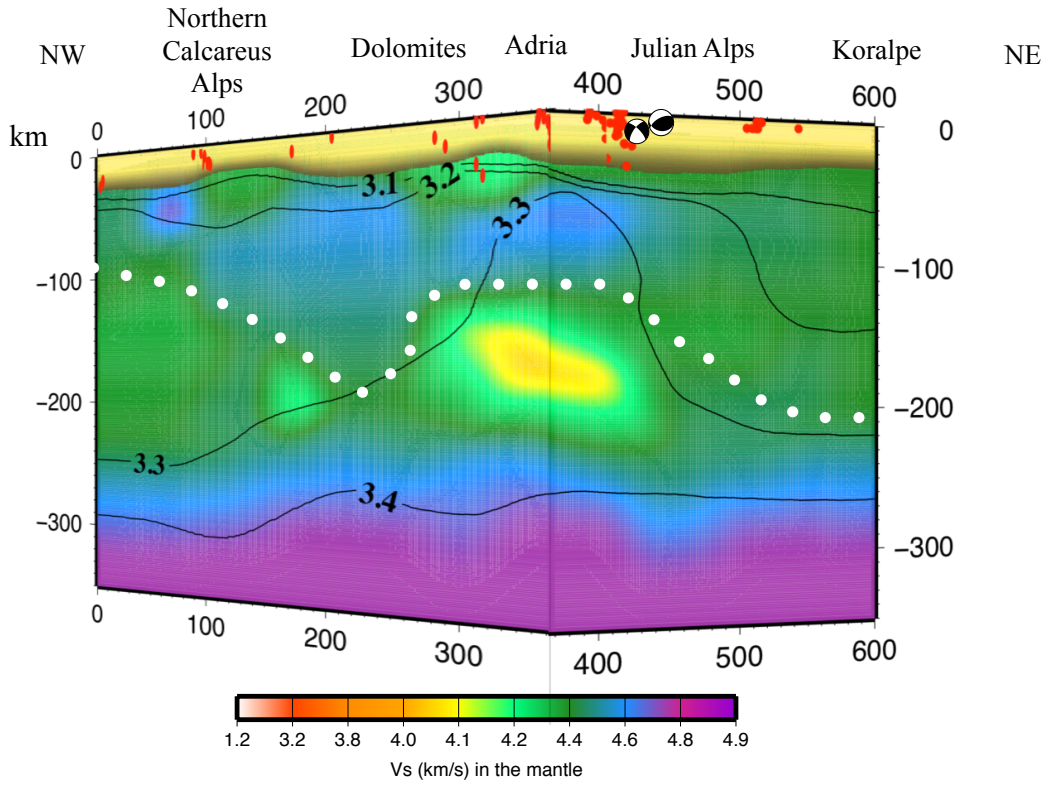

Figure 5.8: 3D section of Eastern Alps obtained from $0.5° \times 0.5°$ model presented in Chapter 4. V_S and density model along a NW-SE-NE profile from Constance Lake (Bodensee) through Friuli (southern vertex) to Koralpe. The labelling is the same of Figure 5.5. The double verging collision between Europe and Adria is clearly evinced by high velocity lid and lithospheric roots reaching about 180 km of depth below southern Alps. An about 30 km thick soft mantle layer is found beneath Dolomites, in agreement with the V_P model of Di Stefano et al. (2009). A marked LVZ is present below Adria plate, between 140 and 210 km of depth. The subduction below Dinarides is marked by a NE-ward thickening lid.

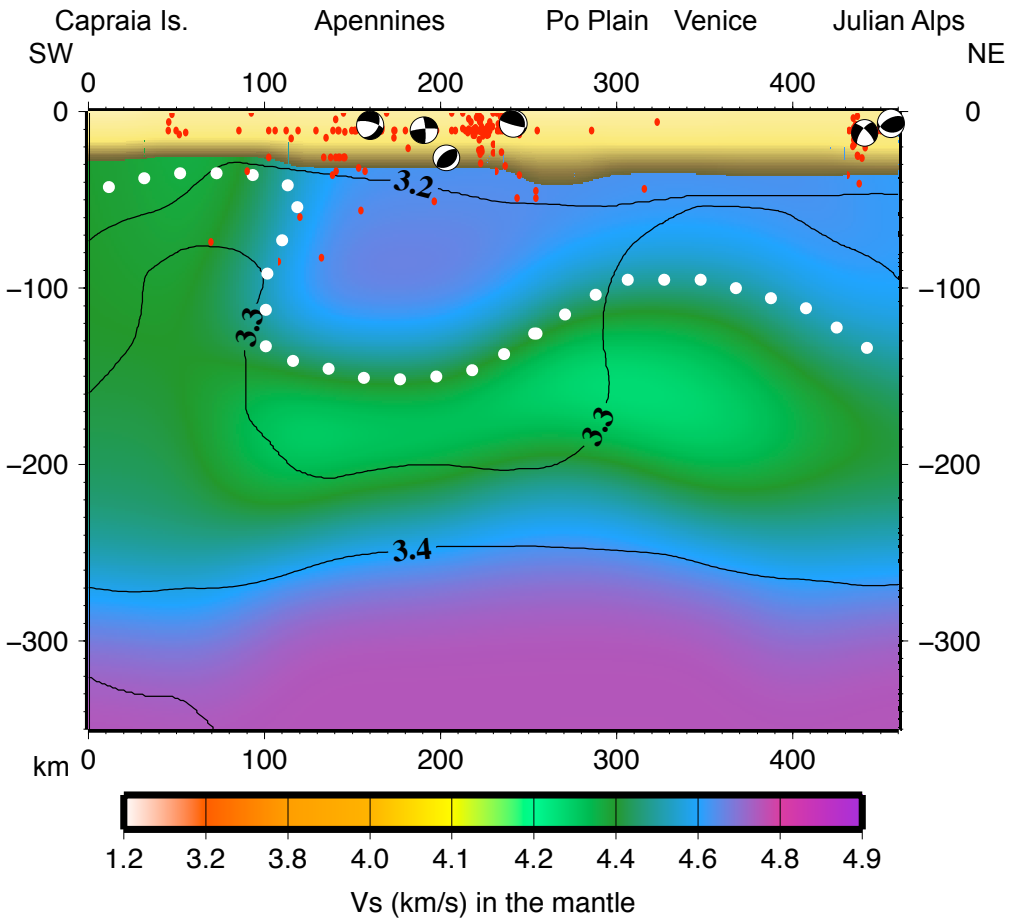

Figure 5.9: V_S and density model along a $SW - NE$ profile from Capraia Island to Julian Alps. The labelling is the same of Figure 5.4. The pronounced high-velocity, almost vertical, slab represents Apennines subduction consistent with significant seismicity at intermediate depth. To the West a low-velocity asthenospheric mantle wedge, mainly aseismic, is present. To the East a high velocity lid about 100 km thick extends towards the NE-dipping Alpine subduction, marked by the shallow to intermediate depth seismicity in the right part of the section. The bottom of the lid is well marked by a LVZ. Striking features of density model are the negative density anomaly beneath Apennines and Julian Alps, with the exception of the relatively high-density value found beneath Tuscany, probably related to mantle wedge. Po plain and Northern Adriatic are instead characterized by relatively high-density mantle at depths ranging from 60 to 200 km.

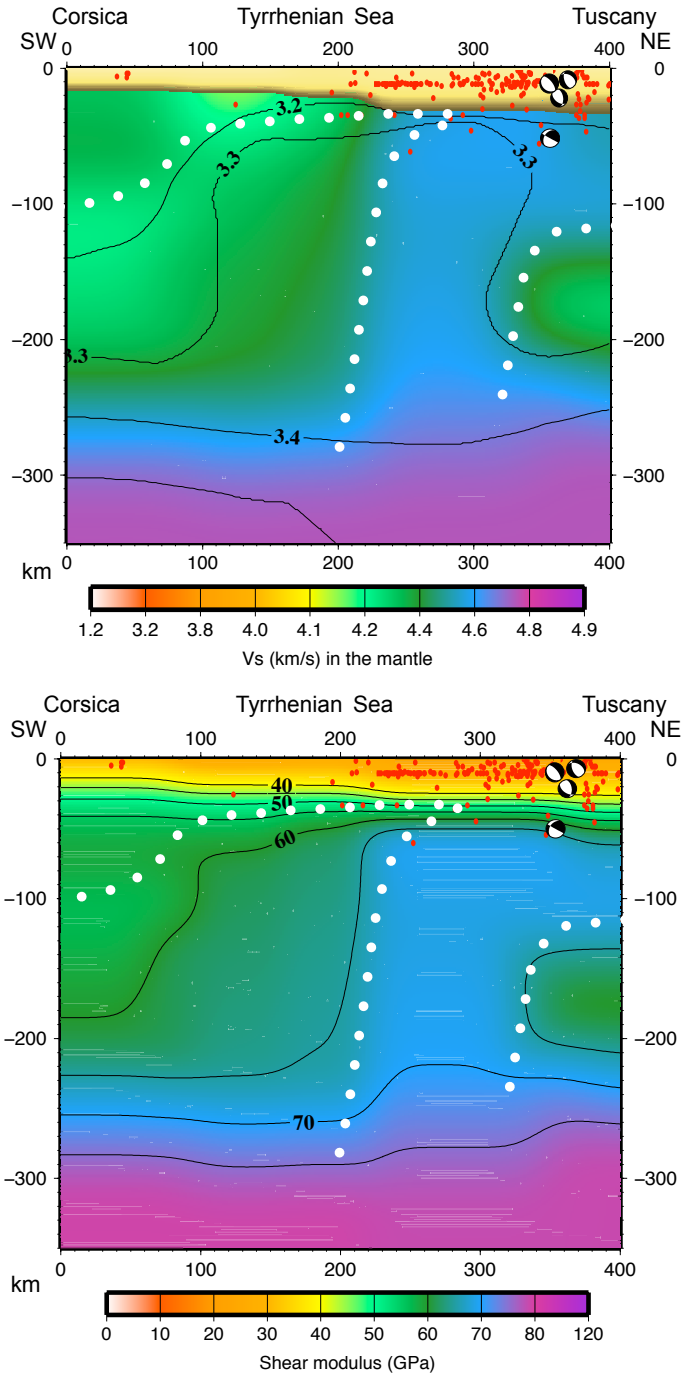

Figure 5.10: a) V_S and density model along a $SW - NE$ profile from northern Corsica to Adriatic Sea. The labelling is the same of Figure 5.5. The pronounced high-velocity, almost vertical, slab represents Apennines subduction. To the West an asthenospheric LVZ emerging from about 100 km depth beneath Corsica to about 40 km depth beneath Tuscany clearly marks the bottom of the lid. To the East of the subduction, a high velocity lid extends beneath Adria down to about 120 km of depth, lying on a well marked LVZ. A high density body is seen below Tuscany and in the subducting slab, while lower density characterizes both Corsica block and Adriatic mantle. b) the shear modulus (μ), in GPa, along the same section, gives a more clear-cut picture of the subducting slab.

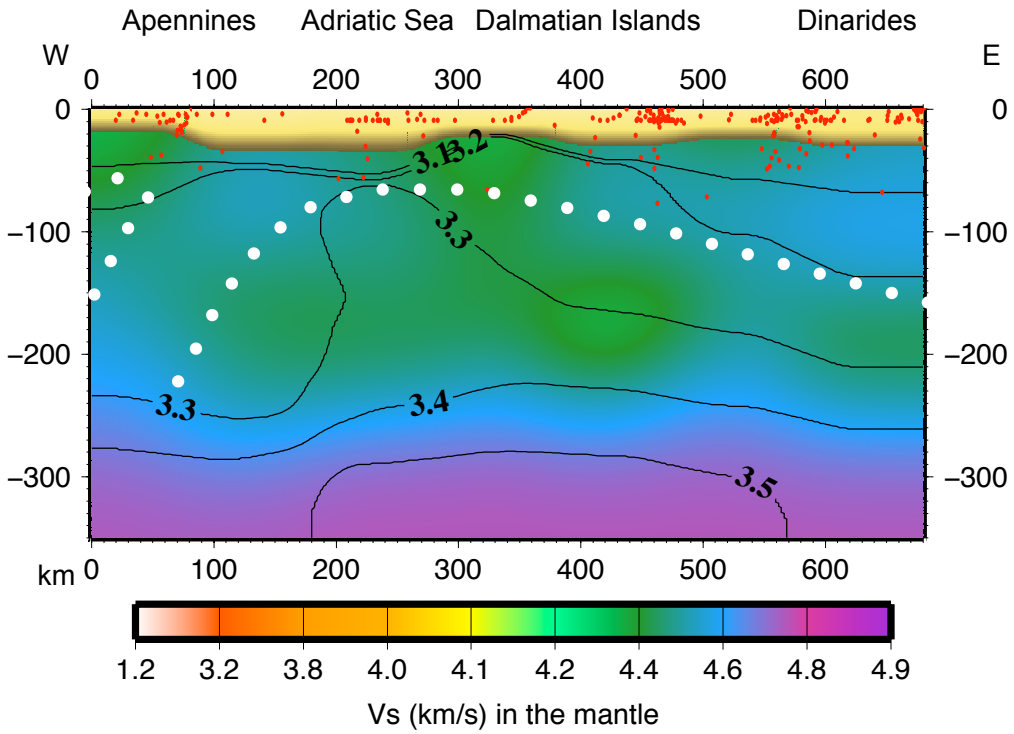

Figure 5.11: V_S and density model along a W-E profile from central Apennines to Dinarides. The labelling is the same of Figure 5.5. In this section, as in section Crop03, Apennines slab is marked by a high-velocity almost vertical body, with some intermediate depth seismicity reaching about 60 km of depth. To the West, the low velocity at a depth of about 50 to 100 km, just above the sinking slab, is probably related to mantle wedge dynamics (e.g. dehydration). To the east, a relative low velocity, mainly aseismic, mantle lid extends for about 100 km just beneath the Adriatic crust. In the easternmost portion of the section an eastward thickening lid is well marked by high velocity and intense intermediate depth seismicity, in fair agreement with a low angle Dinaric slab. Prominent negative density anomalies characterize both the Apennines and Dinarides at depth between 100 and 200 km, while high-density material seems to be related to the Adriatic plate, both in the lid and in the asthenospheric LVZ.

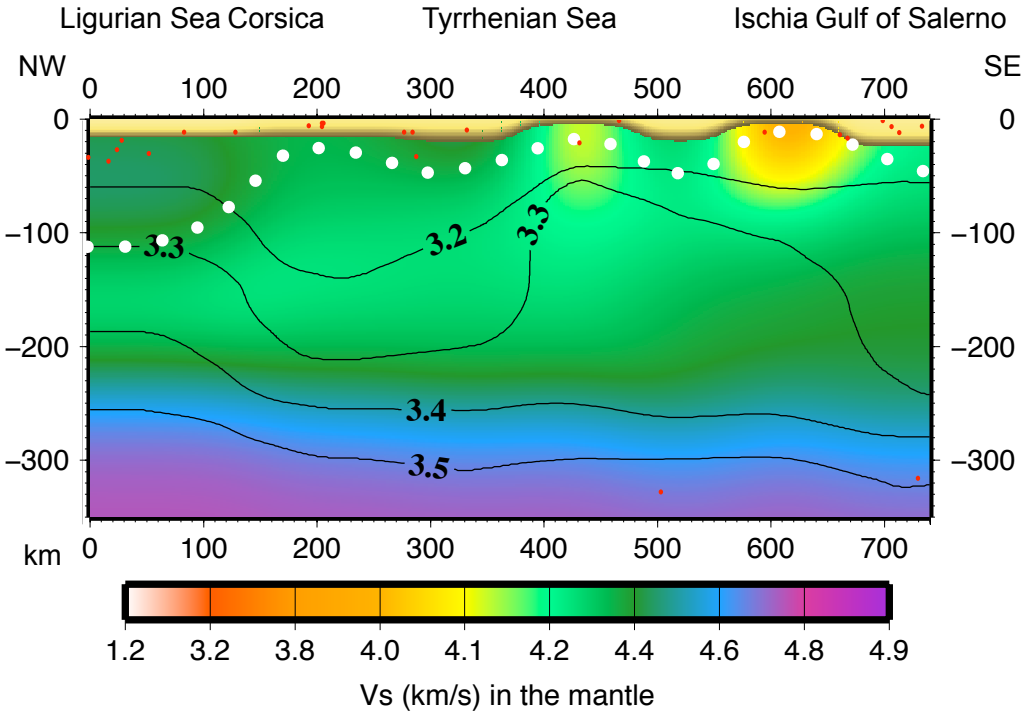

Figure 5.12: V_S and density model along a NW-SE profile from Ligurian Sea to Gulf of Salerno. The labelling is the same of Figure 5.5. This profile samples the Tyrrhenian Sea along its supposed direction of opening. It is clearly characterized by a south-eastward emerging LVZ from about 100 km of depth beneath Ligurian Sea and northern Corsica to about 30 km in the Ischia volcanic zone. The V_S model, the seismicity distribution and the so inferred lid-LVZ boundary fairly agree with extensive *boudinage*, at different scales (Ramsay and Huber, 1983, and references therein), that characterized the evolution of the basin still going on in present days. The northern part of the basin is characterized by relatively low-density mantle, in contrast with the southern active part, where density increases, as seen in other sections. Density is relatively low again east of Ischia, in the vicinity of Apennines subduction.

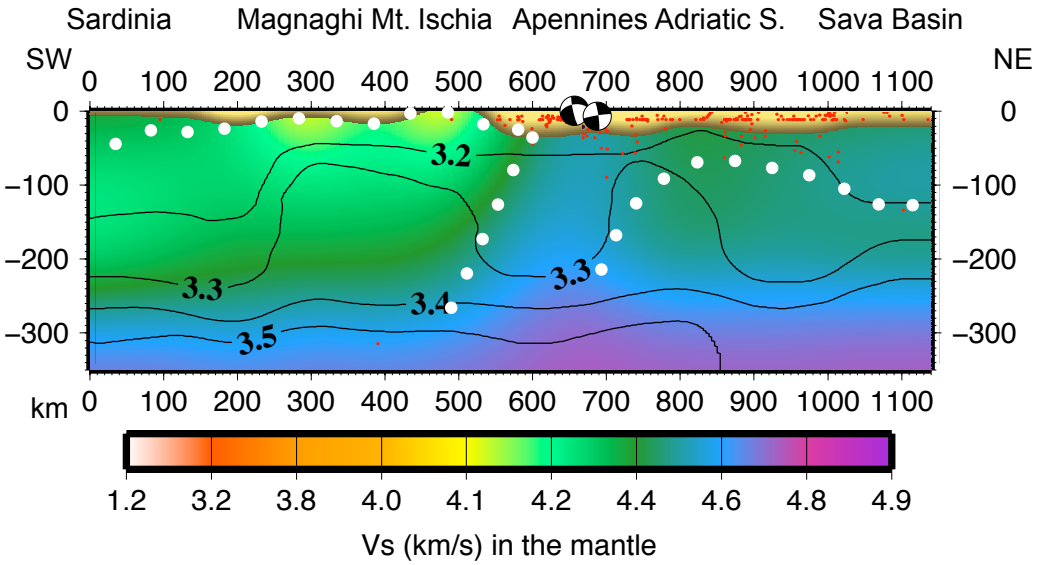

Figure 5.13: V_S and density model along a SW-NE profile from southern Sardinia to Sava Basin. The labelling is the same of Figure 5.5. This profile samples the main geological and tectonic features of the central Mediterranean: 1) the southernmost part of the Corsica-Sardinia block characterized by scarce seismicity and rather low velocities in the lid, down to about 70 *km* of depth; 2) the active part of Tyrrhenian basin, characterized by an asthenospheric LVZ emerging eastward from 70 *km* depth in the western part of the basin to 30 *km* depth below Ischia and well visible lithospheric *boudinage*; 3) the westward dipping Apennines, characterized by high seismicity even at intermediate depth and high velocities; 4) a relatively low velocity and mostly aseismic lid beneath the Adriatic sea (as in section Adria42); 5) eastward dipping Dinaric slab, characterized by relatively high velocity and intermediate depth seismicity. Relatively low-density mantle is seen beneath Corsica-Sardinia block, Apennines and Dinarides, while a prominent positive density anomaly is found below Tyrrhenian and Adriatic seas.

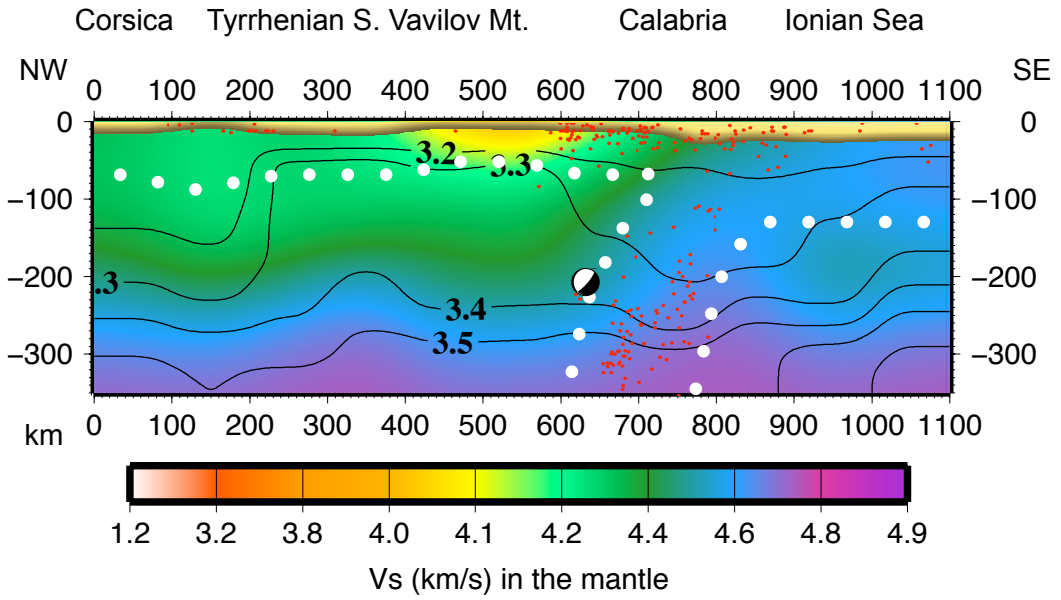

Figure 5.14: V_S and density model along a NW-SE profile from southern Corsica to Ionian Sea. The labelling is the same of Figure 5.5. Prominent feature of the section is the high velocity body representing subducting lid beneath Calabrian Arc, seismically active at all depths. To the west, the active part of the Tyrrhenian is marked by a lid about 60-70 km thick, with some very low velocity soft mantle lid beneath volcanic areas. Lid is slightly thicker beneath Sardinia-Corsica block and reaches about 90 km of thickness. To the east of the Calabrian Arc, the Ionian lid is about 130 km thick, and the underlying mantle is relatively faster than the Tyrrhenian one. Generally, the mantle velocity is higher in the Ionian plate than in the Tyrrhenian basin. A prominent negative density anomaly characterizes the subducting slab and the Sardinia-Corsica block, while a positive anomaly characterizes both the active Tyrrhenian, with a 3.3 g/cm^3 density at about 60-70 km of depth, and the Ionian mantle, with a 3.3 g/cm^3 density reaching about 80 km of depth and a 3.4 g/cm^3 density at about 170 km of depth.

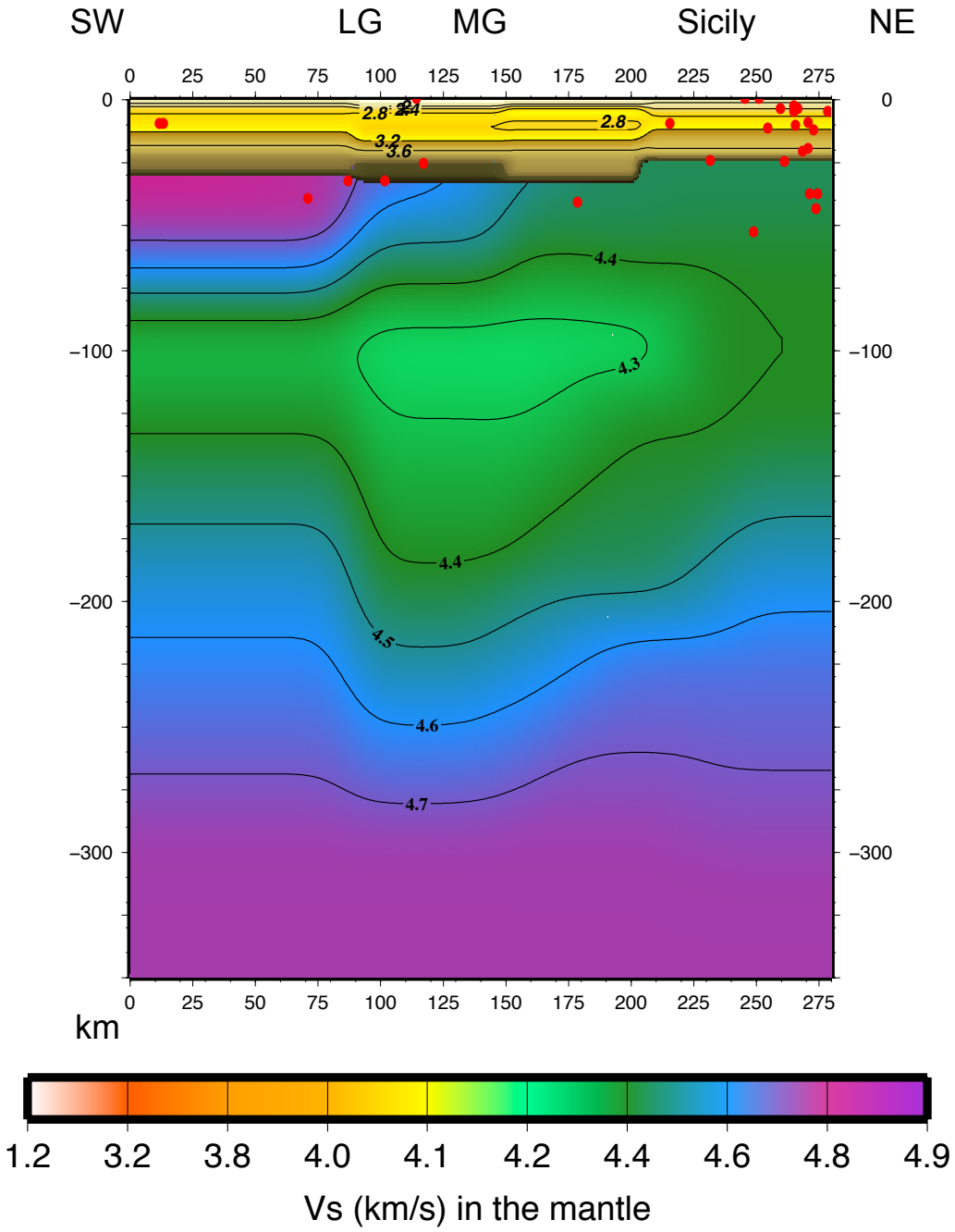

Figure 5.15: V_S model along the CROPM24 SW-NE directed profile across the Sicily Channel. An high velocity lid characterizes the Pelagian platform, while a lower velocity eastward thinning lid is found below Linosa graben (LG) and Malta graben (MG). To the west, below Sicily, the lid extends down to about 80 km of depth and is marked by intermediate depth seismicity, almost absent in the Sicily Channel. A marked LVZ is present at about 100 km of depth below MG, emerging northward.

5.3 Conclusions

A structural model for the lithosphere-asthenosphere system of Italy and neighbouring areas consistent with V_S- V_P- and ρ-depth distribution is proposed. The multidisciplinary approach is used to better constrain our model with the independent geological, geophysical and petrological information. The obtained picture of the lithosphere-asthenosphere system confirms the existence of some known features: the lithospheric roots in the western and central Alps, the extended LVZ beneath the Tyrrhenian Sea, steep subduction beneath Calabrian arc, low-angle subduction under the Dinarides. New evidences reinforce the hypothesis of an asymmetric expansion process of the Tyrrhenian Sea, as the presence of the lithospheric *boudinage* extended along a NW-SE direction through the whole Tyrrhenian Sea, likely representing fragments of the Alpine-Betic collision dragged by the eastward migrating process of the Apennines subduction. Another feature enlightened is the easterly rising shallow low-velocity layer from about 140 km to about 30 km in the Tyrrhenian active part of the backarc basin. Further proofs indicate the double verging collision between Adria and Europe in Eastern Alps, while the Adriatic lithosphere is involved at the same time in two other, opposite directed, subductions (NE- directed Dinaric W-SW-directed Apenninic subduction) which show significantly different dip angles. The Tertiary to present subduction processes in the Italian area occurring on a Mesozoic disrupted lithosphere (Doglioni et al., 1991) can account for the relevant lateral anisotropies visible in the mantle. The arc-shaped Ionian-Adriatic lithosphere supports a strong connection between Hellenic subduction and Ionian-Tyrrhenian subduction, possibly endorsing an upduction-subduction counterflow mechanism in the upper mantle. A wide use of seismicity analysis, both from catalogues and moment tensor inversion by $INPAR$ method, supplies a significant constraint to the model interpretation. $INPAR$ allows the use of relatively short period waveforms, significantly improving the depth determination for shallow events, usually fixed by CMT and RCMT. The asymmetry between E-verging and W-verging subduction zones, clearly evidenced by V_S, V_P and density model, supports the hypothesis of a eastward mantle flow, especially in the LVZ, between 120 and 200 km of depth, that is likely to represent the decoupling between the lithosphere and the underlying mantle at global scale (Panza et al., 2010). The flow is very shallow in the active Tyrrhenian basin, due to mantle compensation induced by the eastward migration of the Apennines subduction. High densities ($\geq 3.3\ g/cm^3$) in the mantle seem to be strictly related to the eastward flow itself and to its ascent beneath the back-arc basin, or to other extensional tectonics or to volcanism. On the contrary, slabs are not denser than

the ambient mantle, but they appear to be slightly lighter below all subductions zones, regardless of their geographic polarity; this evidence conflicts with the concept of *slab pull* and thus calls for different actors in subduction dynamics like upper-mantle convection, Earth's rotation and lateral heterogeneities in the viscosity contrast at the lithosphere-asthenosphere boundary (Doglioni et al., 2007; Riguzzi et al., 2010; Doglioni et al., 2011).

Appendix A

Appendix A. Stability of fault plane solutions for $M_W \geq 4.8$ in northern Italy in 2012

A.1 Introduction

In the critical analysis of the moment tensor solutions of the recent seismic sequence in Emilia-Romagna, retrieved by the non-linear method named INPAR (Šílený et al., 1992), the reliability of each solution is discussed in terms of accuracy of source time function (STF), percentage of Compensated Linear Vector Dipole (CLVD) component and statistical significance of the retrieved mechanism. The theoretical and practical limits of linear moment tensor retrieval from both body waves (Dufumier, 1996) and surface waves spectra (Dufumier and Cara, 1995) have been widely discussed, in particular for very shallow earthquakes, suggesting to use full waveforms at regional distance for moment tensor inversion. Reduction to zero of the isotropic component does not ensure stable solutions, since it does not affect off-diagonals elements M_{zx} and M_{zy}. The poor resolution of these elements, which excite Green functions vanishing at the free surface, causes instability in moment tensor solutions for crustal earthquakes whose source depth is significantly exceeded by the dominant wavelengths of data used in the inversion. As a consequence spurious large CLVD components arise and pairs of solutions with nodal planes showing a 180° rotation around the vertical axis (i.e. $\phi \Rightarrow \phi + 180°$, where ϕ is strike angle) are possible, as shown analytically by Henry et al. (2002). The less well determined the M_{zx} and M_{zy} components are, the more likely is the existence of a pair of well-fitting solutions. The conditions for the existence of such a pair are more likely satisfied when dealing with earthquakes close to vertical strike-slip

or near-dip-slip mechanism, whose nodal plane dips $\approx 45°$. Similar conclusions are reached by Bukchin (2006) and Bukchin et al. (2010), which prove that the focal mechanism of a seismic source can be uniquely determined from records of surface waves with lengths significantly exceeding the source depth only if the dip angle of one of its nodal planes is sufficiently small. The real meaning of the retrieved CLVD component is still debated, since it can be even an artifact of the inversion arising from both sparse distribution of stations and inaccurate Earth models (Panza and Saraò, 2000; Henry et al., 2002). The occurrence of sub events with different pure double-couple mechanisms very close in time may lead to the retrieval of a relatively large CLVD component (Guidarelli and Panza, 2007). In this case, different intervals of the source time function can be separately investigated in order to assess how the rupture mechanism changes in time.

A.2 Methodology

The $INPAR$ non-linear method for the inversion of moment tensor, developed at the Department of Mathematics and Geosciences of the University of Trieste, adopts a point-source approximation. It uses only the dominant part of complete waveforms from events at regional distances (up to 2500 km), thus it maximizes the signal-to-noise ratio. It is particularly suitable in determining shallow event's solutions, due to the possible use of relatively short periods (as short as 10 s). It consists of two steps: in the first, linear, step of the inversion the time functions describing the development in time of the individual components of the moment tensor, namely the moment tensor rate functions (MTRFs), are introduced. Using Einstein summation notation, the k_{th} component of displacement at the surface is the convolution product of the MTRFs and the Green's function spatial derivatives (hereafter Green's functions):

$$u_k(t) = M'_{ij}(t) * G_{ki,j}(t) \tag{A.1}$$

The moment rate functions are obtained by deconvolution of the Green's functions from the data. Using the modal-summation technique (Panza, 1985; Florsch et al., 1991; Panza et al., 2000), the synthetic Green's functions are computed at each grid point of a model space defined by a pre-assigned range of possible hypocentral coordinates, and, by interpolation, in the intermediate points, since a bad location of the focus may strongly affect the result of the inversion. The hypocentral location is searched until the difference between synthetic and observed seismograms is minimized. Considering the MTRFs as independent functions in

the first step leads to an over-parameterization of the problem which is advantageous for absorbing poor modeling of the structure (Kravanja et al. 1999a). In the non-linear step, the mechanism and the source time function are obtained after factorization of the MTRFs in a time constant moment tensor m_{ij} and a common source time function $f(t)$:

$$\frac{\partial M_{ij}}{\partial t} = m_{ij} \cdot f(t) \tag{A.2}$$

routinely assuming the same time dependence for all moment tensor components, i.e. a rupture mechanism constant in time, thus we consider the MTRFs as linearly dependent, taking only their coherent part. The predicted MTRFs are then matched to the observed MTRFs obtained as output of the first step (Panza and Saraó, 2000). The final solution, obtained by means of a genetic algorithm that allows the estimate of the confidence areas for the different source parameters as well (Šílený, 1998) is consistent with P-wave polarities.

A.3 Results

A.3.1 Comparison of the solutions

The major events ($M_w \geq 4.8$) that affected northern Italy since January 25^{th} 2012, are relocated and their fault plane solution is retrieved, using broadband stations from MEDNET, French, Swiss and Italian Seismic Networks. The events are chronologically numbered and their source parameters are listed in Table A.1. The fault plane solutions retrieved by $INPAR$, reduced to best double couple, are shown in Figure A.1a, compared to TDMT solutions (Fig. A.1b, Dreger and Helmberger, 1993), RCMT (Fig. A.1c, Pondrelli et al., 2006), both retrieved by the Istituto Nazionale di Geofisica e Vulcanologia (INGV), and CMT-Harvard solutions (Fig. A.1d, Dziewonski et al., 1981). In Figure A.1e are shown, for each event, the fault plane solutions and their confidence areas, obtained by $INPAR$. In order to test the effect of the signals period content on the stability of solutions, the inversion is performed considering cutoff periods varying from 10 to 30 s. In the rightmost column the TDMT solution is shown for comparison. For each event relevant parameters such as source depth, percentage of CLVD and cutoff period are shown.

The solutions obtained by the inversion at the shortest period (Fig. A.1e, first column) are in all cases preferable in terms of confidence areas, percentage of CLVD or both, with the exception of event 1. The most similar solutions between

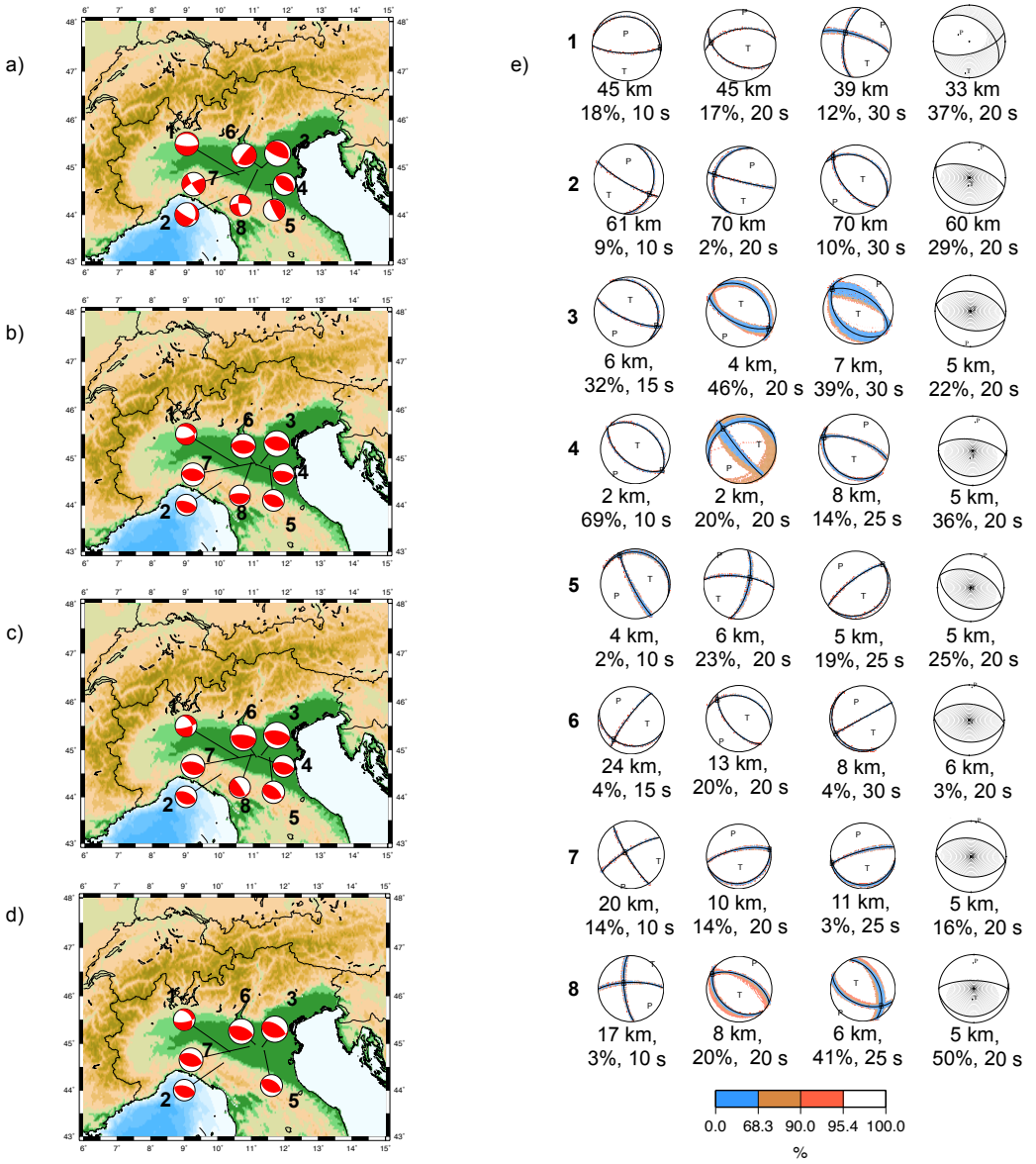

Figure A.1: Fault plane solutions (best double couple) determined by: a) INPAR, inverting at 10-15 s cutoff period (details in Table 1); b) TDMT-INGV (20 s cutoff period); c) RCMT (30-40 s cutoff period); d) CMT (40-50 s cutoff period). The beachballs are scaled to magnitude. e) Fault plane solutions determined by INPAR inverting at different cut off periods, with their confidence areas. For each solution, source depth, percentage of CLVD and low pass gaussian filtering period are given. TDMT solutions are reported for comparison in the rightmost column, with the filling of the beachballs denoting the percentage of CLVD component.

INPAR and results reported by other agencies are found inverting at longer period (Fig. A.1e, third column), with the exception of event 1, possibly contaminated by high noise level. Solutions of the events 1, 3 and for 4 are quite in agreement also at shortest period, while event 5 shows a minor strike-slip component not reported by other agencies, that on account of the low percentage of CLVD seems to be reliable. Event 2, reported as an inverse mechanisms by other agencies, is

retrieved by $INPAR$ at the shortest period as a normal mechanism with a minor strike-slip component. Major differences both in source depth and in the fault plane solutions are found for events 6 to 8 (May 29^{th} main shock and aftershocks). $INPAR$ locates these events at a depth ranging from 17 to 24 km and retrieves a significant strike-slip component, while other agencies report shallow and near to 45° dip-slip events, with the exception of event 8 which is reported as a low angle dip-slip both by TDMT and RCMT (Fig. 1b,c). Performing INPAR inversion at longer periods, where the resolution is lost, the strike-slip behavior vanishes and the source depth becomes shallow for all three events. In the case of the event 3 and 4 a 180° rotation of ϕ around the vertical axis is observed in the longer periods $INPAR$ inversion. This can be naturally explained by the poor resolution of M_{zx} and M_{zy} when dealing with shallow events.

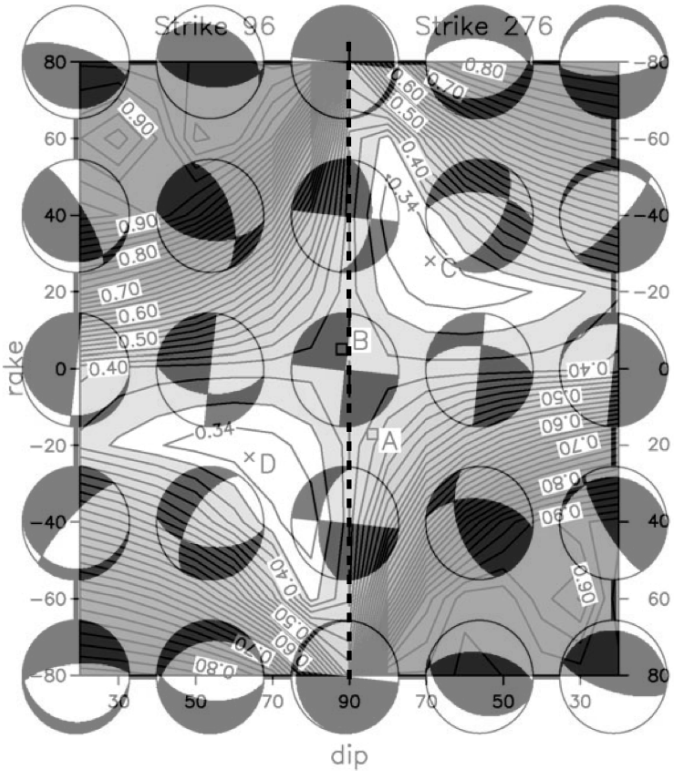

Figure A.2: Contour plot of the variance ratio for the March 25^{th}, 1998 Antarctic earthquake, at strike 96° or 276°, and for a range of dip and rake values, following the Aki and Richards (1980) convention. Points to the left of the vertical dashed line at the center of the figure have strike 96° and rakes corresponding to the left ordinate. Points to the right of the line have strike 276° and rakes corresponding to the right ordinate. The sample moment tensors from the mechanism space, clearly showing the pairs of solutions arising from the two-fold rotational symmetry of the misfit function, are superimposed (modified after Henry et al., 2002).

This poor resolution, as shown in Figure 2, gives rise to pairs of equally probable solutions that satisfy the transformation $\phi \Rightarrow \phi + 180°$ (Henry et al., 2002). The

conditions for the existence of such a pair are even more likely satisfied by near-dip-slip earthquake mechanisms with nodal plane dipping $\approx 45°$, as in the case of events 3 and 4. The effect of this instability tends to vanish at low (or high) dip angles, which threshold depends on source depth, structure of the medium and spectral content of the inverted signal, but can be generally estimated in $15 - 20°$ (Bukchin, 2006).

A.3.2 Test on STFs and depth constrain

To assess the reliability of event's 6 solution, inversion constrained at shallow depths is performed (1-11 km, Fig. A.3a). The STF exhibits two peaks and the mechanism solution presents a 43% of CLVD. If the STF is constrained to two sub-intervals, 0-3 s and 3-6 s, the source depth retrieved remains shallow (8 km, quite in agreement with the 6 km retrieved by TDMT) but the still large percentage of CLVD for both solutions obtained considering two separated time intervals for the STFs (*split solutions*), is a strong indicator that the whole solution is unreliable. Similar results are shown for events 7 and 8 (Figs. A.3b and A.3c respectively): the double peaked STF is inverted considering two separated time intervals. In both cases the split solutions show percentage of CLVD larger than the whole one, and thus we consider the latter more reliable. Furthermore event 7 shows high instability, with varying source depth and mechanism changing from almost strike-slip to dip-slip between the two time intervals (Fig. A.3b), while event 8 shows minor instability (Fig. A.3c).

A.3.3 Conclusions

The differences in moment tensor solutions retrieved using signals with different period content are pointed out. In particular, for shallow crustal earthquakes, instability in the determination of moment tensor solutions arises when signals with a cutoff period longer than 20 s are inverted. Such instability is mainly due to the poor resolution of tensor components M_{zx} and M_{zy}, which excite Green functions vanishing at free surface, and it affects both source depth and fault plane solution retrieval. In some cases pairs of equally probable solutions are observed, with a strike angle rotation of 180° around the vertical axis, in particular for near dip-slip events with dip angle of $\approx 45°$. Thus, in order to assess the reliable fault plane solutions the inversion of full waveforms at periods shorter than 20 s should be preferred.

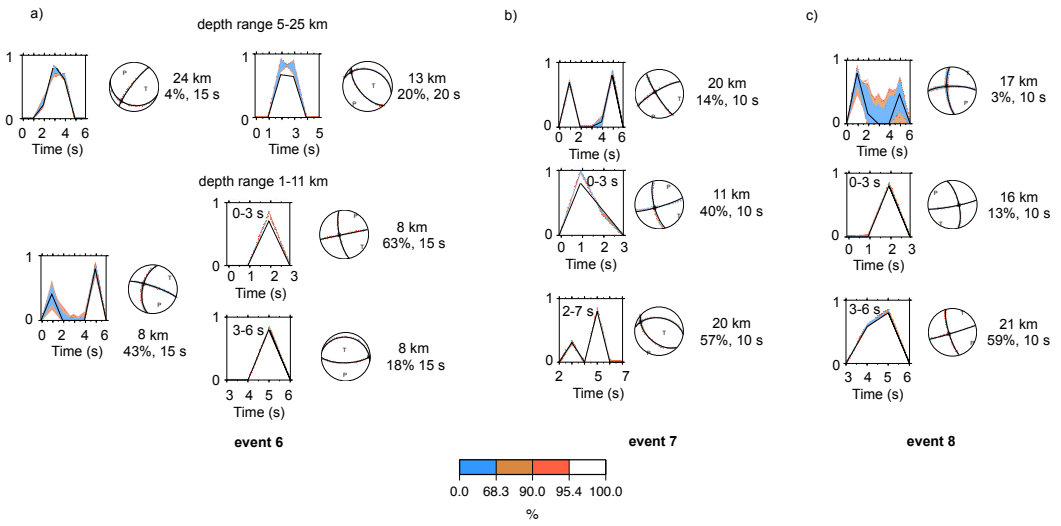

Figure A.3: a) Top: STF and fault plane solution for event 6 inverted in the depth range 5-25 *km*. Bottom: results of the inversion of the same event with depth constrained to the range 1-11 km; the double peaked STF is split in two time intervals. The shallow solution seems not reliable due to large percentage of CLVD. b) results of the inversion of event 7 splitting STF in two time intervals. c) results of the inversion of event 8 splitting STF in two time intervals. For each solution source depth, percentage of CLVD and cutoff period are given. The STFs are normalized to unity.

Event ID	Date (yy-m-dd)	UTC Time (hh:mm:ss)	Lon (deg)	Lat (deg)	Depth (km)	strike, dip, rake (deg)	M_w
1	12-1-25	08:06:37	10.54±.1	44.85±.1	45±2	92 74 -94	5.4
2	12-1-27	14:53:14	10.19±.1	44.38±.1	61±1	120 79 -117	5.5
3	12-5-20	02:03:53	11.23±.1	45.00±.1	6±1	114 72 78	6.0
4	12-5-20	03:02:50	11.34±.1	44.64±.1	2±1	128 54 89	5.2
5	12-5-20	13:18:02	11.48±.1	44.65±.1	4±1	153 82 98	5.1
6	12-5-29	07:00:03	11.21±.1	45.00±.3	24±14	107 26 158	5.7
7	12-5-29	10:55:57	10.70±.1	44.94±.1	20±1	148 81 167	5.4
8	12-6-03	19:20:43	11.10±.2	44.95±.1	17±1	269 75 -162	4.9

Table A.1: Source parameters of the events retrieved by *INPAR* inversion at the shortest period (preferred solution)

Appendix B

Appendix B. Venturi effect as trigger of deep seismicity

B.1 Introduction

The Venturi's effect is the well known statement of fluid dynamics according to which an incompressible fluid in laminar flow through a narrowing tube increases its velocity on the expenses of its internal pressure, the total energy to be conserved. It can be derived by Bernoulli principle of conservation of energy:

$$\frac{v^2}{2} + gz + \frac{p}{\rho} = const \tag{B.1}$$

where v is the velocity of the fluid, z is the depth, g is gravitational acceleration, p is the fluid pressure and ρ is its density. From eq. B.1, it comes that for an apparatus like that in figure B.1, we have:

$$\frac{{v_1}^2}{2} + gz_1 + \frac{p_1}{\rho} = \frac{{v_2}^2}{2} + gz_2 + \frac{p_2}{\rho} \tag{B.2}$$

where the subscripts 1,2 refer respectively to the wider and to the narrower section of the tube. Therefore, rearranging the terms:

$$\rho\frac{{v_2}^2 - {v_1}^2}{2} + \rho g(z_2 - z_1) = p_1 - p_2 \tag{B.3}$$

That is the formulation of Venturi's effect, provided that the second term at LHS is negligible, i.e. the vertical dimension of the apparatus are negligible with respect to the variation of the potential energy.

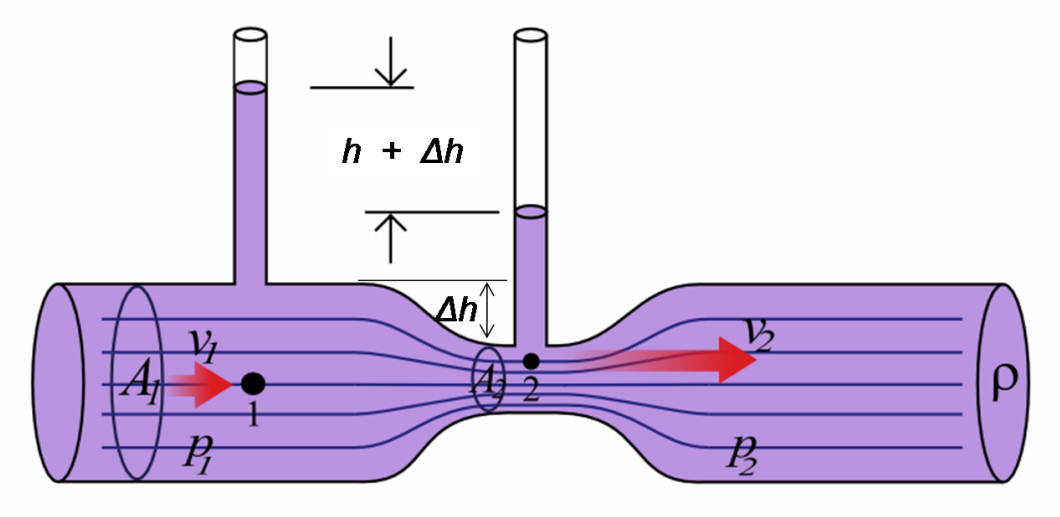

Figure B.1: Schematic sketch of the Venturi's effect (source Wikipedia)

B.2 Application to the upper mantle

In order to prove whether or not such an effect can occur in a mantle flow narrowed by a subducting slab and thus evaluate at least the order of magnitude of different terms, we have to take some simplifying assumptions. At first we take in eq. B.3 for v_1 and v_2 the reference velocities of the overlying plates (i.e. the hanging and the footing plate involved in the subduction). This is not a shortcoming assumption, at least in the Stokes flow approximation validity range, in which the motion is transferred instantaneously between the plate and the underlying mantle. Then we impose the mantle flow to take place between 120 and 670 km of depth, therefore z_1 is fixed. First of all we evaluate the order of magnitude of the kinetic term (i.e. the first member at LHS in eq. B.3) from given parameters. It comes that:

$$\rho \frac{{v_2}^2 - {v_1}^2}{2} = 1.42 \cdot 10^{-14} Pa \tag{B.4}$$

where ρ has a mean value of 3750 kg/m^3, $v_1 = 1.58 \cdot 10^{-9} m/s$ (i.e. 5 cm/yr) and $v_2 = 3.17 \cdot 10^{-9} m/s$ (i.e. 10 cm/yr). It follows that the kinetic terms is negligible with respect to the potential term, that for $z_2 = 300$ km (i.e. a slab reaching 300 km of depth), is:

$$\rho g(z_2 - z_1) = -7.26 \cdot 10^9 Pa \tag{B.5}$$

where g has a reference value of $10.7 m/s^2$ and $z_2 - z_1 = -180$ km. Therefore, due to the vertical dimension involved, Venturi's effect is negligible.

Thus a parametric test is undertaken on different values of z_2, in order to find

Z_{sub} (m)	z_2 (m)	$z_2 - z_1$ (m)	ΔP (Pa)
$1.50 \cdot 10^5$	$5.20 \cdot 10^5$	$-3.00 \cdot 10^4$	$-1.21 \cdot 10^9$
$1.80 \cdot 10^5$	$4.90 \cdot 10^5$	$-6.00 \cdot 10^4$	$-2.42 \cdot 10^9$
$2.10 \cdot 10^5$	$4.60 \cdot 10^5$	$-9.00 \cdot 10^4$	$-3.63 \cdot 10^9$
$2.40 \cdot 10^5$	$4.30 \cdot 10^5$	$-1.20 \cdot 10^5$	$-4.84 \cdot 10^9$
$2.70 \cdot 10^5$	$4.00 \cdot 10^5$	$-1.50 \cdot 10^5$	$-6.05 \cdot 10^9$
$3.00 \cdot 10^5$	$3.70 \cdot 10^5$	$-1.80 \cdot 10^5$	$-7.26 \cdot 10^9$
$3.60 \cdot 10^5$	$3.10 \cdot 10^5$	$-2.40 \cdot 10^5$	$-9.67 \cdot 10^9$
$3.90 \cdot 10^5$	$2.80 \cdot 10^5$	$-2.70 \cdot 10^5$	$-1.09 \cdot 10^{10}$
$4.20 \cdot 10^5$	$2.50 \cdot 10^5$	$-3.00 \cdot 10^5$	$-1.21 \cdot 10^{10}$
$4.50 \cdot 10^5$	$2.20 \cdot 10^5$	$-3.30 \cdot 10^5$	$-1.33 \cdot 10^{10}$

Table B.1: Parametric test on the pressure variation (ΔP) with slab reaching different depth (Z_{sub})

Z_{sub} (m)	z_2 (m)	$z_2 - z_1$ (m)	v_2 (m/s)	$\Delta v / v_1$
$1.50 \cdot 10^5$	$5.20 \cdot 10^5$	$-3.00 \cdot 10^4$	$1.77 \cdot 10^{-9}$	$1.19 \cdot 10^{-1}$
$1.80 \cdot 10^5$	$4.90 \cdot 10^5$	$-6.00 \cdot 10^4$	$1.99 \cdot 10^{-9}$	$2.60 \cdot 10^{-1}$
$2.10 \cdot 10^5$	$4.60 \cdot 10^5$	$-9.00 \cdot 10^4$	$2.26 \cdot 10^{-9}$	$4.30 \cdot 10^{-1}$
$2.40 \cdot 10^5$	$4.30 \cdot 10^5$	$-1.20 \cdot 10^5$	$2.58 \cdot 10^{-9}$	$6.36 \cdot 10^{-1}$
$2.70 \cdot 10^5$	$4.00 \cdot 10^5$	$-1.50 \cdot 10^5$	$2.99 \cdot 10^{-9}$	$8.91 \cdot 10^{-1}$
$3.00 \cdot 10^5$	$3.70 \cdot 10^5$	$-1.80 \cdot 10^5$	$3.49 \cdot 10^{-9}$	1.21
$3.30 \cdot 10^5$	$3.40 \cdot 10^5$	$-2.10 \cdot 10^5$	$4.13 \cdot 10^{-9}$	1.62
$3.60 \cdot 10^5$	$3.10 \cdot 10^5$	$-2.40 \cdot 10^5$	$4.97 \cdot 10^{-9}$	2.15
$3.90 \cdot 10^5$	$2.80 \cdot 10^5$	$-2.70 \cdot 10^5$	$6.10 \cdot 10^{-9}$	2.86
$4.20 \cdot 10^5$	$2.50 \cdot 10^5$	$-3.00 \cdot 10^5$	$7.65 \cdot 10^{-9}$	3.84
$4.50 \cdot 10^5$	$2.20 \cdot 10^5$	$-3.30 \cdot 10^5$	$9.88 \cdot 10^{-9}$	5.25

Table B.2: Parametric test on the upper plate velocity variation (v_2) with slab reaching different depths

the effect on pressure (i.e. on stress) for different depths of subducting slab.

As shown in Table B.1 values of ΔP vary from 1 to 10 GPa, that is a significant fraction of ambient mantle pressure at any given depth. On the other hand, if we apply the conservation of the flow rate through an upper mantle section, narrowing from A_1 to A_2 (Fig. B.1), we can estimate v_2, v_1 being fixed:

$$v_2 = v_1 \cdot \frac{A_1}{A_2} \tag{B.6}$$

For different depth of the slab (Z_{sub}) thus we have:

As we can see from Table B.2, the value of $3.49 \cdot 10^{-9} m/s$ (about 10 cm/yr) is gained for a 300 km deep slab. Thus this value is compatible with the velocity of the Hellenic plate in the shallow hotspot reference frame (Doglioni et al. 2007)

Appendix C

Appendix C. Measurements of attenuation curves and their inversion for the retrieval of Q value as a function of depth: synthetic tests in 2D lateral heterogeneous media

C.1 Introduction

Some synthetic tests were performed to measure the spatial attenuation curves with the aim to invert these curves to obtain a structure of Q as a function of depth. The synthetic signals calculated for two receivers placed at known distances on a great circle, not necessarily considering the same one-dimensional anelastic structure, are processed through FTAN in order to extract only the fundamental mode. According to the definition of Ben-Menahem (1965) the attenuation coefficient for a propagating wave between two stations can be defined as:

$$\gamma(\omega) = \frac{\ln\left(\frac{A_1(\omega,\theta,X_1)}{A_2(\omega,\theta,X_2)} \cdot \frac{\sqrt{\sin\Delta 1}}{\sqrt{\sin\Delta 2}}\right)}{X_2 - X_1} \tag{C.1}$$

where A_1 and A_2 are the spectral amplitudes (in the case of real signals corrected for instrumental response) observed at the receivers at a distance of X_1 and X_2 respectively, and $\Delta 1$, $\Delta 2$ are the respective radial distances of the receivers from the

source. Is well known that the intrinsic attenuation measures are affected by elastic propagation and multipathing. If the effect due to multipathing can be controlled by choosing two stations that lie as much as possible on the same azimuth with respect to the source (great circle), the elastic effect due to the propagation is more difficult to be controlled. One way consists in considering, instead of the ratio of the spectral amplitudes of the signals at the two sites, the amplitudes of the envelope of the phase equalized signals, i.e. of the signals obtained removing as accurately as possible the dispersion (Figure C.1).

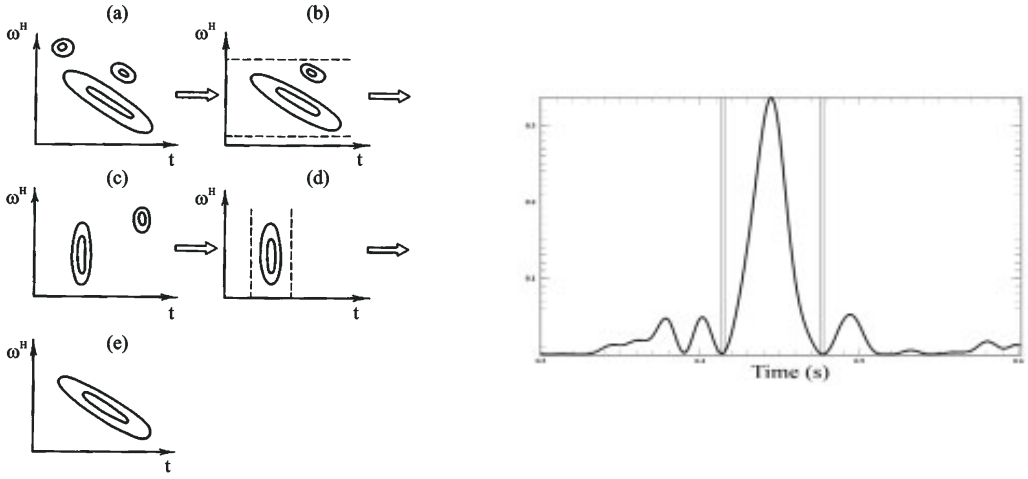

Figure C.1: (left panel) working scheme of the phase equalization filter. A band-pass filter is combined to a time-windowing filter in order to eliminate the noise. At stage (d) an almost not-dispersed signal is obtained, so it has the form of a short pulse in time domain (phase equalized signal, right panel).

More specifically, the phase equalization consists in applying a floating filter that reduces as much as possible the effect due to the dispersive elastic propagation (the signal is propagated backward at an average group velocity, thus tending to a pulse signal, deprived mainly of the energy lost during propagation due to anelasticity. The amplitudes of phase equalized signals obtained by FTAN are then scaled to the maximum amplitude of the respective fundamental modes:

$$A_{i_{ph}}(\omega, \theta, X) = A_{i_{ph}}(\omega, \theta, X) \cdot max(A_i(\omega, \theta, X)) \tag{C.2}$$

The structures used in the synthetic test are taken from Panza et al. (1972) and from Panza and Calcagnile (1974). The first (in the following referred to as Structure A) is a typical shield structure with a low velocity channel (LVC) in the mantle. The second (Structure B) is a Jeffreys-Bullen type structure without a LVC. The point source is embedded in the Structure A at a depth of 35 km, and two focal mechanisms are used following Calcagnile and Panza (1973):

a) strike = 30°; dip = 90°; rake = 180°
b) strike = 30°; dip = 90°; rake = 270°

C.2 2D coupling test

Signals are computed by means of Rayleigh wave propagation in 2D media according to Gregersen coupling theory. The basic idea is that, in the laterally heterogeneous structure, from now on 2D structure, the unknown wavefield is generated by the lateral heterogeneities and is written as a linear combination of base functions representing the normal modes (Love and Rayleigh) of the considered structures forming the 2D medium, therefore the problem reduces to the computation of the coefficients of this expansion. The coupling coefficients represent how the energy carried out by the normal modes of a structure is transmitted to the normal modes of the second structure that is in welded contact with the first one. A detailed description of the analytical computation of the coupling coefficients can be found in Alsop (1966), Vaccari et al. (1989), Romanelli et al. (1996), Panza et al. (2001). In this way the source effect can be discarded and the interstation attenuation can be computed. Structure A extends for 500 km, where receiver A is placed. Structure B extends from 500 to 1000 km from the source, where receiver B is placed, on the same great circle of receiver A with respect to the source. The theoretical attenuation for the structure B is computed according to the relation:

$$\gamma(\omega) = \frac{\omega}{2c_0^2} \sum \left[\frac{\partial c_0}{\partial \beta} \beta Q_\beta^{-1} + \frac{\partial c_0}{\partial \alpha} \alpha Q_\alpha^{-1} \right] \tag{C.3}$$

and is proven to be equal to $c_2 \cdot \omega$, where c_2 is the phase attenuation and ω is the angular frequency. The attenuation curves obtained by the spectral amplitude of the phase-equalized signals are compared to the ones computed by means of the spectral ratios of the signals itself extracted by FTAN (only fundamental mode), according to the formulation of Levshin et al. (2010):

$$I_{12} = \int_{L_{12}} \gamma_R(\omega, l) dl = \ln \frac{A_1 B_2 \sqrt{\sin \Delta 1}}{A_2 B_1 \sqrt{\sin \Delta 2}} \tag{C.4}$$

where:

$$B(\omega) = \left(I_0(\omega) \cdot U_R(\omega) \cdot k_R(\omega) \right)^{-\frac{1}{2}} \tag{C.5}$$

is a correction for the structure near the receiver. Here $I_0(\omega)$ is the normalized kinetic energy and $k_R(\omega)$ and $U_R(\omega)$ are the wave number and the group velocity of the local structure model at the given frequency.

C.2.1 Case a)

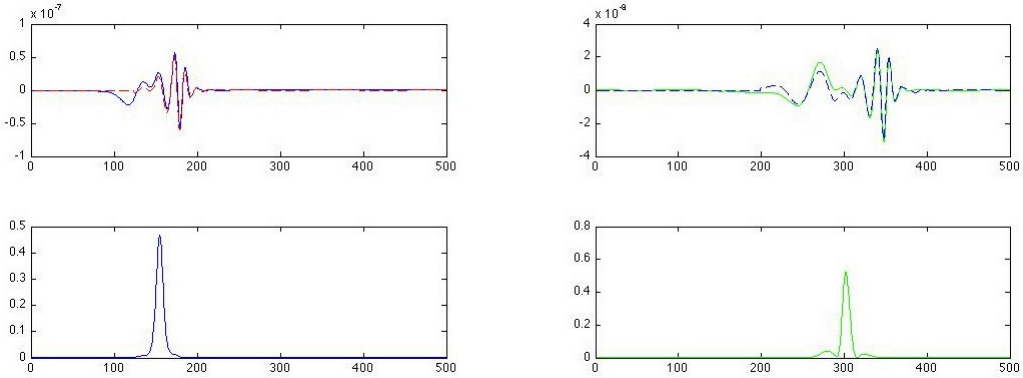

Figure C.2: Top: synthetic signals (solid line) and extracted fundamental mode (dashed line) respectively at 500 (left, structure A) and 1000 (right, structure B) km from the source. Bottom: phase equalized signal at the same distances.

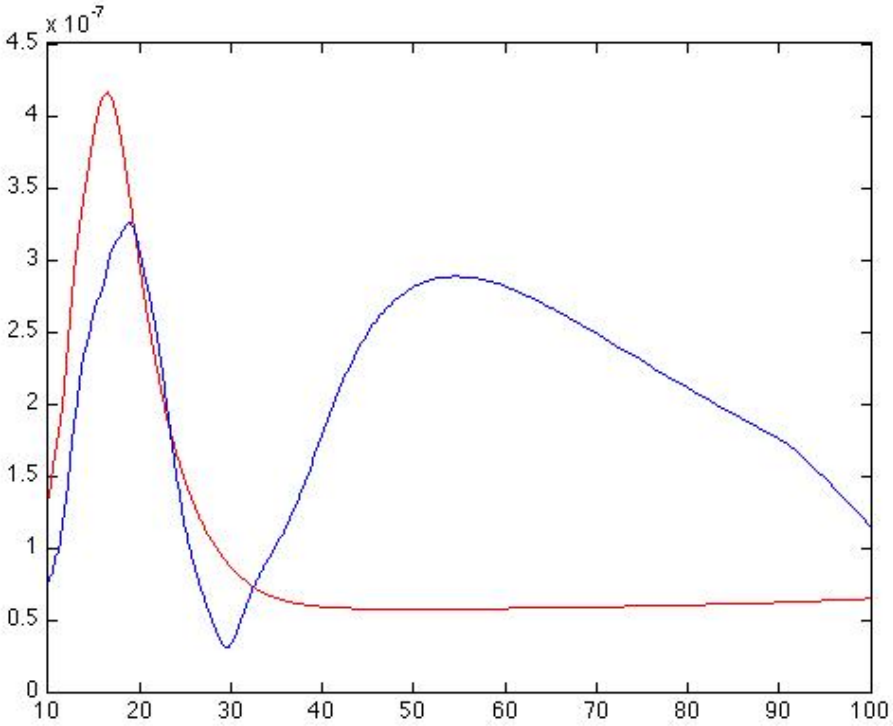

Figure C.3: Spectra of the extracted fundamental mode respectively at 500 (red, structure A) and 1000 (blue, structure B) km from the source.

The attenuation measure obtained in case a) is strongly affected by the source configuration which causes a pronounced minimum in the spectral amplitude at receiver B at a period of about 30 s, while long period amplitudes are very low at

receiver A, due to LVC. Negative values of attenuation are obtained by Levshin method at periods longer than 35 s.

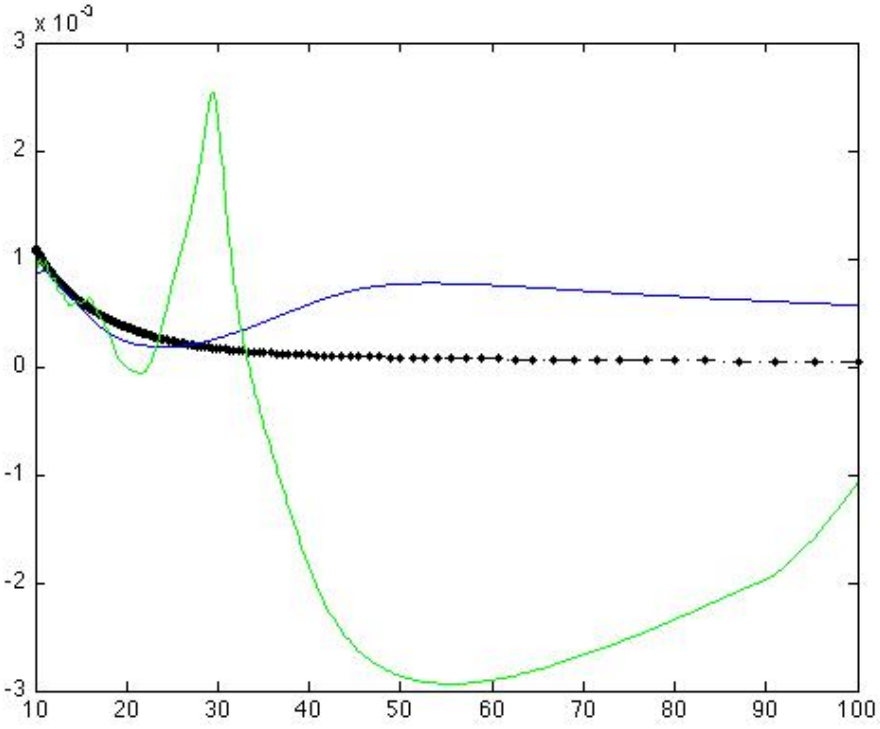

Figure C.4: Attenuation curves ($1/km$ versus period), measured by the method of phase equalization (blue) and by Levshin method (green) compared to the theoretical gamma (dark).

C.2.2 Case b)

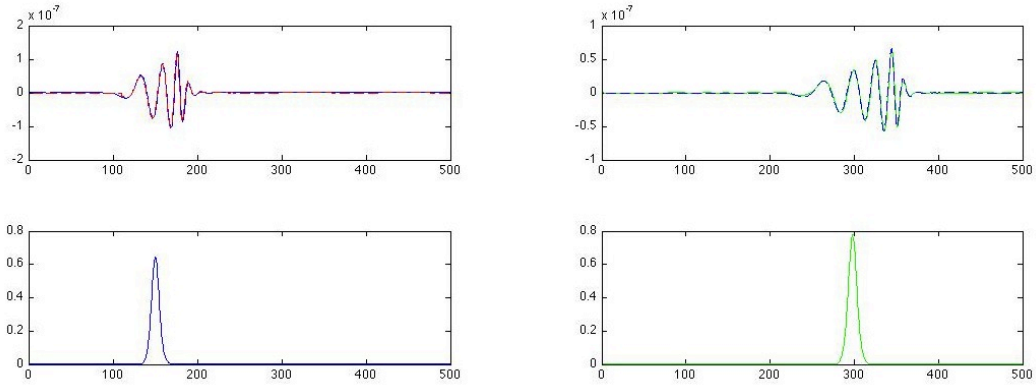

Figure C.5: Top: synthetic signals (solid line) and extracted fundamental mode (dashed line) respectively at 500 (left, structure A) and 1000 (right, structure B) km from the source. Bottom: phase equalized signal at the same distances.

In case b) no spectral *hole* is present, even if the effect of LVC is still noted at periods longer than 30 s. The accuracy of the attenuation curves is comparable at periods shorter than 30 s, but still negative values are obtained by Levshin method at long periods (35-85 s). Note that case a) and b) differ only in rake orientation of the source, so a strong influence of the source characteristics is highlighted by this test.

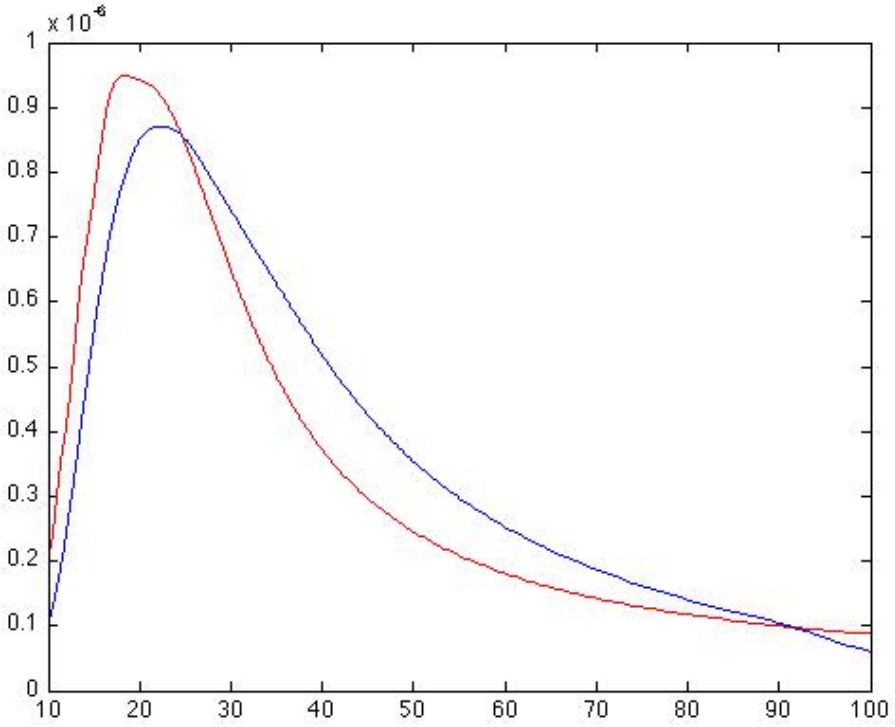

Figure C.6: Spectra of the extracted fundamental mode respectively at 500 (red, structure A) and 1000 (blue, structure B) km from the source.

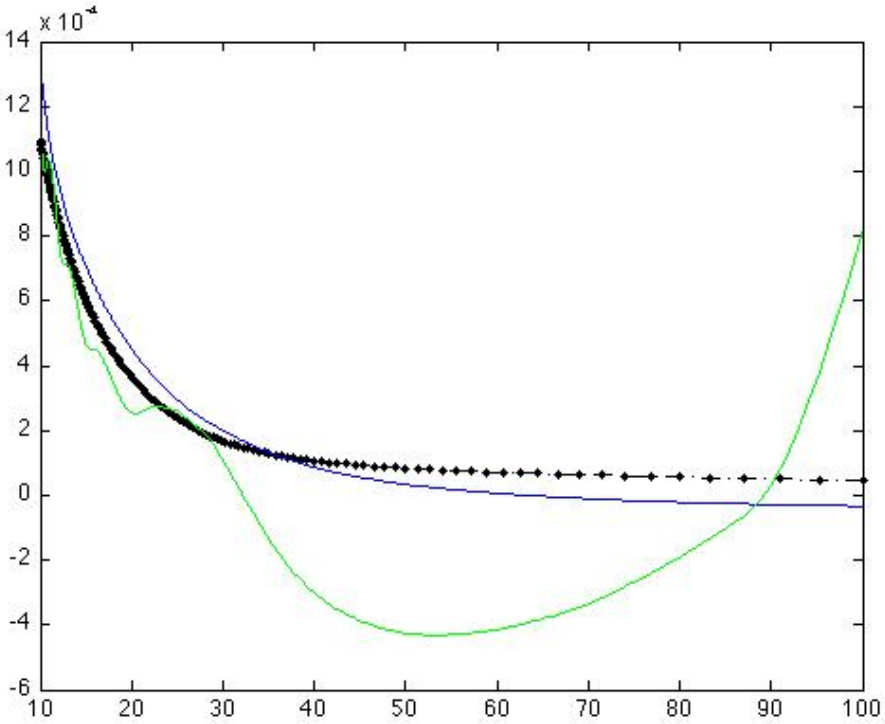

Figure C.7: Attenuation curves ($1/km$ versus period), measured by the method of phase equalization (blue) and by Levshin method (green) compared to the theoretical attenuation (dark).

C.3 WKBJ approximation test

A lateral variation in the thicknesses of the layers and in the elastic parameters characterizing each layer, can be expressed as a perturbation by a small parameter, ϵ, of the original properties in such a way that, if $\epsilon = 0$, the medium is a laterally homogeneous layered structure. When a perturbation in ϵ is small within a wavelength, an approximate solution corresponding to the surface wave field can be obtained by mean of a procedure based on the ray method (Woodhouse, 1974; Levshin et al., 1989). The principal quantities that ray methods use are travel time and geometrical spreading, which are characteristics of rays. Treating the propagation of waves from the point of view of ray theory requires that the minimum wavelength involved in the problem must be bigger than the lateral gradient (a step in our case) between the constituent structures. If the lateral heterogeneous model is made up of two or more vertically heterogeneous structures juxtaposed each other, this means that two adjacent structures have to be very close in the parameter's space where they are determined by a point, or, analogously, they have to be very similar, in the sense of the elastic parameters, to allow the application of the WKBJ approximation (acronym of the names Wentzel, Kramers, Brillouin and Jeffreys). If we focus our attention on a model made up by only two structures, this problem is solved introducing between them a set of sub-structures that have the goal to *smooth* the gradient of the lateral variation (the step between the two structures is sufficiently small), so that the new laterally varying model presents weak lateral heterogeneities, where weak is meant in the sense of the wavelength. In the framework of WKBJ approximation, the strongest smoothness condition suggested to handle such an inhomogeneity is the following:

$$|\nabla_{\perp} p| << \frac{\omega}{C} \cdot p \tag{C.6}$$

where p is an elastic parameter. Equation (C.6) can be written as follows in terms of the maximum wavelength:

$$|\nabla_{\perp} p| << \frac{2\pi}{\lambda_{max}} \cdot p \tag{C.7}$$

So, the smooth condition involves the horizontal gradient of each elastic parameter. Such a horizontal gradient is computed along the direction of the lateral heterogeneity, so it does contain the minimum length we are looking for. Assuming a reference system with a downward z axis and the x axis positive from left to right, (C.7) can be written as

$$\left|\frac{\partial p}{\partial x}\right| << \frac{2\pi}{\lambda_{max}} \cdot p \tag{C.8}$$

In order to test the WKBJ approximation without interpolating structures, we started from Structure A and B, slightly modifying their elastic properties till the condition C.8 has been satisfied. This in practice led to a reduction in thickness and in velocity gradient of the LVC. The Q value, as in the previous case, is assumed the same for both structures, A_{mod} and B_{mod}. Three source configurations are tested:

a) depth 35; strike = 30°; dip = 90°; rake = 180°

b) depth 35; strike = 30°; dip = 90°; rake = 270°

c) depth 20; strike = 30°; dip = 90°; rake = 270°

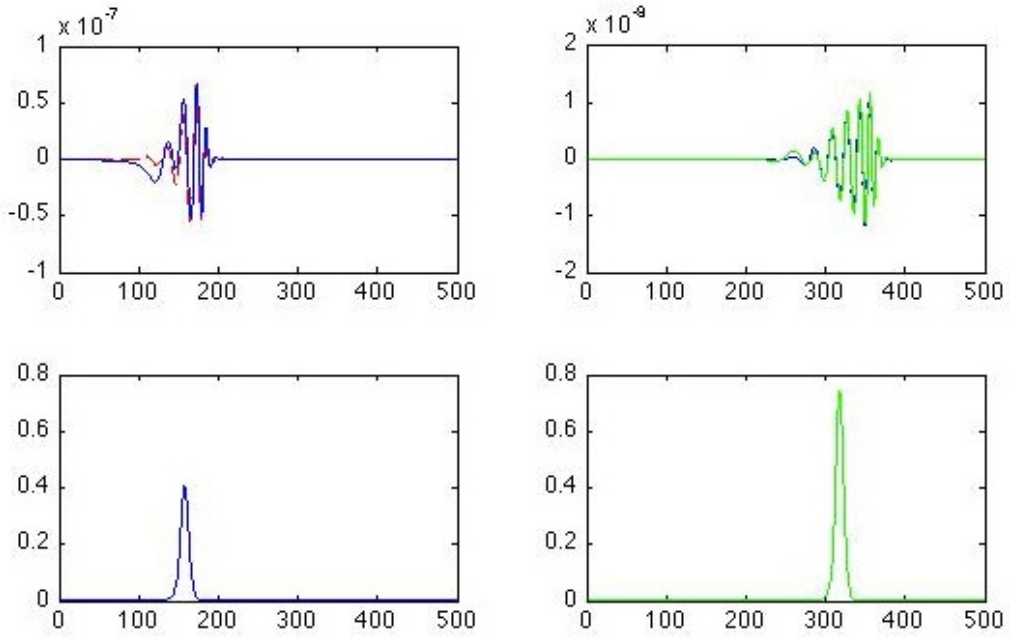

Figure C.8: Configuration a). Top: synthetic signals (solid line) and extracted fundamental mode (dashed line) respectively at 500 (left, structure A_{mod}) and 1000 (right, structure B_{mod}) km from the source. Bottom: phase equalized signal at the same distances.

In all considered configurations we can note that signal at receiver B is strongly attenuated with respect to 2D-coupling cases previously described. This can be due both to the differences in structures (B and B_{mod}) and to the WKBJ method itself, that tends to loose some of the transmitted energy at the interface with respect to the modal coupling. Therefore both attenuations curves are higher than the theoretical one, but still the ones obtained by phase equalized signals show better accuracy.

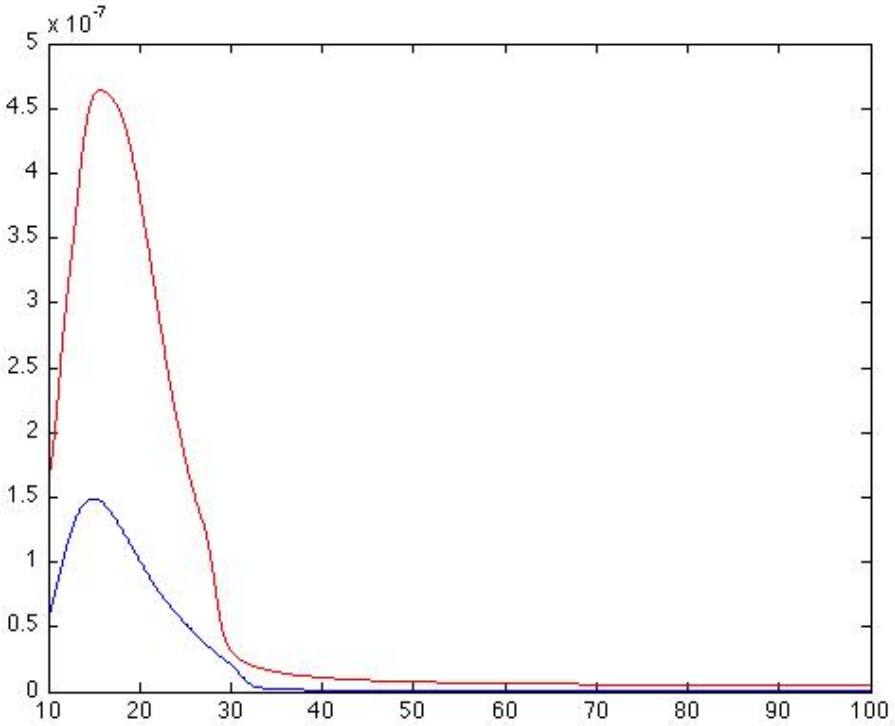

Figure C.9: Configuration a). Spectra of the extracted fundamental mode respectively at 500 (red, structure A_{mod}) and 1000 (blue, structure B_{mod}) km from the source.

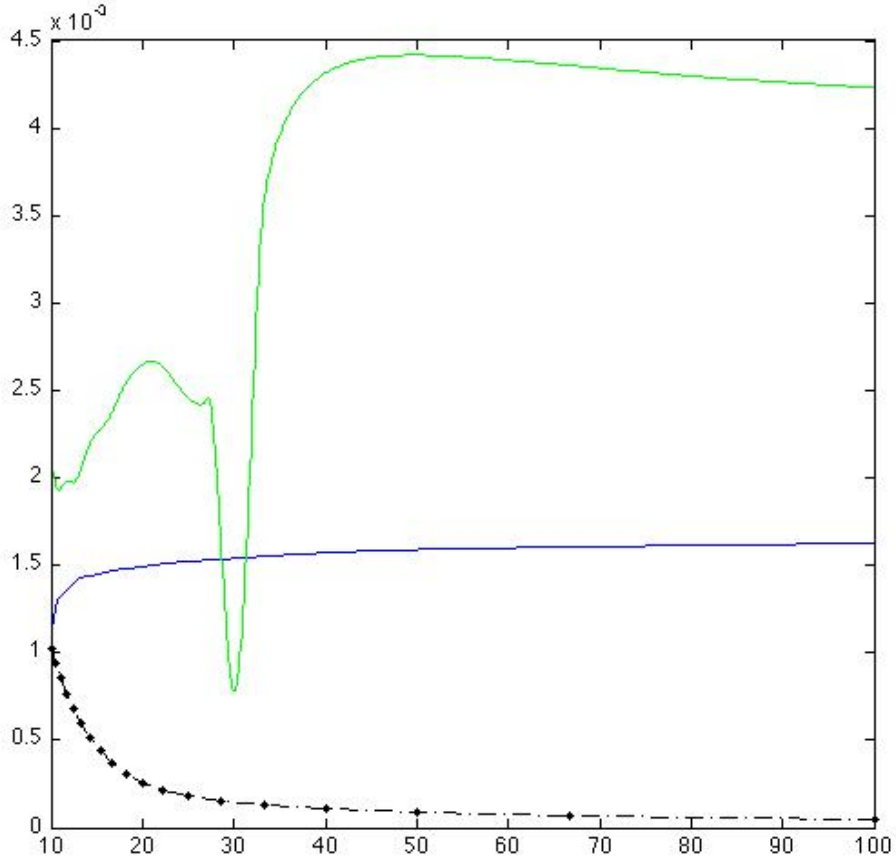

Figure C.10: Configuration a). Attenuation curves ($1/km$ versus period), measured by the method of phase equalization (blue) and by Levshin method (green) compared to the theoretical attenuation (dark).

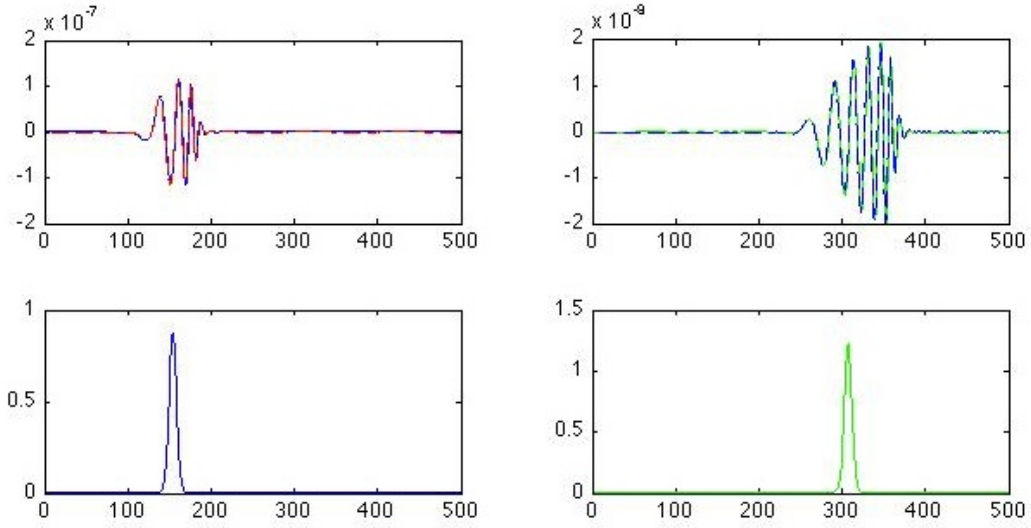

Figure C.11: Configuration b). Top: synthetic signals (solid line) and extracted fundamental mode (dashed line) respectively at 500 (left, structure A_{mod}) and 1000 (right, structure B_{mod}) km from the source. Bottom: phase equalized signal at the same distances.

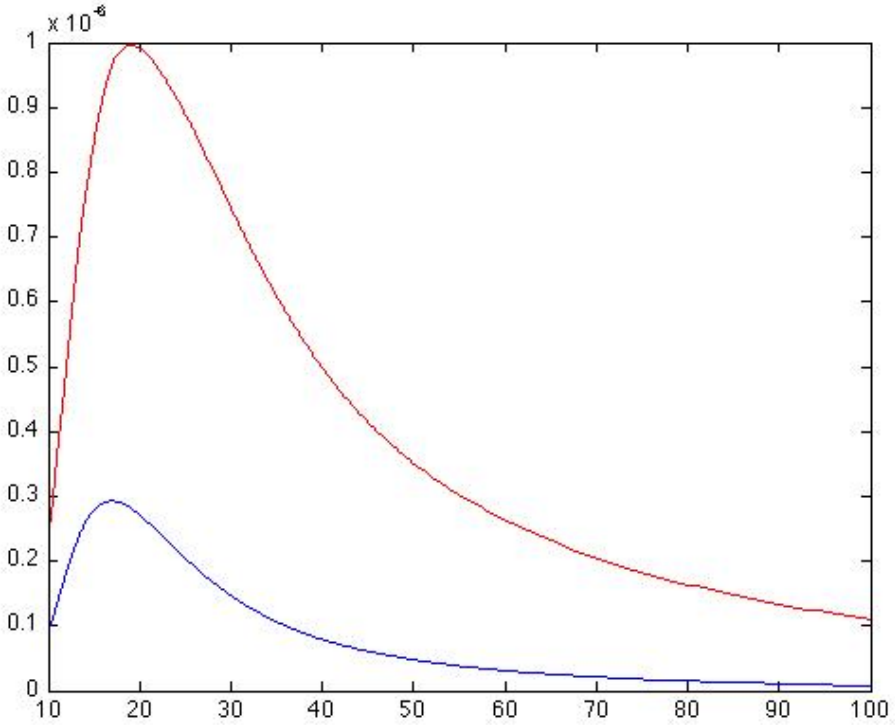

Figure C.12: Configuration b). Spectra of the extracted fundamental mode respectively at 500 (red, structure A_{mod}) and 1000 (blue, structure B_{mod}) km from the source.

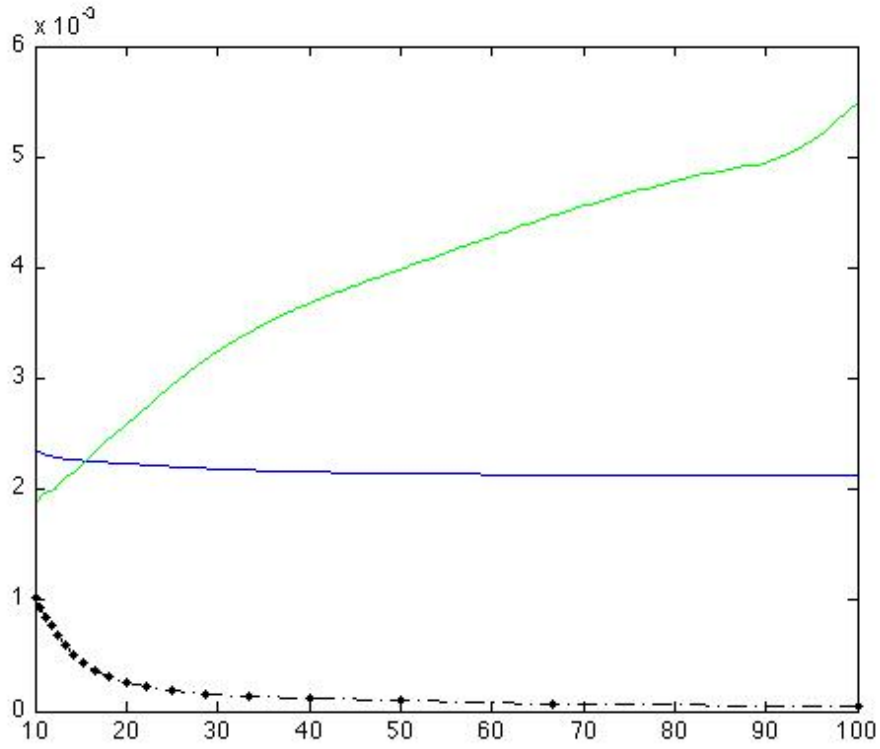

Figure C.13: Configuration b). Attenuation curves ($1/km$ versus period), measured by the method of phase equalization (blue) and by Levshin method (green) compared to the theoretical attenuation (dark).

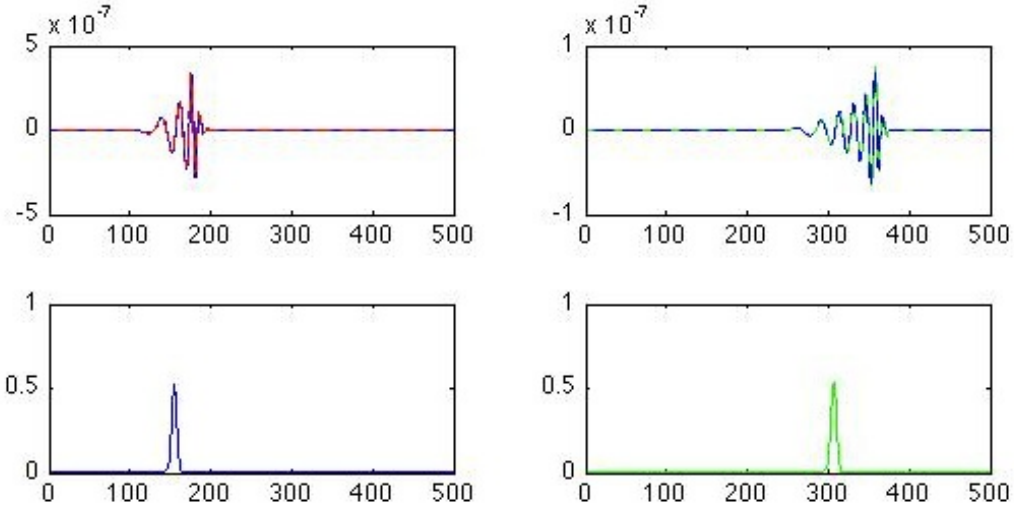

Figure C.14: Configuration c). Top: synthetic signals (solid line) and extracted fundamental mode (dashed line) respectively at 500 (left, structure A_{mod}) and 1000 (right, structure B_{mod}) km from the source. Bottom: phase equalized signal at the same distances.

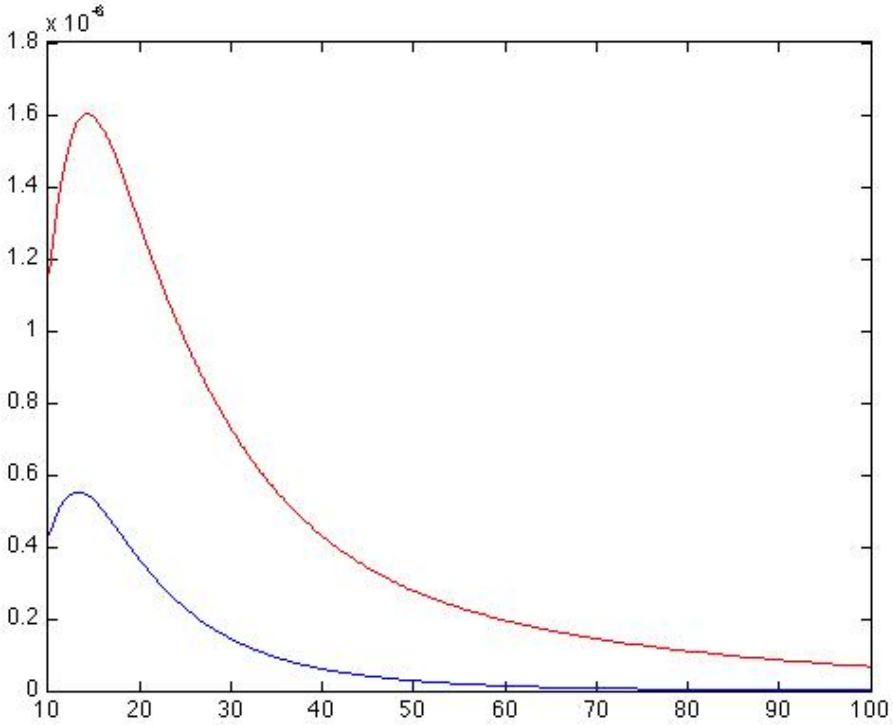

Figure C.15: Configuration c). Spectra of the extracted fundamental mode respectively at 500 (red, structure A_{mod}) and 1000 (blue, structure B_{mod}) km from the source.

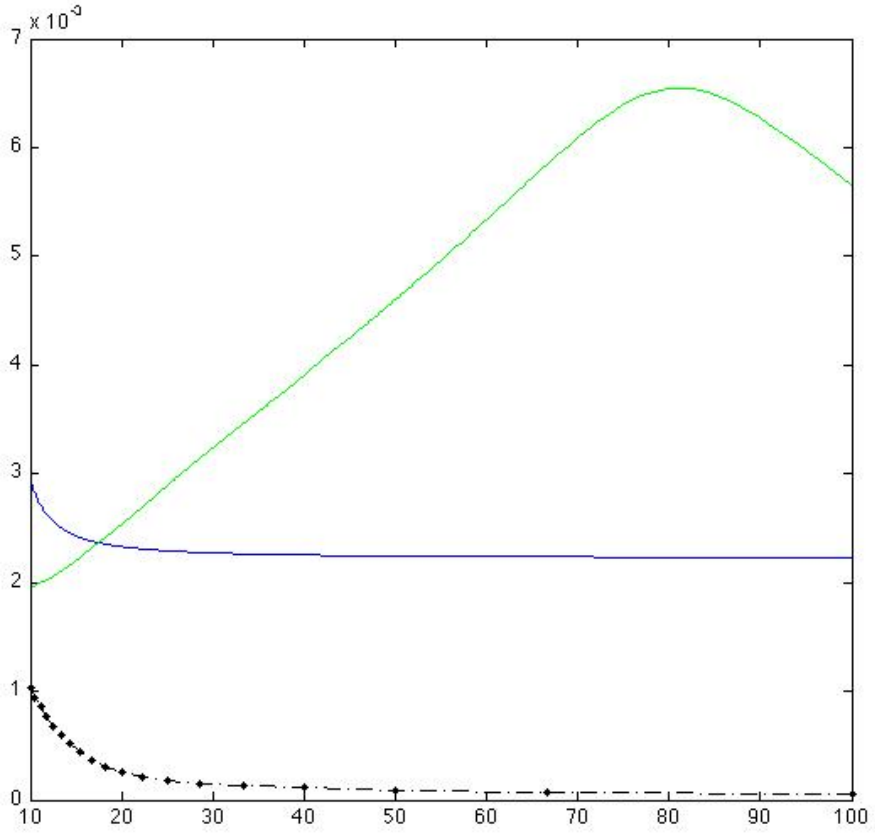

Figure C.16: Configuration c). Attenuation curves ($1/km$ versus period), measured by the method of phase equalization (blue) and by Levshin method (green) compared to the theoretical attenuation (dark).

C.4 Quantification of attenuation effect due to elastic propagation

In order to quantify the effect of elastic propagation on the attenuation measure by Levshin method is useful to repeat the attenuation measure for two perfect elastic structures ($Q_S = 20000$). This curve (γ_{el}) can be subtracted from the γ_{an} in order to remove the effect that is not due to the intrinsic attenuation. Obviously, this proof can be done since we know exactly the structures on the source-receivers path. The same measure is done with computed signals and with FTAN processed signals, in order to remove the error due to the picking of the dispersion curve. In Figure C.17 the computed (solid lines) and FTAN processed (dash lines) γ_{an} and $\gamma_{corr} = \gamma_{an} - \gamma_{el}$ are shown, for the configuration b) of WKBJ test presented in Figure C.13. The elastic propagation effect is dominant on the FTAN picking error, and the γ_{corr} nicely fit the theoretical curve (dark line). Although in most of cases such attenuation measure is comparable in accuracy to that made by means of phase equalized signals, such correction cannot actually used in practice, when structures are not perfectly known.

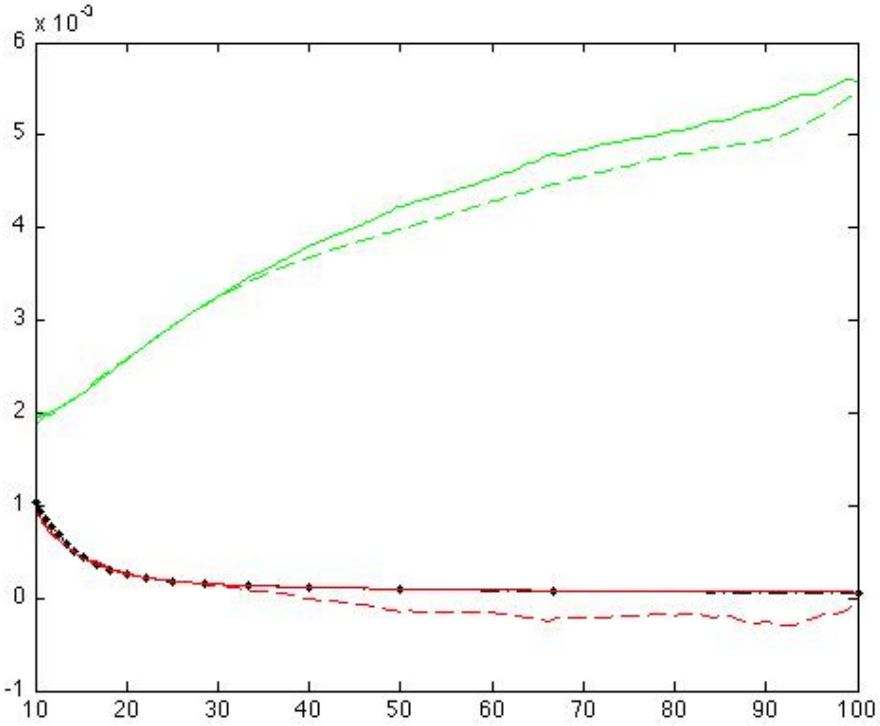

Figure C.17: Attenuation curves ($1/km$ versus period), measured by Levshin method for computed (solid lines) and extracted by FTAN (dash lines) compared to the theoretical attenuation (dark) for configuration b). The greens lines are measured anelastic attenuation, red lines are attenuations curves from which elastic attenuation (that is attenuation curve measured from perfect elastic structures) is removed.

C.5 Influence of anelasticity on elastic properties: a test by mean of hedgehog inversion

This last test is aimed to quantify the influence of anelasticity on the elastic properties of a structural model, in particular on the quantities involved in the receiver correction $B(\omega)$ of eq. C.5, $U_R(\omega)$ and $I_0(\omega)$. Thus we invert with the *hedgehog* method a set of dispersion data in a perfectly elastic case ($Q_S = 10000$) and with the Q value varying with depth. The effect on structure is evident, and for the most two similar models obtained from the inversion the variation at the given periods of 67 and 100 s is up to 3% for $U_R(\omega)$ and up to 4% for $I_0(\omega)$.

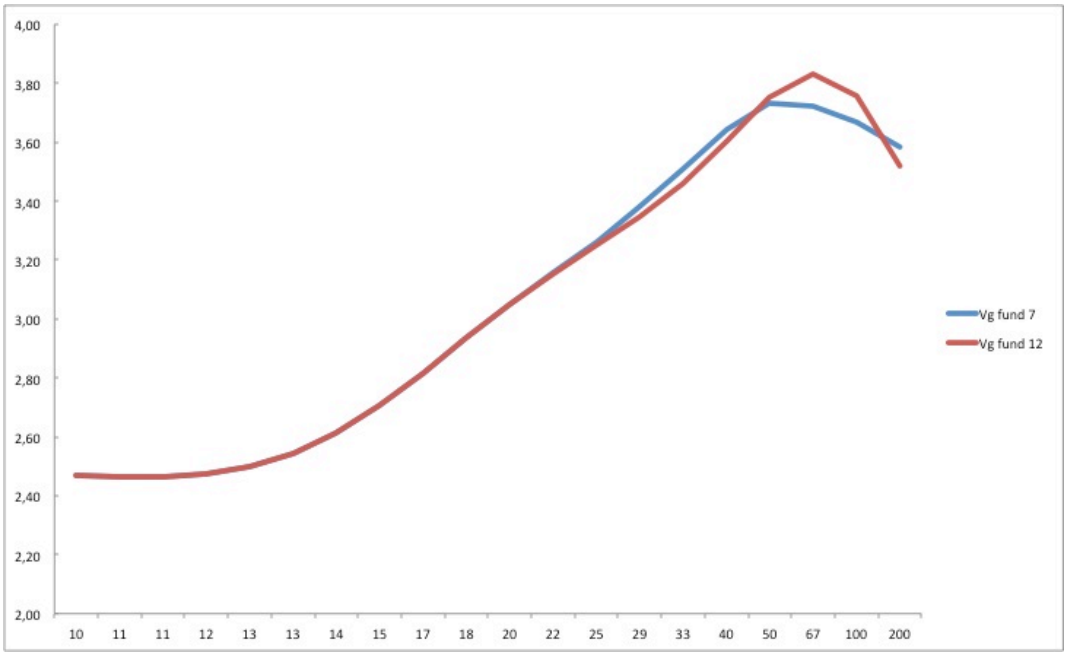

Figure C.18: Dispersion curves of the fundamental mode only in the perfect elastic case (blue) and in the anelastic case (red).

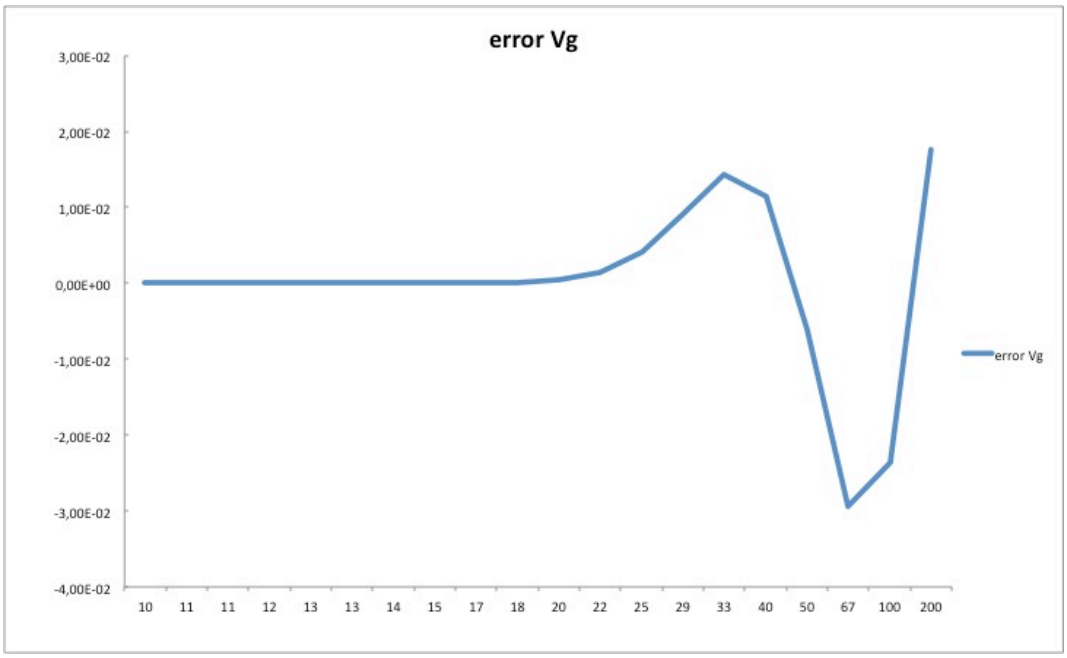

Figure C.19: Relative error in group velocity at selected periods between perfect elastic case and the anelastic case.

Figure C.20: Relative error in normalized kinetic energy at selected periods between perfect elastic case and the anelastic case.

C.6 Conclusions

Through some synthetic tests have been investigated some conditions that can affect real attenuation measurements when structural characteristics on the considered path are unknown. Even if source term is correctly removed, strong influence of the source mechanism is still present in the measure. Both methods are affected by measurement error arising from picking of dispersion curve by FTAN. Propagation effect strongly affect the measures obtained by Levshin method, which cannot be fully removed by the receiver correction proposed, as yet stressed in Levshin et al. (2010). This propagation effect, on the contrary, is removed by phase equalization, as accurately as possible according to the picking error. The quantification of this propagation effect for a perfect elastic structure and its removal from attenuation measure shows that it can be largely dominant on the other sources of error. A rough quantification of the influence of the anelasticity on the correction parameter $B(\omega)$ lead to an estimated error up to 7% on the attenuation measure.

Appendix D

Appendix D

Relevant parameters of the cellular model at a resolution of $1° \times 1°$. For each layers thickness (H, km), density (ρ, g/cm^3), V_P (km/s), V_S (km/s), depth of the lower bottom (Z, km), upper (ΔV_S+, km/s) and lower (ΔV_S+, km/s) V_S uncertainties, upper ($\Delta H+$, km) and lower ($\Delta H-$, km) thickness uncertainties. Layers with both upper and lower zero uncertainties on V_S and H are fixed in the inversion. V_P in the crust are dependent from V_S according to the relation $V_P/V_S = \sqrt{3}$. V_P in the mantle are taken from Piromallo and Morelli (2003) and V_S are migrated in their range of uncertainties to satisfy at best the relation $V_P/V_S = 1.82$ (Kennett et al., 1995). Thus the uncertainties values coming from inversion are consequently reduced, and the V_S value for each layer can be not symmetric with respect to the given uncertainties range.

47.5N 8.5E (g-2)								
H	ρ	VP	VS	Z	ΔV_S+	ΔV_S-	$\Delta H+$	$\Delta H-$
0,50	2,39	4,00	2,30	0,50	0,00	0,00	0,00	0,00
0,50	2,39	4,60	2,65	1,00	0,00	0,00	0,00	0,00
1,00	2,59	5,00	2,90	2,00	0,00	0,00	0,00	0,00
2,00	2,59	5,95	3,45	4,00	0,00	0,00	0,00	0,00
2,00	2,64	5,90	3,40	6,00	0,00	0,00	0,00	0,00
13,00	2,64	5,60	3,25	19,00	0,05	0,05	1,50	1,50
30,00	2,99	8,10	4,30	49,00	0,00	0,10	10,00	0,00
30,00	3,19	8,20	4,55	79,00	0,10	0,00	15,00	0,00
60,00	3,35	8,20	4,40	139,00	0,00	0,10	0,00	20,00
110,00	3,38	8,45	4,65	249,00	0,00	0,20	20,00	0,00
101,00	3,53	8,80	4,75	350,00	0,00	0,00	0,00	0,00

47.5N 9.5E (g-1)

H	ρ	VP	VS	Z	ΔV_S+	ΔV_S-	$\Delta H+$	$\Delta H-$
2,00	2,55	4,75	2,75	2,00	0,00	0,00	0,00	0,00
5,00	2,70	5,90	3,40	7,00	0,00	0,00	0,00	0,00
8,00	2,79	5,35	3,10	15,00	0,10	0,10	2,00	0,00
29,00	2,94	7,10	4,10	44,00	0,00	0,15	4,50	4,50
50,00	3,29	8,30	4,55	94,00	0,10	0,00	0,00	10,00
110,00	3,29	8,25	4,45	204,00	0,00	0,10	20,00	0,00
70,00	3,26	8,50	4,70	274,00	0,05	0,15	20,00	0,00
76,00	3,47	8,80	4,75	350,00	0,00	0,00	0,00	0,00

47.5N 10.5E (g0)

H	ρ	VP	VS	Z	ΔV_S+	ΔV_S-	$\Delta H+$	$\Delta H-$
3,00	2,56	5,90	3,40	3,00	0,00	0,00	0,00	0,00
2,00	2,56	6,05	3,50	5,00	0,00	0,00	0,00	0,00
7,00	2,66	4,95	2,85	12,00	0,15	0,15	2,50	0,00
20,00	2,71	6,50	3,75	32,00	0,15	0,15	7,00	0,00
35,00	3,30	8,00	4,45	67,00	0,15	0,15	10,00	0,00
70,00	3,30	8,30	4,55	137,00	0,05	0,10	0,00	20,00
70,00	3,25	8,30	4,55	207,00	0,00	0,20	20,00	0,00
143,00	3,43	8,80	4,75	350,00	0,00	0,00	0,00	0,00

47.5N 11.5E (g1)

H	ρ	VP	VS	Z	ΔV_S+	ΔV_S-	$\Delta H+$	$\Delta H-$
3,00	2,60	4,65	2,70	3,00	0,00	0,00	0,00	0,00
3,00	2,60	5,20	3,00	6,00	0,00	0,00	0,00	0,00
12,00	2,65	6,15	3,55	18,00	0,10	0,10	3,00	3,00
15,00	2,95	6,40	3,70	33,00	0,15	0,15	5,00	0,00
50,00	3,29	8,05	4,45	83,00	0,10	0,10	0,00	20,00
60,00	3,29	8,25	4,55	143,00	0,05	0,15	17,50	0,00
60,00	3,29	8,25	4,50	203,00	0,00	0,25	20,00	0,00
147,00	3,44	8,85	4,75	350,00	0,00	0,00	0,00	0,00

47.5N 12.5E (g2)

H	ρ	VP	VS	Z	ΔV_S+	ΔV_S-	$\Delta H+$	$\Delta H-$
1,80	2,34	3,80	2,20	1,80	0,00	0,00	0,00	0,00
3,20	2,49	5,55	3,20	5,00	0,00	0,00	0,00	0,00
17,00	2,49	6,05	3,50	22,00	0,10	0,10	3,50	3,50
13,00	2,69	7,10	4,10	35,00	0,00	0,25	6,50	0,00
30,00	3,23	8,05	4,40	65,00	0,05	0,15	15,00	0,00
60,00	3,27	8,20	4,55	125,00	0,20	0,15	20,00	0,00
110,00	3,27	8,40	4,60	235,00	0,00	0,20	0,00	20,00
115,00	3,44	8,90	4,75	350,00	0,00	0,00	0,00	0,00

47.5N 13.5E (g3)

H	ρ	VP	VS	Z	ΔV_S+	ΔV_S-	$\Delta H+$	$\Delta H-$
1,80	2,39	3,80	2,20	1,80	0,00	0,00	0,00	0,00
3,20	2,63	5,35	3,10	5,00	0,00	0,00	0,00	0,00
7,00	2,68	5,60	3,25	12,00	0,10	0,10	3,50	3,50
24,00	2,78	6,55	3,80	36,00	0,00	0,25	6,50	0,00
90,00	3,32	8,10	4,40	126,00	0,05	0,15	15,00	0,00
100,00	3,32	8,30	4,55	226,00	0,20	0,15	20,00	0,00
110,00	3,32	8,80	4,85	336,00	0,00	0,20	0,00	20,00
14,00	3,47	8,85	4,75	350,00	0,00	0,00	0,00	0,00

46.5N 7.5E (f-3)

H	ρ	VP	VS	Z	ΔV_S+	ΔV_S-	$\Delta H+$	$\Delta H-$
1,00	2,37	4,95	2,85	1,00	0,00	0,00	0,00	0,00
2,00	2,52	5,35	3,10	3,00	0,00	0,00	0,00	0,00
2,00	2,62	5,95	3,45	5,00	0,00	0,00	0,00	0,00
12,00	2,76	5,20	3,00	17,00	0,05	0,05	1,50	1,50
26,00	2,91	6,85	3,95	43,00	0,15	0,15	4,00	4,00
35,00	3,26	8,10	4,45	78,00	0,10	0,15	12,50	0,00
70,00	3,26	8,20	4,40	148,00	0,00	0,05	20,00	0,00
110,00	3,27	8,55	4,70	258,00	0,05	0,20	0,00	20,00
92,00	3,47	8,75	4,75	350,00	0,00	0,00	0,00	0,00

46.5N 8.5E (f-2)

H	ρ	VP	VS	Z	ΔV_S+	ΔV_S-	$\Delta H+$	$\Delta H-$
1,00	2,39	4,95	2,85	1,00	0,00	0,00	0,00	0,00
1,00	2,49	5,35	3,10	2,00	0,00	0,00	0,00	0,00
3,00	2,69	5,95	3,45	5,00	0,00	0,00	0,00	0,00
11,00	2,69	5,30	3,05	16,00	0,15	0,15	2,00	2,00
24,00	2,94	6,75	3,90	40,00	0,05	0,10	3,00	3,00
35,00	3,28	8,25	4,60	75,00	0,15	0,15	17,50	0,00
70,00	3,28	8,30	4,45	145,00	0,00	0,15	20,00	0,00
110,00	3,28	8,60	4,75	255,00	0,00	0,25	0,00	20,00
95,00	3,49	8,80	4,75	350,00	0,00	0,00	0,00	0,00

46.5N 9.5E (f-1)

H	ρ	VP	VS	Z	ΔV_S+	ΔV_S-	$\Delta H+$	$\Delta H-$
0,10	2,08	2,10	1,20	0,10	0,00	0,00	0,00	0,00
7,90	2,53	5,70	3,30	8,00	0,00	0,00	0,00	0,00
4,00	2,57	4,40	2,55	12,00	0,10	0,15	1,00	1,00
25,00	2,87	6,55	3,80	37,00	0,10	0,05	4,00	4,00
50,00	3,27	8,10	4,50	87,00	0,05	0,05	15,00	0,00
100,00	3,27	8,20	4,45	187,00	0,20	0,25	0,00	17,50
110,00	3,27	8,70	4,70	297,00	0,00	0,25	20,00	0,00
53,00	3,47	8,80	4,75	350,00	0,00	0,00	0,00	0,00

46.5N 10.5E (f0)

H	ρ	VP	VS	Z	ΔV_S+	ΔV_S-	$\Delta H+$	$\Delta H-$
3,00	2,48	5,55	3,20	3,00	0,00	0,00	0,00	0,00
2,00	2,53	6,05	3,50	5,00	0,00	0,00	0,00	0,00
6,00	2,53	4,95	2,85	11,00	0,05	0,05	1,00	1,00
22,00	2,67	6,40	3,70	33,00	0,10	0,10	5,00	5,00
35,00	3,27	8,20	4,45	68,00	0,10	0,15	15,00	0,00
70,00	3,27	8,05	4,50	138,00	0,15	0,15	20,00	0,00
70,00	3,27	8,20	4,25	208,00	0,00	0,25	20,00	0,00
142,00	3,45	8,85	4,75	350,00	0,00	0,00	0,00	0,00

46.5N 11.5E (f1)

H	ρ	VP	VS	Z	ΔV_S+	ΔV_S-	$\Delta H+$	$\Delta H-$
0,10	2,09	2,10	1,20	0,10	0,00	0,00	0,00	0,00
0,90	2,53	5,80	3,35	1,00	0,00	0,00	0,00	0,00
3,00	2,53	5,45	3,15	4,00	0,00	0,00	0,00	0,00
5,00	2,53	4,85	2,80	9,00	0,10	0,10	1,50	1,50
18,00	2,68	6,05	3,50	27,00	0,10	0,10	3,50	3,50
45,00	3,23	8,00	4,35	72,00	0,00	0,10	0,00	15,00
65,00	3,28	7,95	4,60	137,00	0,15	0,00	0,00	17,50
70,00	3,28	8,10	4,20	207,00	0,00	0,20	20,00	0,00
143,00	3,46	8,80	4,75	350,00	0,00	0,00	0,00	0,00

46.5N 12.5E (f2)

H	ρ	VP	VS	Z	ΔV_S+	ΔV_S-	$\Delta H+$	$\Delta H-$
0,50	2,55	6,05	3,50	0,50	0,00	0,00	0,00	0,00
6,50	2,55	4,95	2,85	7,00	0,00	0,00	0,00	0,00
7,00	2,70	5,60	3,25	14,00	0,10	0,05	3,50	3,50
17,00	2,85	6,05	3,50	31,00	0,20	0,20	4,50	0,00
35,00	3,30	8,00	4,35	66,00	0,15	0,15	10,00	0,00
110,00	3,30	8,00	4,40	176,00	0,10	0,05	0,00	20,00
110,00	3,30	8,45	4,65	286,00	0,15	0,15	0,00	25,00
64,00	3,47	8,75	4,75	350,00	0,00	0,00	0,00	0,00

46.5N 13.5E (f3)

H	ρ	VP	VS	Z	ΔV_S+	ΔV_S-	$\Delta H+$	$\Delta H-$
0,25	2,19	2,95	1,70	0,25	0,00	0,00	0,00	0,00
1,00	2,49	4,15	2,40	1,25	0,00	0,00	0,00	0,00
6,75	2,49	5,45	3,15	8,00	0,00	0,00	0,00	0,00
10,00	2,59	5,45	3,15	18,00	0,00	0,15	4,00	0,00
25,00	2,84	6,65	3,85	43,00	0,20	0,20	12,50	0,00
30,00	3,29	8,15	4,40	73,00	0,20	0,20	10,00	0,00
100,00	3,29	8,05	4,40	173,00	0,20	0,20	0,00	20,00
70,00	3,29	8,25	4,55	243,00	0,05	0,15	20,00	0,00
107,00	3,48	8,65	4,75	350,00	0,00	0,00	0,00	0,00

46.5N 14.5E (f4)

H	ρ	VP	VS	Z	ΔV_S+	ΔV_S-	$\Delta H+$	$\Delta H-$
3,00	2,50	4,05	2,35	3,00	0,00	0,00	0,00	0,00
0,50	2,65	5,60	3,25	3,50	0,00	0,00	0,00	0,00
0,50	2,70	5,80	3,35	4,00	0,00	0,00	0,00	0,00
10,00	2,80	5,55	3,20	14,00	0,05	0,05	2,00	2,00
24,00	2,90	6,65	3,85	38,00	0,10	0,15	5,00	5,00
35,00	3,09	8,05	4,40	73,00	0,20	0,20	12,50	0,00
105,00	3,19	8,15	4,40	178,00	0,20	0,20	0,00	20,00
65,00	3,30	8,30	4,55	243,00	0,05	0,15	22,50	0,00
107,00	3,50	8,65	4,75	350,00	0,00	0,00	0,00	0,00

46.5N 15.5E (f5)

H	ρ	VP	VS	Z	ΔV_S+	ΔV_S-	$\Delta H+$	$\Delta H-$
0,15	2,40	3,80	2,20	0,15	0,00	0,00	0,00	0,00
0,85	2,50	4,15	2,40	1,00	0,00	0,00	0,00	0,00
0,70	2,55	4,75	2,75	1,70	0,00	0,00	0,00	0,00
0,80	2,65	5,70	3,30	2,50	0,00	0,00	0,00	0,00
0,50	2,70	5,80	3,35	3,00	0,00	0,00	0,00	0,00
4,00	2,80	4,85	2,80	7,00	0,10	0,10	2,00	0,00
18,00	2,90	6,05	3,50	25,00	0,10	0,10	3,50	3,50
30,00	3,10	7,95	4,40	55,00	0,00	0,15	15,00	0,00
65,00	3,20	8,00	4,40	120,00	0,10	0,05	17,50	0,00
110,00	3,30	8,20	4,50	230,00	0,10	0,10	0,00	20,00
120,00	3,51	8,75	4,75	350,00	0,00	0,00	0,00	0,00

45.5N 6.5E (e-4)

H	ρ	VP	VS	Z	ΔV_S+	ΔV_S-	$\Delta H+$	$\Delta H-$
0,50	2,08	2,10	1,20	0,50	0,00	0,00	0,00	0,00
4,50	2,57	5,00	2,90	5,00	0,00	0,00	0,00	0,00
8,00	2,72	4,95	2,85	13,00	0,05	0,05	1,00	1,00
20,00	2,92	6,85	3,95	33,00	0,15	0,20	3,00	3,00
75,00	3,06	8,00	4,45	108,00	0,00	0,05	0,00	10,00
65,00	3,16	8,30	4,60	173,00	0,10	0,10	17,50	0,00
110,00	3,25	8,65	4,55	283,00	0,00	0,20	0,00	22,50
67,00	3,44	8,80	4,75	350,00	0,00	0,00	0,00	0,00

45.5N 7.5E (e-3)

H	ρ	VP	VS	Z	ΔV_S+	ΔV_S-	$\Delta H+$	$\Delta H-$
0,10	2,10	2,10	1,20	0,10	0,00	0,00	0,00	0,00
5,90	2,65	4,85	2,80	6,00	0,00	0,00	0,00	0,00
7,00	2,80	4,95	2,85	13,00	0,10	0,10	1,00	0,00
26,00	2,95	6,90	4,00	39,00	0,00	0,10	3,50	3,50
85,00	3,29	8,20	4,55	124,00	0,05	0,05	0,00	15,00
45,00	3,29	8,25	4,55	169,00	0,00	0,25	0,00	27,50
110,00	3,29	8,60	4,75	279,00	0,00	0,25	27,50	0,00
71,00	3,46	8,75	4,75	350,00	0,00	0,00	0,00	0,00

45.5N 8.5E (e-2)

H	ρ	VP	VS	Z	ΔV_S+	ΔV_S-	$\Delta H+$	$\Delta H-$
3,00	2,60	4,20	2,43	3,00	0,00	0,00	0,00	0,00
3,00	2,74	5,00	2,90	6,00	0,00	0,00	0,00	0,00
10,00	2,74	5,45	3,15	16,00	0,15	0,10	2,00	2,00
25,00	2,94	6,90	4,00	41,00	0,10	0,10	4,00	4,00
80,00	3,29	8,20	4,45	121,00	0,10	0,10	15,00	0,00
60,00	3,29	8,25	4,50	181,00	0,15	0,00	0,00	20,00
110,00	3,29	8,60	4,60	291,00	0,00	0,20	20,00	0,00
59,00	3,48	8,75	4,75	350,00	0,00	0,00	0,00	0,00

45.5N 9.5E (e-1)

H	ρ	VP	VS	Z	ΔV_S+	ΔV_S-	$\Delta H+$	$\Delta H-$
3,00	2,60	4,00	2,30	3,00	0,00	0,00	0,00	0,00
3,00	2,70	4,50	2,60	6,00	0,00	0,00	0,00	0,00
10,00	2,75	5,45	3,15	16,00	0,15	0,10	2,50	0,00
25,00	2,94	6,90	4,00	41,00	0,00	0,10	0,00	4,00
50,00	3,29	8,10	4,55	91,00	0,15	0,00	15,00	0,00
100,00	3,29	8,20	4,50	191,00	0,00	0,15	0,00	17,50
70,00	3,29	8,50	4,60	261,00	0,00	0,20	20,00	0,00
89,00	3,48	8,90	4,75	350,00	0,00	0,00	0,00	0,00

45.5N 10.5E (e0)

H	ρ	VP	VS	Z	ΔV_S+	ΔV_S-	$\Delta H+$	$\Delta H-$
1,00	2,38	3,45	2,00	1,00	0,00	0,00	0,00	0,00
2,00	2,43	4,45	2,56	3,00	0,00	0,00	0,00	0,00
3,00	2,58	5,20	3,01	6,00	0,00	0,00	0,00	0,00
5,00	2,73	5,10	2,95	11,00	0,10	0,10	1,00	0,00
27,00	2,83	6,50	3,75	38,00	0,10	0,10	3,00	3,00
50,00	3,33	8,15	4,55	88,00	0,10	0,00	20,00	0,00
50,00	3,33	8,00	4,40	138,00	0,10	0,15	20,00	0,00
70,00	3,33	8,20	4,40	208,00	0,00	0,40	20,00	0,00
142,00	3,47	8,85	4,75	350,00	0,00	0,00	0,00	0,00

45.5N 11.5E (e1)

H	ρ	VP	VS	Z	ΔV_S+	ΔV_S-	$\Delta H+$	$\Delta H-$
4,50	2,60	4,40	2,55	4,50	0,00	0,00	0,00	0,00
1,50	2,66	5,50	3,18	6,00	0,00	0,00	0,00	0,00
1,00	2,66	5,70	3,30	7,00	0,00	0,00	0,00	0,00
4,00	2,86	4,85	2,80	11,00	0,10	0,15	1,50	0,00
21,00	2,97	6,15	3,55	32,00	0,10	0,15	3,50	3,50
40,00	3,36	8,30	4,50	72,00	0,10	0,10	0,00	20,00
70,00	3,36	8,00	4,55	142,00	0,15	0,00	0,00	20,00
105,00	3,32	8,35	4,25	247,00	0,00	0,25	22,50	0,00
103,00	3,48	8,85	4,75	350,00	0,00	0,00	0,00	0,00

45.5N 12.5E (e2)

H	ρ	VP	VS	Z	ΔV_S+	ΔV_S-	$\Delta H+$	$\Delta H-$
1,00	2,26	3,65	2,10	1,00	0,00	0,00	0,00	0,00
4,00	2,36	4,35	2,50	5,00	0,00	0,00	0,00	0,00
2,00	2,46	5,00	2,90	7,00	0,00	0,00	0,00	0,00
14,00	2,77	5,80	3,35	21,00	0,05	0,05	3,50	3,50
20,00	2,97	6,75	3,90	41,00	0,20	0,15	10,00	0,00
60,00	3,32	7,90	4,55	101,00	0,10	0,00	0,00	15,00
50,00	3,32	7,80	4,30	151,00	0,10	0,05	0,00	20,00
50,00	3,32	8,10	4,20	201,00	0,00	0,20	0,00	25,00
149,00	3,49	8,70	4,75	350,00	0,00	0,00	0,00	0,00

45.5N 13.5E (e3)

H	ρ	VP	VS	Z	ΔV_S+	ΔV_S-	$\Delta H+$	$\Delta H-$
1,00	2,32	3,65	2,10	1,00	0,00	0,00	0,00	0,00
4,00	2,47	4,50	2,60	5,00	0,00	0,00	0,00	0,00
1,00	2,52	5,20	3,00	6,00	0,00	0,00	0,00	0,00
2,00	2,52	5,55	3,20	8,00	0,00	0,00	0,00	0,00
12,00	2,72	5,70	3,30	20,00	0,05	0,05	3,00	0,00
25,00	2,97	6,85	3,95	45,00	0,15	0,15	2,50	2,50
60,00	3,32	8,00	4,60	105,00	0,05	0,00	15,00	15,00
90,00	3,32	8,10	4,40	195,00	0,00	0,05	0,00	20,00
90,00	3,32	8,50	4,70	285,00	0,00	0,20	0,00	20,00
65,00	3,50	8,70	4,75	350,00	0,00	0,00	0,00	0,00

45.5N 14.5E (e4)

H	ρ	VP	VS	Z	ΔV_S+	ΔV_S-	$\Delta H+$	$\Delta H-$
4,00	2,40	4,00	2,30	4,00	0,00	0,00	0,00	0,00
1,50	2,50	5,60	3,25	5,50	0,00	0,00	0,00	0,00
1,50	2,55	5,80	3,35	7,00	0,00	0,00	0,00	0,00
1,00	2,55	5,95	3,45	8,00	0,00	0,00	0,00	0,00
15,00	2,60	6,05	3,50	23,00	0,05	0,05	5,00	0,00
17,00	2,95	6,90	4,00	40,00	0,00	0,20	4,30	4,30
13,00	3,25	8,20	4,20	53,00	0,00	0,20	3,20	3,20
30,00	3,30	8,20	4,70	83,00	0,10	0,00	10,00	0,00
100,00	3,30	8,20	4,50	183,00	0,10	0,10	0,00	20,00
60,00	3,31	8,35	4,60	243,00	0,10	0,10	25,00	0,00
107,00	3,51	8,65	4,75	350,00	0,00	0,00	0,00	0,00

45.5N 15.5E (e5)

H	ρ	VP	VS	Z	ΔV_S+	ΔV_S-	$\Delta H+$	$\Delta H-$
4,00	2,25	3,65	2,10	4,00	0,00	0,00	0,00	0,00
1,50	2,60	5,70	3,30	5,50	0,00	0,00	0,00	0,00
2,50	2,60	6,25	3,60	8,00	0,00	0,00	0,00	0,00
24,00	2,70	6,50	3,75	32,00	0,10	0,10	4,00	4,00
25,00	3,25	8,05	4,40	57,00	0,10	0,10	12,50	0,00
60,00	3,30	8,05	4,40	117,00	0,15	0,10	0,00	15,00
90,00	3,30	8,20	4,45	207,00	0,00	0,15	0,00	20,00
50,00	3,31	8,40	4,60	257,00	0,15	0,10	25,00	0,00
93,00	3,50	8,70	4,75	350,00	0,00	0,00	0,00	0,00

45.5N 16.5E (e6)

H	ρ	VP	VS	Z	ΔV_S+	ΔV_S-	$\Delta H+$	$\Delta H-$
1,50	2,50	4,15	2,40	1,50	0,00	0,00	0,00	0,00
1,00	2,55	4,50	2,60	2,50	0,00	0,00	0,00	0,00
0,50	2,60	5,20	3,00	3,00	0,00	0,00	0,00	0,00
1,00	2,68	5,55	3,20	4,00	0,00	0,00	0,00	0,00
12,00	2,80	5,70	3,30	16,00	0,05	0,05	2,00	2,00
21,00	2,90	6,55	3,80	37,00	0,10	0,15	3,50	3,50
50,00	3,11	8,00	4,40	87,00	0,10	0,05	17,50	0,00
85,00	3,21	8,10	4,45	172,00	0,10	0,10	0,00	17,50
65,00	3,31	8,25	4,55	237,00	0,15	0,15	22,50	0,00
113,00	3,50	8,85	4,75	350,00	0,00	0,00	0,00	0,00

45.5N 17.5E (e7)

H	ρ	VP	VS	Z	ΔV_S+	ΔV_S-	$\Delta H+$	$\Delta H-$
1,00	2,21	2,60	1,50	1,00	0,00	0,00	0,00	0,00
0,60	2,51	5,30	3,05	1,60	0,00	0,00	0,00	0,00
1,90	2,56	5,45	3,14	3,50	0,00	0,00	0,00	0,00
1,50	2,64	5,55	3,20	5,00	0,00	0,00	0,00	0,00
10,00	2,81	5,80	3,35	15,00	0,10	0,10	2,50	0,00
25,00	2,91	6,65	3,85	40,00	0,10	0,15	5,00	5,00
50,00	3,12	8,00	4,45	90,00	0,10	0,00	17,50	0,00
60,00	3,22	8,15	4,35	150,00	0,00	0,15	20,00	0,00
70,00	3,31	8,30	4,55	220,00	0,05	0,15	22,50	0,00
130,00	3,49	8,90	4,75	350,00	0,00	0,00	0,00	0,00

44.5N 6.5E (d-4)

H	ρ	VP	VS	Z	ΔV_S+	ΔV_S-	$\Delta H+$	$\Delta H-$
2,00	2,42	4,75	2,75	2,00	0,00	0,00	0,00	0,00
2,00	2,42	5,20	3,00	4,00	0,00	0,00	0,00	0,00
1,00	2,57	5,45	3,15	5,00	0,00	0,00	0,00	0,00
8,00	2,66	5,00	2,90	13,00	0,15	0,10	1,50	1,50
22,00	2,71	6,75	3,90	35,00	0,15	0,10	2,50	2,50
70,00	3,25	7,90	4,35	105,00	0,05	0,05	0,00	15,00
60,00	3,25	8,10	4,45	165,00	0,05	0,10	0,00	25,00
110,00	3,25	8,55	4,60	275,00	0,00	0,20	25,00	0,00
75,00	3,45	8,80	4,75	350,00	0,00	0,00	0,00	0,00

44.5N 7.5E (d-3)

H	ρ	VP	VS	Z	ΔV_S+	ΔV_S-	$\Delta H+$	$\Delta H-$
1,00	2,43	4,75	2,75	1,00	0,00	0,00	0,00	0,00
1,00	2,47	4,95	2,85	2,00	0,00	0,00	0,00	0,00
1,00	2,47	5,20	3,00	3,00	0,00	0,00	0,00	0,00
2,00	2,47	5,35	3,10	5,00	0,00	0,00	0,00	0,00
6,00	2,67	4,60	2,65	11,00	0,15	0,10	2,00	0,00
20,00	2,92	6,55	3,80	31,00	0,15	0,15	10,00	0,00
85,00	3,27	7,80	4,30	116,00	0,10	0,00	0,00	17,50
60,00	3,27	8,05	4,35	176,00	0,20	0,20	0,00	20,00
100,00	3,28	8,50	4,70	276,00	0,05	0,20	20,00	0,00
74,00	3,49	8,80	4,75	350,00	0,00	0,00	0,00	0,00

44.5N 8.5E (d-2)

H	ρ	VP	VS	Z	ΔV_S+	ΔV_S-	$\Delta H+$	$\Delta H-$
2,00	2,67	4,00	2,30	2,00	0,00	0,00	0,00	0,00
4,00	2,69	4,35	2,50	6,00	0,00	0,00	0,00	0,00
10,00	2,94	5,80	3,35	16,00	0,10	0,15	1,50	1,50
29,00	2,99	7,10	4,10	45,00	0,00	0,15	4,50	4,50
50,00	3,29	7,95	4,45	95,00	0,15	0,00	15,00	0,00
100,00	3,29	8,15	4,45	195,00	0,00	0,15	0,00	20,00
70,00	3,30	8,40	4,60	265,00	0,20	0,10	20,00	0,00
85,00	3,51	8,90	4,75	350,00	0,00	0,00	0,00	0,00

44.5N 9.5E (d-1)

H	ρ	VP	VS	Z	ΔV_S+	ΔV_S-	$\Delta H+$	$\Delta H-$
2,00	2,60	4,00	2,30	2,00	0,00	0,00	0,00	0,00
4,00	2,70	4,35	2,50	6,00	0,00	0,00	0,00	0,00
5,00	2,85	5,10	2,95	11,00	0,20	0,20	2,50	0,00
12,00	2,95	6,05	3,50	23,00	0,15	0,15	4,00	4,00
25,00	3,29	7,90	4,20	48,00	0,00	0,05	0,00	15,00
105,00	3,29	8,10	4,45	153,00	0,15	0,05	17,50	17,50
70,00	3,29	8,35	4,25	223,00	0,00	0,25	0,00	20,00
127,00	3,50	8,80	4,75	350,00	0,00	0,00	0,00	0,00

44.5N 10.5E (d0)

H	ρ	VP	VS	Z	ΔV_S+	ΔV_S-	$\Delta H+$	$\Delta H-$
3,00	2,22	3,45	2,00	3,00	0,00	0,00	0,00	0,00
1,40	2,32	3,80	2,20	4,40	0,00	0,00	0,00	0,00
1,60	2,47	4,85	2,80	6,00	0,00	0,00	0,00	0,00
1,00	2,56	5,60	3,25	7,00	0,00	0,00	0,00	0,00
11,00	2,76	5,70	3,30	18,00	0,05	0,05	0,50	0,50
20,00	2,91	6,85	3,95	38,00	0,10	0,10	10,00	0,00
30,00	3,25	7,95	4,45	68,00	0,15	0,20	15,00	0,00
100,00	3,25	8,20	4,45	168,00	0,20	0,25	0,00	25,00
50,00	3,27	8,40	4,20	218,00	0,00	0,20	25,00	0,00
132,00	3,48	8,90	4,75	350,00	0,00	0,00	0,00	0,00

44.5N 11.5E (d1)

H	ρ	VP	VS	Z	ΔV_S+	ΔV_S-	$\Delta H+$	$\Delta H-$
2,00	2,17	3,45	2,00	2,00	0,00	0,00	0,00	0,00
2,40	2,17	3,70	2,15	4,40	0,00	0,00	0,00	0,00
1,60	2,37	4,85	2,80	6,00	0,00	0,00	0,00	0,00
1,00	2,47	5,60	3,25	7,00	0,00	0,00	0,00	0,00
9,00	2,77	5,60	3,25	16,00	0,10	0,10	4,00	0,00
20,00	2,91	6,55	3,80	36,00	0,15	0,20	5,00	5,00
50,00	3,26	8,10	4,50	86,00	0,15	0,15	0,00	10,00
60,00	3,26	8,25	4,55	146,00	0,15	0,05	20,00	0,00
60,00	3,26	8,30	4,20	206,00	0,00	0,20	20,00	0,00
144,00	3,47	8,90	4,75	350,00	0,00	0,00	0,00	0,00

44.5N 12.5E (d2)

H	ρ	VP	VS	Z	ΔV_S+	ΔV_S-	$\Delta H+$	$\Delta H-$
0,40	1,02	1,45	0,00	0,40	0,00	0,00	0,00	0,00
3,60	2,29	3,45	2,00	4,00	0,00	0,00	0,00	0,00
2,00	2,54	5,70	3,30	6,00	0,00	0,00	0,00	0,00
2,00	2,58	6,05	3,50	8,00	0,00	0,00	0,00	0,00
12,00	2,63	5,70	3,30	20,00	0,10	0,05	3,00	0,00
32,00	2,68	6,85	3,95	52,00	0,20	0,20	6,00	0,00
60,00	3,27	8,00	4,65	112,00	0,15	0,00	0,00	15,00
55,00	3,27	8,10	4,20	167,00	0,00	0,20	25,00	0,00
60,00	3,27	8,60	4,65	227,00	0,00	0,20	25,00	0,00
123,00	3,47	8,90	4,75	350,00	0,00	0,00	0,00	0,00

44.5N 13.5E (d3)

H	ρ	VP	VS	Z	ΔV_S+	ΔV_S-	$\Delta H+$	$\Delta H-$
0,05	1,03	1,45	0,00	0,05	0,00	0,00	0,00	0,00
2,95	2,30	3,05	1,76	3,00	0,00	0,00	0,00	0,00
1,00	2,40	3,90	2,25	4,00	0,00	0,00	0,00	0,00
1,00	2,55	5,95	3,45	5,00	0,00	0,00	0,00	0,00
1,00	2,60	6,05	3,50	6,00	0,00	0,00	0,00	0,00
19,00	2,65	5,95	3,45	25,00	0,05	0,05	3,50	3,50
12,00	2,95	7,10	4,10	37,00	0,00	0,15	2,00	2,00
15,00	3,30	8,20	4,30	52,00	0,00	0,15	7,50	0,00
80,00	3,30	7,95	4,50	132,00	0,10	0,00	15,00	15,00
70,00	3,30	8,15	4,10	202,00	0,00	0,10	20,00	0,00
148,00	3,49	8,85	4,75	350,00	0,00	0,00	0,00	0,00

44.5N 14.5E (d4)

H	ρ	VP	VS	Z	ΔV_S+	ΔV_S-	$\Delta H+$	$\Delta H-$
0,05	1,03	1,45	0,00	0,05	0,00	0,00	0,00	0,00
2,95	2,25	3,05	1,76	3,00	0,00	0,00	0,00	0,00
1,00	2,50	3,90	2,25	4,00	0,00	0,00	0,00	0,00
2,00	2,60	5,90	3,40	6,00	0,00	0,00	0,00	0,00
7,00	2,60	6,05	3,50	13,00	0,05	0,05	1,00	1,00
13,00	2,86	6,15	3,55	26,00	0,05	0,05	1,00	1,00
36,00	3,16	8,10	4,20	62,00	0,00	0,05	1,00	1,00
60,00	3,31	8,05	4,75	122,00	0,05	0,00	5,00	5,00
80,00	3,31	8,20	4,15	202,00	0,00	0,05	7,50	7,50
148,00	3,50	8,70	4,75	350,00	0,00	0,00	0,00	0,00

44.5N 15.5E (d5)

H	ρ	VP	VS	Z	ΔV_S+	ΔV_S-	$\Delta H+$	$\Delta H-$
4,00	2,39	3,65	2,10	4,00	0,00	0,00	0,00	0,00
1,50	2,49	5,70	3,30	5,50	0,00	0,00	0,00	0,00
2,50	2,59	6,25	3,60	8,00	0,00	0,00	0,00	0,00
21,00	2,64	6,05	3,50	29,00	0,05	0,05	4,00	4,00
30,00	3,19	8,05	4,40	59,00	0,15	0,10	5,00	5,00
30,00	3,29	8,10	4,55	89,00	0,05	0,00	10,00	0,00
100,00	3,29	8,21	4,50	189,00	0,05	0,10	0,00	20,00
60,00	3,29	8,40	4,60	249,00	0,00	0,20	30,00	0,00
101,00	3,50	8,65	4,75	350,00	0,00	0,00	0,00	0,00

44.5N 16.5E (d6)

H	ρ	VP	VS	Z	ΔV_S+	ΔV_S-	$\Delta H+$	$\Delta H-$
3,00	2,43	3,80	2,20	3,00	0,00	0,00	0,00	0,00
1,00	2,68	4,00	2,30	4,00	0,00	0,00	0,00	0,00
1,50	2,68	5,70	3,30	5,50	0,00	0,00	0,00	0,00
1,50	2,68	5,95	3,45	7,00	0,00	0,00	0,00	0,00
4,00	2,78	7,20	4,15	11,00	0,10	0,10	2,00	0,00
20,00	2,93	6,05	3,50	31,00	0,10	0,10	4,00	4,00
40,00	3,08	8,20	4,50	71,00	0,00	0,10	0,00	15,00
60,00	3,18	8,25	4,40	131,00	0,00	0,10	25,00	0,00
110,00	3,29	8,40	4,60	241,00	0,05	0,15	0,00	25,00
109,00	3,49	8,75	4,75	350,00	0,00	0,00	0,00	0,00

44.5N 17.5E (d7)

H	ρ	VP	VS	Z	ΔV_S+	ΔV_S-	$\Delta H+$	$\Delta H-$
3,00	2,45	3,80	2,20	3,00	0,00	0,00	0,00	0,00
1,00	2,45	4,00	2,30	4,00	0,00	0,00	0,00	0,00
1,00	2,70	5,70	3,30	5,00	0,00	0,00	0,00	0,00
1,00	2,75	6,05	3,50	6,00	0,00	0,00	0,00	0,00
7,00	2,80	6,30	3,65	13,00	0,15	0,10	1,50	0,00
16,00	2,80	6,05	3,50	29,00	0,10	0,10	3,00	3,00
40,00	3,09	8,20	4,50	69,00	0,00	0,10	0,00	15,00
110,00	3,19	8,25	4,55	179,00	0,00	0,15	0,00	0,00
60,00	3,29	8,40	4,60	239,00	0,15	0,10	30,00	0,00
111,00	3,48	8,80	4,75	350,00	0,00	0,00	0,00	0,00

44.5N 18.5E (d8)

H	ρ	VP	VS	Z	ΔV_S+	ΔV_S-	$\Delta H+$	$\Delta H-$
4,00	2,55	4,00	2,30	4,00	0,00	0,00	0,00	0,00
1,50	2,70	5,60	3,25	5,50	0,00	0,00	0,00	0,00
1,50	2,70	5,95	3,45	7,00	0,00	0,00	0,00	0,00
22,00	2,80	6,15	3,55	29,00	0,05	0,10	5,50	5,50
30,00	3,00	8,05	4,40	59,00	0,05	0,20	7,50	0,00
40,00	3,10	8,25	4,55	99,00	0,15	0,00	17,00	0,00
50,00	3,20	8,35	4,60	149,00	0,00	0,20	0,00	20,00
50,00	3,30	8,30	4,25	199,00	0,00	0,25	0,00	25,00
151,00	3,49	8,80	4,75	350,00	0,00	0,00	0,00	0,00

44.5N 19.5E (d9)

H	ρ	VP	VS	Z	ΔV_S+	ΔV_S-	$\Delta H+$	$\Delta H-$
0,50	2,55	3,46	2,00	0,50	0,00	0,00	0,00	0,00
2,50	2,71	4,33	2,50	3,00	0,00	0,00	0,00	0,00
1,00	2,71	5,80	3,35	4,00	0,00	0,00	0,00	0,00
2,00	2,81	6,06	3,50	6,00	0,00	0,00	0,00	0,00
9,00	2,81	5,45	3,15	15,00	0,15	0,15	2,00	2,00
22,00	2,91	6,31	3,65	37,00	0,10	0,10	5,00	5,00
35,00	3,11	8,20	4,40	72,00	0,15	0,15	10,00	0,00
70,00	3,21	8,25	4,45	142,00	0,15	0,20	20,00	0,00
115,00	3,30	8,40	4,60	257,00	0,00	0,20	0,00	22,50
93,00	3,50	8,75	4,75	350,00	0,00	0,00	0,00	0,00

43.5N 8.5E (c-2)

H	ρ	VP	VS	Z	ΔV_S+	ΔV_S-	$\Delta H+$	$\Delta H-$
2,10	1,04	1,45	0,00	2,10	0,00	0,00	0,00	0,00
1,00	2,21	2,10	1,20	3,10	0,00	0,00	0,00	0,00
1,90	2,32	2,75	1,60	5,00	0,00	0,00	0,00	0,00
1,00	2,62	4,35	2,50	6,00	0,00	0,00	0,00	0,00
10,00	2,98	6,15	3,55	16,00	0,10	0,10	2,50	2,50
15,00	3,04	7,40	4,10	31,00	0,15	0,10	7,50	0,00
15,00	3,14	8,10	4,45	46,00	0,05	0,15	12,50	0,00
70,00	3,26	8,00	4,40	116,00	0,20	0,20	0,00	17,50
100,00	3,37	8,30	4,40	216,00	0,00	0,25	20,00	20,00
134,00	3,54	8,80	4,75	350,00	0,00	0,00	0,00	0,00

43.5N 9.5E (c-1)

H	ρ	VP	VS	Z	ΔV_S+	ΔV_S-	$\Delta H+$	$\Delta H-$
0,68	1,03	1,45	0,00	0,68	0,00	0,00	0,00	0,00
1,32	2,21	1,90	1,10	2,00	0,00	0,00	0,00	0,00
0,50	2,31	2,75	1,60	2,50	0,00	0,00	0,00	0,00
2,50	2,72	5,90	3,40	5,00	0,00	0,00	0,00	0,00
1,00	2,82	6,05	3,50	6,00	0,00	0,00	0,00	0,00
4,00	2,98	4,85	2,80	10,00	0,10	0,15	1,00	1,00
19,00	2,98	6,50	3,75	29,00	0,10	0,10	5,00	5,00
70,00	3,14	7,90	4,40	99,00	0,10	0,10	0,00	15,00
75,00	3,25	8,10	4,40	174,00	0,00	0,20	0,00	17,50
105,00	3,34	8,60	4,60	279,00	0,00	0,15	20,00	20,00
71,00	3,52	8,80	4,75	350,00	0,00	0,00	0,00	0,00

43.5N 10.5E (c0)

H	ρ	VP	VS	Z	ΔV_S+	ΔV_S-	$\Delta H+$	$\Delta H-$
4,00	2,41	3,80	2,20	4,00	0,00	0,00	0,00	0,00
1,00	2,51	4,60	2,65	5,00	0,00	0,00	0,00	0,00
1,00	2,67	5,20	3,00	6,00	0,00	0,00	0,00	0,00
8,00	2,82	5,55	3,20	14,00	0,10	0,10	3,50	0,00
14,00	2,97	6,55	3,80	28,00	0,15	0,15	6,50	0,00
60,00	3,32	7,85	4,35	88,00	0,05	0,00	0,00	12,50
100,00	3,32	8,20	4,50	188,00	0,05	0,10	0,00	20,00
110,00	3,32	8,75	4,65	298,00	0,00	0,20	0,00	25,00
52,00	3,50	8,90	4,75	350,00	0,00	0,00	0,00	0,00

43.5N 11.5E (c1)

H	ρ	VP	VS	Z	ΔV_S+	ΔV_S-	$\Delta H+$	$\Delta H-$
4,00	2,36	3,80	2,20	4,00	0,00	0,00	0,00	0,00
1,00	2,56	4,60	2,65	5,00	0,00	0,00	0,00	0,00
2,00	2,67	5,55	3,20	7,00	0,00	0,00	0,00	0,00
8,00	2,82	5,45	3,15	15,00	0,10	0,10	3,00	3,00
18,00	3,07	6,55	3,80	33,00	0,15	0,15	5,00	0,00
35,00	3,32	7,90	4,45	68,00	0,10	0,00	15,00	0,00
105,00	3,32	8,25	4,55	173,00	0,00	0,15	0,00	20,00
50,00	3,32	8,70	4,20	223,00	0,00	0,20	0,00	25,00
127,00	3,48	8,90	4,75	350,00	0,00	0,00	0,00	0,00

43.5N 12.5E (c2)

H	ρ	VP	VS	Z	ΔV_S+	ΔV_S-	$\Delta H+$	$\Delta H-$
0,50	2,30	2,75	1,60	0,50	0,00	0,00	0,00	0,00
1,00	2,40	4,00	2,30	1,50	0,00	0,00	0,00	0,00
1,00	2,50	5,20	3,00	2,50	0,00	0,00	0,00	0,00
1,50	2,60	6,05	3,50	4,00	0,00	0,00	0,00	0,00
6,00	2,60	4,65	2,70	10,00	0,10	0,10	1,00	1,00
24,00	2,75	6,25	3,60	34,00	0,05	0,10	2,00	2,00
35,00	3,30	7,90	4,50	69,00	0,10	0,00	15,00	0,00
100,00	3,30	8,20	4,50	169,00	0,05	0,10	0,00	20,00
110,00	3,30	8,65	4,60	279,00	0,00	0,20	0,00	25,00
71,00	3,47	8,90	4,75	350,00	0,00	0,00	0,00	0,00

43.5N 13.5E (c3)

H	ρ	VP	VS	Z	ΔV_S+	ΔV_S-	$\Delta H+$	$\Delta H-$
1,10	2,29	2,70	1,55	1,10	0,00	0,00	0,00	0,00
2,40	2,34	3,60	2,08	3,50	0,00	0,00	0,00	0,00
1,50	2,59	5,50	3,18	5,00	0,00	0,00	0,00	0,00
1,00	2,69	6,05	3,50	6,00	0,00	0,00	0,00	0,00
10,00	2,69	5,35	3,10	16,00	0,10	0,10	2,50	2,50
27,00	2,79	6,85	3,95	43,00	0,15	0,15	3,50	3,50
30,00	3,29	7,90	4,35	73,00	0,15	0,00	0,00	15,00
70,00	3,29	8,15	4,50	143,00	0,10	0,05	0,00	20,00
70,00	3,29	8,35	4,20	213,00	0,00	0,20	20,00	0,00
137,00	3,48	9,00	4,75	350,00	0,00	0,00	0,00	0,00

43.5N 14.5E (c4)

H	ρ	VP	VS	Z	ΔV_S+	ΔV_S-	$\Delta H+$	$\Delta H-$
0,15	1,04	1,45	0,00	0,15	0,00	0,00	0,00	0,00
2,85	2,36	3,05	1,76	3,00	0,00	0,00	0,00	0,00
1,00	2,51	3,90	2,25	4,00	0,00	0,00	0,00	0,00
2,00	2,61	5,95	3,45	6,00	0,00	0,00	0,00	0,00
10,00	2,66	5,80	3,35	16,00	0,05	0,05	2,50	2,50
14,00	2,76	6,05	3,50	30,00	0,20	0,20	7,00	7,00
60,00	3,31	8,00	4,40	90,00	0,20	0,20	15,00	0,00
50,00	3,31	8,05	4,45	140,00	0,15	0,00	0,00	25,00
50,00	3,31	8,20	4,20	190,00	0,00	0,20	25,00	0,00
160,00	3,49	8,90	4,75	350,00	0,00	0,00	0,00	0,00

43.5N 15.5E (c5)

H	ρ	VP	VS	Z	ΔV_S+	ΔV_S-	$\Delta H+$	$\Delta H-$
0,18	1,03	1,45	0,00	0,18	0,00	0,00	0,00	0,00
2,82	2,45	3,40	1,96	3,00	0,00	0,00	0,00	0,00
1,00	2,50	3,95	2,28	4,00	0,00	0,00	0,00	0,00
2,00	2,70	5,95	3,45	6,00	0,00	0,00	0,00	0,00
14,00	2,80	5,70	3,30	20,00	0,10	0,10	3,00	3,00
15,00	2,95	6,85	3,95	35,00	0,15	0,15	4,00	0,00
40,00	3,10	7,90	4,40	75,00	0,15	0,15	15,00	0,00
100,00	3,20	8,10	4,40	175,00	0,20	0,20	0,00	25,00
60,00	3,30	8,40	4,60	235,00	0,00	0,20	25,00	0,00
115,00	3,50	8,80	4,75	350,00	0,00	0,00	0,00	0,00

43.5N 16.5E (c6)

H	ρ	VP	VS	Z	ΔV_S+	ΔV_S-	$\Delta H+$	$\Delta H-$
4,00	2,30	3,65	2,10	4,00	0,00	0,00	0,00	0,00
1,50	2,55	5,70	3,30	5,50	0,00	0,00	0,00	0,00
2,50	2,55	6,25	3,60	8,00	0,00	0,00	0,00	0,00
18,00	2,55	5,95	3,45	26,00	0,10	0,05	3,00	3,00
10,00	2,75	7,25	4,20	36,00	0,00	0,15	5,00	0,00
30,00	3,30	8,05	4,35	66,00	0,10	0,15	15,00	0,00
100,00	3,30	8,10	4,40	166,00	0,15	0,15	0,00	25,00
60,00	3,30	8,35	4,60	226,00	0,00	0,20	25,00	0,00
124,00	3,50	8,70	4,75	350,00	0,00	0,00	0,00	0,00

43.5N 17.5E (c7)

H	ρ	VP	VS	Z	ΔV_S+	ΔV_S-	$\Delta H+$	$\Delta H-$
2,00	2,24	3,80	2,20	2,00	0,00	0,00	0,00	0,00
2,00	2,29	3,90	2,25	4,00	0,00	0,00	0,00	0,00
1,50	2,48	5,90	3,40	5,50	0,00	0,00	0,00	0,00
2,50	2,53	6,25	3,60	8,00	0,00	0,00	0,00	0,00
11,00	2,53	5,55	3,20	19,00	0,10	0,10	2,00	2,00
17,00	2,53	6,50	3,75	36,00	0,20	0,20	8,50	0,00
60,00	3,27	8,00	4,40	96,00	0,10	0,10	0,00	15,00
95,00	3,27	8,20	4,45	191,00	0,00	0,15	20,00	0,00
60,00	3,27	8,50	4,70	251,00	0,05	0,20	0,00	25,00
99,00	3,49	8,80	4,75	350,00	0,00	0,00	0,00	0,00

43.5N 18.5E (c8)

H	ρ	VP	VS	Z	ΔV_S+	ΔV_S-	$\Delta H+$	$\Delta H-$
4,00	2,43	3,80	2,20	4,00	0,00	0,00	0,00	0,00
1,00	2,67	5,60	3,25	5,00	0,00	0,00	0,00	0,00
1,00	2,67	5,95	3,45	6,00	0,00	0,00	0,00	0,00
3,00	2,72	6,85	3,95	9,00	0,10	0,05	1,00	0,00
9,00	2,77	5,20	3,00	18,00	0,10	0,10	1,50	1,50
24,00	2,87	6,65	3,85	42,00	0,10	0,10	5,50	5,50
60,00	3,17	8,00	4,40	102,00	0,10	0,10	30,00	0,00
120,00	3,28	8,25	4,55	222,00	0,05	0,15	0,00	30,00
128,00	3,49	8,70	4,75	350,00	0,00	0,00	0,00	0,00

43.5N 19.5E (c9)

H	ρ	VP	VS	Z	ΔV_S+	ΔV_S-	$\Delta H+$	$\Delta H-$
2,50	2,49	4,40	2,55	2,50	0,00	0,00	0,00	0,00
1,50	2,59	5,60	3,25	4,00	0,00	0,00	0,00	0,00
2,00	2,67	5,95	3,45	6,00	0,00	0,00	0,00	0,00
16,00	2,77	5,70	3,30	22,00	0,10	0,10	4,00	0,00
3,00	2,77	5,70	3,30	25,00	0,20	0,20	4,50	0,00
25,00	3,09	8,10	4,10	50,00	0,00	0,10	15,00	0,00
30,00	3,23	8,10	4,40	80,00	0,20	0,20	0,00	17,50
110,00	3,23	8,20	4,50	190,00	0,10	0,10	0,00	20,00
160,00	3,49	8,75	4,75	350,00	0,00	0,00	0,00	0,00

43.5N 20.5E (c10)

H	ρ	VP	VS	Z	ΔV_S+	ΔV_S-	$\Delta H+$	$\Delta H-$
2,50	2,53	4,60	2,65	2,50	0,00	0,00	0,00	0,00
1,50	2,65	5,90	3,40	4,00	0,00	0,00	0,00	0,00
2,00	2,70	6,05	3,50	6,00	0,00	0,00	0,00	0,00
12,00	2,76	5,55	3,20	18,00	0,10	0,10	3,00	0,00
20,00	2,80	6,55	3,80	38,00	0,10	0,15	5,00	5,00
45,00	3,10	8,15	4,45	83,00	0,00	0,15	15,00	0,00
100,00	3,20	8,25	4,50	183,00	0,20	0,20	0,00	20,00
65,00	3,30	8,50	4,70	248,00	0,00	0,30	22,50	0,00
102,00	3,49	8,85	4,75	350,00	0,00	0,00	0,00	0,00

43.5N 21.5E (c11)

H	ρ	VP	VS	Z	ΔV_S+	ΔV_S-	$\Delta H+$	$\Delta H-$
4,00	2,56	4,85	2,80	4,00	0,00	0,00	0,00	0,00
3,00	2,69	5,30	3,05	7,00	0,00	0,00	0,00	0,00
12,00	2,76	5,90	3,40	19,00	0,10	0,05	4,00	4,00
16,00	2,81	6,50	3,75	35,00	0,15	0,15	4,00	4,00
40,00	3,11	7,95	4,30	75,00	0,20	0,20	17,50	0,00
60,00	3,21	8,10	4,45	135,00	0,20	0,20	17,50	0,00
110,00	3,30	8,45	4,65	245,00	0,00	0,25	0,00	22,50
105,00	3,49	8,90	4,75	350,00	0,00	0,00	0,00	0,00

42.5N 8.5E (b-2)

H	ρ	VP	VS	Z	ΔV_S+	ΔV_S-	$\Delta H+$	$\Delta H-$
1,50	1,03	1,45	0,00	1,50	0,00	0,00	0,00	0,00
0,50	2,20	2,10	1,20	2,00	0,00	0,00	0,00	0,00
1,00	2,30	3,70	2,15	3,00	0,00	0,00	0,00	0,00
1,50	2,50	3,90	2,25	4,50	0,00	0,00	0,00	0,00
1,50	2,59	4,50	2,60	6,00	0,00	0,00	0,00	0,00
8,00	2,94	5,80	3,35	14,00	0,10	0,10	1,50	1,50
15,00	2,99	7,20	4,25	29,00	0,10	0,00	7,50	0,00
65,00	3,10	8,00	4,40	94,00	0,20	0,20	0,00	12,50
75,00	3,20	8,10	4,35	169,00	0,00	0,20	0,00	17,50
100,00	3,32	8,45	4,65	269,00	0,10	0,15	22,50	22,50
81,00	3,54	8,75	4,75	350,00	0,00	0,00	0,00	0,00

42.5N 9.5E (b-1)

H	ρ	VP	VS	Z	ΔV_S+	ΔV_S-	$\Delta H+$	$\Delta H-$
0,06	1,02	1,45	0,00	0,06	0,00	0,00	0,00	0,00
1,44	2,09	2,10	1,20	1,50	0,00	0,00	0,00	0,00
0,50	2,19	2,35	1,35	2,00	0,00	0,00	0,00	0,00
1,00	2,58	4,85	2,80	3,00	0,00	0,00	0,00	0,00
1,00	2,78	5,20	3,00	4,00	0,00	0,00	0,00	0,00
14,00	2,92	6,25	3,60	18,00	0,05	0,10	2,00	2,00
30,00	2,92	8,00	4,30	48,00	0,00	0,10	4,00	4,00
25,00	3,06	8,00	4,40	73,00	0,00	0,10	7,50	0,00
70,00	3,16	8,00	4,30	143,00	0,00	0,10	15,00	15,00
120,00	3,28	8,40	4,45	263,00	0,00	0,15	0,00	25,00
87,00	3,51	8,80	4,75	350,00	0,00	0,00	0,00	0,00

42.5N 10.5E (b0)

H	ρ	VP	VS	Z	ΔV_S+	ΔV_S-	$\Delta H+$	$\Delta H-$
0,50	1,03	1,45	0,00	0,50	0,00	0,00	0,00	0,00
0,50	2,60	5,20	3,00	1,00	0,00	0,00	0,00	0,00
6,00	2,60	4,60	2,65	7,00	0,00	0,00	0,00	0,00
11,00	2,75	5,70	3,30	18,00	0,10	0,05	2,50	0,00
17,00	3,05	7,40	4,10	35,00	0,10	0,05	0,00	2,50
60,00	3,30	7,95	4,30	95,00	0,05	0,05	15,00	0,00
70,00	3,30	8,10	4,35	165,00	0,00	0,05	0,00	20,00
120,00	3,30	8,65	4,60	285,00	0,00	0,20	0,00	30,00
65,00	3,51	8,85	4,75	350,00	0,00	0,00	0,00	0,00

42.5N 11.5E (b1)

H	ρ	VP	VS	Z	ΔV_S+	ΔV_S-	$\Delta H+$	$\Delta H-$
0,25	2,45	5,20	3,00	0,25	0,00	0,00	0,00	0,00
0,75	2,60	6,05	3,50	1,00	0,00	0,00	0,00	0,00
6,00	2,65	4,60	2,65	7,00	0,00	0,00	0,00	0,00
16,00	2,70	6,00	3,45	23,00	0,10	0,10	2,00	2,00
18,00	3,20	7,55	4,20	41,00	0,05	0,10	8,00	0,00
30,00	3,30	7,95	4,35	71,00	0,10	0,10	15,00	0,00
110,00	3,30	8,15	4,40	181,00	0,00	0,10	0,00	25,00
100,00	3,30	8,80	4,65	281,00	0,00	0,20	0,00	25,00
69,00	3,50	8,95	4,75	350,00	0,00	0,00	0,00	0,00

42.5N 12.5E (b2)

H	ρ	VP	VS	Z	ΔV_S+	ΔV_S-	$\Delta H+$	$\Delta H-$
1,20	2,30	2,80	1,60	1,20	0,00	0,00	0,00	0,00
0,80	2,50	4,00	2,30	2,00	0,00	0,00	0,00	0,00
1,50	2,60	5,20	3,00	3,50	0,00	0,00	0,00	0,00
0,50	2,80	5,70	3,30	4,00	0,00	0,00	0,00	0,00
10,00	2,80	5,80	3,35	14,00	0,05	0,10	2,50	2,50
19,00	2,80	6,50	3,75	33,00	0,15	0,15	2,50	2,50
55,00	3,30	7,80	4,35	88,00	0,05	0,05	0,00	12,50
70,00	3,30	8,00	4,40	158,00	0,00	0,10	20,00	0,00
120,00	3,30	8,80	4,60	278,00	0,00	0,20	0,00	25,00
72,00	3,49	8,90	4,75	350,00	0,00	0,00	0,00	0,00

42.5N 13.5E (b3)

H	ρ	VP	VS	Z	ΔV_S+	ΔV_S-	$\Delta H+$	$\Delta H-$
1,20	2,29	2,70	1,55	1,20	0,00	0,00	0,00	0,00
0,80	2,49	3,70	2,13	2,00	0,00	0,00	0,00	0,00
1,50	2,58	5,35	3,10	3,50	0,00	0,00	0,00	0,00
12,00	2,73	5,70	3,30	15,50	0,05	0,05	3,00	3,00
20,00	2,78	6,40	3,70	35,50	0,15	0,10	10,00	10,00
60,00	3,27	7,90	4,40	95,50	0,15	0,00	0,00	30,00
60,00	3,27	8,00	4,35	155,50	0,00	0,15	50,00	0,00
110,00	3,27	8,70	4,60	265,50	0,00	0,20	0,00	50,00
84,50	3,48	8,95	4,75	350,00	0,00	0,00	0,00	0,00

42.5N 14.5E (b4)

H	ρ	VP	VS	Z	ΔV_S+	ΔV_S-	$\Delta H+$	$\Delta H-$
0,20	1,03	1,45	0,00	0,20	0,00	0,00	0,00	0,00
3,80	2,49	3,60	2,08	4,00	0,00	0,00	0,00	0,00
3,00	2,49	5,55	3,20	7,00	0,00	0,00	0,00	0,00
10,00	2,69	5,45	3,15	17,00	0,10	0,10	1,50	1,50
24,00	2,94	6,75	3,90	41,00	0,15	0,15	5,00	5,00
60,00	3,28	7,95	4,40	101,00	0,20	0,00	0,00	15,00
110,00	3,28	8,25	4,45	211,00	0,00	0,15	0,00	20,00
70,00	3,28	8,70	4,75	281,00	0,00	0,25	25,00	0,00
69,00	3,49	8,90	4,75	350,00	0,00	0,00	0,00	0,00

42.5N 15.5E (b5)

H	ρ	VP	VS	Z	ΔV_S+	ΔV_S-	$\Delta H+$	$\Delta H-$
0,15	1,03	1,45	0,00	0,15	0,00	0,00	0,00	0,00
3,90	2,25	3,30	1,91	4,05	0,00	0,00	0,00	0,00
1,95	2,55	6,15	3,55	6,00	0,00	0,00	0,00	0,00
3,00	2,60	6,65	3,85	9,00	0,20	0,20	0,50	0,00
7,00	2,66	5,10	2,95	16,00	0,15	0,15	1,50	0,00
21,00	2,71	6,75	3,90	37,00	0,10	0,10	4,00	4,00
130,00	3,31	8,10	4,45	167,00	0,05	0,05	0,00	25,00
70,00	3,31	8,45	4,60	237,00	0,00	0,20	30,00	0,00
113,00	3,51	8,80	4,75	350,00	0,00	0,00	0,00	0,00

42.5N 16.5E (b6)

H	ρ	VP	VS	Z	ΔV_S+	ΔV_S-	$\Delta H+$	$\Delta H-$
0,19	1,03	1,45	0,00	0,19	0,00	0,00	0,00	0,00
3,70	2,20	3,30	1,92	3,89	0,00	0,00	0,00	0,00
1,61	2,55	6,15	3,55	5,50	0,00	0,00	0,00	0,00
2,50	2,60	6,05	3,50	8,00	0,00	0,00	0,00	0,00
8,00	2,60	5,55	3,20	16,00	0,05	0,05	2,00	0,00
9,00	2,70	6,25	3,60	25,00	0,15	0,20	4,00	0,00
14,00	3,29	7,50	4,20	39,00	0,20	0,20	5,00	0,00
70,00	3,29	7,85	4,35	109,00	0,05	0,00	20,00	0,00
120,00	3,31	8,30	4,55	229,00	0,00	0,15	0,00	25,00
121,00	3,52	8,48	4,75	350,00	0,00	0,00	0,00	0,00

42.5N 17.5E (b7)

H	ρ	VP	VS	Z	ΔV_S+	ΔV_S-	$\Delta H+$	$\Delta H-$
0,50	1,03	1,45	0,00	0,50	0,00	0,00	0,00	0,00
3,30	2,30	3,30	1,91	3,80	0,00	0,00	0,00	0,00
4,20	2,65	6,15	3,55	8,00	0,00	0,00	0,00	0,00
11,00	2,70	5,55	3,20	19,00	0,05	0,05	1,50	1,50
19,00	2,85	6,85	3,95	38,00	0,15	0,20	4,00	0,00
30,00	3,20	8,05	4,40	68,00	0,15	0,10	15,00	0,00
50,00	3,25	7,90	4,35	118,00	0,20	0,20	20,00	0,00
120,00	3,31	8,30	4,50	238,00	0,25	0,25	0,00	30,00
112,00	3,52	8,70	4,75	350,00	0,00	0,00	0,00	0,00

42.5N 18.5E (b8)

H	ρ	VP	VS	Z	ΔV_S+	ΔV_S-	$\Delta H+$	$\Delta H-$
0,20	1,03	1,45	0,00	0,20	0,00	0,00	0,00	0,00
3,30	2,35	3,30	1,91	3,50	0,00	0,00	0,00	0,00
3,50	2,76	6,15	3,55	7,00	0,00	0,00	0,00	0,00
20,00	2,81	5,80	3,35	27,00	0,05	0,05	2,50	2,50
20,00	3,02	8,25	4,20	47,00	0,00	0,10	5,00	5,00
30,00	3,12	8,10	4,50	77,00	0,15	0,15	0,00	15,00
60,00	3,21	7,90	4,35	137,00	0,15	0,15	20,00	0,00
110,00	3,31	8,35	4,60	247,00	0,15	0,10	22,50	0,00
103,00	3,50	8,80	4,75	350,00	0,00	0,00	0,00	0,00

42.5N 19.5E (b9)

H	ρ	VP	VS	Z	ΔV_S+	ΔV_S-	$\Delta H+$	$\Delta H-$
3,00	2,51	4,35	2,50	3,00	0,00	0,00	0,00	0,00
1,00	2,58	5,80	3,35	4,00	0,00	0,00	0,00	0,00
2,00	2,71	6,05	3,50	6,00	0,00	0,00	0,00	0,00
15,00	2,77	5,45	3,15	21,00	0,10	0,05	3,50	3,50
12,00	2,87	6,25	3,60	33,00	0,10	0,15	5,00	0,00
35,00	3,07	8,20	4,50	68,00	0,00	0,10	10,00	0,00
70,00	3,16	8,10	4,50	138,00	0,15	0,15	20,00	0,00
115,00	3,27	8,40	4,55	253,00	0,00	0,20	0,00	22,50
97,00	3,48	8,75	4,75	350,00	0,00	0,00	0,00	0,00

42.5N 20.5E (b10)

H	ρ	VP	VS	Z	ΔV_S+	ΔV_S-	$\Delta H+$	$\Delta H-$
2,50	2,57	4,75	2,75	2,50	0,00	0,00	0,00	0,00
0,50	2,69	5,80	3,35	3,00	0,00	0,00	0,00	0,00
2,00	2,74	6,05	3,50	5,00	0,00	0,00	0,00	0,00
12,00	2,74	5,55	3,20	17,00	0,05	0,05	5,50	0,00
25,00	2,94	6,40	3,70	42,00	0,20	0,20	0,00	5,50
80,00	3,19	8,30	4,60	122,00	0,10	0,15	15,00	0,00
55,00	3,19	8,30	4,55	177,00	0,05	0,15	17,50	0,00
70,00	3,19	8,45	4,60	247,00	0,00	0,20	20,00	0,00
103,00	3,47	8,90	4,75	350,00	0,00	0,00	0,00	0,00

42.5N 21.5E (b11)

H	ρ	VP	VS	Z	ΔV_S+	ΔV_S-	$\Delta H+$	$\Delta H-$
2,00	2,53	5,20	3,00	2,00	0,00	0,00	0,00	0,00
3,00	2,68	5,55	3,20	5,00	0,00	0,00	0,00	0,00
14,00	2,75	5,80	3,35	19,00	0,05	0,10	4,00	4,00
16,00	2,95	6,40	3,70	35,00	0,20	0,20	5,00	5,00
50,00	3,10	8,20	4,45	85,00	0,00	0,10	17,50	0,00
100,00	3,20	8,30	4,55	185,00	0,05	0,10	0,00	20,00
70,00	3,29	8,55	4,65	255,00	0,00	0,25	20,00	0,00
95,00	3,38	8,90	4,75	350,00	0,00	0,00	0,00	0,00

41.5N 8.5E (a-2)

H	ρ	VP	VS	Z	ΔV_S+	ΔV_S-	$\Delta H+$	$\Delta H-$
1,00	1,04	1,45	0,00	1,00	0,00	0,00	0,00	0,00
1,50	2,21	2,10	1,20	2,50	0,00	0,00	0,00	0,00
1,50	2,31	3,65	2,10	4,00	0,00	0,00	0,00	0,00
1,00	2,51	3,80	2,20	5,00	0,00	0,00	0,00	0,00
1,00	2,62	4,35	2,50	6,00	0,00	0,00	0,00	0,00
12,00	2,97	6,75	3,90	18,00	0,05	0,05	2,00	2,00
45,00	3,02	8,10	4,40	63,00	0,00	0,05	0,00	7,50
50,00	3,11	8,05	4,20	113,00	0,00	0,05	10,00	10,00
45,00	3,20	8,10	4,40	158,00	0,15	1,00	17,50	0,00
105,00	3,29	8,40	4,45	263,00	0,00	0,15	0,00	20,00
87,00	3,52	8,70	4,75	350,00	0,00	0,00	0,00	0,00

41.5N 9.5E (a-1)

H	ρ	VP	VS	Z	ΔV_S+	ΔV_S-	$\Delta H+$	$\Delta H-$
0,15	1,03	1,45	0,00	0,15	0,00	0,00	0,00	0,00
0,85	2,10	1,90	1,10	1,00	0,00	0,00	0,00	0,00
0,50	2,20	2,10	1,20	1,50	0,00	0,00	0,00	0,00
1,50	2,79	4,85	2,80	3,00	0,00	0,00	0,00	0,00
2,00	2,89	5,20	3,00	5,00	0,00	0,00	0,00	0,00
11,00	2,94	6,15	3,55	16,00	0,05	0,05	1,50	1,50
12,00	2,98	7,10	4,15	28,00	0,05	0,00	6,00	0,00
70,00	3,07	8,00	4,30	98,00	0,00	0,05	12,50	12,50
70,00	3,16	8,15	4,35	168,00	0,00	0,15	0,00	17,50
105,00	3,26	8,50	4,55	273,00	0,00	0,15	0,00	20,00
77,00	3,49	8,75	4,75	350,00	0,00	0,00	0,00	0,00

41.5N 10.5E (a0)

H	ρ	VP	VS	Z	ΔV_S+	ΔV_S-	$\Delta H+$	$\Delta H-$
1,25	1,01	1,45	0,00	1,25	0,00	0,00	0,00	0,00
1,75	2,10	2,10	1,20	3,00	0,00	0,00	0,00	0,00
0,70	2,20	2,35	1,35	3,70	0,00	0,00	0,00	0,00
1,20	2,61	6,50	3,75	4,90	0,00	0,00	0,00	0,00
1,10	2,81	6,75	3,90	6,00	0,00	0,00	0,00	0,00
25,00	2,96	6,75	3,90	31,00	0,05	0,00	2,50	2,50
10,00	3,01	7,70	4,55	41,00	0,10	0,00	2,50	2,50
25,00	3,11	8,10	4,20	66,00	0,00	0,10	5,00	5,00
80,00	3,21	8,10	4,25	146,00	0,00	0,50	0,00	10,00
130,00	3,31	8,55	4,35	276,00	0,00	0,50	10,00	10,00
74,00	3,52	8,80	4,75	350,00	0,00	0,00	0,00	0,00

41.5N 11.5E (a1)

H	ρ	VP	VS	Z	ΔV_S+	ΔV_S-	$\Delta H+$	$\Delta H-$
1,00	1,03	1,45	0,00	1,00	0,00	0,00	0,00	0,00
2,50	2,10	2,30	1,33	3,50	0,00	0,00	0,00	0,00
1,10	2,40	5,00	2,90	4,60	0,00	0,00	0,00	0,00
1,40	2,60	5,70	3,30	6,00	0,00	0,00	0,00	0,00
4,00	2,80	8,20	4,75	10,00	0,05	0,05	0,50	0,50
13,00	2,90	6,50	3,75	23,00	0,10	0,10	1,50	1,50
60,00	3,31	8,05	4,25	83,00	0,00	0,05	0,00	7,50
50,00	3,31	8,05	4,20	133,00	0,00	0,05	10,00	10,00
140,00	3,32	8,50	4,35	273,00	0,00	0,05	15,00	15,00
77,00	3,53	8,80	4,75	350,00	0,00	0,00	0,00	0,00

41.5N 12.5E (a2)

H	ρ	VP	VS	Z	ΔV_S+	ΔV_S-	$\Delta H+$	$\Delta H-$
0,40	1,03	1,45	0,00	0,40	0,00	0,00	0,00	0,00
2,10	2,15	2,30	1,32	2,50	0,00	0,00	0,00	0,00
1,00	2,49	5,30	3,06	3,50	0,00	0,00	0,00	0,00
2,50	2,64	5,70	3,30	6,00	0,00	0,00	0,00	0,00
19,00	2,89	6,75	3,90	25,00	0,05	0,00	0,50	0,50
10,00	3,03	7,25	3,95	35,00	0,00	0,05	0,50	0,50
12,00	3,28	7,75	4,60	47,00	0,10	0,00	3,00	0,00
40,00	3,28	7,90	4,15	87,00	0,00	0,05	10,00	10,00
70,00	3,28	8,05	4,30	157,00	0,00	0,05	20,00	0,00
110,00	3,30	8,55	4,45	267,00	0,00	0,15	0,00	20,00
83,00	3,52	8,75	4,75	350,00	0,00	0,00	0,00	0,00

41.5N 13.5E (a3)

H	ρ	VP	VS	Z	ΔV_S+	ΔV_S-	$\Delta H+$	$\Delta H-$
2,50	2,19	3,25	1,87	2,50	0,00	0,00	0,00	0,00
1,50	2,29	3,80	2,19	4,00	0,00	0,00	0,00	0,00
1,00	2,54	5,65	3,26	5,00	0,00	0,00	0,00	0,00
6,00	2,79	6,75	3,90	11,00	0,15	0,10	3,00	0,00
10,00	2,83	6,00	3,45	21,00	0,15	0,10	3,00	0,00
30,00	3,07	7,85	4,30	51,00	0,00	0,10	15,00	0,00
110,00	3,27	8,05	4,35	161,00	0,15	0,15	0,00	25,00
120,00	3,27	8,65	4,60	281,00	0,00	0,20	0,00	25,00
69,00	3,49	8,85	4,75	350,00	0,00	0,00	0,00	0,00

41.5N 14.5E (a4)

H	ρ	VP	VS	Z	ΔV_S+	ΔV_S-	$\Delta H+$	$\Delta H-$
2,45	2,28	3,90	2,25	2,45	0,00	0,00	0,00	0,00
2,05	2,43	4,25	2,45	4,50	0,00	0,00	0,00	0,00
0,50	2,48	4,40	2,55	5,00	0,00	0,00	0,00	0,00
1,00	2,58	5,30	3,06	6,00	0,00	0,00	0,00	0,00
6,00	2,63	6,00	3,45	12,00	0,20	0,20	1,00	1,00
5,00	2,68	5,60	3,25	17,00	0,20	0,20	2,50	0,00
24,00	2,77	6,75	3,90	41,00	0,10	0,10	5,50	5,50
110,00	3,27	8,00	4,45	151,00	0,05	0,05	0,00	20,00
120,00	3,27	8,65	4,60	271,00	0,00	0,20	0,00	20,00
79,00	3,50	8,95	4,75	350,00	0,00	0,00	0,00	0,00

41.5N 15.5E (a5)

H	ρ	VP	VS	Z	ΔV_S+	ΔV_S-	$\Delta H+$	$\Delta H-$
3,00	2,29	3,45	2,00	3,00	0,00	0,00	0,00	0,00
2,00	2,34	3,95	2,28	5,00	0,00	0,00	0,00	0,00
3,00	2,64	5,20	3,00	8,00	0,00	0,00	0,00	0,00
2,00	2,79	5,60	3,25	10,00	0,00	0,00	0,00	0,00
8,00	2,84	6,05	3,50	18,00	0,10	0,10	4,00	0,00
25,00	3,19	7,70	4,10	43,00	0,00	0,10	10,00	0,00
30,00	3,19	8,00	4,55	73,00	0,15	0,00	15,00	0,00
100,00	3,29	8,15	4,40	173,00	0,20	0,20	0,00	20,00
100,00	3,30	8,70	4,75	273,00	0,00	0,25	0,00	25,00
77,00	3,51	9,00	4,75	350,00	0,00	0,00	0,00	0,00

41.5N 16.5E (a6)

H	ρ	VP	VS	Z	ΔV_S+	ΔV_S-	$\Delta H+$	$\Delta H-$
0,10	1,03	1,45	0,00	0,10	0,00	0,00	0,00	0,00
4,45	2,41	3,85	2,22	4,55	0,00	0,00	0,00	0,00
1,45	2,61	5,55	3,20	6,00	0,00	0,00	0,00	0,00
4,00	2,76	5,60	3,25	10,00	0,05	0,05	1,00	0,00
10,00	2,92	5,45	3,15	20,00	0,10	0,10	1,50	1,50
26,00	3,32	7,70	4,20	46,00	0,15	0,15	6,00	6,00
70,00	3,32	8,00	4,45	116,00	0,05	0,05	20,00	0,00
120,00	3,32	8,45	4,50	236,00	0,00	0,10	0,00	25,00
114,00	3,52	8,85	4,75	350,00	0,00	0,00	0,00	0,00

41.5N 17.5E (a7)

H	ρ	VP	VS	Z	ΔV_S+	ΔV_S-	$\Delta H+$	$\Delta H-$
1,30	1,03	1,45	0,00	1,30	0,00	0,00	0,00	0,00
3,70	2,45	3,60	2,08	5,00	0,00	0,00	0,00	0,00
4,00	2,60	5,30	3,06	9,00	0,00	0,00	0,00	0,00
15,00	2,80	5,70	3,30	24,00	0,10	0,10	2,50	2,50
15,00	2,96	7,10	4,05	39,00	0,10	0,00	7,50	0,00
30,00	3,31	8,00	4,40	69,00	0,10	0,00	0,00	15,00
100,00	3,31	8,00	4,40	169,00	0,15	0,10	20,00	0,00
70,00	3,32	8,40	4,55	239,00	0,00	0,20	20,00	0,00
111,00	3,53	8,80	4,75	350,00	0,00	0,00	0,00	0,00

41.5N 18.5E (a8)

H	ρ	VP	VS	Z	ΔV_S+	ΔV_S-	$\Delta H+$	$\Delta H-$
1,10	1,03	1,45	0,00	1,10	0,00	0,00	0,00	0,00
3,90	2,45	3,60	2,08	5,00	0,00	0,00	0,00	0,00
2,00	2,70	5,25	3,03	7,00	0,00	0,00	0,00	0,00
19,00	2,80	5,70	3,30	26,00	0,10	0,10	3,00	3,00
30,00	3,00	8,05	4,40	56,00	0,20	0,20	10,00	0,00
30,00	3,10	7,95	4,40	86,00	0,10	0,05	0,00	15,00
60,00	3,20	7,90	4,40	146,00	0,15	0,15	20,00	0,00
100,00	3,31	8,35	4,60	246,00	0,15	0,10	20,00	0,00
104,00	3,51	8,70	4,75	350,00	0,00	0,00	0,00	0,00

41.5N 19.5E (a9)

H	ρ	VP	VS	Z	ΔV_S+	ΔV_S-	$\Delta H+$	$\Delta H-$
4,00	2,35	3,20	1,85	4,00	0,00	0,00	0,00	0,00
1,00	2,74	6,05	3,50	5,00	0,00	0,00	0,00	0,00
2,00	2,74	6,15	3,56	7,00	0,00	0,00	0,00	0,00
22,00	2,79	6,00	3,45	29,00	0,05	0,05	4,00	0,00
30,00	2,98	8,30	4,55	59,00	0,05	0,10	10,00	0,00
30,00	3,08	8,10	4,40	89,00	0,20	0,20	10,00	0,00
60,00	3,18	8,05	4,50	149,00	0,25	0,25	20,00	0,00
105,00	3,27	8,40	4,60	254,00	0,20	0,10	0,00	22,50
96,00	3,48	8,70	4,75	350,00	0,00	0,00	0,00	0,00

41.5N 20.5E (a10)

H	ρ	VP	VS	Z	ΔV_S+	ΔV_S-	$\Delta H+$	$\Delta H-$
1,20	2,54	3,40	1,97	1,20	0,00	0,00	0,00	0,00
1,80	2,59	4,40	2,54	3,00	0,00	0,00	0,00	0,00
2,00	2,72	6,05	3,49	5,00	0,00	0,00	0,00	0,00
19,00	2,74	6,00	3,45	24,00	0,10	0,10	0,00	3,50
18,00	2,94	6,30	3,65	42,00	0,15	0,15	0,00	3,00
80,00	3,09	8,20	4,55	122,00	0,15	0,10	0,00	15,00
95,00	3,18	8,40	4,60	217,00	0,05	0,10	0,00	20,00
75,00	3,32	8,65	4,75	292,00	0,05	0,20	22,50	0,00
58,00	3,32	8,75	4,75	350,00	0,00	0,00	0,00	0,00

41.5N 21.5E (a11)

H	ρ	VP	VS	Z	ΔV_S+	ΔV_S-	$\Delta H+$	$\Delta H-$
1,20	2,55	3,80	2,19	1,20	0,00	0,00	0,00	0,00
2,00	2,65	4,60	2,66	3,20	0,00	0,00	0,00	0,00
2,80	2,75	6,20	3,58	6,00	0,00	0,00	0,00	0,00
12,00	2,75	6,00	3,45	18,00	0,10	0,05	2,00	0,00
20,00	2,95	6,25	3,60	38,00	0,10	0,10	0,00	2,00
50,00	3,10	8,15	4,40	88,00	0,05	0,05	20,00	0,00
95,00	3,20	8,30	4,50	183,00	0,15	0,15	0,00	20,00
65,00	3,28	8,60	4,55	248,00	0,00	0,20	22,50	0,00
102,00	3,38	8,85	4,75	350,00	0,00	0,00	0,00	0,00

40.5N 8.5E (A-2)

H	ρ	VP	VS	Z	ΔV_S+	ΔV_S-	$\Delta H+$	$\Delta H-$
2,00	2,42	3,20	1,85	2,00	0,00	0,00	0,00	0,00
1,00	2,57	4,60	2,66	3,00	0,00	0,00	0,00	0,00
0,80	2,62	5,00	2,89	3,80	0,00	0,00	0,00	0,00
1,20	2,72	5,80	3,35	5,00	0,00	0,00	0,00	0,00
11,00	2,77	5,80	3,35	16,00	0,05	0,10	1,00	0,00
8,00	2,97	7,00	4,75	24,00	0,05	0,00	3,50	0,00
45,00	3,07	8,20	4,35	69,00	0,00	0,05	17,50	17,50
90,00	3,17	8,15	4,25	159,00	0,00	0,05	0,00	17,50
110,00	3,28	8,50	4,50	269,00	0,00	0,10	0,00	20,00
81,00	3,50	8,75	4,75	350,00	0,00	0,00	0,00	0,00

40.5N 9.5E (A-1)

H	ρ	VP	VS	Z	ΔV_S+	ΔV_S-	$\Delta H+$	$\Delta H-$
1,50	2,42	3,20	1,85	1,50	0,00	0,00	0,00	0,00
1,50	2,57	4,80	2,78	3,00	0,00	0,00	0,00	0,00
0,50	2,62	5,00	2,89	3,50	0,00	0,00	0,00	0,00
1,50	2,72	5,80	3,35	5,00	0,00	0,00	0,00	0,00
4,00	2,72	5,35	3,10	9,00	0,15	0,20	1,50	0,00
10,00	2,91	6,65	3,85	19,00	0,10	0,15	2,50	0,00
40,00	3,06	8,05	4,45	59,00	0,05	0,05	15,00	0,00
80,00	3,16	8,10	4,30	139,00	0,00	0,10	0,00	17,50
160,00	3,27	8,70	4,55	299,00	0,00	0,20	0,00	35,00
51,00	3,50	8,80	4,75	350,00	0,00	0,00	0,00	0,00

40.5N 10.5E (A0)

H	ρ	VP	VS	Z	ΔV_S+	ΔV_S-	$\Delta H+$	$\Delta H-$
1,80	1,03	1,45	0,00	1,80	0,00	0,00	0,00	0,00
1,20	2,20	2,00	1,16	3,00	0,00	0,00	0,00	0,00
2,00	2,56	5,20	3,01	5,00	0,00	0,00	0,00	0,00
2,00	2,61	5,40	3,12	7,00	0,00	0,00	0,00	0,00
1,00	2,66	5,60	3,24	8,00	0,00	0,00	0,00	0,00
12,00	2,91	6,65	3,85	20,00	0,10	0,10	4,00	4,00
50,00	3,32	8,05	4,40	70,00	0,05	0,10	0,00	10,00
80,00	3,32	8,15	4,30	150,00	0,00	0,10	0,00	15,00
85,00	3,32	8,45	4,65	235,00	0,05	0,25	0,00	12,50
65,00	3,43	8,70	4,70	300,00	0,00	0,30	20,00	0,00
50,00	3,54	8,80	4,75	350,00	0,00	0,00	0,00	0,00

40.5N 11.5E (A1)

H	ρ	VP	VS	Z	ΔV_S+	ΔV_S-	$\Delta H+$	$\Delta H-$
2,50	1,04	1,45	0,00	2,50	0,00	0,00	0,00	0,00
0,70	2,21	2,40	1,38	3,20	0,00	0,00	0,00	0,00
1,00	2,61	6,00	3,45	4,20	0,00	0,00	0,00	0,00
1,80	2,71	6,10	3,52	6,00	0,00	0,00	0,00	0,00
16,00	2,96	6,25	3,60	22,00	0,05	0,05	2,00	2,00
49,00	3,31	8,05	4,40	71,00	0,00	0,10	0,00	12,00
30,00	3,32	8,00	4,10	101,00	0,00	0,10	15,00	0,00
100,00	3,33	8,30	4,55	201,00	0,05	0,15	0,00	20,00
110,00	3,50	8,70	4,75	311,00	0,00	0,20	0,00	20,00
39,00	3,56	8,80	4,75	350,00	0,00	0,00	0,00	0,00

40.5N 12.5E (A2)

H	ρ	VP	VS	Z	ΔV_S+	ΔV_S-	$\Delta H+$	$\Delta H-$
2,50	1,04	1,45	0,00	2,50	0,00	0,00	0,00	0,00
0,70	2,16	2,10	1,20	3,20	0,00	0,00	0,00	0,00
1,00	2,67	6,00	3,45	4,20	0,00	0,00	0,00	0,00
1,80	2,82	6,85	3,95	6,00	0,00	0,00	0,00	0,00
20,00	3,03	6,30	3,65	26,00	0,05	0,05	5,00	5,00
12,00	3,14	7,50	4,20	38,00	0,20	0,00	5,00	0,00
60,00	3,29	7,95	4,20	98,00	0,00	0,05	0,00	15,00
100,00	3,35	8,25	4,50	198,00	0,00	0,15	0,00	20,00
100,00	3,36	8,65	4,60	298,00	0,00	0,20	0,00	20,00
52,00	3,57	8,80	4,75	350,00	0,00	0,00	0,00	0,00

40.5N 13.5E (A3)

H	ρ	VP	VS	Z	ΔV_S+	ΔV_S-	$\Delta H+$	$\Delta H-$
1,50	1,03	1,45	0,00	1,50	0,00	0,00	0,00	0,00
2,20	2,20	2,10	1,20	3,70	0,00	0,00	0,00	0,00
1,00	2,65	6,00	3,45	4,70	0,00	0,00	0,00	0,00
1,30	2,95	6,85	3,95	6,00	0,00	0,00	0,00	0,00
5,00	2,95	7,60	4,20	11,00	0,20	0,00	1,00	0,00
10,00	2,95	6,05	3,40	21,00	0,10	0,00	5,00	0,00
40,00	3,15	7,90	4,15	61,00	0,00	0,15	15,00	0,00
110,00	3,31	8,10	4,40	171,00	0,00	0,05	0,00	15,00
110,00	3,32	8,60	4,60	281,00	0,00	0,20	0,00	20,00
69,00	3,55	8,80	4,75	350,00	0,00	0,00	0,00	0,00

40.5N 14.5E (A4)

H	ρ	VP	VS	Z	ΔV_S+	ΔV_S-	$\Delta H+$	$\Delta H-$
0,50	1,03	1,45	0,00	0,50	0,00	0,00	0,00	0,00
1,00	2,34	4,50	2,60	1,50	0,00	0,00	0,00	0,00
1,50	2,44	5,20	3,00	3,00	0,00	0,00	0,00	0,00
3,00	2,59	5,80	3,35	6,00	0,00	0,00	0,00	0,00
4,00	2,69	4,40	2,55	10,00	0,15	0,15	1,50	0,00
13,00	2,89	6,05	3,50	23,00	0,20	0,20	5,00	0,00
50,00	3,19	7,90	4,25	73,00	0,00	0,05	0,00	10,00
110,00	3,29	8,20	4,50	183,00	0,05	0,10	0,00	20,00
120,00	3,30	8,80	4,60	303,00	0,00	0,20	0,00	25,00
47,00	3,53	8,90	4,75	350,00	0,00	0,00	0,00	0,00

40.5N 15.5E (A5)

H	ρ	VP	VS	Z	ΔV_S+	ΔV_S-	$\Delta H+$	$\Delta H-$
1,10	2,28	2,60	1,50	1,10	0,00	0,00	0,00	0,00
2,40	2,43	3,65	2,10	3,50	0,00	0,00	0,00	0,00
1,50	2,53	5,00	2,90	5,00	0,00	0,00	0,00	0,00
4,00	2,72	6,05	3,49	9,00	0,00	0,00	0,00	0,00
12,00	2,77	5,60	3,25	21,00	0,10	0,10	2,00	2,00
50,00	2,97	8,10	4,35	71,00	0,00	0,10	0,00	10,00
30,00	3,07	8,05	4,60	101,00	0,20	0,00	10,00	0,00
60,00	3,16	8,20	4,45	161,00	0,00	0,15	25,00	0,00
110,00	3,27	8,75	4,65	271,00	0,00	0,20	0,00	25,00
79,00	3,52	9,00	4,75	350,00	0,00	0,00	0,00	0,00

40.5N 16.5E (A6)

H	ρ	VP	VS	Z	ΔV_S+	ΔV_S-	$\Delta H+$	$\Delta H-$
1,10	2,18	2,60	1,50	1,10	0,00	0,00	0,00	0,00
2,40	2,23	3,65	2,10	3,50	0,00	0,00	0,00	0,00
1,50	2,43	5,00	2,90	5,00	0,00	0,00	0,00	0,00
4,00	2,52	6,05	3,49	9,00	0,00	0,00	0,00	0,00
10,00	2,72	5,35	3,10	19,00	0,20	0,20	2,50	2,50
17,00	2,72	7,20	4,15	36,00	0,00	0,10	2,50	2,50
13,00	3,07	8,00	4,25	49,00	0,00	0,10	5,00	5,00
30,00	3,26	8,00	4,65	79,00	0,15	0,00	15,00	0,00
60,00	3,26	8,10	4,45	139,00	0,10	0,10	25,00	0,00
110,00	3,27	8,60	4,70	249,00	0,00	0,20	0,00	20,00
101,00	3,51	8,90	4,75	350,00	0,00	0,00	0,00	0,00

40.5N 17.5E (A7)

H	ρ	VP	VS	Z	ΔV_S+	ΔV_S-	$\Delta H+$	$\Delta H-$
4,60	2,41	3,90	2,25	4,60	0,00	0,00	0,00	0,00
3,40	2,57	5,30	3,06	8,00	0,00	0,00	0,00	0,00
12,00	2,72	5,30	3,05	20,00	0,05	0,05	1,00	1,00
20,00	2,82	7,10	4,10	40,00	0,00	0,10	5,00	5,00
50,00	3,22	8,00	4,55	90,00	0,05	0,00	15,00	0,00
100,00	3,32	8,20	4,45	190,00	0,05	0,05	0,00	20,00
60,00	3,32	8,40	4,60	250,00	0,00	0,20	20,00	0,00
100,00	3,51	8,70	4,75	350,00	0,00	0,00	0,00	0,00

40.5N 18.5E (A8)

H	ρ	VP	VS	Z	ΔV_S+	ΔV_S-	$\Delta H+$	$\Delta H-$
0,35	1,03	1,45	0,00	0,35	0,00	0,00	0,00	0,00
2,45	2,45	3,90	2,25	2,80	0,00	0,00	0,00	0,00
1,90	2,50	4,50	2,60	4,70	0,00	0,00	0,00	0,00
2,30	2,70	5,25	3,03	7,00	0,00	0,00	0,00	0,00
20,00	2,81	5,70	3,30	27,00	0,05	0,05	1,00	1,00
60,00	3,21	7,95	4,55	87,00	0,05	0,00	10,00	10,00
30,00	3,31	7,90	4,30	117,00	0,15	0,15	10,00	0,00
105,00	3,31	8,20	4,50	222,00	0,15	0,15	0,00	15,00
65,00	3,31	8,45	4,60	287,00	0,00	0,20	20,00	0,00
63,00	3,51	8,65	4,75	350,00	0,00	0,00	0,00	0,00

40.5N 19.5E (A9)

H	ρ	VP	VS	Z	ΔV_S+	ΔV_S-	$\Delta H+$	$\Delta H-$
0,80	2,33	3,20	1,85	0,80	0,00	0,00	0,00	0,00
4,20	2,43	3,40	1,95	5,00	0,00	0,00	0,00	0,00
3,00	2,73	6,05	3,50	8,00	0,00	0,00	0,00	0,00
5,00	2,78	6,75	3,90	13,00	0,20	0,20	2,00	0,00
19,00	2,93	6,05	3,50	32,00	0,15	0,15	3,50	3,50
60,00	3,07	8,00	4,45	92,00	0,10	0,00	0,00	10,00
120,00	3,17	8,20	4,45	212,00	0,05	0,05	0,00	20,00
70,00	3,27	8,45	4,55	282,00	0,00	0,15	20,00	0,00
68,00	3,48	8,70	4,75	350,00	0,00	0,00	0,00	0,00

40.5N 20.5E (A10)

H	ρ	VP	VS	Z	ΔV_S+	ΔV_S-	$\Delta H+$	$\Delta H-$
3,00	2,52	4,35	2,50	3,00	0,00	0,00	0,00	0,00
3,00	2,66	5,70	3,30	6,00	0,00	0,00	0,00	0,00
18,00	2,74	5,90	3,40	24,00	0,10	0,05	0,00	3,00
14,00	2,89	6,05	3,50	38,00	0,15	0,15	5,00	0,00
50,00	3,08	8,10	4,55	88,00	0,10	0,00	17,50	0,00
60,00	3,18	8,10	4,45	148,00	0,10	0,00	17,50	0,00
75,00	3,27	8,40	4,60	223,00	0,00	0,20	20,00	0,00
127,00	3,38	8,80	4,75	350,00	0,00	0,00	0,00	0,00

39.5N 8.5E (B-2)

H	ρ	VP	VS	Z	ΔV_S+	ΔV_S-	$\Delta H+$	$\Delta H-$
2,00	2,42	3,20	1,85	2,00	0,00	0,00	0,00	0,00
1,00	2,57	4,60	2,66	3,00	0,00	0,00	0,00	0,00
0,80	2,62	5,00	2,89	3,80	0,00	0,00	0,00	0,00
1,20	2,72	5,80	3,35	5,00	0,00	0,00	0,00	0,00
10,00	2,77	5,80	3,35	15,00	0,10	0,10	1,00	0,00
20,00	2,96	7,50	4,75	35,00	0,05	0,00	2,50	2,50
30,00	3,06	8,20	4,30	65,00	0,00	0,10	15,00	0,00
95,00	3,16	8,20	4,35	160,00	0,00	0,15	0,00	17,50
110,00	3,28	8,60	4,35	270,00	0,00	0,15	0,00	20,00
80,00	3,50	8,85	4,75	350,00	0,00	0,00	0,00	0,00

39.5N 9.5E (B-1)

H	ρ	VP	VS	Z	ΔV_S+	ΔV_S-	$\Delta H+$	$\Delta H-$
1,50	2,43	3,20	1,85	1,50	0,00	0,00	0,00	0,00
1,50	2,58	4,80	2,78	3,00	0,00	0,00	0,00	0,00
0,50	2,62	5,00	2,89	3,50	0,00	0,00	0,00	0,00
1,50	2,72	5,80	3,35	5,00	0,00	0,00	0,00	0,00
6,00	2,72	5,55	3,20	11,00	0,20	0,20	1,50	1,50
8,00	2,92	7,10	4,10	19,00	0,00	0,15	2,50	0,00
35,00	3,08	8,10	4,40	54,00	0,10	0,10	17,50	0,00
40,00	3,17	8,10	4,10	94,00	0,00	0,10	0,00	17,50
160,00	3,28	8,55	4,45	254,00	0,00	0,10	0,00	30,00
96,00	3,50	8,85	4,75	350,00	0,00	0,00	0,00	0,00

39.5N 10.5E (B0)

H	ρ	VP	VS	Z	ΔV_S+	ΔV_S-	$\Delta H+$	$\Delta H-$
2,30	1,04	1,45	0,00	2,30	0,00	0,00	0,00	0,00
0,70	2,21	2,00	1,16	3,00	0,00	0,00	0,00	0,00
2,00	2,61	5,20	3,01	5,00	0,00	0,00	0,00	0,00
2,00	2,62	5,40	3,12	7,00	0,00	0,00	0,00	0,00
1,00	2,67	5,60	3,24	8,00	0,00	0,00	0,00	0,00
12,00	2,93	6,40	3,70	20,00	0,10	0,10	2,00	2,00
60,00	3,03	8,00	4,35	80,00	0,00	0,05	0,00	12,50
80,00	3,14	8,20	4,50	160,00	0,00	0,20	0,00	15,00
80,00	3,24	8,50	4,70	240,00	0,00	0,30	0,00	15,00
60,00	3,34	8,80	4,80	300,00	0,00	0,40	20,00	0,00
50,00	3,54	8,80	4,75	350,00	0,00	0,00	0,00	0,00

39.5N 11.5E (B1)

H	ρ	VP	VS	Z	ΔV_S+	ΔV_S-	$\Delta H+$	$\Delta H-$
3,00	1,03	1,45	0,00	3,00	0,00	0,00	0,00	0,00
0,70	2,10	2,10	1,20	3,70	0,00	0,00	0,00	0,00
1,00	2,70	6,00	3,45	4,70	0,00	0,00	0,00	0,00
2,30	2,81	6,85	3,95	7,00	0,00	0,00	0,00	0,00
8,00	2,96	6,60	3,80	15,00	0,25	0,25	2,00	2,00
13,00	3,11	7,00	3,85	28,00	0,05	0,15	2,00	2,00
90,00	3,32	8,00	4,30	118,00	0,00	0,05	0,00	15,00
60,00	3,33	8,20	4,45	178,00	0,00	0,15	20,00	0,00
100,00	3,35	8,60	4,60	278,00	0,00	0,20	0,00	20,00
72,00	3,57	8,80	4,75	350,00	0,00	0,00	0,00	0,00

39.5N 12.5E (B2)

H	ρ	VP	VS	Z	ΔV_S+	ΔV_S-	$\Delta H+$	$\Delta H-$
3,00	1,04	1,45	0,00	3,00	0,00	0,00	0,00	0,00
0,70	2,11	2,10	1,20	3,70	0,00	0,00	0,00	0,00
1,00	2,76	6,00	3,45	4,70	0,00	0,00	0,00	0,00
2,30	2,96	6,85	3,95	7,00	0,00	0,00	0,00	0,00
9,00	2,97	6,40	3,70	16,00	0,20	0,15	1,50	1,50
11,00	3,12	6,90	3,60	27,00	0,00	0,15	1,54	1,50
70,00	3,32	7,85	4,30	97,00	0,00	0,10	0,00	15,00
70,00	3,33	8,10	4,40	167,00	0,00	0,10	20,00	0,00
110,00	3,36	8,60	4,60	277,00	0,00	0,20	0,00	25,00
73,00	3,59	8,85	4,75	350,00	0,00	0,00	0,00	0,00

39.5N 13.5E (B3)

H	ρ	VP	VS	Z	ΔV_S+	ΔV_S-	$\Delta H+$	$\Delta H-$
3,00	1,04	1,45	0,00	3,00	0,00	0,00	0,00	0,00
0,70	2,11	2,10	1,20	3,70	0,00	0,00	0,00	0,00
1,00	2,71	6,00	3,45	4,70	0,00	0,00	0,00	0,00
2,30	2,92	6,85	3,95	7,00	0,00	0,00	0,00	0,00
11,00	3,07	6,60	3,80	18,00	0,20	0,20	2,00	2,00
8,00	3,13	6,95	3,30	26,00	0,00	0,20	1,50	1,50
60,00	3,34	7,95	4,30	86,00	0,00	0,10	0,00	10,00
70,00	3,35	8,15	4,40	156,00	0,00	0,10	20,00	0,00
120,00	3,36	8,65	4,60	276,00	0,00	0,20	0,00	20,00
74,00	3,59	8,80	4,75	350,00	0,00	0,00	0,00	0,00

39.5N 14.5E (B4)

H	ρ	VP	VS	Z	ΔV_S+	ΔV_S-	$\Delta H+$	$\Delta H-$
2,50	1,04	1,45	0,00	2,50	0,00	0,00	0,00	0,00
0,50	2,31	2,25	1,30	3,00	0,00	0,00	0,00	0,00
2,00	2,66	6,00	3,45	5,00	0,00	0,00	0,00	0,00
1,00	2,97	6,85	3,95	6,00	0,00	0,00	0,00	0,00
17,00	3,17	5,70	3,30	23,00	0,10	0,10	2,00	2,00
60,00	3,18	8,00	4,30	83,00	0,00	0,10	0,00	15,00
60,00	3,34	8,20	4,50	143,00	0,00	0,15	0,00	15,00
90,00	3,34	8,45	4,60	233,00	0,00	0,20	0,00	20,00
70,00	3,35	8,70	4,60	303,00	0,00	0,20	20,00	0,00
47,00	3,58	8,75	4,75	350,00	0,00	0,00	0,00	0,00

39.5N 15.5E (B5)

H	ρ	VP	VS	Z	ΔV_S+	ΔV_S-	$\Delta H+$	$\Delta H-$
0,90	1,03	1,45	0,00	0,90	0,00	0,00	0,00	0,00
2,10	2,25	2,00	1,15	3,00	0,00	0,00	0,00	0,00
3,00	2,70	5,00	2,90	6,00	0,00	0,00	0,00	0,00
18,00	2,86	6,05	3,50	24,00	0,05	0,05	4,00	4,00
8,00	2,96	6,75	3,90	32,00	0,20	0,20	2,50	0,00
40,00	3,31	8,15	4,20	72,00	0,00	0,05	10,00	10,00
70,00	3,31	8,20	4,50	142,00	0,10	0,00	20,00	0,00
110,00	3,31	8,65	4,60	252,00	0,00	0,20	0,00	20,00
98,00	3,55	8,80	4,75	350,00	0,00	0,00	0,00	0,00

39.5N 16.5E (B6)

H	ρ	VP	VS	Z	ΔV_S+	ΔV_S-	$\Delta H+$	$\Delta H-$
4,00	2,48	4,25	2,45	4,00	0,00	0,00	0,00	0,00
9,00	2,53	4,85	2,80	13,00	0,00	0,00	0,00	0,00
8,00	2,78	5,90	3,40	21,00	0,10	0,05	3,00	0,00
15,00	2,92	6,40	3,70	36,00	0,20	0,20	5,00	0,00
30,00	3,07	8,25	4,55	66,00	0,05	0,15	15,00	0,00
60,00	3,15	8,05	4,40	126,00	0,20	0,10	25,00	0,00
110,00	3,25	8,30	4,50	236,00	0,25	0,25	0,00	25,00
114,00	3,52	8,85	4,75	350,00	0,00	0,00	0,00	0,00

39.5N 17.5E (B7)

H	ρ	VP	VS	Z	ΔV_S+	ΔV_S-	$\Delta H+$	$\Delta H-$
1,50	1,02	1,45	0,00	1,50	0,00	0,00	0,00	0,00
1,50	2,39	5,00	2,90	3,00	0,00	0,00	0,00	0,00
2,00	2,58	6,10	3,52	5,00	0,00	0,00	0,00	0,00
8,00	2,67	4,50	2,60	13,00	0,05	0,05	1,00	1,00
20,00	2,67	6,05	3,50	33,00	0,15	0,15	3,00	3,00
60,00	3,06	8,05	4,50	93,00	0,15	0,11	15,00	0,00
70,00	3,25	8,10	4,45	163,00	0,10	0,05	0,00	20,00
60,00	3,25	8,30	4,55	223,00	0,05	0,15	25,00	0,00
127,00	3,51	8,70	4,75	350,00	0,00	0,00	0,00	0,00

39.5N 18.5E (B8)

H	ρ	VP	VS	Z	ΔV_S+	ΔV_S-	$\Delta H+$	$\Delta H-$
1,00	1,03	1,45	0,00	1,00	0,00	0,00	0,00	0,00
3,10	2,50	3,90	2,25	4,10	0,00	0,00	0,00	0,00
3,90	2,65	5,30	3,05	8,00	0,00	0,00	0,00	0,00
19,00	2,75	5,60	3,25	27,00	0,05	0,05	0,00	1,50
50,00	3,05	8,05	4,45	77,00	0,15	0,00	0,00	10,00
60,00	3,20	8,10	4,45	137,00	0,10	0,15	12,50	0,00
50,00	3,29	8,15	4,65	187,00	0,20	0,00	20,00	0,00
60,00	3,29	8,35	4,25	247,00	0,00	0,25	0,00	30,00
103,00	3,52	8,70	4,75	350,00	0,00	0,00	0,00	0,00

39.5N 19.5E (B9)

H	ρ	VP	VS	Z	ΔV_S+	ΔV_S-	$\Delta H+$	$\Delta H-$
1,73	1,03	1,45	0,00	1,73	0,00	0,00	0,00	0,00
3,27	2,45	4,00	2,30	5,00	0,00	0,00	0,00	0,00
2,00	2,70	5,20	3,00	7,00	0,00	0,00	0,00	0,00
20,00	2,80	5,70	3,30	27,00	0,05	0,05	2,00	2,00
60,00	3,00	8,00	4,45	87,00	0,05	0,00	0,00	10,00
40,00	3,09	8,00	4,35	127,00	0,20	0,20	10,00	10,00
70,00	3,19	8,15	4,60	197,00	0,10	0,00	10,00	10,00
100,00	3,27	8,55	4,30	297,00	0,00	0,10	0,00	20,00
53,00	3,51	8,75	4,75	350,00	0,00	0,00	0,00	0,00

38.5N 11.5E (C1)

H	ρ	VP	VS	Z	ΔV_S+	ΔV_S-	$\Delta H+$	$\Delta H-$
1,50	1,02	1,45	0,00	1,50	0,00	0,00	0,00	0,00
0,90	2,29	1,90	1,10	2,40	0,00	0,00	0,00	0,00
0,40	2,49	4,00	2,31	2,80	0,00	0,00	0,00	0,00
4,20	2,54	5,00	2,90	7,00	0,00	0,00	0,00	0,00
12,00	2,88	6,25	3,60	19,00	0,15	0,15	3,00	3,00
32,00	3,18	7,80	4,25	51,00	0,00	0,10	8,00	8,00
60,00	3,28	7,90	4,40	111,00	0,05	0,10	0,00	15,00
60,00	3,28	8,15	4,45	171,00	0,00	0,15	20,00	0,00
110,00	3,30	8,55	4,65	281,00	0,00	0,20	0,00	25,00
69,00	3,54	8,75	4,75	350,00	0,00	0,00	0,00	0,00

38.5N 12.5E (C2)

H	ρ	VP	VS	Z	ΔV_S+	ΔV_S-	$\Delta H+$	$\Delta H-$
1,00	1,03	1,45	0,00	1,00	0,00	0,00	0,00	0,00
1,50	2,10	1,90	1,10	2,50	0,00	0,00	0,00	0,00
0,40	2,39	3,80	2,20	2,90	0,00	0,00	0,00	0,00
3,10	2,49	4,55	2,63	6,00	0,00	0,00	0,00	0,00
20,00	2,79	6,50	3,75	26,00	0,05	0,05	2,50	2,50
30,00	3,12	7,75	4,25	56,00	0,05	0,05	5,00	5,00
60,00	3,28	7,90	4,40	116,00	0,05	0,05	0,00	15,00
100,00	3,28	8,25	4,50	216,00	0,00	0,10	0,00	20,00
60,00	3,30	8,50	4,45	276,00	0,00	0,15	20,00	0,00
74,00	3,56	8,80	4,75	350,00	0,00	0,00	0,00	0,00

38.5N 13.5E (C3)

H	ρ	VP	VS	Z	ΔV_S+	ΔV_S-	$\Delta H+$	$\Delta H-$
2,00	1,03	1,45	0,00	2,00	0,00	0,00	0,00	0,00
0,40	2,14	1,90	1,10	2,40	0,00	0,00	0,00	0,00
0,40	2,49	4,00	2,31	2,80	0,00	0,00	0,00	0,00
3,20	2,64	5,00	2,90	6,00	0,00	0,00	0,00	0,00
13,00	2,79	5,70	3,30	19,00	0,05	0,05	1,50	1,50
24,00	3,08	7,50	4,10	43,00	0,05	0,05	6,00	6,00
60,00	3,28	7,90	4,40	103,00	0,10	0,10	15,00	15,00
55,00	3,28	8,05	4,40	158,00	0,10	0,10	17,50	0,00
110,00	3,31	8,50	4,65	268,00	0,00	0,15	0,00	20,00
82,00	3,59	8,80	4,75	350,00	0,00	0,00	0,00	0,00

38.5N 14.5E (C4)

H	ρ	VP	VS	Z	ΔV_S+	ΔV_S-	$\Delta H+$	$\Delta H-$
2,36	1,03	1,45	0,00	2,36	0,00	0,00	0,00	0,00
0,04	2,10	1,75	1,00	2,40	0,00	0,00	0,00	0,00
0,40	2,49	4,00	2,31	2,80	0,00	0,00	0,00	0,00
3,20	2,59	6,15	3,55	6,00	0,00	0,00	0,00	0,00
9,00	2,74	5,00	2,90	15,00	0,05	0,10	2,00	2,00
12,00	3,09	6,85	3,65	27,00	0,00	0,20	6,00	0,00
60,00	3,23	7,85	4,30	87,00	0,15	0,15	15,00	0,00
60,00	3,29	8,00	4,45	147,00	0,10	0,00	20,00	0,00
120,00	3,32	8,45	4,60	267,00	0,00	0,20	0,00	20,00
83,00	3,61	8,70	4,75	350,00	0,00	0,00	0,00	0,00

38.75N 15.5E (C5-N)

H	ρ	VP	VS	Z	ΔV_S+	ΔV_S-	$\Delta H+$	$\Delta H-$
1,00	1,03	1,45	0,00	1,00	0,00	0,00	0,00	0,00
2,00	2,71	4,50	2,60	3,00	0,00	0,00	0,00	0,00
14,00	2,81	5,02	2,90	17,00	0,10	0,05	1,50	1,50
27,00	3,16	7,85	4,00	44,00	0,00	0,10	4,50	4,50
60,00	3,26	8,05	4,45	104,00	0,15	0,00	0,00	15,00
110,00	3,31	8,25	4,50	214,00	0,10	0,10	0,00	20,00
70,00	3,32	8,55	4,70	284,00	0,10	0,20	20,00	0,00
66,00	3,59	8,75	4,75	350,00	0,00	0,00	0,00	0,00

38.25N 15.5E (C5-S)

H	ρ	VP	VS	Z	ΔV_S+	ΔV_S-	$\Delta H+$	$\Delta H-$
1,00	2,59	4,50	2,60	1,00	0,00	0,00	0,00	0,00
2,00	2,68	4,50	2,60	3,00	0,00	0,00	0,00	0,00
14,00	2,68	5,00	2,90	17,00	0,10	0,05	1,50	1,50
27,00	2,92	6,75	3,90	44,00	0,10	0,10	4,50	4,50
60,00	3,26	8,05	4,45	104,00	0,15	0,00	0,00	15,00
110,00	3,26	8,25	4,50	214,00	0,00	0,10	0,00	20,00
70,00	3,29	8,55	4,70	284,00	0,10	0,20	20,00	0,00
66,00	3,62	8,75	4,75	350,00	0,00	0,00	0,00	0,00

38.5N 16.5E (C6)

H	ρ	VP	VS	Z	ΔV_S+	ΔV_S-	$\Delta H+$	$\Delta H-$
3,80	2,32	4,25	2,45	3,80	0,00	0,00	0,00	0,00
9,20	2,67	4,75	2,74	13,00	0,00	0,00	0,00	0,00
14,00	2,67	6,00	3,45	27,00	0,10	0,05	0,00	3,00
24,00	2,91	7,20	4,15	51,00	0,10	0,10	3,00	3,00
30,00	3,25	8,10	4,50	81,00	0,15	0,15	10,00	0,00
70,00	3,25	8,00	4,50	151,00	0,15	0,00	20,00	0,00
70,00	3,26	8,20	4,50	221,00	0,10	0,10	20,00	0,00
129,00	3,58	8,75	4,75	350,00	0,00	0,00	0,00	0,00

38.5N 17.5E (C7)

H	ρ	VP	VS	Z	ΔV_S+	ΔV_S-	$\Delta H+$	$\Delta H-$
2,40	1,03	1,45	0,00	2,40	0,00	0,00	0,00	0,00
2,10	2,39	3,65	2,10	4,50	0,00	0,00	0,00	0,00
0,70	2,49	3,90	2,25	5,20	0,00	0,00	0,00	0,00
1,80	2,63	5,60	3,25	7,00	0,00	0,00	0,00	0,00
18,00	2,63	5,55	3,20	25,00	0,10	0,10	2,50	2,50
28,00	3,17	8,20	4,40	53,00	0,00	0,15	5,00	5,00
30,00	3,26	8,15	4,65	83,00	0,15	0,00	15,00	0,00
60,00	3,26	8,10	4,40	143,00	0,20	0,20	20,00	0,00
100,00	3,27	8,25	4,50	243,00	0,25	0,25	0,00	20,00
107,00	3,59	8,65	4,75	350,00	0,00	0,00	0,00	0,00

38.5N 18.5E (C8)

H	ρ	VP	VS	Z	ΔV_S+	ΔV_S-	$\Delta H+$	$\Delta H-$
2,90	1,03	1,45	0,00	2,90	0,00	0,00	0,00	0,00
1,20	2,60	3,90	2,25	4,10	0,00	0,00	0,00	0,00
1,10	2,60	4,10	2,35	5,20	0,00	0,00	0,00	0,00
2,80	2,75	5,75	3,32	8,00	0,00	0,00	0,00	0,00
15,00	2,75	5,30	3,05	23,00	0,10	0,10	2,50	2,50
30,00	3,30	8,15	4,40	53,00	0,00	0,15	10,00	0,00
30,00	3,30	8,15	4,70	83,00	0,20	0,00	12,50	0,00
95,00	3,30	8,20	4,45	178,00	0,25	0,25	0,00	17,50
70,00	3,35	8,40	4,60	248,00	0,20	0,10	25,00	0,00
102,00	3,62	8,65	4,75	350,00	0,00	0,00	0,00	0,00

38.5N 19.5E (C9)

H	ρ	VP	VS	Z	ΔV_S+	ΔV_S-	$\Delta H+$	$\Delta H-$
2,80	1,03	1,45	0,00	2,80	0,00	0,00	0,00	0,00
1,20	2,44	3,50	2,02	4,00	0,00	0,00	0,00	0,00
12,00	2,68	5,80	3,35	16,00	0,10	0,15	3,00	3,00
10,00	2,68	5,20	3,00	26,00	0,20	0,20	4,50	0,00
60,00	3,06	8,10	4,45	86,00	0,10	0,00	15,00	0,00
70,00	3,15	8,20	4,70	156,00	0,10	0,00	0,00	20,00
80,00	3,29	8,40	4,60	236,00	0,00	0,15	0,00	20,00
114,00	3,59	8,70	4,75	350,00	0,00	0,00	0,00	0,00

37.5N 11.5E (D1)

H	ρ	VP	VS	Z	ΔV_S+	ΔV_S-	$\Delta H+$	$\Delta H-$
0,60	1,03	1,45	0,00	0,60	0,00	0,00	0,00	0,00
2,50	2,10	3,00	1,73	3,10	0,00	0,00	0,00	0,00
2,00	2,40	3,00	1,73	5,10	0,00	0,00	0,00	0,00
3,90	2,55	5,90	3,40	9,00	0,00	0,00	0,00	0,00
5,00	2,70	5,60	3,25	14,00	0,10	0,10	1,00	0,00
15,00	2,94	6,75	3,90	29,00	0,05	0,05	2,00	0,00
15,00	3,24	7,65	4,25	44,00	0,05	0,00	5,00	0,00
110,00	3,28	8,10	4,45	154,00	0,05	0,05	0,00	20,00
110,00	3,28	8,45	4,45	264,00	0,00	0,05	0,00	25,00
86,00	3,51	8,70	4,75	350,00	0,00	0,00	0,00	0,00

37.5N 12.5E (D2)

H	ρ	VP	VS	Z	ΔV_S+	ΔV_S-	$\Delta H+$	$\Delta H-$
0,50	1,03	1,45	0,00	0,50	0,00	0,00	0,00	0,00
2,50	2,39	3,20	1,85	3,00	0,00	0,00	0,00	0,00
2,00	2,49	4,60	2,65	5,00	0,00	0,00	0,00	0,00
2,00	2,53	5,00	2,89	7,00	0,00	0,00	0,00	0,00
10,00	2,63	6,25	3,60	17,00	0,10	0,15	3,00	0,00
12,00	3,02	7,05	3,90	29,00	0,00	0,20	6,00	0,00
30,00	3,21	7,95	4,45	59,00	0,05	0,00	15,00	0,00
110,00	3,21	8,10	4,40	169,00	0,05	0,00	0,00	20,00
110,00	3,28	8,50	4,55	279,00	0,00	0,15	0,00	20,00
71,00	3,56	8,70	4,75	350,00	0,00	0,00	0,00	0,00

37.5N 13.5E (D3)

H	ρ	VP	VS	Z	ΔV_S+	ΔV_S-	$\Delta H+$	$\Delta H-$
2,50	2,20	3,00	1,73	2,50	0,00	0,00	0,00	0,00
2,50	2,39	4,50	2,60	5,00	0,00	0,00	0,00	0,00
5,00	2,43	5,00	2,90	10,00	0,00	0,00	0,00	0,00
13,00	2,57	6,15	3,55	23,00	0,10	0,15	6,00	0,00
30,00	3,02	8,10	4,45	53,00	0,00	0,15	10,00	0,00
30,00	3,16	8,00	4,40	83,00	0,10	0,10	15,00	0,00
90,00	3,17	8,10	4,40	173,00	0,20	0,20	0,00	20,00
100,00	3,28	8,45	4,65	273,00	0,10	0,30	0,00	20,00
77,00	3,61	8,75	4,75	350,00	0,00	0,00	0,00	0,00

37.5N 14.5E (D4)

H	ρ	VP	VS	Z	ΔV_S+	ΔV_S-	$\Delta H+$	$\Delta H-$
3,00	2,22	3,00	1,73	3,00	0,00	0,00	0,00	0,00
2,00	2,41	4,50	2,60	5,00	0,00	0,00	0,00	0,00
5,00	2,50	5,00	2,90	10,00	0,00	0,00	0,00	0,00
17,00	2,55	6,40	3,70	27,00	0,10	0,10	2,50	2,50
30,00	3,00	8,15	4,50	57,00	0,10	0,10	10,00	0,00
30,00	3,10	8,05	4,40	87,00	0,20	0,20	15,00	0,00
100,00	3,22	8,10	4,45	187,00	0,20	0,20	0,00	20,00
100,00	3,31	8,50	4,70	287,00	0,05	0,20	0,00	20,00
63,00	3,67	8,75	4,75	350,00	0,00	0,00	0,00	0,00

37.5N 15.5E (D5)

H	ρ	VP	VS	Z	ΔV_S+	ΔV_S-	$\Delta H+$	$\Delta H-$
1,50	1,02	1,45	0,00	1,50	0,00	0,00	0,00	0,00
2,40	2,38	3,85	2,22	3,90	0,00	0,00	0,00	0,00
1,30	2,47	4,00	2,31	5,20	0,00	0,00	0,00	0,00
1,80	2,56	5,45	3,15	7,00	0,00	0,00	0,00	0,00
14,00	2,75	5,35	3,10	21,00	0,05	0,05	1,00	1,00
45,00	3,04	8,10	4,35	66,00	0,00	0,05	0,00	10,00
30,00	3,19	8,00	4,65	96,00	0,15	0,00	10,00	0,00
65,00	3,24	8,00	4,40	161,00	0,20	0,20	0,00	20,00
65,00	3,32	8,20	4,50	226,00	0,20	0,20	20,00	0,00
124,00	3,70	8,70	4,75	350,00	0,00	0,00	0,00	0,00

37.5N 16.5E (D6)

H	ρ	VP	VS	Z	ΔV_S+	ΔV_S-	$\Delta H+$	$\Delta H-$
2,70	1,03	1,45	0,00	2,70	0,00	0,00	0,00	0,00
1,40	2,39	3,90	2,25	4,10	0,00	0,00	0,00	0,00
1,10	2,44	4,00	2,31	5,20	0,00	0,00	0,00	0,00
2,80	2,58	5,75	3,32	8,00	0,00	0,00	0,00	0,00
13,00	2,67	5,35	3,10	21,00	0,10	0,15	2,00	2,00
40,00	3,06	8,10	4,30	61,00	0,00	0,10	10,00	10,00
30,00	3,20	8,05	4,65	91,00	0,15	0,00	15,00	0,00
60,00	3,26	8,05	4,40	151,00	0,20	0,20	0,00	20,00
60,00	3,33	8,20	4,45	211,00	0,20	0,25	20,00	0,00
139,00	3,70	8,75	4,75	350,00	0,00	0,00	0,00	0,00

37.5N 17.5E (D7)

H	ρ	VP	VS	Z	ΔV_S+	ΔV_S-	$\Delta H+$	$\Delta H-$
3,10	1,03	1,45	0,00	3,10	0,00	0,00	0,00	0,00
0,90	2,40	3,60	2,08	4,00	0,00	0,00	0,00	0,00
0,20	2,49	3,85	2,22	4,20	0,00	0,00	0,00	0,00
1,10	2,59	4,00	2,31	5,30	0,00	0,00	0,00	0,00
2,70	2,79	5,75	3,31	8,00	0,00	0,00	0,00	0,00
17,00	2,79	5,60	3,25	25,00	0,05	0,05	0,50	0,50
60,00	3,19	8,05	4,50	85,00	0,05	0,05	0,00	15,00
60,00	3,29	8,10	4,60	145,00	0,15	0,00	0,00	15,00
60,00	3,30	8,20	4,45	205,00	0,00	0,15	20,00	0,00
60,00	3,38	8,40	4,60	265,00	0,15	0,10	20,00	0,00
85,00	3,74	8,70	4,75	350,00	0,00	0,00	0,00	0,00

37.5N 18.5E (D8)

H	ρ	VP	VS	Z	ΔV_S+	ΔV_S-	$\Delta H+$	$\Delta H-$
2,90	1,03	1,45	0,00	2,90	0,00	0,00	0,00	0,00
1,20	2,40	3,90	2,25	4,10	0,00	0,00	0,00	0,00
1,10	2,49	4,00	2,31	5,20	0,00	0,00	0,00	0,00
2,80	2,69	5,75	3,31	8,00	0,00	0,00	0,00	0,00
17,00	2,75	5,55	3,20	25,00	0,10	0,10	1,50	1,50
30,00	3,25	8,00	4,45	55,00	0,15	0,00	10,00	0,00
30,00	3,26	8,05	4,50	85,00	0,10	0,00	12,50	0,00
60,00	3,33	8,15	4,55	145,00	0,20	0,00	20,00	0,00
70,00	3,42	8,30	4,55	215,00	0,10	0,15	20,00	0,00
135,00	3,77	8,70	4,75	350,00	0,00	0,00	0,00	0,00

37.5N 19.5E (D9)

H	ρ	VP	VS	Z	ΔV_S+	ΔV_S-	$\Delta H+$	$\Delta H-$
2,90	1,03	1,45	0,00	2,90	0,00	0,00	0,00	0,00
1,20	2,40	3,90	2,25	4,10	0,00	0,00	0,00	0,00
1,10	2,49	4,00	2,31	5,20	0,00	0,00	0,00	0,00
2,80	2,64	5,75	3,31	8,00	0,00	0,00	0,00	0,00
5,00	2,69	5,30	3,05	13,00	0,20	0,20	2,00	0,00
16,00	2,84	5,70	3,30	29,00	0,15	0,20	3,00	3,00
30,00	3,30	7,95	4,45	59,00	0,15	0,00	10,00	0,00
60,00	3,42	8,05	4,50	119,00	0,10	0,00	0,00	20,00
60,00	3,50	8,20	4,50	179,00	0,25	0,25	0,00	25,00
171,00	3,74	8,75	4,75	350,00	0,00	0,00	0,00	0,00

Appendix E

Appendix E

Relevant parameters of the cellular model at a resolution of $0.5° \times 0.5°$ for the Alpine region. For each layers thickness (H, km), density (ρ, g/cm^3), V_P (km/s), V_S (km/s), depth of the lower bottom (Z, km), upper (ΔV_S+, km/s) and lower (ΔV_S+, km/s) V_S uncertainties, upper ($\Delta H+$, km) and lower ($\Delta H-$, km) thickness uncertainties. Layers with both upper and lower zero uncertainties on V_S and H are fixed in the inversion. V_P in the crust are dependent from V_S according to the relation $V_P/V_S = \sqrt{3}$. V_P in the mantle are taken from Piromallo and Morelli (2003) and V_S are migrated in their range of uncertainties to satisfy at best the relation $V_P/V_S = 1.82$ (Kennett et al., 1995). Thus the uncertainties values coming from inversion are consequently reduced, and the V_S value for each layer can be not symmetric with respect to the given uncertainties range.

47.75N 6.75E (g-4 I)								
H	ρ	VP	VS	Z	ΔV_S+	ΔV_S-	$\Delta H+$	$\Delta H-$
0,50	2,35	4,15	2,40	0,50	0,00	0,00	0,00	0,00
0,50	2,40	4,50	2,60	1,00	0,00	0,00	0,00	0,00
2,00	2,55	4,85	2,80	3,00	0,00	0,00	0,00	0,00
1,00	2,70	5,45	3,15	4,00	0,00	0,00	0,00	0,00
2,00	2,70	5,45	3,15	6,00	0,00	0,00	0,00	0,00
8,00	2,75	5,55	3,20	14,00	0,05	0,05	0,50	0,50
17,00	2,85	6,85	3,95	31,00	0,05	0,05	1,00	1,00
40,00	3,20	8,13	4,50	71,00	0,05	0,05	12,50	12,50
70,00	3,34	8,06	4,40	141,0	0,05	0,05	17,50	17,50
110,00	3,34	8,34	4,55	251,0	0,00	0,10	17,50	17,50
99,00	3,39	8,76	4,75	350,0	0,00	0,00	0,00	0,00

47.25N 6.75E (g-4 II)

H	ρ	VP	VS	Z	ΔV_S+	ΔV_S-	$\Delta H+$	$\Delta H-$
0,50	2,35	4,15	2,40	0,50	0,00	0,00	0,00	0,00
0,50	2,40	4,50	2,60	1,00	0,00	0,00	0,00	0,00
2,00	2,55	4,84	2,80	3,00	0,00	0,00	0,00	0,00
1,00	2,70	5,40	3,15	4,00	0,00	0,00	0,00	0,00
2,00	2,70	5,40	3,15	6,00	0,00	0,00	0,00	0,00
8,00	2,75	5,54	3,20	14,00	0,05	0,05	0,50	0,50
17,00	2,85	6,84	3,95	31,00	0,05	0,05	1,00	1,00
40,00	3,20	8,22	4,50	71,00	0,05	0,05	12,50	12,50
70,00	3,35	8,04	4,40	141,0	0,05	0,05	17,50	17,50
110,00	3,33	8,36	4,55	251,0	0,00	0,10	17,50	17,50
99,00	3,38	8,72	4,75	350,0	0,00	0,00	0,00	0,00

47.25N 6.25E (g-4 III)

H	ρ	VP	VS	Z	ΔV_S+	ΔV_S-	$\Delta H+$	$\Delta H-$
0,50	2,35	4,15	2,40	0,50	0,00	0,00	0,00	0,00
0,50	2,45	4,50	2,60	1,00	0,00	0,00	0,00	0,00
2,00	2,65	5,20	3,00	3,00	0,00	0,00	0,00	0,00
1,00	2,70	5,45	3,15	4,00	0,00	0,00	0,00	0,00
2,00	2,70	5,45	3,15	6,00	0,00	0,00	0,00	0,00
10,00	2,75	5,70	3,30	16,00	0,10	0,10	1,00	1,00
14,00	2,86	6,85	3,95	30,00	0,05	0,05	1,00	1,00
40,00	3,22	8,25	4,50	70,00	0,00	0,05	12,50	12,50
70,00	3,36	8,04	4,45	140,0	0,05	0,05	17,50	17,50
110,00	3,33	8,35	4,50	250,0	0,00	0,05	17,50	17,50
100,00	3,38	8,74	4,75	350,0	0,00	0,00	0,00	0,00

47.75N 6.25E (g-4 IV)

H	ρ	VP	VS	Z	ΔV_S+	ΔV_S-	$\Delta H+$	$\Delta H-$
0,50	2,45	4,15	2,40	0,50	0,00	0,00	0,00	0,00
0,50	2,65	4,50	2,60	1,00	0,00	0,00	0,00	0,00
2,00	2,70	4,85	2,80	3,00	0,00	0,00	0,00	0,00
1,00	2,70	5,45	3,15	4,00	0,00	0,00	0,00	0,00
2,00	2,70	5,45	3,15	6,00	0,00	0,00	0,00	0,00
8,00	2,75	5,55	3,20	14,00	0,05	0,05	1,00	1,00
17,00	2,85	6,85	3,95	31,00	0,05	0,05	1,00	1,00
40,00	3,19	8,13	4,50	71,00	0,03	0,03	10,00	10,00
70,00	3,33	8,06	4,40	141,00	0,05	0,05	17,50	17,50
110,00	3,33	8,34	4,50	251,00	0,00	0,05	20,00	20,00
99,00	3,38	8,76	4,75	350,00	0,00	0,00	0,00	0,00

47.75N 7.75E (g-3 I)

H	ρ	VP	VS	Z	ΔV_S+	ΔV_S-	$\Delta H+$	$\Delta H-$
0,50	2,45	4,40	2,55	0,50	0,00	0,00	0,00	0,00
0,50	2,50	4,40	2,55	1,00	0,00	0,00	0,00	0,00
1,00	2,55	4,93	2,85	2,00	0,00	0,00	0,00	0,00
1,50	2,55	5,01	2,90	3,50	0,00	0,00	0,00	0,00
2,50	2,65	5,80	3,35	6,00	0,00	0,00	0,00	0,00
13,00	2,75	5,70	3,30	19,00	0,03	0,03	0,50	0,50
20,00	3,01	7,76	4,20	39,00	0,00	0,05	2,00	2,00
75,00	3,22	8,12	4,45	114,0	0,05	0,05	12,50	12,5
110,00	3,39	8,24	4,55	224,0	0,00	0,10	17,50	17,50
60,00	3,37	8,55	4,60	284,0	0,00	0,10	22,50	22,50
66,00	3,40	8,83	4,75	350,0	0,00	0,00	0,00	0,00

47.25N 7.75E (g-3 II)

H	ρ	VP	VS	Z	ΔV_S+	ΔV_S-	$\Delta H+$	$\Delta H-$
0,50	2,45	4,40	2,55	0,50	0,00	0,00	0,00	0,00
0,50	2,50	4,40	2,55	1,00	0,00	0,00	0,00	0,00
1,00	2,55	4,93	2,85	2,00	0,00	0,00	0,00	0,00
1,50	2,55	5,01	2,90	3,50	0,00	0,00	0,00	0,00
2,50	2,65	5,80	3,35	6,00	0,00	0,00	0,00	0,00
13,00	2,75	5,70	3,30	19,00	0,03	0,03	0,50	0,50
20,00	2,99	7,18	4,15	39,00	0,00	0,05	2,00	2,00
75,00	3,19	8,14	4,50	114,0	0,00	0,05	12,50	12,50
110,00	3,34	8,22	4,50	224,0	0,05	0,10	17,50	17,50
60,00	3,35	8,54	4,60	284,0	0,00	0,10	22,50	22,50
66,00	3,39	8,82	4,75	350,0	0,00	0,00	0,00	0,00

47.25N 7.25E (g-3 III)

H	ρ	VP	VS	Z	ΔV_S+	ΔV_S-	$\Delta H+$	$\Delta H-$
0,50	2,45	4,40	2,55	0,50	0,00	0,00	0,00	0,00
0,50	2,50	4,40	2,55	1,00	0,00	0,00	0,00	0,00
1,00	2,55	4,93	2,85	2,00	0,00	0,00	0,00	0,00
1,50	2,55	5,01	2,90	3,50	0,00	0,00	0,00	0,00
2,50	2,65	5,80	3,35	6,00	0,00	0,00	0,00	0,00
13,00	2,75	5,70	3,30	19,00	0,03	0,03	0,50	0,50
20,00	3,00	7,67	4,20	39,00	0,00	0,05	2,00	2,00
75,00	3,19	8,10	4,45	114,0	0,05	0,05	12,50	12,50
110,00	3,35	8,24	4,55	224,0	0,00	0,10	17,50	17,50
60,00	3,34	8,51	4,60	284,0	0,00	0,10	22,50	22,50
66,00	3,39	8,75	4,75	350,0	0,00	0,00	0,00	0,00

47.75N 7.25E (g-3 IV)

H	ρ	VP	VS	Z	ΔV_S+	ΔV_S-	$\Delta H+$	$\Delta H-$
0,50	2,45	4,40	2,55	0,50	0,00	0,00	0,00	0,00
0,50	2,50	4,40	2,55	1,00	0,00	0,00	0,00	0,00
1,00	2,55	4,93	2,85	2,00	0,00	0,00	0,00	0,00
1,50	2,55	5,02	2,90	3,50	0,00	0,00	0,00	0,00
2,50	2,65	5,80	3,35	6,00	0,00	0,00	0,00	0,00
13,00	2,75	5,71	3,30	19,0	0,03	0,03	0,50	0,50
20,00	3,00	7,72	4,20	39,0	0,00	0,05	2,00	2,00
75,00	3,21	8,10	4,45	114	0,05	0,05	12,50	12,50
110,00	3,37	8,25	4,50	224	0,00	0,10	17,50	17,50
60,00	3,36	8,54	4,55	284	0,00	0,10	22,50	22,50
66,00	3,40	8,81	4,75	350	0,00	0,00	0,00	0,00

47.75N 8.75E (g-2 I)

H	ρ	VP	VS	Z	ΔV_S+	ΔV_S-	$\Delta H+$	$\Delta H-$
0,50	2,39	4,33	2,50	0,50	0,00	0,00	0,00	0,00
0,50	2,39	4,40	2,55	1,00	0,00	0,00	0,00	0,00
1,00	2,59	4,40	2,55	2,00	0,00	0,00	0,00	0,00
1,00	2,59	4,76	2,75	3,00	0,00	0,00	0,00	0,00
0,50	2,59	5,02	2,90	3,50	0,00	0,00	0,00	0,00
19,00	2,70	5,89	3,40	22,50	0,03	0,03	1,00	1,00
17,00	2,99	7,65	4,25	39,50	0,10	0,00	3,00	3,00
80,00	3,25	8,11	4,45	119,50	0,10	0,10	12,50	12,50
60,00	3,37	8,12	4,40	179,50	0,00	0,10	20,00	20,00
110,00	3,44	8,56	4,70	289,50	0,00	0,20	20,00	20,00
60,50	3,53	8,86	4,75	350,00	0,00	0,00	0,00	0,00

47.25N 8.75E (g-2 II)

H	ρ	VP	VS	Z	ΔV_S+	ΔV_S-	$\Delta H+$	$\Delta H-$
0,50	2,38	4,58	2,65	0,50	0,00	0,00	0,00	0,00
0,50	2,38	4,67	2,70	1,00	0,00	0,00	0,00	0,00
1,00	2,58	4,93	2,85	2,00	0,00	0,00	0,00	0,00
1,00	2,58	5,02	2,90	3,00	0,00	0,00	0,00	0,00
1,00	2,58	5,02	2,90	4,00	0,00	0,00	0,00	0,00
18,00	2,69	5,80	3,35	22,0	0,03	0,03	1,00	1,00
15,00	2,97	7,35	4,20	37,0	0,10	0,00	5,00	5,00
70,00	3,19	8,33	4,55	107	0,00	0,05	12,50	12,50
70,00	3,33	8,24	4,40	177	0,00	0,10	20,00	20,00
110,00	3,41	8,50	4,70	287	0,00	0,25	20,00	20,00
63,00	3,52	8,77	4,75	350	0,00	0,00	0,00	0,00

47.25N 8.25E (g-2 III)

H	ρ	VP	VS	Z	ΔV_S+	ΔV_S-	$\Delta H+$	$\Delta H-$
0,50	2,38	4,58	2,65	0,50	0,00	0,00	0,00	0,00
0,50	2,38	4,67	2,70	1,00	0,00	0,00	0,00	0,00
1,00	2,58	4,93	2,85	2,00	0,00	0,00	0,00	0,00
1,00	2,58	5,01	2,90	3,00	0,00	0,00	0,00	0,00
1,00	2,58	5,01	2,90	4,00	0,00	0,00	0,00	0,00
18,00	2,69	5,80	3,35	22,00	0,03	0,03	1,00	1,00
15,00	2,98	7,52	4,20	37,00	0,10	0,00	5,00	5,00
70,00	3,20	8,22	4,50	107,0	0,05	0,05	12,50	12,50
70,00	3,35	8,15	4,40	177,0	0,00	0,10	20,00	20,00
110,00	3,43	8,53	4,70	287,0	0,03	0,23	20,00	20,00
63,00	3,52	8,81	4,75	350,0	0,00	0,00	0,00	0,00

47.75N 8.25E (g-2 IV)

H	ρ	VP	VS	Z	ΔV_S+	ΔV_S-	$\Delta H+$	$\Delta H-$
0,50	2,39	4,33	2,50	0,50	0,00	0,00	0,00	0,00
0,50	2,39	4,40	2,55	1,00	0,00	0,00	0,00	0,00
1,00	2,59	4,40	2,55	2,00	0,00	0,00	0,00	0,00
1,00	2,59	4,76	2,75	3,00	0,00	0,00	0,00	0,00
0,50	2,59	5,01	2,90	3,50	0,00	0,00	0,00	0,00
19,00	2,70	5,88	3,40	22,50	0,03	0,03	1,00	1,00
17,00	2,99	7,79	4,25	39,50	0,10	0,00	3,00	3,00
80,00	3,26	8,13	4,45	119,50	0,08	0,08	12,50	12,50
60,00	3,40	8,11	4,40	179,50	0,00	0,10	20,00	20,00
110,00	3,45	8,58	4,70	289,50	0,00	0,20	20,00	20,00
60,50	3,54	8,85	4,75	350,00	0,00	0,00	0,00	0,00

47.75N 9.75E (g-1 I)

H	ρ	VP	VS	Z	ΔV_S+	ΔV_S-	$\Delta H+$	$\Delta H-$
0,50	2,55	4,15	2,40	0,50	0,00	0,00	0,00	0,00
0,50	2,55	4,33	2,50	1,00	0,00	0,00	0,00	0,00
1,00	2,55	4,33	2,50	2,00	0,00	0,00	0,00	0,00
1,00	2,70	4,67	2,70	3,00	0,00	0,00	0,00	0,00
1,00	2,70	5,02	2,90	4,00	0,00	0,00	0,00	0,00
14,00	2,80	6,05	3,50	18,0	0,03	0,03	2,00	2,00
20,00	2,93	6,75	3,90	38,0	0,20	0,25	5,00	5,00
30,00	3,21	8,12	4,60	68,0	0,20	0,00	12,50	12,50
105,00	3,25	8,18	4,50	173	0,05	0,15	20,00	20,00
110,00	3,25	8,56	4,60	283	0,00	0,20	20,00	20,00
67,00	3,45	8,86	4,75	350	0,00	0,00	0,00	0,00

47.25N 9.75E (g-1 II)

H	ρ	VP	VS	Z	ΔV_S+	ΔV_S-	$\Delta H+$	$\Delta H-$
0,50	2,54	4,15	2,40	0,50	0,00	0,00	0,00	0,00
0,50	2,54	4,33	2,50	1,00	0,00	0,00	0,00	0,00
1,00	2,54	4,33	2,50	2,00	0,00	0,00	0,00	0,00
1,00	2,69	4,67	2,70	3,00	0,00	0,00	0,00	0,00
1,00	2,69	5,02	2,90	4,00	0,00	0,00	0,00	0,00
17,00	2,81	5,97	3,45	21,00	0,03	0,03	2,00	2,00
14,00	2,92	7,20	4,15	35,00	0,00	0,20	6,00	6,00
80,00	3,21	8,26	4,55	115,0	0,10	0,20	12,50	12,50
65,00	3,23	8,26	4,55	180,0	0,00	0,20	17,50	17,50
110,00	3,25	8,61	4,60	290,0	0,00	0,20	20,00	20,00
60,00	3,44	8,83	4,75	350,0	0,00	0,00	0,00	0,00

47.25N 9.25E (g-1 III)

H	ρ	VP	VS	Z	ΔV_S+	ΔV_S-	$\Delta H+$	$\Delta H-$
0,50	2,54	3,98	2,30	0,50	0,00	0,00	0,00	0,00
0,50	2,54	4,33	2,50	1,00	0,00	0,00	0,00	0,00
1,00	2,54	4,33	2,50	2,00	0,00	0,00	0,00	0,00
1,00	2,69	4,67	2,70	3,00	0,00	0,00	0,00	0,00
1,00	2,69	5,02	2,90	4,00	0,00	0,00	0,00	0,00
14,00	2,79	5,97	3,45	18,0	0,05	0,05	1,50	1,50
10,00	2,92	6,40	3,70	28,0	0,10	0,10	2,50	2,50
80,00	3,18	8,34	4,60	108	0,00	0,15	12,50	12,50
70,00	3,23	8,29	4,50	178	0,00	0,15	17,50	17,50
110,00	3,26	8,55	4,60	288	0,00	0,20	20,00	20,00
62,00	3,45	8,78	4,75	350	0,00	0,00	0,00	0,00

47.75N 9.25E (g-1 IV)

H	ρ	VP	VS	Z	ΔV_S+	ΔV_S-	$\Delta H+$	$\Delta H-$
0,50	2,55	3,98	2,30	0,50	0,00	0,00	0,00	0,00
0,50	2,55	4,33	2,50	1,00	0,00	0,00	0,00	0,00
1,00	2,55	4,33	2,50	2,00	0,00	0,00	0,00	0,00
1,00	2,70	4,67	2,70	3,00	0,00	0,00	0,00	0,00
1,00	2,70	5,02	2,90	4,00	0,00	0,00	0,00	0,00
14,00	2,81	5,97	3,45	18,00	0,05	0,05	1,50	1,50
10,00	2,94	6,40	3,70	28,00	0,10	0,10	2,50	2,50
80,00	3,21	8,14	4,50	108,0	0,10	0,15	12,50	12,50
70,00	3,26	8,15	4,50	178,0	0,00	0,15	17,50	17,50
110,00	3,27	8,58	4,60	288,0	0,00	0,20	20,00	20,00
62,00	3,46	8,86	4,75	350,0	0,00	0,00	0,00	0,00

47.75N 10.75E (g0 I)

H	ρ	VP	VS	Z	ΔV_S+	ΔV_S-	$\Delta H+$	$\Delta H-$
0,50	2,56	3,98	2,30	0,50	0,00	0,00	0,00	0,00
1,00	2,56	4,33	2,50	1,50	0,00	0,00	0,00	0,00
1,00	2,56	4,84	2,80	2,50	0,00	0,00	0,00	0,00
1,50	2,56	4,84	2,80	4,00	0,00	0,00	0,00	0,00
2,00	2,61	5,54	3,20	6,00	0,00	0,00	0,00	0,00
19,00	2,70	6,23	3,60	25,00	0,05	0,05	1,50	1,50
15,00	3,03	7,76	4,25	40,00	0,10	0,20	7,50	7,50
25,00	3,31	8,27	4,55	65,00	0,15	0,20	12,50	12,50
95,00	3,26	8,02	4,40	160,0	0,20	0,20	20,00	20,00
110,00	3,31	8,57	4,70	270,0	0,00	0,25	25,00	25,00
80,00	3,39	8,81	4,75	350,0	0,00	0,00	0,00	0,00

47.25N 10.75E (g0 II)

H	ρ	VP	VS	Z	ΔV_S+	ΔV_S-	$\Delta H+$	$\Delta H-$
0,50	2,55	3,98	2,30	0,50	0,00	0,00	0,00	0,00
1,00	2,55	4,33	2,50	1,50	0,00	0,00	0,00	0,00
1,00	2,55	4,84	2,80	2,50	0,00	0,00	0,00	0,00
1,00	2,55	4,84	2,80	3,50	0,00	0,00	0,00	0,00
2,50	2,59	5,71	3,30	6,00	0,00	0,00	0,00	0,00
17,00	2,68	6,14	3,55	23,00	0,08	0,08	3,00	3,00
30,00	3,12	7,53	4,35	53,00	0,15	0,15	7,50	7,50
50,00	3,28	8,14	4,45	103,0	0,15	0,10	12,50	12,50
95,00	3,22	8,16	4,45	198,0	0,15	0,15	20,00	20,00
60,00	3,36	8,45	4,65	258,0	0,05	0,20	25,00	25,00
92,00	3,40	8,81	4,75	350,0	0,00	0,00	0,00	0,00

47.25N 10.25E (g0 III)

H	ρ	VP	VS	Z	ΔV_S+	ΔV_S-	$\Delta H+$	$\Delta H-$
0,50	2,55	3,98	2,30	0,50	0,00	0,00	0,00	0,00
1,00	2,55	4,33	2,50	1,50	0,00	0,00	0,00	0,00
1,00	2,55	4,85	2,80	2,50	0,00	0,00	0,00	0,00
1,00	2,55	4,85	2,80	3,50	0,00	0,00	0,00	0,00
2,50	2,59	5,71	3,30	6,00	0,00	0,00	0,00	0,00
17,00	2,68	6,14	3,55	23,0	0,08	0,08	3,00	3,00
30,00	3,12	7,53	4,35	53,0	0,18	0,18	7,50	7,50
50,00	3,27	8,18	4,50	103	0,15	0,15	12,50	12,50
55,00	3,23	8,16	4,50	158	0,15	0,20	20,00	20,00
110,00	3,30	8,50	4,70	268	0,00	0,25	25,00	25,00
82,00	3,40	8,83	4,75	350	0,00	0,00	0,00	0,00

47.75N 10.25E (g0 IV)

H	ρ	VP	VS	Z	ΔV_S+	ΔV_S-	$\Delta H+$	$\Delta H-$
0,50	2,56	3,98	2,30	0,50	0,00	0,00	0,00	0,00
1,00	2,56	4,33	2,50	1,50	0,00	0,00	0,00	0,00
1,00	2,56	4,85	2,80	2,50	0,00	0,00	0,00	0,00
1,50	2,56	4,85	2,80	4,00	0,00	0,00	0,00	0,00
2,00	2,61	5,54	3,20	6,00	0,00	0,00	0,00	0,00
19,00	2,69	6,23	3,60	25,00	0,05	0,05	1,50	1,50
15,00	3,03	7,76	4,25	40,00	0,10	0,20	7,50	7,50
25,00	3,31	8,25	4,50	65,00	0,20	0,10	12,50	12,50
95,00	3,26	7,99	4,40	160,0	0,20	0,20	20,00	20,00
110,00	3,31	8,51	4,70	270,0	0,00	0,25	25,00	25,00
80,00	3,39	8,81	4,75	350,0	0,00	0,00	0,00	0,00

47.75N 11.75E (g1 I)

H	ρ	VP	VS	Z	ΔV_S+	ΔV_S-	$\Delta H+$	$\Delta H-$
0,50	2,60	3,98	2,30	0,50	0,00	0,00	0,00	0,00
1,00	2,60	4,33	2,50	1,50	0,00	0,00	0,00	0,00
1,00	2,60	4,84	2,80	2,50	0,00	0,00	0,00	0,00
2,00	2,60	4,84	2,80	4,50	0,00	0,00	0,00	0,00
1,50	2,60	5,36	3,10	6,00	0,00	0,00	0,00	0,00
8,00	2,65	6,14	3,55	14,00	0,08	0,08	2,50	2,50
15,00	2,87	6,40	3,70	29,00	0,15	0,15	4,00	4,00
25,00	3,24	8,19	4,50	54,00	0,05	0,15	12,50	12,50
95,00	3,26	8,25	4,55	149,0	0,20	0,20	20,00	20,00
110,00	3,31	8,56	4,70	259,0	0,00	0,25	25,00	25,00
91,00	3,41	8,86	4,75	350,0	0,00	0,00	0,00	0,00

47.25N 11.75E (g1 II)

H	ρ	VP	VS	Z	ΔV_S+	ΔV_S-	$\Delta H+$	$\Delta H-$
0,50	2,59	3,98	2,30	0,50	0,00	0,00	0,00	0,00
1,00	2,59	4,33	2,50	1,50	0,00	0,00	0,00	0,00
1,00	2,59	4,84	2,80	2,50	0,00	0,00	0,00	0,00
1,00	2,59	4,84	2,80	3,50	0,00	0,00	0,00	0,00
2,50	2,59	5,36	3,10	6,00	0,00	0,00	0,00	0,00
8,00	2,64	5,80	3,35	14,00	0,10	0,10	4,00	4,00
15,00	2,86	6,40	3,70	29,00	0,18	0,18	5,00	5,00
25,00	3,22	8,02	4,40	54,00	0,15	0,20	12,50	12,50
95,00	3,26	8,28	4,55	149,00	0,20	0,20	20,00	20,00
110,00	3,31	8,50	4,70	259,00	0,00	0,25	25,00	25,00
91,00	3,41	8,88	4,75	350,00	0,00	0,00	0,00	0,00

47.25N 11.25E (g1 III)

H	ρ	VP	VS	Z	ΔV_S+	ΔV_S-	$\Delta H+$	$\Delta H-$
0,50	2,59	3,98	2,30	0,50	0,00	0,00	0,00	0,00
1,00	2,59	4,33	2,50	1,50	0,00	0,00	0,00	0,00
1,50	2,59	4,84	2,80	3,00	0,00	0,00	0,00	0,00
0,50	2,59	5,36	3,10	3,50	0,00	0,00	0,00	0,00
2,50	2,59	5,36	3,10	6,00	0,00	0,00	0,00	0,00
8,00	2,64	5,80	3,35	14,00	0,10	0,10	4,00	4,00
15,00	2,86	6,40	3,70	29,00	0,15	0,15	5,00	5,00
25,00	3,22	8,10	4,45	54,00	0,10	0,20	12,50	12,50
95,00	3,25	8,26	4,55	149,0	0,20	0,20	20,00	20,00
110,00	3,32	8,48	4,65	259,0	0,05	0,20	25,00	25,00
91,00	3,41	8,84	4,75	350,0	0,00	0,00	0,00	0,00

47.75N 11.25E (g1 IV)

H	ρ	VP	VS	Z	ΔV_S+	ΔV_S-	$\Delta H+$	$\Delta H-$
0,50	2,60	3,98	2,30	0,50	0,00	0,00	0,00	0,00
1,00	2,60	4,33	2,50	1,50	0,00	0,00	0,00	0,00
1,00	2,60	4,84	2,80	2,50	0,00	0,00	0,00	0,00
2,00	2,60	4,84	2,80	4,50	0,00	0,00	0,00	0,00
1,50	2,60	5,36	3,10	6,00	0,00	0,00	0,00	0,00
8,00	2,65	6,14	3,55	14,00	0,08	0,08	2,50	2,50
15,00	2,87	6,40	3,70	29,00	0,18	0,18	4,00	4,00
25,00	3,24	8,27	4,55	54,00	0,00	0,20	12,50	12,50
95,00	3,27	8,14	4,45	149,0	0,20	0,10	20,00	20,00
110,00	3,31	8,55	4,70	259,0	0,00	0,25	25,00	25,00
91,00	3,41	8,83	4,75	350,0	0,00	0,00	0,00	0,00

47.75N 12.75E (g2 I)

H	ρ	VP	VS	Z	ΔV_S+	ΔV_S-	$\Delta H+$	$\Delta H-$
2,00	2,35	3,98	2,30	2,00	0,00	0,00	0,00	0,00
0,50	2,49	4,39	2,54	2,50	0,00	0,00	0,00	0,00
0,50	2,49	4,39	2,54	3,00	0,00	0,00	0,00	0,00
1,00	2,49	4,99	2,89	4,00	0,00	0,00	0,00	0,00
1,00	2,49	5,39	3,12	5,00	0,00	0,00	0,00	0,00
17,00	2,49	6,05	3,50	22,0	0,08	0,08	3,50	3,50
13,00	2,68	7,27	4,20	35,0	0,00	0,15	6,50	6,50
30,00	3,21	8,04	4,40	65,0	0,00	0,20	12,50	12,50
100,00	3,23	8,26	4,55	165	0,20	0,20	20,00	20,00
70,00	3,21	8,44	4,65	235	0,05	0,20	20,00	20,00
115,00	3,38	8,90	4,75	350	0,00	0,00	0,00	0,00

47.25N 12.75E (g2 II)

H	ρ	VP	VS	Z	ΔV_S+	ΔV_S-	$\Delta H+$	$\Delta H-$
2,00	2,35	3,98	2,30	2,00	0,00	0,00	0,00	0,00
0,50	2,49	4,39	2,54	2,50	0,00	0,00	0,00	0,00
0,50	2,49	5,40	3,12	3,00	0,00	0,00	0,00	0,00
1,00	2,49	5,54	3,20	4,00	0,00	0,00	0,00	0,00
1,00	2,49	5,71	3,30	5,00	0,00	0,00	0,00	0,00
15,00	2,49	6,05	3,50	20,00	0,08	0,08	2,50	2,50
15,00	2,66	6,75	3,90	35,00	0,15	0,15	7,50	7,50
35,00	3,22	8,08	4,45	70,00	0,00	0,20	10,00	10,00
100,00	3,24	8,26	4,55	170,0	0,10	0,20	20,00	20,00
70,00	3,23	8,43	4,65	240,0	0,05	0,25	20,00	20,00
110,00	3,39	8,88	4,75	350,0	0,00	0,00	0,00	0,00

47.25N 12.25E (g2 III)

H	ρ	VP	VS	Z	ΔV_S+	ΔV_S-	$\Delta H+$	$\Delta H-$
2,00	2,35	3,98	2,30	2,00	0,00	0,00	0,00	0,00
1,00	2,49	4,39	2,54	3,00	0,00	0,00	0,00	0,00
1,00	2,49	4,99	2,89	4,00	0,00	0,00	0,00	0,00
0,50	2,49	5,54	3,20	4,50	0,00	0,00	0,00	0,00
0,50	2,49	5,79	3,35	5,00	0,00	0,00	0,00	0,00
14,00	2,49	5,79	3,35	19,00	0,05	0,05	3,00	3,00
30,00	2,91	7,18	4,15	49,00	0,00	0,20	7,50	7,50
35,00	3,24	8,07	4,45	84,00	0,15	0,05	10,00	10,00
100,00	3,24	8,24	4,50	184,0	0,15	0,20	20,00	20,00
70,00	3,27	8,49	4,65	254,0	0,00	0,25	20,00	20,00
96,00	3,40	8,90	4,75	350,0	0,00	0,00	0,00	0,00

47.75N 12.25E (g2 IV)

H	ρ	VP	VS	Z	ΔV_S+	ΔV_S-	$\Delta H+$	$\Delta H-$
2,00	2,35	3,98	2,30	2,00	0,00	0,00	0,00	0,00
0,50	2,49	4,39	2,54	2,50	0,00	0,00	0,00	0,00
0,50	2,49	4,39	2,54	3,00	0,00	0,00	0,00	0,00
1,00	2,49	4,58	2,65	4,00	0,00	0,00	0,00	0,00
1,00	2,49	4,99	2,89	5,00	0,00	0,00	0,00	0,00
15,00	2,49	5,97	3,45	20,0	0,08	0,08	3,00	3,00
25,00	2,89	7,18	4,15	45,0	0,00	0,20	5,00	5,00
30,00	3,24	8,11	4,45	75,0	0,20	0,25	15,00	15,00
100,00	3,24	8,23	4,55	175	0,20	0,15	0,25	20,00
65,00	3,23	8,47	4,45	240	0,00	0,25	22,50	22,50
110,00	3,39	8,88	4,75	350	0,00	0,00	0,00	0,00

47.75N 13.75E (g3 I)

H	ρ	VP	VS	Z	ΔV_S+	ΔV_S-	$\Delta H+$	$\Delta H-$
2,00	2,41	3,98	2,30	2,00	0,00	0,00	0,00	0,00
0,50	2,62	4,40	2,54	2,50	0,00	0,00	0,00	0,00
0,50	2,62	4,40	2,54	3,00	0,00	0,00	0,00	0,00
1,00	2,62	5,00	2,89	4,00	0,00	0,00	0,00	0,00
1,00	2,62	5,40	3,12	5,00	0,00	0,00	0,00	0,00
19,00	2,73	6,23	3,60	24,00	0,08	0,08	4,50	4,50
15,00	2,87	7,19	4,15	39,00	0,00	0,20	5,00	5,00
25,00	3,29	8,11	4,45	64,00	0,00	0,20	12,50	12,50
60,00	3,28	8,05	4,40	124,0	0,20	0,20	20,00	20,00
110,00	3,27	8,46	4,65	234,0	0,05	0,20	20,00	20,00
116,00	3,27	8,92	4,75	350,0	0,00	0,00	0,00	0,00

47.25N 13.75E (g3 II)

H	ρ	VP	VS	Z	ΔV_S+	ΔV_S-	$\Delta H+$	$\Delta H-$
2,00	2,41	3,81	2,20	2,00	0,00	0,00	0,00	0,00
0,50	2,63	5,54	3,20	2,50	0,00		0,00	0,00
0,50	2,63	5,54	3,20	3,00	0,00	0,00	0,00	0,00
1,00	2,62	6,06	3,50	4,00	0,00	0,00	0,00	0,00
1,00	2,63	6,06	3,50	5,00	0,00	0,00	0,00	0,00
12,00	2,72	5,80	3,35	17,0	0,08	0,08	3,00	3,00
30,00	2,97	6,93	4,00	47,0	0,10	0,15	5,00	5,00
75,00	3,31	8,08	4,45	122	0,15	0,10	12,50	12,50
100,00	3,29	8,41	4,60	222	0,00	0,20	20,00	20,00
70,00	3,27	8,69	4,75	292	0,20	0,10	20,00	20,00
58,00	3,31	8,85	4,75	350	0,00	0,00	0,00	0,00

47.25N 13.25E (g3 III)

H	ρ	VP	VS	Z	ΔV_S+	ΔV_S-	$\Delta H+$	$\Delta H-$
2,00	2,41	3,81	2,20	2,00	0,00	0,00	0,00	0,00
1,00	2,63	5,53	3,20	3,00	0,00	0,00	0,00	0,00
1,00	2,63	5,53	3,20	4,00	0,00	0,00	0,00	0,00
0,50	2,63	5,71	3,30	4,50	0,00	0,00	0,00	0,00
0,50	2,63	5,71	3,30	5,00	0,00	0,00	0,00	0,00
18,00	2,74	5,97	3,45	23,0	0,08	0,08	3,00	3,00
10,00	2,77	7,18	4,15	33,0	0,00	0,15	5,00	5,00
25,00	3,24	8,11	4,40	58,0	0,00	0,20	12,50	12,50
100,00	3,29	8,24	4,50	158	0,10	0,20	20,00	20,00
110,00	3,27	8,59	4,75	268	0,00	0,25	20,00	20,00
82,00	3,29	8,86	4,75	350	0,00	0,00	0,00	0,00

47.75N 13.25E (g3 IV)

H	ρ	VP	VS	Z	ΔV_S+	ΔV_S-	$\Delta H+$	$\Delta H-$
2,00	2,41	3,98	2,30	2,00	0,00	0,00	0,00	0,00
0,50	2,63	4,39	2,54	2,50	0,00	0,00	0,00	0,00
0,50	2,63	4,39	2,54	3,00	0,00	0,00	0,00	0,00
1,00	2,63	4,99	2,89	4,00	0,00	0,00	0,00	0,00
1,00	2,63	5,40	3,12	5,00	0,00	0,00	0,00	0,00
19,00	2,74	6,22	3,60	24,00	0,08	0,08	4,50	4,50
15,00	2,88	7,18	4,15	39,00	0,00	0,20	5,00	5,00
25,00	3,30	8,13	4,45	64,00	0,00	0,20	12,50	12,50
60,00	3,27	8,06	4,40	124,0	0,20	0,20	20,00	20,00
110,00	3,26	8,48	4,65	234,0	0,05	0,20	20,00	20,00
116,00	3,26	8,91	4,75	350,0	0,00	0,00	0,00	0,00

46.75N 6.75E (f-4 I)

H	ρ	VP	VS	Z	ΔV_S+	ΔV_S-	$\Delta H+$	$\Delta H-$
0,50	2,35	4,40	2,55	0,50	0,00	0,00	0,00	0,00
1,50	2,45	4,58	2,65	2,00	0,00	0,00	0,00	0,00
1,00	2,55	4,93	2,85	3,00	0,00	0,00	0,00	0,00
1,00	2,55	4,93	2,85	4,00	0,00	0,00	0,00	0,00
1,00	2,65	5,55	3,20	5,00	0,00	0,00	0,00	0,00
5,00	2,75	5,01	2,90	10,00	0,10	0,10	1,50	1,50
20,00	2,89	6,50	3,75	30,00	0,10	0,10	4,00	4,00
85,00	3,29	8,09	4,45	115,0	0,05	0,05	12,50	12,50
70,00	3,34	8,17	4,50	185,0	0,10	0,10	17,50	17,50
110,00	3,32	8,59	4,70	295,0	0,05	0,20	25,00	25,00
55,00	3,37	8,74	4,75	350,0	0,00	0,00	0,00	0,00

46.25N 6.75E (f-4 II)

H	ρ	VP	VS	Z	ΔV_S+	ΔV_S-	$\Delta H+$	$\Delta H-$
0,50	2,35	4,40	2,55	0,50	0,00	0,00	0,00	0,00
1,50	2,45	4,58	2,65	2,00	0,00	0,00	0,00	0,00
1,00	2,55	4,93	2,85	3,00	0,00	0,00	0,00	0,00
0,50	2,55	4,93	2,85	3,50	0,00	0,00	0,00	0,00
1,50	2,65	5,55	3,20	5,00	0,00	0,00	0,00	0,00
8,00	2,75	5,20	3,00	13,00	0,10	0,10	1,50	1,50
18,00	2,90	6,65	3,85	31,00	0,10	0,10	3,00	3,00
85,00	3,29	8,10	4,45	116,00	0,05	0,05	12,50	12,50
70,00	3,31	8,25	4,60	186,00	0,10	0,00	17,50	17,50
110,00	3,30	8,66	4,40	296,00	0,00	0,15	25,00	25,00
54,00	3,36	8,76	4,75	350,00	0,00	0,00	0,00	0,00

46.25N 6.25E (f-4 III)

H	ρ	VP	VS	Z	ΔV_S+	ΔV_S-	$\Delta H+$	$\Delta H-$
0,50	2,35	4,40	2,55	0,50	0,00	0,00	0,00	0,00
1,50	2,45	4,58	2,65	2,00	0,00	0,00	0,00	0,00
1,00	2,55	4,93	2,85	3,00	0,00	0,00	0,00	0,00
0,50	2,55	4,93	2,85	3,50	0,00	0,00	0,00	0,00
1,50	2,65	5,53	3,20	5,00	0,00	0,00	0,00	0,00
8,00	2,75	5,20	3,00	13,00	0,10	0,10	1,50	1,50
18,00	2,90	6,65	3,85	31,00	0,10	0,10	3,00	3,00
85,00	3,30	8,06	4,45	116,0	0,05	0,05	12,50	12,50
70,00	3,32	8,21	4,50	186,0	0,10	0,10	17,50	17,50
110,00	3,30	8,60	4,70	296,0	0,00	0,15	25,00	25,00
54,00	3,36	8,73	4,75	350,0	0,00	0,00	0,00	0,00

46.75N 6.25E (f-4 IV)

H	ρ	VP	VS	Z	ΔV_S+	ΔV_S-	$\Delta H+$	$\Delta H-$
0,50	2,35	4,40	2,55	0,50	0,00	0,00	0,00	0,00
1,50	2,45	4,58	2,65	2,00	0,00	0,00	0,00	0,00
1,00	2,55	4,93	2,85	3,00	0,00	0,00	0,00	0,00
1,00	2,65	5,55	3,20	4,00	0,00	0,00	0,00	0,00
1,00	2,65	5,55	3,20	5,00	0,00	0,00	0,00	0,00
5,00	2,75	5,01	2,90	10,00	0,10	0,10	1,50	1,50
20,00	2,90	6,50	3,75	30,00	0,10	0,10	4,00	4,00
85,00	3,31	8,06	4,45	115,0	0,05	0,05	12,50	12,50
70,00	3,36	8,15	4,50	185,0	0,10	0,10	17,50	17,50
110,00	3,33	8,57	4,70	295,0	0,10	0,20	20,00	20,00
55,00	3,37	8,74	4,75	350,0	0,00	0,00	0,00	0,00

46.75N 7.75E (f-3 I)

H	ρ	VP	VS	Z	ΔV_S+	ΔV_S-	$\Delta H+$	$\Delta H-$
0,50	2,36	4,40	2,55	0,50	0,00	0,00	0,00	0,00
1,50	2,45	4,58	2,65	2,00	0,00	0,00	0,00	0,00
1,00	2,50	4,95	2,85	3,00	0,00	0,00	0,00	0,00
1,00	2,60	4,95	2,85	4,00	0,00	0,00	0,00	0,00
1,00	2,60	5,20	3,00	5,00	0,00	0,00	0,00	0,00
10,00	2,74	5,20	3,00	15,00	0,10	0,10	2,00	2,00
18,00	2,86	6,92	4,00	33,00	0,10	0,10	3,00	3,00
85,00	3,18	8,22	4,50	118,0	0,05	0,10	12,50	12,50
110,00	3,22	8,34	4,50	228,0	0,00	0,15	20,00	20,00
110,00	3,39	8,78	4,75	338,0	0,00	0,20	20,00	20,00
12,00	3,46	8,82	4,75	350,0	0,00	0,00	0,00	0,00

46.25N 7.75E (f-3 II)

H	ρ	VP	VS	Z	ΔV_S+	ΔV_S-	$\Delta H+$	$\Delta H-$
0,50	2,35	4,40	2,55	0,50	0,00	0,00	0,00	0,00
1,50	2,45	4,58	2,65	2,00	0,00	0,00	0,00	0,00
1,00	2,50	4,95	2,85	3,00	0,00	0,00	0,00	0,00
1,00	2,60	5,54	3,20	4,00	0,00	0,00	0,00	0,00
1,00	2,59	5,88	3,40	5,00	0,00	0,00	0,00	0,00
7,00	2,73	5,02	2,90	12,00	0,10	0,10	1,50	1,50
24,00	2,84	6,75	3,90	36,00	0,10	0,10	4,00	4,00
35,00	3,15	8,20	4,55	71,00	0,10	0,00	12,50	12,50
105,00	3,22	8,30	4,50	176,0	0,00	0,15	17,50	17,50
110,00	3,29	8,69	4,75	286,0	0,00	0,20	20,00	20,00
64,00	3,47	8,80	4,75	350,0	0,00	0,00	0,00	0,00

46.25N 7.25E (f-3 III)

H	ρ	VP	VS	Z	ΔV_S+	ΔV_S-	$\Delta H+$	$\Delta H-$
0,50	2,35	4,40	2,55	0,50	0,00	0,00	0,00	0,00
1,50	2,45	4,58	2,65	2,00	0,00	0,00	0,00	0,00
0,50	2,50	4,93	2,85	2,50	0,00	0,00	0,00	0,00
1,50	2,56	5,55	3,20	4,00	0,00	0,00	0,00	0,00
1,00	2,60	5,88	3,40	5,00	0,00	0,00	0,00	0,00
7,00	2,73	5,01	2,90	12,00	0,10	0,10	1,50	1,50
24,00	2,84	6,75	3,90	36,00	0,10	0,10	4,00	4,00
35,00	3,14	8,17	4,55	71,00	0,10	0,00	12,50	12,50
105,00	3,21	8,24	4,50	176,0	0,05	0,10	17,50	17,50
110,00	3,28	8,67	4,75	286,0	0,00	0,20	20,00	20,00
64,00	3,45	8,79	4,75	350,0	0,00	0,00	0,00	0,00

46.75N 7.25E (f-3 IV)

H	ρ	VP	VS	Z	ΔV_S+	ΔV_S-	$\Delta H+$	$\Delta H-$
0,50	2,36	4,40	2,55	0,50	0,00	0,00	0,00	0,00
1,50	2,46	4,58	2,65	2,00	0,00	0,00	0,00	0,00
1,00	2,51	4,93	2,85	3,00	0,00	0,00	0,00	0,00
1,00	2,61	4,93	2,85	4,00	0,00	0,00	0,00	0,00
1,00	2,61	5,20	3,00	5,00	0,00	0,00	0,00	0,00
10,00	2,75	5,20	3,00	15,0	0,10	0,10	2,00	2,00
18,00	2,88	6,90	4,00	33,0	0,10	0,10	3,00	3,00
85,00	3,19	8,16	4,45	118	0,10	0,10	12,50	12,50
110,00	3,23	8,38	4,60	228	0,15	0,10	20,00	20,00
70,00	3,36	8,64	4,40	298	0,00	0,20	20,00	20,00
52,00	3,45	8,77	4,75	350	0,00	0,00	0,00	0,00

46.75N 8.75E (f-2 I)

H	ρ	VP	VS	Z	ΔV_S+	ΔV_S-	$\Delta H+$	$\Delta H-$
0,50	2,37	4,58	2,65	0,50	0,00	0,00	0,00	0,00
0,50	2,37	4,67	2,70	1,00	0,00	0,00	0,00	0,00
1,00	2,47	4,93	2,85	2,00	0,00	0,00	0,00	0,00
1,00	2,67	4,93	2,85	3,00	0,00	0,00	0,00	0,00
0,50	2,67	5,01	2,90	3,50	0,00	0,00	0,00	0,00
16,00	2,72	5,55	3,20	19,50	0,50	0,50	1,00	1,00
30,00	3,02	8,14	4,15	49,50	0,00	0,10	5,00	5,00
45,00	3,25	8,27	4,45	94,50	0,00	0,15	12,50	12,50
110,00	3,24	8,35	4,55	204,50	0,00	0,20	20,00	20,00
110,00	3,36	8,71	4,75	314,50	0,00	0,25	20,00	20,00
35,50	3,48	8,77	4,75	350,00	0,00	0,00	0,00	0,00

46.25N 8.75E (f-2 II)

H	ρ	VP	VS	Z	ΔV_S+	ΔV_S-	$\Delta H+$	$\Delta H-$
0,50	2,40	4,58	2,65	0,50	0,00	0,00	0,00	0,00
0,50	2,40	4,67	2,70	1,00	0,00	0,00	0,00	0,00
1,00	2,50	4,93	2,85	2,00	0,00	0,00	0,00	0,00
1,00	2,70	4,93	2,85	3,00	0,00	0,00	0,00	0,00
0,50	2,70	4,93	2,85	3,50	0,00	0,00	0,00	0,00
16,00	2,76	5,55	3,20	19,50	0,05	0,05	1,00	1,00
30,00	3,07	8,14	4,15	49,50	0,00	0,10	5,00	5,00
45,00	3,30	8,18	4,45	94,50	0,00	0,15	12,50	12,50
110,00	3,26	8,26	4,55	204,50	0,00	0,20	20,00	20,00
110,00	3,37	8,73	4,75	314,50	0,00	0,25	20,00	20,00
35,50	3,50	8,81	4,75	350,00	0,00	0,00	0,00	0,00

46.25N 8.25E (f-2 III)

H	ρ	VP	VS	Z	ΔV_S+	ΔV_S-	$\Delta H+$	$\Delta H-$
0,50	2,39	4,58	2,65	0,50	0,00	0,00	0,00	0,00
0,50	2,39	4,67	2,70	1,00	0,00	0,00	0,00	0,00
1,00	2,49	4,93	2,85	2,00	0,00	0,00	0,00	0,00
1,00	2,69	4,93	2,85	3,00	0,00	0,00	0,00	0,00
0,50	2,69	5,01	2,90	3,50	0,00	0,00	0,00	0,00
16,00	2,75	5,55	3,20	19,50	0,05	0,05	1,00	1,00
30,00	3,06	8,14	4,15	49,50	0,00	0,10	5,00	5,00
45,00	3,28	8,27	4,45	94,50	0,00	0,15	12,50	12,50
110,00	3,25	8,35	4,55	204,50	0,00	0,20	20,00	20,00
110,00	3,37	8,71	4,75	314,50	0,00	0,25	20,00	20,00
35,50	3,50	8,77	4,75	350,00	0,00	0,00	0,00	0,00

46.75N 8.25E (f-2 IV)

H	ρ	VP	VS	Z	ΔV_S+	ΔV_S-	$\Delta H+$	$\Delta H-$
0,50	2,38	4,58	2,65	0,50	0,00	0,00	0,00	0,00
0,50	2,38	4,67	2,70	1,00	0,00	0,00	0,00	0,00
1,00	2,48	4,93	2,85	2,00	0,00	0,00	0,00	0,00
1,00	2,68	4,93	2,85	3,00	0,00	0,00	0,00	0,00
1,00	2,67	5,01	2,90	4,00	0,00	0,00	0,00	0,00
16,00	2,73	5,55	3,20	20,00	0,03	0,03	1,00	1,00
30,00	3,04	8,18	4,15	50,00	0,00	0,10	5,00	5,00
45,00	3,26	8,32	4,45	95,00	0,00	0,15	12,50	12,50
110,00	3,24	8,24	4,55	205,00	0,00	0,20	20,00	20,00
110,00	3,37	8,63	4,75	315,00	0,00	0,25	20,00	20,00
35,00	3,48	8,76	4,75	350,00	0,00	0,00	0,00	0,00

46.75N 9.75E (f-1 I)

H	ρ	VP	VS	Z	ΔV_S+	ΔV_S-	$\Delta H+$	$\Delta H-$
0,10	2,06	2,08	1,20	0,10	0,00	0,00	0,00	0,00
0,90	2,51	4,33	2,50	1,00	0,00	0,00	0,00	0,00
1,50	2,51	4,50	2,60	2,50	0,00	0,00	0,00	0,00
2,50	2,51	5,35	3,10	5,00	0,00	0,00	0,00	0,00
1,00	2,51	5,35	3,10	6,00	0,00	0,00	0,00	0,00
7,00	2,57	5,35	3,10	13,00	0,08	0,08	2,00	2,00
15,00	2,83	6,57	3,80	28,00	0,15	0,15	5,00	5,00
30,00	3,10	7,96	4,35	58,00	0,15	0,15	12,50	12,50
100,00	3,21	8,29	4,55	158,0	0,15	0,20	17,50	17,50
110,00	3,22	8,53	4,60	268,0	0,00	0,20	20,00	20,00
82,00	3,37	8,80	4,75	350,0	0,00	0,00	0,00	0,00

46.25N 9.75E (f-1 II)

H	ρ	VP	VS	Z	ΔV_S+	ΔV_S-	$\Delta H+$	$\Delta H-$
0,10	2,07	2,08	1,20	0,10	0,00	0,00	0,00	0,00
0,90	2,52	4,33	2,50	1,00	0,00	0,00	0,00	0,00
1,00	2,52	4,50	2,60	2,00	0,00	0,00	0,00	0,00
3,00	2,52	5,35	3,10	5,00	0,00	0,00	0,00	0,00
1,00	2,52	5,35	3,10	6,00	0,00	0,00	0,00	0,00
7,00	2,59	5,62	3,25	13,0	0,10	0,10	2,00	2,00
15,00	2,86	6,50	3,75	28,0	0,18	0,18	5,00	5,00
30,00	3,13	8,14	4,45	58,0	0,05	0,15	12,50	12,50
100,00	3,23	8,16	4,50	158	0,20	0,20	17,50	17,50
110,00	3,24	8,53	4,60	268	0,00	0,20	20,00	20,00
82,00	3,40	8,85	4,75	350	0,00	0,00	0,00	0,00

46.25N 9.25E (f-1 III)

H	ρ	VP	VS	Z	ΔV_S+	ΔV_S-	$\Delta H+$	$\Delta H-$
0,10	2,09	2,08	1,20	0,10	0,00	0,00	0,00	0,00
0,90	2,54	4,33	2,50	1,00	0,00	0,00	0,00	0,00
2,50	2,54	4,50	2,60	3,50	0,00	0,00	0,00	0,00
1,50	2,54	5,35	3,10	5,00	0,00	0,00	0,00	0,00
1,00	2,54	5,35	3,10	6,00	0,00	0,00	0,00	0,00
7,00	2,61	5,62	3,25	13,00	0,10	0,15	2,00	2,00
15,00	2,88	6,57	3,80	28,00	0,15	0,15	5,00	5,00
30,00	3,15	8,17	4,50	58,00	0,05	0,15	12,50	12,50
100,00	3,24	8,12	4,45	158,0	0,20	0,15	17,50	17,50
110,00	3,24	8,53	4,60	268,0	0,00	0,20	20,00	20,00
82,00	3,40	8,84	4,75	350,0	0,00	0,00	0,00	0,00

46.75N 9.25E (f-1 IV)

H	ρ	VP	VS	Z	ΔV_S+	ΔV_S-	$\Delta H+$	$\Delta H-$
0,10	2,06	2,08	1,20	0,10	0,00	0,00	0,00	0,00
0,90	2,51	4,33	2,50	1,00	0,00	0,00	0,00	0,00
2,00	2,51	4,50	2,60	3,00	0,00	0,00	0,00	0,00
2,00	2,51	5,35	3,10	5,00	0,00	0,00	0,00	0,00
1,00	2,51	5,35	3,10	6,00	0,00	0,00	0,00	0,00
7,00	2,58	5,62	3,25	13,0	0,13	0,13	2,00	2,00
15,00	2,84	6,57	3,80	28,0	0,13	0,13	5,00	5,00
30,00	3,11	8,05	4,45	58,0	0,05	0,15	12,50	12,50
100,00	3,21	8,29	4,55	158	0,15	0,20	17,50	17,50
110,00	3,23	8,48	4,60	268	0,00	0,20	20,00	20,00
82,00	3,38	8,76	4,75	350	0,00	0,00	0,00	0,00

46.75N 10.75E (f0 I)

H	ρ	VP	VS	Z	ΔV_S+	ΔV_S-	$\Delta H+$	$\Delta H-$
0,50	2,46	3,98	2,30	0,50	0,00	0,00	0,00	0,00
1,50	2,46	4,33	2,50	2,00	0,00	0,00	0,00	0,00
0,50	2,46	5,19	3,00	2,50	0,00	0,00	0,00	0,00
1,00	2,49	5,36	3,10	3,50	0,00	0,00	0,00	0,00
1,00	2,51	5,36	3,10	4,50	0,00	0,00	0,00	0,00
10,00	2,55	5,79	3,35	14,50	0,08	0,08	2,00	2,00
20,00	2,69	6,40	3,70	34,50	0,15	0,15	5,00	5,00
30,00	3,23	7,97	4,35	64,50	0,20	0,00	15,00	15,00
105,00	3,22	8,24	4,55	169,50	0,15	0,15	20,00	20,00
60,00	3,30	8,31	4,35	229,50	0,00	0,20	20,00	20,00
120,50	3,42	8,83	4,75	350,00	0,00	0,00	0,00	0,00

46.25N 10.75E (f0 II)

H	ρ	VP	VS	Z	ΔV_S+	ΔV_S-	$\Delta H+$	$\Delta H-$
0,50	2,48	3,98	2,30	0,50	0,00	0,00	0,00	0,00
1,50	2,48	4,33	2,50	2,00	0,00	0,00	0,00	0,00
0,50	2,47	4,85	2,80	2,50	0,00	0,00	0,00	0,00
1,00	2,50	5,02	2,90	3,50	0,00	0,00	0,00	0,00
1,00	2,52	5,02	2,90	4,50	0,00	0,00	0,00	0,00
10,00	2,57	5,89	3,40	14,50	0,05	0,05	2,50	2,50
20,00	2,71	6,40	3,70	34,50	0,15	0,15	5,00	5,00
30,00	3,26	7,96	4,35	64,50	0,20	0,00	15,00	15,00
105,00	3,25	8,12	4,45	169,50	0,20	0,15	20,00	20,00
60,00	3,31	8,23	4,30	229,50	0,00	0,25	25,00	25,00
120,50	3,44	8,85	4,75	350,00	0,00	0,00	0,00	0,00

46.25N 10.25E (f0 III)

H	ρ	VP	VS	Z	ΔV_S+	ΔV_S-	$\Delta H+$	$\Delta H-$
0,50	2,48	3,98	2,30	0,50	0,00	0,00	0,00	0,00
1,00	2,47	4,33	2,50	1,50	0,00	0,00	0,00	0,00
1,00	2,47	5,19	3,00	2,50	0,00	0,00	0,00	0,00
1,00	2,50	5,36	3,10	3,50	0,00	0,00	0,00	0,00
1,00	2,52	5,36	3,10	4,50	0,00	0,00	0,00	0,00
10,00	2,57	5,80	3,35	14,50	0,10	0,10	2,00	2,00
20,00	2,71	6,40	3,70	34,50	0,10	0,15	5,00	5,00
30,00	3,25	8,02	4,40	64,50	0,20	0,05	15,00	15,00
105,00	3,24	8,20	4,50	169,50	0,20	0,20	20,00	20,00
60,00	3,30	8,30	4,35	229,50	0,00	0,20	25,00	25,00
120,50	3,44	8,86	4,75	350,00	0,00	0,00	0,00	0,00

46.75N 10.25E (f0 IV)

H	ρ	VP	VS	Z	ΔV_S+	ΔV_S-	$\Delta H+$	$\Delta H-$
0,50	2,46	3,98	2,30	0,50	0,00	0,00	0,00	0,00
1,50	2,46	4,33	2,50	2,00	0,00	0,00	0,00	0,00
0,50	2,46	4,33	2,50	2,50	0,00	0,00	0,00	0,00
1,00	2,48	5,36	3,10	3,50	0,00	0,00	0,00	0,00
1,00	2,51	5,36	3,10	4,50	0,00	0,00	0,00	0,00
5,00	2,50	5,45	3,15	9,50	0,10	0,10	2,50	2,50
25,00	2,67	6,40	3,70	34,50	0,15	0,15	5,00	5,00
30,00	3,23	7,97	4,35	64,50	0,20	0,00	15,00	15,00
105,00	3,21	8,26	4,55	169,50	0,15	0,15	20,00	20,00
60,00	3,29	8,34	4,35	229,50	0,00	0,20	20,00	20,00
120,50	3,42	8,83	4,75	350,00	0,00	0,00	0,00	0,00

46.75N 11.75E (f1 I)

H	ρ	VP	VS	Z	ΔV_S+	ΔV_S-	$\Delta H+$	$\Delta H-$
0,50	2,43	3,98	2,30	0,50	0,00	0,00	0,00	0,00
1,00	2,52	4,33	2,50	1,50	0,00	0,00	0,00	0,00
1,00	2,52	4,84	2,80	2,50	0,00	0,00	0,00	0,00
1,00	2,52	5,36	3,10	3,50	0,00	0,00	0,00	0,00
1,50	2,52	5,36	3,10	5,00	0,00	0,00	0,00	0,00
8,00	2,59	5,54	3,20	13,00	0,10	0,10	3,00	3,00
27,00	2,93	6,49	3,75	40,00	0,13	0,13	4,50	4,50
25,00	3,21	8,01	4,50	65,00	0,15	0,00	12,50	12,50
105,00	3,25	8,18	4,50	170,0	0,15	0,20	20,00	20,00
60,00	3,32	8,31	4,55	230,0	0,05	0,20	25,00	25,00
120,00	3,43	8,84	4,75	350,0	0,00	0,00	0,00	0,00

46.25N 11.75E (f1 II)

H	ρ	VP	VS	Z	ΔV_S+	ΔV_S-	$\Delta H+$	$\Delta H-$
0,50	2,44	3,98	2,30	0,50	0,00	0,00	0,00	0,00
1,50	2,53	4,33	2,50	2,00	0,00	0,00	0,00	0,00
0,50	2,53	4,84	2,80	2,50	0,00	0,00	0,00	0,00
1,00	2,53	5,02	2,90	3,50	0,00	0,00	0,00	0,00
1,50	2,53	5,02	2,90	5,00	0,00	0,00	0,00	0,00
10,00	2,62	5,71	3,30	15,0	0,05	0,05	2,50	2,50
20,00	2,90	6,40	3,70	35,0	0,15	0,15	5,00	5,00
30,00	3,23	8,02	4,40	65,0	0,10	0,15	15,00	15,00
105,00	3,28	8,04	4,40	170	0,15	0,10	20,00	20,00
110,00	3,39	8,46	4,65	280	0,00	0,20	25,00	25,00
70,00	3,45	8,77	4,75	350	0,00	0,00	0,00	0,00

46.25N 11.25E (f1 III)

H	ρ	VP	VS	Z	ΔV_S+	ΔV_S-	$\Delta H+$	$\Delta H-$
0,50	2,43	3,98	2,30	0,50	0,00	0,00	0,00	0,00
1,50	2,52	4,33	2,50	2,00	0,00	0,00	0,00	0,00
0,50	2,52	4,84	2,80	2,50	0,00	0,00	0,00	0,00
1,00	2,52	5,02	2,90	3,50	0,00	0,00	0,00	0,00
1,50	2,52	5,02	2,90	5,00	0,00	0,00	0,00	0,00
10,00	2,61	5,71	3,30	15,0	0,05	0,05	2,50	2,50
20,00	2,89	6,40	3,70	35,0	0,15	0,15	5,00	5,00
30,00	3,22	7,96	4,35	65,0	0,15	0,15	15,00	15,00
105,00	3,27	8,05	4,40	170	0,20	0,10	20,00	20,00
110,00	3,39	8,47	4,65	280	0,00	0,20	25,00	25,00
70,00	3,45	8,82	4,75	350	0,00	0,00	0,00	0,00

46.75N 11.25E (f1 IV)

H	ρ	VP	VS	Z	ΔV_S+	ΔV_S-	$\Delta H+$	$\Delta H-$
0,50	2,43	3,98	2,30	0,50	0,00	0,00	0,00	0,00
1,00	2,52	4,33	2,50	1,50	0,00	0,00	0,00	0,00
0,50	2,52	4,84	2,80	2,00	0,00	0,00	0,00	0,00
1,50	2,52	5,36	3,10	3,50	0,00	0,00	0,00	0,00
1,50	2,52	5,36	3,10	5,00	0,00	0,00	0,00	0,00
8,00	2,59	5,54	3,20	13,00	0,08	0,08	2,50	2,50
27,00	2,92	6,49	3,75	40,00	0,13	0,13	4,50	4,50
25,00	3,19	8,02	4,40	65,00	0,20	0,00	12,50	12,50
105,00	3,23	8,23	4,50	170,0	0,20	0,20	20,00	20,00
60,00	3,31	8,32	4,60	230,0	0,00	0,20	25,00	25,00
120,00	3,43	8,84	4,75	350,0	0,00	0,00	0,00	0,00

46.75N 12.75E (f2 I)

H	ρ	VP	VS	Z	ΔV_S+	ΔV_S-	$\Delta H+$	$\Delta H-$
2,00	2,55	3,98	2,30	2,00	0,00	0,00	0,00	0,00
0,50	2,55	4,39	2,54	2,50	0,00	0,00	0,00	0,00
0,50	2,55	4,58	2,65	3,00	0,00	0,00	0,00	0,00
0,50	2,55	4,99	2,89	3,50	0,00	0,00	0,00	0,00
1,50	2,55	5,54	3,20	5,00	0,00	0,00	0,00	0,00
7,00	2,66	5,54	3,20	12,00	0,08	0,08	2,00	2,00
20,00	2,85	6,23	3,60	32,00	0,13	0,13	7,50	7,50
35,00	3,29	8,02	4,40	67,00	0,10	0,15	10,00	10,00
65,00	3,28	8,12	4,45	132,0	0,15	0,10	20,00	20,00
110,00	3,26	8,37	4,60	242,0	0,10	0,20	25,00	25,00
108,00	3,36	8,83	4,75	350,0	0,00	0,00	0,00	0,00

46.25N 12.75E (f2 II)

H	ρ	VP	VS	Z	ΔV_S+	ΔV_S-	$\Delta H+$	$\Delta H-$
0,50	2,55	3,81	2,20	0,50	0,00	0,00	0,00	0,00
1,50	2,55	3,98	2,30	2,00	0,00	0,00	0,00	0,00
1,00	2,55	4,33	2,50	3,00	0,00	0,00	0,00	0,00
0,50	2,55	4,41	2,55	3,50	0,00	0,00	0,00	0,00
1,50	2,55	4,99	2,89	5,00	0,00	0,00	0,00	0,00
21,00	2,77	6,05	3,50	26,0	0,08	0,08	3,50	3,50
28,00	3,22	8,05	4,30	54,0	0,00	0,15	7,00	7,00
35,00	3,30	8,01	4,40	89,0	0,20	0,00	10,00	10,00
65,00	3,30	8,10	4,45	154	0,20	0,15	20,00	20,00
60,00	3,28	8,20	4,35	214	0,00	0,20	25,00	25,00
136,00	3,36	8,73	4,75	350	0,00	0,00	0,00	0,00

46.25N 12.25E (f2 III)

H	ρ	VP	VS	Z	ΔV_S+	ΔV_S-	$\Delta H+$	$\Delta H-$
0,50	2,56	3,80	2,20	0,50	0,00	0,00	0,00	0,00
1,50	2,56	3,98	2,30	2,00	0,00	0,00	0,00	0,00
1,00	2,56	4,33	2,50	3,00	0,00	0,00	0,00	0,00
0,50	2,56	4,41	2,55	3,50	0,00	0,00	0,00	0,00
1,50	2,56	4,99	2,89	5,00	0,00	0,00	0,00	0,00
21,00	2,78	6,05	3,50	26,00	0,08	0,08	3,50	3,50
28,00	3,23	8,09	4,30	54,00	0,00	0,15	7,00	7,00
55,00	3,31	7,97	4,40	109,0	0,20	0,00	10,00	10,00
65,00	3,30	8,03	4,30	174,0	0,00	0,20	20,00	20,00
110,00	3,28	8,44	4,60	284,0	0,15	0,20	25,00	25,00
66,00	3,45	8,71	4,75	350,0	0,00	0,00	0,00	0,00

46.75N 12.25E (f2 IV)

H	ρ	VP	VS	Z	ΔV_S+	ΔV_S-	$\Delta H+$	$\Delta H-$
2,00	2,55	3,98	2,30	2,00	0,00	0,00	0,00	0,00
0,50	2,55	4,39	2,54	2,50	0,00	0,00	0,00	0,00
0,50	2,55	4,58	2,65	3,00	0,00	0,00	0,00	0,00
0,50	2,55	4,99	2,89	3,50	0,00	0,00	0,00	0,00
1,50	2,55	5,54	3,20	5,00	0,00	0,00	0,00	0,00
7,00	2,65	5,54	3,20	12,0	0,08	0,08	2,00	2,00
20,00	2,85	6,23	3,60	32,0	0,13	0,13	7,50	7,50
35,00	3,29	8,02	4,40	67,0	0,10	0,15	10,00	10,00
65,00	3,28	8,11	4,45	132	0,15	0,10	20,00	20,00
110,00	3,26	8,35	4,60	242	0,10	0,20	25,00	25,00
108,00	3,36	8,82	4,75	350	0,00	0,00	0,00	0,00

46.75N 13.75E (f3 I)

H	ρ	VP	VS	Z	ΔV_S+	ΔV_S-	$\Delta H+$	$\Delta H-$
0,50	2,34	3,81	2,20	0,50	0,00	0,00	0,00	0,00
1,50	2,49	3,98	2,30	2,00	0,00	0,00	0,00	0,00
1,00	2,49	5,37	3,10	3,00	0,00	0,00	0,00	0,00
1,00	2,49	5,45	3,15	4,00	0,00	0,00	0,00	0,00
3,00	2,49	5,54	3,20	7,00	0,00	0,00	0,00	0,00
17,00	2,68	6,06	3,50	24,00	0,05	0,05	2,50	2,50
30,00	3,01	7,10	4,10	54,00	0,00	0,15	7,50	7,50
50,00	3,29	8,02	4,40	104,0	0,20	0,15	12,50	12,50
60,00	3,28	8,17	4,50	164,0	0,05	0,25	20,00	20,00
110,00	3,31	8,52	4,65	274,0	0,05	0,25	20,00	20,00
76,00	3,45	8,74	4,75	350,0	0,00	0,00	0,00	0,00

46.25N 13.75E (f3 II)

H	ρ	VP	VS	Z	ΔV_S+	ΔV_S-	$\Delta H+$	$\Delta H-$
0,50	2,34	5,77	2,30	0,50	0,00	0,00	0,00	0,00
1,00	2,49	5,82	2,40	1,50	0,00	0,00	0,00	0,00
1,50	2,49	5,89	2,45	3,00	0,00	0,00	0,00	0,00
1,00	2,49	5,94	2,55	4,00	0,00	0,00	0,00	0,00
4,00	2,49	6,13	3,30	8,00	0,00	0,00	0,00	0,00
12,00	2,63	6,70	3,30	20,00	0,13	0,13	3,00	3,00
30,00	2,94	8,12	4,00	50,00	0,10	0,20	7,50	7,50
50,00	3,29	8,10	4,45	100,0	0,20	0,20	12,50	12,50
100,00	3,29	8,18	4,35	200,0	0,20	0,20	20,00	20,00
70,00	3,35	8,40	4,45	270,0	0,25	0,25	20,00	20,00
80,00	3,46	8,68	4,75	350,0	0,00	0,00	0,00	0,00

46.25N 13.25E (f3 III)

H	ρ	VP	VS	Z	ΔV_S+	ΔV_S-	$\Delta H+$	$\Delta H-$
0,50	2,33	3,81	2,20	0,50	0,00	0,00	0,00	0,00
1,50	2,48	3,98	2,30	2,00	0,00	0,00	0,00	0,00
1,00	2,48	4,33	2,50	3,00	0,00	0,00	0,00	0,00
1,00	2,48	4,41	2,55	4,00	0,00	0,00	0,00	0,00
2,00	2,48	5,02	2,90	6,00	0,00	0,00	0,00	0,00
15,00	2,62	5,88	3,40	21,00	0,10	0,10	5,00	5,00
30,00	2,95	6,92	4,00	51,00	0,10	0,20	7,50	7,50
60,00	3,28	8,06	4,45	111,0	0,20	0,15	15,00	15,00
100,00	3,28	8,22	4,50	211,0	0,10	0,20	20,00	20,00
70,00	3,38	8,51	4,70	281,0	0,00	0,25	20,00	20,00
69,00	3,46	8,73	4,75	350,0	0,00	0,00	0,00	0,00

46.75N 13.25E (f3 IV)

H	ρ	VP	VS	Z	ΔV_S+	ΔV_S-	$\Delta H+$	$\Delta H-$
0,50	2,34	3,81	2,20	0,50	0,00	0,00	0,00	0,00
1,50	2,49	3,98	2,30	2,00	0,00	0,00	0,00	0,00
1,00	2,49	4,15	2,40	3,00	0,00	0,00	0,00	0,00
1,00	2,49	5,45	3,15	4,00	0,00	0,00	0,00	0,00
3,00	2,49	5,54	3,20	7,00	0,00	0,00	0,00	0,00
17,00	2,67	5,88	3,40	24,0	0,10	0,10	2,50	2,50
30,00	3,00	7,09	4,10	54,0	0,00	0,20	7,50	7,50
50,00	3,29	8,04	4,45	104	0,20	0,20	12,50	12,50
60,00	3,27	8,18	4,50	164	0,05	0,25	20,00	20,00
110,00	3,31	8,53	4,70	274	0,00	0,25	20,00	20,00
76,00	3,44	8,79	4,75	350	0,00	0,00	0,00	0,00

46.75N 14.75E (f4 I)

H	ρ	VP	VS	Z	ΔV_S+	ΔV_S-	$\Delta H+$	$\Delta H-$
1,00	2,50	4,06	2,35	1,00	0,00	0,00	0,00	0,00
1,00	2,50	4,06	2,35	2,00	0,00	0,00	0,00	0,00
0,50	2,50	4,06	2,35	2,50	0,00	0,00	0,00	0,00
1,00	2,57	5,62	3,25	3,50	0,00	0,00	0,00	0,00
0,50	2,70	5,62	3,25	4,00	0,00	0,00	0,00	0,00
10,00	2,80	5,45	3,15	14,00	0,05	0,05	2,00	2,00
24,00	2,90	6,67	3,85	38,00	0,15	0,15	5,00	5,00
35,00	3,09	7,96	4,40	73,00	0,20	0,15	12,50	12,50
105,00	3,18	8,13	4,50	178,0	0,10	0,20	20,00	20,00
65,00	3,28	8,35	4,60	243,0	0,00	0,20	22,50	22,50
107,00	3,47	8,70	4,75	350,0	0,00	0,00	0,00	0,00

46.25N 14.75E (f4 II)

H	ρ	VP	VS	Z	ΔV_S+	ΔV_S-	$\Delta H+$	$\Delta H-$
0,50	2,50	3,98	2,30	0,50	0,00	0,00	0,00	0,00
0,50	2,50	3,98	2,30	1,00	0,00	0,00	0,00	0,00
1,00	2,50	4,25	2,45	2,00	0,00	0,00	0,00	0,00
0,50	2,50	4,40	2,55	2,50	0,00	0,00	0,00	0,00
0,50	2,50	4,40	2,55	3,00	0,00	0,00	0,00	0,00
10,00	2,79	5,45	3,15	13,0	0,05	0,05	2,50	2,50
28,00	2,92	6,75	3,90	41,0	0,15	10,00	6,00	6,00
50,00	3,12	7,95	4,40	91,0	0,15	0,05	10,00	10,00
60,00	3,19	8,07	4,45	151	0,15	0,15	20,00	20,00
60,00	3,24	8,17	4,20	211	0,00	0,20	25,00	25,00
139,00	3,44	8,70	4,75	350	0,00	0,00	0,00	0,00

46.25N 14.25E (f4 III)

H	ρ	VP	VS	Z	ΔV_S+	ΔV_S-	$\Delta H+$	$\Delta H-$
0,50	2,50	3,98	2,30	0,50	0,00	0,00	0,00	0,00
0,50	2,50	4,06	2,35	1,00	0,00	0,00	0,00	0,00
1,00	2,50	4,25	2,45	2,00	0,00	0,00	0,00	0,00
1,00	2,50	4,25	2,45	3,00	0,00	0,00	0,00	0,00
0,50	2,65	4,40	2,55	3,50	0,00	0,00	0,00	0,00
18,00	2,84	5,80	3,35	21,50	0,03	0,03	1,50	1,50
30,00	2,99	7,19	4,15	51,50	0,00	0,15	7,50	7,50
30,00	3,12	8,06	4,45	81,50	0,15	0,15	10,00	10,00
100,00	3,19	8,16	4,50	181,50	0,10	0,20	20,00	20,00
60,00	3,29	8,26	4,55	241,50	0,20	0,25	25,00	25,00
108,50	3,48	8,66	4,75	350,00	0,00	0,00	0,00	0,00

46.75N 14.25E (f4 IV)

H	ρ	VP	VS	Z	ΔV_S+	ΔV_S-	$\Delta H+$	$\Delta H-$
1,00	2,50	4,06	2,35	1,00	0,00	0,00	0,00	0,00
1,00	2,50	4,06	2,35	2,00	0,00	0,00	0,00	0,00
0,50	2,50	5,35	3,10	2,50	0,00	0,00	0,00	0,00
1,00	2,58	5,45	3,15	3,50	0,00	0,00	0,00	0,00
0,50	2,71	5,45	3,15	4,00	0,00	0,00	0,00	0,00
12,00	2,82	5,45	3,15	16,0	0,08	0,08	2,00	2,00
24,00	2,92	6,75	3,90	40,0	0,13	0,13	5,00	5,00
60,00	3,14	7,98	4,35	100	0,10	0,15	12,50	12,50
65,00	3,18	8,15	4,50	165	0,10	0,20	20,00	20,00
65,00	3,26	8,34	4,55	230	0,10	0,25	22,50	22,50
120,00	3,45	8,72	4,75	350	0,00	0,00	0,00	0,00

45.75N 6.75E (e-4 I)

H	ρ	VP	VS	Z	ΔV_S+	ΔV_S-	$\Delta H+$	$\Delta H-$
0,50	2,07	4,40	2,55	0,50	0,00	0,00	0,00	0,00
0,50	2,56	4,58	2,65	1,00	0,00	0,00	0,00	0,00
1,00	2,56	4,95	2,85	2,00	0,00	0,00	0,00	0,00
1,50	2,56	5,54	3,20	3,50	0,00	0,00	0,00	0,00
1,50	2,56	5,54	3,20	5,00	0,00	0,00	0,00	0,00
10,00	2,74	5,02	2,90	15,00	0,03	0,03	0,50	0,50
18,00	2,90	7,01	4,05	33,00	0,05	0,05	3,50	3,50
60,00	3,02	8,06	4,40	93,00	0,05	0,05	12,50	12,50
100,00	3,10	8,30	4,55	193,0	0,15	0,05	17,50	17,50
110,00	3,23	8,66	4,55	303,0	0,00	0,20	22,50	22,50
47,00	3,40	8,73	4,75	350,0	0,00	0,00	0,00	0,00

45.25N 6.75E (e-4 II)

H	ρ	VP	VS	Z	ΔV_S+	ΔV_S-	$\Delta H+$	$\Delta H-$
0,50	2,07	4,00	2,30	0,50	0,00	0,00	0,00	0,00
0,50	2,56	4,58	2,65	1,00	0,00	0,00	0,00	0,00
1,00	2,56	5,36	3,10	2,00	0,00	0,00	0,00	0,00
1,50	2,56	5,54	3,20	3,50	0,00	0,00	0,00	0,00
1,50	2,56	5,54	3,20	5,00	0,00	0,00	0,00	0,00
9,00	2,72	4,85	2,80	14,00	0,03	0,03	0,50	0,50
21,00	2,91	7,01	4,05	35,00	0,05	0,05	4,00	4,00
85,00	3,04	8,17	4,45	120,0	0,00	0,05	12,50	12,50
65,00	3,11	8,31	4,70	185,0	0,15	0,00	17,50	17,50
110,00	3,22	8,66	4,15	295,0	0,00	0,15	22,50	22,50
55,00	3,42	8,76	4,75	350,0	0,00	0,00	0,00	0,00

45.25N 6.25E (e-4 III)

H	ρ	VP	VS	Z	ΔV_S+	ΔV_S-	$\Delta H+$	$\Delta H-$
0,50	2,07	4,40	2,55	0,50	0,00	0,00	0,00	0,00
0,50	2,56	4,58	2,65	1,00	0,00	0,00	0,00	0,00
1,00	2,56	4,93	2,85	2,00	0,00	0,00	0,00	0,00
1,50	2,56	5,53	3,20	3,50	0,00	0,00	0,00	0,00
1,50	2,56	5,53	3,20	5,00	0,00	0,00	0,00	0,00
10,00	2,75	5,01	2,90	15,0	0,03	0,03	0,50	0,50
18,00	2,90	7,00	4,05	33,0	0,05	0,05	3,50	3,50
85,00	3,03	8,07	4,45	118	0,05	0,05	12,5	12,5
65,00	3,08	8,29	4,50	183	0,10	0,05	17,5	17,5
110,00	3,19	8,67	4,55	293	0,00	0,20	22,50	22,50
57,00	3,39	8,77	4,75	350	0,00	0,00	0,00	0,00

45.75N 6.25E (e-4 IV)								
H	ρ	VP	VS	Z	ΔV_S+	ΔV_S-	$\Delta H+$	$\Delta H-$
0,50	2,08	4,40	2,55	0,50	0,00	0,00	0,00	0,00
0,50	2,57	4,58	2,65	1,00	0,00	0,00	0,00	0,00
1,00	2,57	4,58	2,65	2,00	0,00	0,00	0,00	0,00
0,50	2,57	4,93	2,85	2,50	0,00	0,00	0,00	0,00
2,50	2,57	5,53	3,20	5,00	0,00	0,00	0,00	0,00
7,00	2,72	4,76	2,75	12,00	0,05	0,05	1,00	1,00
20,00	2,90	6,75	3,90	32,00	0,10	0,10	4,00	4,00
85,00	3,04	8,06	4,40	117,00	0,05	0,00	10,00	10,00
65,00	3,10	8,27	4,55	182,00	0,10	0,05	17,50	17,50
110,00	3,20	8,64	4,55	292,00	0,00	0,20	22,50	22,50
58,00	3,39	8,76	4,75	350,00	0,00	0,00	0,00	0,00

45.75N 7.75E (e-3 I)

H	ρ	VP	VS	Z	ΔV_S+	ΔV_S-	$\Delta H+$	$\Delta H-$
0,10	2,12	2,10	1,20	0,10	0,00	0,00	0,00	0,00
1,40	2,67	4,60	2,65	1,50	0,00	0,00	0,00	0,00
1,00	2,67	5,20	3,00	2,50	0,00	0,00	0,00	0,00
1,50	2,68	5,54	3,20	4,00	0,00	0,00	0,00	0,00
2,00	2,68	5,70	3,30	6,00	0,00	0,00	0,00	0,00
5,00	2,83	4,60	2,65	11,00	0,08	0,08	1,50	1,50
26,00	2,97	6,66	3,85	37,00	0,10	0,10	4,00	4,00
80,00	3,31	8,27	4,55	117,0	0,15	0,15	12,50	12,50
45,00	3,27	8,29	4,35	162,0	0,00	0,15	27,50	27,50
110,00	3,26	8,67	4,75	272,0	0,00	0,20	27,50	27,50
78,00	3,46	8,78	4,75	350,0	0,00	0,00	0,00	0,00

45.25N 7.75E (e-3 II)

H	ρ	VP	VS	Z	ΔV_S+	ΔV_S-	$\Delta H+$	$\Delta H-$
0,50	2,54	2,60	1,50	0,50	0,00	0,00	0,00	0,00
0,50	2,65	3,50	2,02	1,00	0,00	0,00	0,00	0,00
1,50	2,65	5,20	3,00	2,50	0,00	0,00	0,00	0,00
1,50	2,65	5,54	3,20	4,00	0,00	0,00	0,00	0,00
2,00	2,65	5,70	3,30	6,00	0,00	0,00	0,00	0,00
8,00	2,82	4,94	2,85	14,00	0,08	0,08	1,50	1,50
30,00	3,00	7,91	4,25	44,00	0,00	0,15	5,00	5,00
80,00	3,29	8,29	4,55	124,00	0,15	0,15	12,50	12,50
45,00	3,27	8,31	4,35	169,00	0,00	0,15	27,50	27,50
110,00	3,30	8,67	4,75	279,00	0,00	0,20	27,50	27,50
71,00	3,51	8,79	4,75	350,00	0,00	0,00	0,00	0,00

45.25N 7.25E (e-3 III)

H	ρ	VP	VS	Z	ΔV_S+	ΔV_S-	$\Delta H+$	$\Delta H-$
0,10	2,10	2,08	1,20	0,10	0,00	0,00	0,00	0,00
0,40	2,65	4,58	2,65	0,50	0,00	0,00	0,00	0,00
1,50	2,65	5,20	3,00	2,00	0,00	0,00	0,00	0,00
2,00	2,65	5,55	3,20	4,00	0,00	0,00	0,00	0,00
2,00	2,65	5,70	3,30	6,00	0,00	0,00	0,00	0,00
5,00	2,80	4,50	2,60	11,0	0,05	0,05	1,00	1,00
16,00	2,93	6,30	3,65	27,0	0,10	0,10	5,00	5,00
55,00	3,21	8,38	4,55	82,0	0,00	0,15	12,50	12,50
100,00	3,25	8,35	4,60	182	0,10	0,20	27,50	27,50
110,00	3,29	8,66	4,75	292	0,00	0,20	27,50	27,50
58,00	3,48	8,74	4,75	350	0,00	0,00	0,00	0,00

45.75N 7.25E (e-3 IV)

H	ρ	VP	VS	Z	ΔV_S+	ΔV_S-	$\Delta H+$	$\Delta H-$
0,10	2,07	2,08	1,20	0,10	0,00	0,00	0,00	0,00
0,90	2,62	4,58	2,65	1,00	0,00	0,00	0,00	0,00
1,00	2,62	5,20	3,00	2,00	0,00	0,00	0,00	0,00
2,00	2,62	5,55	3,20	4,00	0,00	0,00	0,00	0,00
2,00	2,62	5,70	3,30	6,00	0,00	0,00	0,00	0,00
5,00	2,77	4,50	2,60	11,00	0,05	0,05	1,00	1,00
16,00	2,89	6,30	3,65	27,00	0,10	0,10	5,00	5,00
55,00	3,17	8,23	4,50	82,00	0,00	0,10	12,50	12,50
100,00	3,24	8,31	4,55	182,00	0,15	0,20	27,50	27,50
110,00	3,26	8,69	4,75	292,00	0,00	0,20	27,50	27,50
58,00	3,45	8,75	4,75	350,00	0,00	0,00	0,00	0,00

45.75N 8.75E (e-2 I)

H	ρ	VP	VS	Z	ΔV_S+	ΔV_S-	$\Delta H+$	$\Delta H-$
1,00	2,60	4,20	2,43	1,00	0,00	0,00	0,00	0,00
1,00	2,60	4,20	2,43	2,00	0,00	0,00	0,00	0,00
1,00	2,60	4,20	2,43	3,00	0,00	0,00	0,00	0,00
1,00	2,74	4,93	2,85	4,00	0,00	0,00	0,00	0,00
2,00	2,74	4,93	2,85	6,00	0,00	0,00	0,00	0,00
10,00	2,74	5,28	3,05	16,00	0,08	0,08	2,00	2,00
30,00	2,99	7,10	4,10	46,00	0,00	0,15	5,00	5,00
50,00	3,28	8,06	4,50	96,00	0,20	0,00	12,50	12,50
60,00	3,26	8,11	4,45	156,0	0,00	0,20	20,00	20,00
110,00	3,28	8,54	4,70	266,0	0,00	0,25	20,00	20,00
84,00	3,46	8,88	4,75	350,0	0,00	0,00	0,00	0,00

45.25N 8.75E (e-2 II)

H	ρ	VP	VS	Z	ΔV_S+	ΔV_S-	$\Delta H+$	$\Delta H-$
1,00	2,57	2,94	1,70	1,00	0,00	0,00	0,00	0,00
1,00	2,57	3,45	2,00	2,00	0,00	0,00	0,00	0,00
1,00	2,57	3,45	2,00	3,00	0,00	0,00	0,00	0,00
1,00	2,71	3,45	2,00	4,00	0,00	0,00	0,00	0,00
2,00	2,70	3,45	2,00	6,00	0,00	0,00	0,00	0,00
10,00	2,70	6,75	3,90	16,00	0,10	0,10	3,50	3,50
20,00	2,88	6,65	3,85	36,00	0,15	0,15	5,00	5,00
25,00	3,14	8,17	4,50	61,00	0,15	0,15	12,50	12,50
100,00	3,23	8,12	4,45	161,0	0,10	0,20	20,00	20,00
110,00	3,33	8,55	4,70	271,0	0,00	0,25	20,00	20,00
79,00	3,52	8,87	4,75	350,0	0,00	0,00	0,00	0,00

45.25N 8.25E (e-2 III)

H	ρ	VP	VS	Z	ΔV_S+	ΔV_S-	$\Delta H+$	$\Delta H-$
1,00	2,57	2,94	1,70	1,00	0,00	0,00	0,00	0,00
1,00	2,57	3,45	2,00	2,00	0,00	0,00	0,00	0,00
1,00	2,57	3,45	2,00	3,00	0,00	0,00	0,00	0,00
2,00	2,71	3,45	2,00	5,00	0,00	0,00	0,00	0,00
1,00	2,71	5,35	3,10	6,00	0,00	0,00	0,00	0,00
10,00	2,71	6,22	3,60	16,00	0,08	0,08	3,50	3,50
30,00	2,95	7,10	4,10	46,00	0,00	0,15	5,00	5,00
50,00	3,23	8,17	4,50	96,00	0,15	0,05	12,50	12,50
60,00	3,25	8,19	4,50	156,0	0,05	0,20	20,00	20,00
110,00	3,32	8,57	4,70	266,0	0,00	0,25	20,00	20,00
84,00	3,50	8,85	4,75	350,0	0,00	0,00	0,00	0,00

45.75N 8.25E (e-2 IV)

H	ρ	VP	VS	Z	ΔV_S+	ΔV_S-	$\Delta H+$	$\Delta H-$
1,00	2,61	4,20	2,43	1,00	0,00	0,00	0,00	0,00
1,00	2,61	4,20	2,43	2,00	0,00	0,00	0,00	0,00
1,00	2,61	4,20	2,43	3,00	0,00	0,00	0,00	0,00
1,00	2,75	4,93	2,85	4,00	0,00	0,00	0,00	0,00
2,00	2,75	4,93	2,85	6,00	0,00	0,00	0,00	0,00
10,00	2,75	5,27	3,05	16,00	0,08	0,08	2,00	2,00
30,00	3,01	7,95	4,25	46,00	0,00	0,15	5,00	5,00
50,00	3,30	8,18	4,50	96,00	0,20	0,00	12,50	12,50
60,00	3,27	8,23	4,45	156,0	0,00	0,20	20,00	20,00
110,00	3,28	8,62	4,70	266,0	0,00	0,25	20,00	20,00
84,00	3,46	8,82	4,75	350,0	0,00	0,00	0,00	0,00

45.75N 9.75E (e-1 I)

H	ρ	VP	VS	Z	ΔV_S+	ΔV_S-	$\Delta H+$	$\Delta H-$
1,00	2,61	3,98	2,30	1,00	0,00	0,00	0,00	0,00
1,00	2,61	3,98	2,30	2,00	0,00	0,00	0,00	0,00
1,00	2,61	3,98	2,30	3,00	0,00	0,00	0,00	0,00
1,00	2,71	4,50	2,60	4,00	0,00	0,00	0,00	0,00
2,00	2,71	4,50	2,60	6,00	0,00	0,00	0,00	0,00
10,00	2,76	5,88	3,40	16,00	0,13	0,13	2,50	2,50
17,00	2,95	6,50	3,75	33,00	0,13	0,13	4,00	4,00
50,00	3,24	8,13	4,50	83,00	0,05	0,15	15,00	15,00
65,00	3,26	8,09	4,50	148,00	0,15	0,00	17,50	17,50
70,00	3,27	8,29	4,20	218,00	0,00	0,20	20,00	20,00
132,00	3,44	8,88	4,75	350,00	0,00	0,00	0,00	0,00

45.25N 9.75E (e-1 II)

H	ρ	VP	VS	Z	ΔV_S+	ΔV_S-	$\Delta H+$	$\Delta H-$
1,00	2,58	2,94	1,70	1,00	0,00	0,00	0,00	0,00
1,00	2,58	3,46	2,00	2,00	0,00	0,00	0,00	0,00
1,00	2,57	3,46	2,00	3,00	0,00	0,00	0,00	0,00
1,00	2,67	3,46	2,00	4,00	0,00	0,00	0,00	0,00
2,00	2,67	3,46	2,00	6,00	0,00	0,00	0,00	0,00
9,00	2,72	7,00	4,05	15,0	0,10	0,10	3,00	3,00
20,00	2,89	6,50	3,75	35,0	0,13	0,13	4,00	4,00
90,00	3,20	8,06	4,45	125	0,10	0,15	15,00	15,00
65,00	3,23	8,16	4,45	190	0,00	0,20	17,50	17,50
105,00	3,36	8,70	4,70	295	0,00	0,25	20,00	20,00
55,00	3,56	8,85	4,75	350	0,00	0,00	0,00	0,00

45.25N 9.25E (e-1 III)

H	ρ	VP	VS	Z	ΔV_S+	ΔV_S-	$\Delta H+$	$\Delta H-$
1,00	2,57	2,94	1,70	1,00	0,00	0,00	0,00	0,00
1,00	2,57	3,46	2,00	2,00	0,00	0,00	0,00	0,00
1,00	2,57	3,46	2,00	3,00	0,00	0,00	0,00	0,00
1,00	2,67	3,46	2,00	4,00	0,00	0,00	0,00	0,00
2,00	2,67	3,46	2,00	6,00	0,00	0,00	0,00	0,00
9,00	2,71	7,00	4,05	15,00	0,05	0,10	3,00	3,00
20,00	2,88	6,50	3,75	35,00	0,13	0,13	4,00	4,00
90,00	3,20	8,09	4,45	125,0	0,10	0,10	15,00	15,00
65,00	3,23	8,18	4,45	190,0	0,00	0,20	17,50	17,50
105,00	3,38	8,67	4,70	295,0	0,00	0,25	20,00	20,00
55,00	3,57	8,86	4,75	350,0	0,00	0,00	0,00	0,00

45.75N 9.25E (e-1 IV)

H	ρ	VP	VS	Z	ΔV_S+	ΔV_S-	$\Delta H+$	$\Delta H-$
1,00	2,60	3,98	2,30	1,00	0,00	0,00	0,00	0,00
1,00	2,60	3,98	2,30	2,00	0,00	0,00	0,00	0,00
1,00	2,60	3,98	2,30	3,00	0,00	0,00	0,00	0,00
1,00	2,70	4,50	2,60	4,00	0,00	0,00	0,00	0,00
2,00	2,70	4,50	2,60	6,00	0,00	0,00	0,00	0,00
10,00	2,75	5,88	3,40	16,0	0,10	0,15	2,50	2,50
17,00	2,94	6,50	3,75	33,0	0,10	0,15	4,00	4,00
80,00	3,25	8,00	4,40	113	0,15	0,15	15,00	15,00
65,00	3,26	8,16	4,50	178	0,00	0,15	17,50	17,50
110,00	3,32	8,67	4,60	288	0,00	0,20	20,00	20,00
62,00	3,52	8,87	4,75	350	0,00	0,00	0,00	0,00

45.75N 10.75E (e0 I)

H	ρ	VP	VS	Z	ΔV_S+	ΔV_S-	$\Delta H+$	$\Delta H-$
0,50	2,40	3,63	2,10	0,50	0,00	0,00	0,00	0,00
1,00	2,43	4,41	2,55	1,50	0,00	0,00	0,00	0,00
1,00	2,45	4,67	2,70	2,50	0,00	0,00	0,00	0,00
1,00	2,53	4,85	2,80	3,50	0,00	0,00	0,00	0,00
1,50	2,60	4,85	2,80	5,00	0,00	0,00	0,00	0,00
6,00	2,73	4,85	2,80	11,00	0,10	0,10	1,00	1,00
20,00	2,87	6,31	3,65	31,00	0,10	0,10	5,00	5,00
50,00	3,30	8,00	4,40	81,00	0,15	0,05	20,00	20,00
90,00	3,34	8,03	4,40	171,0	0,20	0,10	20,00	20,00
70,00	3,39	8,29	4,20	241,0	0,00	0,20	20,00	20,00
109,00	3,49	8,78	4,75	350,0	0,00	0,00	0,00	0,00

45.25N 10.75E (e0 II)

H	ρ	VP	VS	Z	ΔV_S+	ΔV_S-	$\Delta H+$	$\Delta H-$
1,00	2,38	2,94	1,70	1,00	0,00	0,00	0,00	0,00
1,00	2,43	3,46	2,00	2,00	0,00	0,00	0,00	0,00
1,00	2,43	3,46	2,00	3,00	0,00	0,00	0,00	0,00
1,00	2,58	3,46	2,00	4,00	0,00	0,00	0,00	0,00
2,00	2,58	3,46	2,00	6,00	0,00	0,00	0,00	0,00
10,00	2,77	6,92	4,00	16,00	0,13	0,13	2,00	2,00
12,00	2,82	6,06	3,50	28,00	0,13	0,13	5,00	5,00
30,00	3,15	8,32	4,40	58,00	0,00	0,15	15,00	15,00
100,00	3,31	7,93	4,35	158,0	0,20	0,05	17,50	17,50
65,00	3,36	8,23	4,25	223,0	0,00	0,25	20,00	20,00
127,00	3,50	8,76	4,75	350,0	0,00	0,00	0,00	0,00

45.25N 10.25E (e0 III)

H	ρ	VP	VS	Z	ΔV_S+	ΔV_S-	$\Delta H+$	$\Delta H-$
1,00	2,36	2,94	1,70	1,00	0,00	0,00	0,00	0,00
1,00	2,41	3,46	2,00	2,00	0,00	0,00	0,00	0,00
1,00	2,41	3,46	2,00	3,00	0,00	0,00	0,00	0,00
1,00	2,56	3,46	2,00	4,00	0,00	0,00	0,00	0,00
2,00	2,56	3,46	2,00	6,00	0,00	0,00	0,00	0,00
10,00	2,75	6,92	4,00	16,0	0,10	0,15	2,00	2,00
12,00	2,80	6,05	3,50	28,0	0,15	0,15	5,00	5,00
30,00	3,12	8,38	4,40	58,0	0,00	0,15	15,00	15,00
100,00	3,28	7,98	4,35	158	0,15	0,05	17,50	17,50
65,00	3,36	8,30	4,25	223	0,00	0,25	20,00	20,00
127,00	3,52	8,77	4,75	350	0,00	0,00	0,00	0,00

45.75N 10.25E (e0 IV)

H	ρ	VP	VS	Z	ΔV_S+	ΔV_S-	$\Delta H+$	$\Delta H-$
0,50	2,40	3,63	2,10	0,50	0,00	0,00	0,00	0,00
1,00	2,42	4,41	2,55	1,50	0,00	0,00	0,00	0,00
1,00	2,45	4,67	2,70	2,50	0,00	0,00	0,00	0,00
1,00	2,53	4,85	2,80	3,50	0,00	0,00	0,00	0,00
1,50	2,60	4,85	2,80	5,00	0,00	0,00	0,00	0,00
8,00	2,76	5,19	3,00	13,00	0,10	0,10	1,00	1,00
30,00	2,94	6,66	3,85	43,00	0,10	0,10	5,00	5,00
90,00	3,36	8,05	4,55	133,00	0,15	0,00	20,00	20,00
90,00	3,33	8,26	4,30	223,00	0,00	0,20	20,00	20,00
110,00	3,47	8,78	4,80	333,00	0,05	0,20	20,00	20,00
17,00	3,50	8,83	4,75	350,00	0,00	0,00	0,00	0,00

45.75N 11.75E (e1 I)

H	ρ	VP	VS	Z	ΔV_S+	ΔV_S-	$\Delta H+$	$\Delta H-$
1,00	2,61	3,46	2,00	1,00	0,00	0,00	0,00	0,00
1,00	2,61	4,41	2,55	2,00	0,00	0,00	0,00	0,00
1,00	2,61	4,67	2,70	3,00	0,00	0,00	0,00	0,00
1,00	2,61	4,84	2,80	4,00	0,00	0,00	0,00	0,00
1,00	2,64	4,84	2,80	5,00	0,00	0,00	0,00	0,00
8,00	2,85	5,19	3,00	13,00	0,10	0,10	1,00	1,00
28,00	3,12	6,49	3,75	41,00	0,10	0,10	4,00	4,00
55,00	3,39	7,89	4,50	96,00	0,15	0,00	12,50	12,50
110,00	3,37	8,04	4,45	206,0	0,15	0,20	20,00	20,00
60,00	3,38	8,35	4,55	266,0	0,15	0,20	22,50	22,50
84,00	3,49	8,72	4,75	350,0	0,00	0,00	0,00	0,00

45.25N 11.75E (e1 II)

H	ρ	VP	VS	Z	ΔV_S+	ΔV_S-	$\Delta H+$	$\Delta H-$
1,00	2,61	2,94	1,70	1,00	0,00	0,00	0,00	0,00
1,00	2,61	3,46	2,00	2,00	0,00	0,00	0,00	0,00
1,00	2,61	3,46	2,00	3,00	0,00	0,00	0,00	0,00
1,00	2,61	3,46	2,00	4,00	0,00	0,00	0,00	0,00
2,00	2,66	3,46	2,00	6,00	0,00	0,00	0,00	0,00
10,00	2,91	7,00	4,05	16,00	0,05	0,10	2,00	2,00
12,00	2,99	5,97	3,45	28,00	0,10	0,10	4,00	4,00
30,00	3,35	8,31	4,35	58,00	0,00	0,10	15,00	15,00
100,00	3,38	7,86	4,40	158,0	0,20	0,00	17,50	17,50
65,00	3,33	8,19	4,25	223,0	0,00	0,25	20,00	20,00
127,00	3,46	8,77	4,75	350,0	0,00	0,00	0,00	0,00

45.25N 11.25E (e1 III)

H	ρ	VP	VS	Z	ΔV_S+	ΔV_S-	$\Delta H+$	$\Delta H-$
1,00	2,61	2,94	1,70	1,00	0,00	0,00	0,00	0,00
1,00	2,61	3,46	2,00	2,00	0,00	0,00	0,00	0,00
1,00	2,61	3,46	2,00	3,00	0,00	0,00	0,00	0,00
1,00	2,61	3,46	2,00	4,00	0,00	0,00	0,00	0,00
2,00	2,66	3,46	2,00	6,00	0,00	0,00	0,00	0,00
10,00	2,91	7,00	4,05	16,00	0,05	0,10	2,00	2,00
12,00	2,99	5,97	3,45	28,00	0,10	0,10	4,00	4,00
30,00	3,34	8,34	4,35	58,00	0,00	0,10	15,00	15,00
100,00	3,37	7,88	4,40	158,0	0,20	0,00	17,50	17,50
65,00	3,33	8,17	4,25	223,0	0,00	0,25	20,00	20,00
127,00	3,47	8,78	4,75	350,0	0,00	0,00	0,00	0,00

45.75N 11.25E (e1 IV)

H	ρ	VP	VS	Z	ΔV_S+	ΔV_S-	$\Delta H+$	$\Delta H-$
0,50	2,61	3,63	2,10	0,50	0,00	0,00	0,00	0,00
1,00	2,61	4,41	2,55	1,50	0,00	0,00	0,00	0,00
1,00	2,61	4,67	2,70	2,50	0,00	0,00	0,00	0,00
1,00	2,62	4,84	2,80	3,50	0,00	0,00	0,00	0,00
1,50	2,64	4,84	2,80	5,00	0,00	0,00	0,00	0,00
8,00	2,86	5,19	3,00	13,0	0,10	0,10	2,00	2,00
20,00	3,02	6,14	3,55	33,0	0,10	0,10	4,00	4,00
55,00	3,41	7,92	4,40	88,0	0,15	0,00	12,50	12,50
110,00	3,37	8,03	4,40	198	0,15	0,15	20,00	20,00
60,00	3,35	8,32	4,30	258	0,00	0,20	22,50	22,50
92,00	3,50	8,74	4,75	350	0,00	0,00	0,00	0,00

45.75N 14.75E (e4 I)

H	ρ	VP	VS	Z	ΔV_S+	ΔV_S-	$\Delta H+$	$\Delta H-$
4,00	2,40	3,98	2,30	4,00	0,00	0,00	0,00	0,00
1,00	2,50	5,62	3,25	5,00	0,00	0,00	0,00	0,00
0,50	2,50	5,72	3,30	5,50	0,00	0,00	0,00	0,00
1,00	2,55	5,72	3,30	6,50	0,00	0,00	0,00	0,00
1,50	2,55	5,80	3,35	8,00	0,00	0,00	0,00	0,00
14,00	2,60	5,98	3,45	22,0	0,05	0,05	3,00	3,00
35,00	3,09	8,01	4,15	57,0	0,00	0,10	7,50	7,50
50,00	3,30	8,01	4,70	107	0,10	0,00	10,00	10,00
100,00	3,31	8,15	4,25	207	0,00	0,15	20,00	20,00
60,00	3,37	8,36	4,70	267	0,20	0,00	25,00	25,00
83,00	3,50	8,68	4,75	350	0,00	0,00	0,00	0,00

45.25N 14.75E (e4 II)

H	ρ	VP	VS	Z	ΔV_S+	ΔV_S-	$\Delta H+$	$\Delta H-$
4,00	2,40	3,98	2,30	4,00	0,00	0,00	0,00	0,00
1,00	2,50	5,62	3,25	5,00	0,00	0,00	0,00	0,00
0,50	2,50	5,72	3,30	5,50	0,00	0,00	0,00	0,00
1,00	2,55	5,72	3,30	6,50	0,00	0,00	0,00	0,00
1,50	2,55	5,80	3,35	8,00	0,00	0,00	0,00	0,00
20,00	2,69	6,15	3,55	28,0	0,05	0,05	3,00	3,00
35,00	3,17	8,08	4,35	63,0	0,00	0,10	7,50	7,50
50,00	3,31	8,07	4,70	113	0,10	0,00	10,00	10,00
60,00	3,31	8,11	4,25	173	0,00	0,15	20,00	20,00
60,00	3,30	8,31	4,55	233	0,15	0,20	25,00	25,00
117,00	3,48	8,65	4,75	350	0,00	0,00	0,00	0,00

45.25N 14.25E (e4 III)

H	ρ	VP	VS	Z	ΔV_S+	ΔV_S-	$\Delta H+$	$\Delta H-$
4,00	2,41	3,98	2,30	4,00	0,00	0,00	0,00	0,00
1,00	2,51	5,63	3,25	5,00	0,00	0,00	0,00	0,00
0,50	2,51	5,89	3,40	5,50	0,00	0,00	0,00	0,00
1,00	2,56	5,89	3,40	6,50	0,00	0,00	0,00	0,00
1,50	2,56	5,98	3,45	8,00	0,00	0,00	0,00	0,00
14,00	2,61	5,89	3,40	22,00	0,08	0,08	3,00	3,00
32,00	3,08	8,18	4,15	54,00	0,00	0,10	6,00	6,00
30,00	3,32	8,14	4,70	84,00	0,10	0,00	10,00	10,00
100,00	3,32	8,18	4,50	184,0	0,00	0,15	20,00	20,00
60,00	3,30	8,34	4,60	244,0	0,10	0,20	25,00	25,00
106,00	3,50	8,63	4,75	350,0	0,00	0,00	0,00	0,00

45.75N 14.25E (e4 IV)

H	ρ	VP	VS	Z	ΔV_S+	ΔV_S-	$\Delta H+$	$\Delta H-$
4,00	2,40	3,98	2,30	4,00	0,00	0,00	0,00	0,00
1,00	2,50	5,62	3,25	5,00	0,00	0,00	0,00	0,00
0,50	2,50	5,80	3,35	5,50	0,00	0,00	0,00	0,00
1,00	2,55	5,88	3,40	6,50	0,00	0,00	0,00	0,00
1,50	2,55	5,98	3,45	8,00	0,00	0,00	0,00	0,00
15,00	2,60	6,06	3,50	23,0	0,05	0,05	2,50	2,50
30,00	3,08	8,18	4,10	53,0	0,00	0,10	5,00	5,00
30,00	3,30	8,15	4,65	83,0	0,15	0,00	10,00	10,00
100,00	3,31	8,16	4,45	183	0,10	0,15	20,00	20,00
60,00	3,29	8,28	4,55	243	0,20	0,25	25,00	25,00
107,00	3,51	8,64	4,75	350	0,00	0,00	0,00	0,00

44.75N 6.75E (d-4 I)

H	ρ	VP	VS	Z	ΔV_S+	ΔV_S-	$\Delta H+$	$\Delta H-$
1,00	2,41	4,50	2,60	1,00	0,00	0,00	0,00	0,00
1,00	2,40	5,20	3,00	2,00	0,00	0,00	0,00	0,00
1,00	2,40	5,20	3,00	3,00	0,00	0,00	0,00	0,00
1,00	2,40	5,20	3,00	4,00	0,00	0,00	0,00	0,00
1,00	2,55	5,45	3,15	5,00	0,00	0,00	0,00	0,00
6,00	2,64	4,67	2,70	11,0	0,10	0,10	1,50	1,50
27,00	2,74	6,75	3,90	38,0	0,10	0,10	5,00	5,00
70,00	3,21	8,14	4,45	108	0,00	0,10	15,00	15,00
110,00	3,18	8,38	4,50	218	0,00	0,15	25,00	25,00
110,00	3,31	8,72	4,60	328	0,00	0,20	25,00	25,00
22,00	3,46	8,75	4,75	350	0,00	0,00	0,00	0,00

44.25N 6.75E (d-4 II)

H	ρ	VP	VS	Z	ΔV_S+	ΔV_S-	$\Delta H+$	$\Delta H-$
0,50	2,41	4,50	2,60	0,50	0,00	0,00	0,00	0,00
1,00	2,41	4,75	2,75	1,50	0,00	0,00	0,00	0,00
1,50	2,41	5,20	3,00	3,00	0,00	0,00	0,00	0,00
1,00	2,41	5,20	3,00	4,00	0,00	0,00	0,00	0,00
1,00	2,56	5,45	3,15	5,00	0,00	0,00	0,00	0,00
9,00	2,65	5,01	2,90	14,00	0,10	0,10	1,50	1,50
27,00	2,81	7,10	4,10	41,00	0,10	0,10	5,00	5,00
70,00	3,21	7,93	4,35	111,0	0,10	0,10	15,00	15,00
110,00	3,19	8,31	4,50	221,0	0,00	0,15	25,00	25,00
60,00	3,26	8,51	4,70	281,0	0,20	0,10	25,00	25,00
69,00	3,49	8,74	4,75	350,0	0,00	0,00	0,00	0,00

44.25N 6.25E (d-4 III)

H	ρ	VP	VS	Z	ΔV_S+	ΔV_S-	$\Delta H+$	$\Delta H-$
1,00	2,42	4,76	2,75	1,00	0,00	0,00	0,00	0,00
1,00	2,42	4,76	2,75	2,00	0,00	0,00	0,00	0,00
1,00	2,42	5,19	3,00	3,00	0,00	0,00	0,00	0,00
1,00	2,42	5,19	3,00	4,00	0,00	0,00	0,00	0,00
1,00	2,56	5,45	3,15	5,00	0,00	0,00	0,00	0,00
9,00	2,66	5,01	2,90	14,00	0,10	0,10	1,50	1,50
17,00	2,70	7,09	4,10	31,00	0,10	0,10	5,00	5,00
40,00	3,16	7,88	4,25	71,00	0,00	0,10	15,00	15,00
110,00	3,16	8,14	4,45	181,00	0,05	0,15	25,00	25,00
110,00	3,22	8,61	4,60	291,00	0,00	0,20	25,00	25,00
59,00	3,44	8,79	4,75	350,00	0,00	0,00	0,00	0,00

44.75N 6.25E (d-4 IV)

H	ρ	VP	VS	Z	ΔV_S+	ΔV_S-	$\Delta H+$	$\Delta H-$
1,00	2,41	4,76	2,75	1,00	0,00	0,00	0,00	0,00
1,00	2,41	4,76	2,75	2,00	0,00	0,00	0,00	0,00
1,00	2,41	5,19	3,00	3,00	0,00	0,00	0,00	0,00
1,00	2,41	5,19	3,00	4,00	0,00	0,00	0,00	0,00
1,00	2,56	5,45	3,15	5,00	0,00	0,00	0,00	0,00
9,00	2,66	5,01	2,90	14,00	0,10	0,10	1,50	1,50
17,00	2,69	7,09	4,10	31,00	0,10	0,10	5,00	5,00
40,00	3,15	7,85	4,25	71,00	0,00	0,10	15,00	15,00
110,00	3,15	8,24	4,50	181,00	0,00	0,15	25,00	25,00
110,00	3,20	8,65	4,60	291,00	0,00	0,20	25,00	25,00
59,00	3,42	8,77	4,75	350,00	0,00	0,00	0,00	0,00

44.75N 7.75E (d-3 I)

H	ρ	VP	VS	Z	ΔV_S+	ΔV_S-	$\Delta H+$	$\Delta H-$
0,80	2,40	4,24	2,45	0,80	0,00	0,00	0,00	0,00
1,20	2,44	5,20	3,00	2,00	0,00	0,00	0,00	0,00
1,00	2,44	5,20	3,00	3,00	0,00	0,00	0,00	0,00
1,00	2,44	5,20	3,00	4,00	0,00	0,00	0,00	0,00
1,00	2,44	5,40	3,10	5,00	0,00	0,00	0,00	0,00
8,00	2,70	4,85	2,80	13,00	0,10	0,10	1,00	1,00
30,00	3,02	7,76	4,25	43,00	0,00	0,10	7,50	7,50
70,00	3,22	8,13	4,45	113,0	0,05	0,15	10,00	10,00
60,00	3,27	8,17	4,45	173,0	0,00	0,15	20,00	20,00
110,00	3,38	8,63	4,70	283,0	0,00	0,25	20,00	20,00
67,00	3,61	8,86	4,75	350,0	0,00	0,00	0,00	0,00

44.25N 7.75E (d-3 II)

H	ρ	VP	VS	Z	ΔV_S+	ΔV_S-	$\Delta H+$	$\Delta H-$
0,50	2,40	4,25	2,45	0,50	0,00	0,00	0,00	0,00
1,50	2,43	5,20	3,00	2,00	0,00	0,00	0,00	0,00
1,00	2,44	5,20	3,00	3,00	0,00	0,00	0,00	0,00
1,00	2,44	5,35	3,10	4,00	0,00	0,00	0,00	0,00
1,00	2,44	5,35	3,10	5,00	0,00	0,00	0,00	0,00
8,00	2,69	4,85	2,80	13,00	0,10	0,10	1,00	1,00
20,00	2,92	6,85	3,95	33,00	0,10	0,10	7,50	7,50
70,00	3,25	7,94	4,35	103,0	0,10	0,05	10,00	10,00
100,00	3,35	8,15	4,50	203,0	0,00	0,15	20,00	20,00
110,00	3,50	8,72	4,70	313,0	0,00	0,25	20,00	20,00
37,00	3,67	8,86	4,75	350,0	0,00	0,00	0,00	0,00

44.25N 7.25E (d-3 III)

H	ρ	VP	VS	Z	ΔV_S+	ΔV_S-	$\Delta H+$	$\Delta H-$
0,50	2,40	4,25	2,45	0,50	0,00	0,00	0,00	0,00
1,50	2,44	5,20	3,00	2,00	0,00	0,00	0,00	0,00
1,00	2,44	5,20	3,00	3,00	0,00	0,00	0,00	0,00
1,00	2,44	5,35	3,10	4,00	0,00	0,00	0,00	0,00
1,00	2,44	5,35	3,10	5,00	0,00	0,00	0,00	0,00
8,00	2,70	4,85	2,80	13,0	0,10	0,10	1,00	1,00
20,00	2,91	6,85	3,95	33,0	0,10	0,10	7,50	7,50
70,00	3,22	7,93	4,35	103	0,15	0,10	10,00	10,00
100,00	3,28	8,21	4,45	203	0,00	0,15	20,00	20,00
110,00	3,42	8,68	4,70	313	0,00	0,25	20,00	20,00
37,00	3,60	8,80	4,75	350	0,00	0,00	0,00	0,00

44.75N 7.25E (d-3 IV)

H	ρ	VP	VS	Z	ΔV_S+	ΔV_S-	$\Delta H+$	$\Delta H-$
0,50	2,42	4,25	2,45	0,50	0,00	0,00	0,00	0,00
1,50	2,46	5,20	3,00	2,00	0,00	0,00	0,00	0,00
1,00	2,46	5,20	3,00	3,00	0,00	0,00	0,00	0,00
1,00	2,46	5,35	3,10	4,00	0,00	0,00	0,00	0,00
1,00	2,46	5,35	3,10	5,00	0,00	0,00	0,00	0,00
8,00	2,72	4,85	2,80	13,00	0,10	0,10	1,00	1,00
20,00	2,94	6,85	3,95	33,00	0,10	0,10	7,50	7,50
70,00	3,24	8,15	4,45	103,0	0,10	0,10	10,00	10,00
100,00	3,25	8,28	4,45	203,0	0,00	0,15	20,00	20,00
110,00	3,38	8,70	4,68	313,0	0,00	0,25	20,00	20,00
37,00	3,56	8,78	4,75	350,0	0,00	0,00	0,00	0,00

Acknowledgments

I wish to acknowledge all the people which in different ways allowed me to complete this work, in particular my supervisor, prof. Giuliano Panza, prof. Carlo Doglioni for his interest in my work and prof. Iginio Marson for our useful discussions. I wish to thanks dr. Reneta Raykova and dr. Fabio Romanelli for their help and constructive criticism, dr. Franco Vaccari for his crucial technical support, dr. Cristina La Mura for her true empathy and all my collegues from the Seismology research group. I'm very grateful to my family for supporting me in the last three years relieving me from difficulties we went through. Last but not least I thanks all the people and friends which took part in this journey with me and left for different destinations, I truly cherished your company.

Bibliography

[1] Aitken, A., Salmon, M. and Kennett, B. (2012). Australia's Moho: A test of the usefulness of gravity modelling for the determination of Moho depth, Tectonophysics, doi: 10.1016/j.tecto.2012.06.049

[2] Aki, K. and P.G. Richards (1980). Quantitative Seismology, Freeman and Co. New York.

[3] Alsop L.E. (1966), Transmission and reflection of Love waves at a vertical discontinuity, J.Geophys. Res., 71, 3969-3984.

[4] Anderson, D. (2007) . New Theory of the Earth. Cambridge University Press.

[5] Anderson, D. (2007). The eclogite engine: Chemical geodynamics as a Galileo thermometer. Geological Society of America Special Papers 430, 47-64.

[6] Anderson, D.L. (2010). Hawaii, Boundary Layers and Ambient Mantle - Geophysical Constraints. Journal of Petrology, 0, 1-31.

[7] Backus, G., and J.F. Gilbert (1967). Numerical applications of a formalism for geophysical inverse problems, Geophys. J.R. Astron. Soc., 13, 247-276.

[8] Backus, G., and J.F. Gilbert (1968). The resolving power of gross earth data, Geophys. J.R. Astron. Soc., 16, 169-205.

[9] Ben-Menahem A. (1965). Observed attenuation and Q values of seismic surface waves in the upper mantle, J. Geophys. Res. 70, 4641-4651.

[10] Birch, F. (1964), Density and composition of mantle and core, J. Geophys. Res., 69(20), 4377-4384.

[11] Bostrom, C. (1971). Westward dosplacement of the lithosphere. Nature, 234, 536-538.

[12] Bottinga, Y., Steinmetz, L., (1979). A geophysical, geochemical, petrological model of the sub-marine lithosphere. Tectonophysics 55, 311-347.

[13] Boyadzhiev, G., Brandmayr, E., Pinat, T. and Panza, G.F. (2008). Optimization for non linear inverse problem. Rendiconti Lincei: Sci. Fis. e Nat., 19, 17-43

[14] Brandmayr, E., Marson, I., Romanelli, F. and Panza, G.F. (2011). Lithosphere density model in Italy: no hint for slab pull. Terra Nova, 23, 292-299 doi: 10.1111/j.1365-3121.2011.01012.x

[15] Brandmayr, E., Raykova, R.B., Zuri, M., Romanelli, F., Doglioni, C. and Panza, G.F. (2010). The lithosphere in Italy: structure and seismicity. In: Journal of the Virtual Explorer (Eds. Marco Beltrando, Angelo Peccerillo, Massimo Mattei, Sandro Conticelli, and Carlo Doglioni), 36, doi:10.3809/jvirtex.2010.00224

[16] Brückl, E., M. Behm, K. Decker, M. Grad, A. Guterch, G. R. Keller, and H. Thybo (2010), Crustal structure and active tectonics in the Eastern Alps, Tectonics, 29, TC2011, doi:10.1029/2009TC002491.

[17] Bukchin B.G. (2006). Specific features of surface radiation by shallow source, Izvestiya. Phys Solid Earth 42(8):712-717

[18] Bukchin, B., Clévédé, E., Mostinskiy, A. (2010). Uncertainty of moment tensor determination from surface wave analysis for shallow earthquakes. Journal of Seismology, 14, 3, 601-614, dx.doi.org/10.1007/s10950-009-9185-8

[19] Calcagnile, G. and Panza, G.F. (1973). Magnitude from Rayleigh waves: time domain analysis of the influence of source parameters and structure. Riv. It. Geofis., 22, 117-120.

[20] Carminati E., Doglioni C., Scrocca, D. (2004). Alps Vs Apennines. Special volume of the Italian Geological Society for IGC 32 Florence.

[21] Carminati, E., Doglioni, C. (2004). Europe - Mediterranean tectonics. In Encyclopedia of Geology, Elsevier, 135-146.

[22] Carminati, E., Lustrino, M., Cuffaro, M., Doglioni, C. (2010b). Tectonics, magmatism and geodynamics of Italy: what we know and what we imagine. Journal of the Virtual Explorer 36, 8 ISSN 1441-8142.

[23] Cassinis, R (2006). Reviewing pre-TRANSALP DSS models, Tectonophysics, 414, 79-86.

[24] Chimera G., Aoudia A., Saraò A., Panza, G.F. (2003). Active tectonics in central Italy: constraint from surface wave tomography and source moment tensor inversion. Phys. Earth Planet. Inter. 138:241-262.

[25] Crespi, M., Cuffaro, M., Doglioni, C., Giannone, F., Riguzzi, F. (2007). Space geodesy validation of the global lithospheric flow. Geophys. J. Int. 168, 491-506.

[26] Craglietto A., Panza G.F., Mitchell B.J, Costa G. (1989). Anelastic properties of the crust in the Mediterranean area. American Geophysical Union Geophysical Monograph 51 IUGG 6, 179-196.

[27] Cuffaro, M., and Doglioni, C. (2007). Global kinematics in deep versus shallow hotspot reference frames, In: Foulger, G.R., and Jurdy, D.M. (Eds.), Plates, plumes, and planetary processes: Geological Society of America Special Paper 430, 359-374, doi: 10.1130/2007.2430(18).

[28] Cuffaro M., Doglioni C., Riguzzi, F. (2009). Present geodynamics of the northern Adriatic plate. Rendiconti online Soc. Geol. It. 3.

[29] Cuffaro M., Riguzzi F., Scrocca D., Antonioli F., Carminati E., Livani M., Doglioni C. (2010). On the geodynamics of the northern Adriatic plate. Rend. Fis. Acc. Lincei, 21 (Suppl 1): S253-S279 DOI 10.1007/s12210-010-0098-9

[30] Dal Piaz, G.V. (1997). Alpine geology and historical evolution of the orogenic concept. Mem. Sc. Fis., 21, 49-83.

[31] Debayle E., Kennett, B and Priestley, K. (2005). Global azimuthal seismic anisotropy and the unique plate-motion deformation of Australia Nature 433, 509-512 doi:10.1038/nature03247

[32] Della Vedova, B., Bellani, S., Pellis, G. and Squarci, P. (2001). Deep temperatures and surface heat flow distribution. In: Anatomy of an orogen (Vai and Martini Eds.)

[33] Dezes, P. and Ziegler, P. (2001). Map of the European Moho. EUCOR URGENT

[34] Di Stefano, R., Kissling, E., Chiarabba, C., Amato, A., Giardini, D. (2009). Shallow subduction beneath Italy: Three-dimensional images of the Adriatic-European-Tyrrhenian lithosphere system based on high-quality P wave arrival times. Journal of Geophysical Research 114, B05305. doi:10.1029/2008JB005641.

[35] Doglioni, C. (1991). A proposal of kinematic modelling for W-dipping subductions - Possible applications to the Tyrrhenian-Apennines system. Terra Nova 3, 423-434.

[36] Doglioni, C., Carminati, E., Cuffaro, M. and Scrocca D. (2007). Subduction kinematics and dynamic constraints. Earth Science Reviews, 83, 125-175

[37] Doglioni, C., Carminati, E., Bonatti, E. (2003). Rift asymmetry and continental uplift. Tectonics 22 (3), 1024. doi:10.1029/2002TC001459.

[38] Doglioni, C., Green, D., and Mongelli, F. (2005). On the shallow origin of hotspots and the westward drift of the lithosphere, in Foulger, G.R., et al., eds., Plates, plumes and paradigms: Boulder, Colorado, Geological Society of America Special Paper 388, p. 735-749, doi: 10.1130/2005.2388(42).

[39] Doglioni, C., Gueguen, E., Harabaglia, P., Mongelli, F. (1999). On the origin of west-directed subduction zones and application to the western Mediterranean. In: Durand, Jolivet, Horváth, Séranne The Mediterranean Basins: Tertiary Extension within the Alpine orogen. Geological Society of London 156, 541-561.

[40] Doglioni, C., Ismail-Zadeh, A., Panza, G., Riguzzi, F. (2011). Lithosphere-asthenosphere viscosity contrast and decoupling, Physics of the Earth and Planetary Interiors, Vol 189, Issues 1-2, pp 1-8, ISSN 0031-9201, 10.1016/j.pepi.2011.09.006.

[41] Dreger, D. S. and D. V. Helmberger (1993). Determination of Source Parameters at Regional Distances with Single Station or Sparse Network Data, Journ. Geophys. Res., 98, 8107-8125.

[42] Du, Z.J., Michelini, A., Panza, G.F. (1998). EurID: a regionalized 3D seismological model of Europe. Phys. Earth Planet. Inter. 105, 31-62.

[43] Dufumier, H. (1996). On the Limits of Linear Moment-tensor Inversion of Teleseismic Body Wave Spectra, Pure and Applied Geophysics, 147, n. 3, 467-482.

[44] Dufumier, H. and M. Cara (1995). On the limits of linear moment tensor inversions of surface wave spectra, Pure and Applied Geophysics 145, 235-257.

[45] Dziewonski, A. M. and Anderson, D. L. (1981). Preliminary Reference Earth Model. Physics of the Earth and Planetary Interiors 25, 297-356.

[46] Dziewonski, A.M., T.A. Chou and J.H. Woodhouse, (1981). Determination of earthquake source parameters from waveform data for studies of global and regional seismicity. Journal of Geophysical Research, 86, 2825-2852.

[47] ElGabry, M. N., Panza, G. F., Badawy, A. A. and Korrat, I. M. (2013), Imaging a relic of complex tectonics: the lithosphere-asthenosphere structure in the Eastern Mediterranean. Terra Nova, 25: 102-109. doi: 10.1111/ter.12011

[48] Elsasser, W. M. (1969). Convection and stress propagation in the upper mantle. In: Runcorn, S. K. (Ed.), The Application of Modern Physics to the Earth and Planetary Interiors, 223-246, John Wiley and Sons, New York.

[49] Farafonova, Y.G., Panza, G.F., Yanovskaya, T.B., Doglioni, C. (2007). Upper Mantle Structure in the Alpine Zone from Surface Wave Tomography, Doklady Earth Sciences, Russian Academy of Science, Moscow.

[50] Farina, B.M. (2006). Lithosphere-asthenosphere system in Italy and surrounding areas: optimized non-linear inversion of surface-wave dispersion curves and modelling of gravity bouguer anomalies. Phd Thesis, University of Trieste.

[51] Florsch, N., Fäh, D., Suhadolc, P., and Panza, G.F. (1991). Complete synthetic seismograms for high-frequency multimode SH-waves. Pure and Applied Geophysics, 136, 529-560.

[52] Foulger, G.R., Panza, G.F., Artemieva, I.M., Bastow, I.D., Cammarano, F., Evans, J.R., Hamilton, W.B., Julian, B.R., Lustrino, M., Thybo, H., Yanovskaya, T.B. Caveats on tomographic images: Things are seldom what they seem. Submitted to Terra Nova.

[53] Frezzotti, M.L., Peccerillo, A., Panza, G.F. (2009). Carbonate matasomatism and CO_2 lithosphere-asthenosphere degassing beneath the Western Mediterranean: An integrated model arising from petrological and geophysical data. Chemical Geology 262, 108-120.

[54] Gasperini, P. (2002). Local magnitude revaluation for recent Italian earthquakes (1981-1996). J. Seismol. 6, 503-524.

[55] Gennesseaux, M., Burollet, P., Winnock, E. (1998). Thickness of the Plio-Quaternary sediments (IBCM-PQ). Boll. Geofis. Teor. Appl. 39, 243-284.

[56] Giustini, F., Blessing, M., Brilli, M., Lombardi, S., Voltattorni, N., Widory, D. (2013). Determining the origin of carbon dioxide and methane in the

gaseous emissions of the San Vittorino plain (central Italy) by means of stable isotopes and noble gas analysis, Applied Geochemistry, doi: http://dx.doi.org/10.1016/j.apgeochem.2013.02.015

[57] Grad, M., Tiira, T. (2008). The Moho depth map of the European Plate. Geophysical Journal International 176 I, 279-292.

[58] Green, D.H., Ringwood, A.E. (1967). The genesis of basaltic magmas. Springer Contributions to Mineralogy and Petrology 15 2, 103-190.

[59] Gueguen, E., Doglioni, C., Fernandez, M. (1997). Lithospheric boudinage in the Western Mediterranean back-arc basin. Terra Nova 9, 184-187.

[60] Guidarelli, M., Panza, G.F. (2007). INPAR, CMT and RCMT seismic moment solutions compared for the strongest damaging events (M≥4.8) occurred in the italian region in the last decade. Rendiconti Accademia Nazionale delle Scienze detta dei XL Memorie di Scienze Fisiche e Naturali 124 Vol. XXX P. II, 81-98.

[61] Gutenberg, B. (1959). Wave velocities below the Mohorovicic discontinuity. GeophysicalJournal of the Royal Astronomical Society 2, 348-352.

[62] Hager, B.H. and O'Connell, R.J. 1978. Subduction zone dip angles and flow driven by plate motion. Tectonophysics, 50, 111- 133.

[63] Handy, M.R, Schmid, S., Bousquet, R., Kissling, E., Bernoulli, D. (2010). Reconciling plate-tectonic reconstructions of Alpine Tethys with the geological-geophysical record of spreading and subduction in the Alps, Earth-Science Reviews, V. 102, I. 3-4, pp 121-158, 10.1016/j.earscirev.2010.06.002.

[64] Henry, C., Woodhouse, J.H., and Das, S. (2002). Stability of earthquake moment tensor inversions: effect of the double-couple constraint, Tectonophysics, 356, 115-124.

[65] Hurting, E., Cermak, V., Haenel, R. and Zui, V. (eds), (1991). Geothermal Atlas of Europe. Hermann Haack Verlag, Gotha, 156 pp.

[66] Isacks, B.L. and Barazangi, M. (1977.) Geometry of Benioff zones: lateral segmentation and downward bending of the subducted lithosphere. In: Talwani, M., Pitman, W.M. III (Eds.), Island Arcs, Deep Sea Trenches and Back-arc Basins. Maurice Ewing Series 1, 99-114, AGU, Washington, D. C.

[67] ISC (2007). International Seismological Centre. http://www.isc.ac.uk

[68] ISPRA, ENI, OGS (2009). Cartografia Gravimetrica Digitale d'Italia alla scala 1:250.000.

[69] Karato, S., and B. B. Karki (2001), Origin of lateral variation of seismic wave velocities and density in the deep mantle, J. Geophys. Res., 106(B10), 21,771-21,783, doi:10.1029/2001JB0000214.

[70] Kelly, R.K., Kelemen, P.B. and Jull, M. (2003). Buoyancy of the continental upper mantle. Geochem. Geophys. Geosyst., 4(2), 1017.

[71] Kennett, B.K.N., Engdahl, E.R., Buland, R., (1995). Constraints on seismic velocities in the earth from travel times. Geophys. J. Int. 122, 108-124.

[72] Knopoff, L. and Leeds, A. (1972). Lithospheric momenta and the deceleration of the Earth. Nature, 237, 93-95.

[73] Knopoff, L., Panza, G.F. (1977). Resolution of upper mantle structure using higher modes of Rayleigh waves. Annales Geophysicae 30, 491-505.

[74] Kravanja, S., Batini, F., Fiordelisi, A., Panza, G.F. (2000). Full moment tensor retrieval from waveform inversion in the Larderello geothermal area. Pure and Applied Geophysics 157, 1379-1392.

[75] Kravanja, S., Panza, G.F., Šílený, J. (1999). Robust retrieval of seismic point source time function. Geophysical Journal International 136, 385-394.

[76] Labrosse S., Jaupart, C. (2007). The thermal evolution of the Earth: Long term and fluctuations. Earth Planet. Sci. Lett., 260, 465-481, 2007.

[77] Laske, G., Masters, G. (1997). A global digital maps of sediment thickness. Eos, Trans. Am. Geophys. Union 78 F483

[78] Le Pichon, X. (1968). Sea-floor spreading and continental drift. J. Geophys. Res., 73: 12, 3661-3697.

[79] Levshin, A. L., T. B. Yanovskaya, A. V. Lander, B. G. Bukchin, M. P. Barmin, L. I. Ratnikova, and E. N. Its (1989), Seismic Surface Waves in Laterally Inhomogeneous Earth, edited by V. I. Keilis-Borok, chap. 5, pp. 133-163, Kluwer, Dordrecht, Netherlands.

[80] Levshin, A.L., X. Yang, M.P. Barmin, and M.H. Ritzwoller (2010). Mid-period Rayleigh wave attenuation model for Asia, Geochem. Geophys. Geosyst., 11(8), Q08017, doi:10.1029/2010GC003164.

[81] Li, Y. and Oldenburg, D.W. (1998). 3D inversion of gravity data. Geophysics, 63, No.1, 109-119.

[82] Lodolo, E., Civile, D., Zanolla, C., Geletti, R. (2012). Magnetic signature of the Sicily Channel volcanism. Mar. Geoph. Res. Vol. 33, I 1, pp 33-44.

[83] Lustrino, M., Morra, V., Fedele, L. and Franciosi L. (2009). Beginning of the Apennine subduction system in central western Mediterranean: constraints from Cenozoic "orogenic" magmatic activity of Sardinia (Italy). Tectonics 28, TC5016, doi:10.1029/2008TC002419

[84] Marson, I., Panza, G.F., and Suhadolc, P. (1995). Crust and upper mantle models along the active Tyrrhenian rim. Terra Nova, 7, 348-357

[85] Martinez, Lana, Guinto (2009). Elasto-anelastic regional structures of the crust and upper mantle beneath the Mediterranean basin derived from uncoupled casual inversion of rayleigh wave attenuation coefficient and group velocities. Geophysical research abstracts 11, EGU2009-2420.

[86] Martinez, M.D., Lana, X., Guinto, E.R., (2010). Shear-wave attenuation tomography of the lithosphere-asthenosphere system beneath the Mediterranean region, Tectonophysics 481, 51-67.

[87] Meletti, C. and Valensise, G. (2004). Zonazione sismogenetica ZS9 - App. 2 al Rapporto Conclusivo. In: Gruppo di Lavoro MPS (2004). Redazione della mappa di pericolosità sismica prevista dall'Ordinanza PCM 3274 del 20 marzo 2003. Rapporto Conclusivo per il Dipartimento della Protezione Civile, INGV, Milano-Roma, Aprile 2004, 65 pp. + 5 Allegati.

[88] McKenzie, D. and Bickle, M. J. (1988). The volume and composition of melt generated by extension of the lithosphere. Journal of Petrology 29, 625-679.

[89] Montagner, J.P., and Guillot, L. (2003). Seismic Anisotropy and global geodynamics. Min. Soc.Am., 51,353-385.

[90] Moore, G.W. (1973). Westward tidal lag as the driving force of plate tectonics. Geology 1, 99-100.

[91] Müller, S. and Panza, G.F. (1986). Evidence of a deep-reaching lithospheric root under the Alpine Arc. In: The Origin of Arcs, ed.: F.C. Wezel, Elsevier, 21, pp. 93-113

[92] Nakagawa, T., and Tackley, P. J. (2008). Lateral variations in CMB heat flux and deep mantle seismic velocity caused by a thermal-chemical-phase boundary layer in 3D spherical convection, Earth Planet. Sci. Lett. 271, 348-358.

[93] NEIC (2003) National Earthquake Information Center, US. http://earthquake.usgs.gov.

[94] Nelson, T.H., Temple, P.G. (1972). Mainstream mantle convection: a geologic analysis of plate motion. AAPG Bull. 56 (2), 226-246.

[95] NGDC (2003) National Geophysical Data Center, US. http://www.ngdc.noaa.gov.

[96] O'Connell, R., Gable, C.G. and Hager, B. (1991). Toroidal-poloidal partitioning of lithospheric plate motions. In: Sabadini, R., et al. (Eds.), Glacial Isostasy, Sea-Level and Mantle Rheology, 334, 535-551, Kluwer Academic Publisher.

[97] Panza G. F., Calcagnile G. (1974). Comparison of multimode surface wave response in structures with and without a low velocity channel (Part I. Dip-slip sources on a vertical fault plane), Pure Appl. Geophys., 112, 583-596.

[98] Panza, G.F., and Müller, S. (1979). The plate boundary between Eurasia and Africa in the Alpine area, Memorie di Scienze Geologiche, Università di Padova, v. 33, pp. 43-50.

[99] Panza, G. F., Schwab, F. A. and Knopoff, L. (1972). Channel and Crustal Rayleigh Waves. Geophysical Journal of the Royal Astronomical Society, 30: 273-280. doi: 10.1111/j.1365-246X.1972.tb05813.x

[100] Panza, G.F. (1985). Synthetic Seismograms: the Rayleigh Waves Modal Summation. Journal of Geophysics 58, 125-140.

[101] Panza, G.F. and A. Saraò (2000). Monitoring volcanic and geothermal areas by full seismic moment tensor inversion: are non-double-couple components always artefacts of modelling? Geophysical Journal International, 143, 353-364.

[102] Panza, G.F. and Raykova, R.B. (2008). Structure and rheology of lithosphere in Italy and surrounding. Terra Nova, 20, 194-199. 10.1111/j.1365-3121.2008.00805.x

[103] Panza, G.F., Doglioni, C. and Levshin, A. (2010). Asymmetric ocean basins. Geology, 38, 59-62. 10.1130/G30570.1

[104] Panza, G.F., Peccerillo, A., Aoudia, A., Farina, B.M. (2007a). Geophysical and petrological modelling of the structure and composition of the crust and upper mantle in complex geodynamic settings: The Tyrrhenian Sea and surroundings. Earth-Science Reviews 80, 1-46.

[105] Panza, G.F., Pontevivo, A. (2004). The Calabrian Arc: a detailed structural model of the lithosphere-asthenosphere system. Rend. Accad. Naz. Sci. XL Mem. Sci. Fis. Natur. 28, 51-88.

[106] Panza, G.F., Raykova, R.B. (2008). Structure and rheology of lithosphere in Italy and surrounding. Terra Nova 20, 194-199.

[107] Panza, G.F., Raykova, R.B., Carminati, E., Doglioni, C. (2007b). Upper mantle flow in the western Mediterranean. Earth. Planet. Sci. Lett 257, 200-214.

[108] Panza, G.F., Romanelli F. and Vaccari, F. (2001). Seismic wave propagation in laterally heterogeneous anelastic media: Theory and applications to seismic zonation, Advances in Geophysics, Vol. 43, pp. 1-95, Academic Press, San Diego.

[109] Panza, G.F. (1981). The resolving power of seismic surface waves with respect to crust and upper mantle structural models. In: Cassinis R (ed) The solution of the inverse problem in geophysical interpretation. Plenum Press New York, 39-77.

[110] Parker, R.L. (1994). Geophysical Inverse Theory, Princeton University Press, Princeton, New Jersey.

[111] Peishan, C., Haitong, C. (1989). Scaling law and its applications to earthquake statistical relations. Tectonophysics, 188, 53-72.

[112] Phillips, B., and Bunge, H. P. (2005). Heterogeneity and time dependence in 3D spherical mantle convection models with continental drift. Earth and Planetary Science Letters 233, 121-135.

[113] Piromallo, C. and Morelli, A. (2003). P wave tomography of the mantle under the Alpine-Mediterranean area. Journal of Geophysical Research, 108 (B2), 2065-2088.10.1029/2002JB001757

[114] Pondrelli, S., Salimbeni, S., Ekström, G., Morelli,A., Gasperini, P. and Vannucci, G. (2006). The Italian CMT dataset from 1977 to the present, Phys. Earth Planet. Int., doi:10.1016/j.pepi.2006.07.008, 159/3-4, pp. 286-303.

[115] Ponomarev, V.S. (2007). Denudation and Seismicity of the Earth s Crust. Doklady Earth Sci., 412, 19-21.

[116] Pontevivo, A., Panza, G.F. (2006). The lithosphere-asthenosphere system in the Calabrian Arc and surrounding seas - Southern Italy. Pure Appl. Geophys. 163, 1617-1659.

[117] Ramsay, J.G., Huber, M.I. (1983). The techniques of modern structural analysis. Strain analysis London Academic Press 1.

[118] Raykova, R.B., Panza, G.F. (2010). The shear-wave velocity structure of the lithosphere-asthenosphere system in the Iberian area and surroundings. Rendiconti Lincei di Scienze FF. NN. DOI 10.1007/s12210-010-0077-1 (in press).

[119] Ricard, Y., Doglioni, C. and Sabadini, R. (1991). Differential rotation between lithosphere and mantle: a consequence of lateral viscosity variations. J. Geophys. Res., 96, 8407-8415.

[120] Riguzzi, F., Panza, G.F., Varga, P., Doglioni, C. (2010). Can Earth's rotation and tidal despinning drive plate tectonics? Tectonophysics 484, 60-73.

[121] Ritzwoller M., Levshin, A.L. (1998). Eurasian surface wave tomography: group velocities. J. Geophys. Res. 103, 4839-4878.

[122] Romanelli F., Bing Z., Vaccari F., Panza G. F. (1996). Analytical computation of reflection and transmission coupling coefficients for Love waves, Geophys. J. Int., 125, 132-138.

[123] Royden, L.H., Burchfiel, B.C. (1989). Are systematic variations in thrust belt style related to plate boundary process? (the western Alps versus the Carpathians). Tectonics 8, 51-62.

[124] Scalera G. (2007a). A new model of orogenic evolution. Rend. Soc. Geol. It., Nuova Serie, 5 , 214-218.

[125] Scandone, P. (1980). Origin of the Tyrrhenian Sea and Calabrian Arc. Bollettino della Società Geologica Italiana 98, 27-34.

[126] Schmid, S.M. and Kissling, E. (2000). The arc of the Western Alps in the light of geophysical data on deep crustal structure: Tectonics, v. 19, 10, 62-85.

[127] Schuberth, B. S. A., Bunge, H. P., Steinle-Neumann, G., Moder, C. and Oeser, J. (2009). Thermal versus elastic heterogeneity in highresolution mantle circulation models with pyrolite composition: High plume excess temperatures in the lowermost mantle. Geochemistry, Geophysics, Geosystems 10(1), Q01W01, doi:10.1029/2008GC002235.

[128] Šílený, J. (1998). Earthquake source parameters and their confidence regions by a genetic algorithm with a "memory". Geophysical Journal International, 134, 228-242.

[129] Šílený, J., Panza, G.F. and Campus, P. (1992). Waveform inversion for point source moment tensor retrieval with optimization of hypocentral depth and structural model. Geophysical Journal International 109, 259 274.

[130] Solomon, S., and Sleep, N.H. (1974). Some simple physical models for absolute plate motions: Journal of Geophysical Research, v. 79, p. 2557-2567.

[131] Suhadolc, P., Marson, I., Panza, G.F. (1994). Crust and upper mantle structural properties along the active Tyrrhenian rim. Memorie descrittive della carta geologica d'Italia 49.

[132] Šumanovac, F., Orešković, J., Grad, M., ALP 2002 Working Group (2009). Crustal structure at the contact of the Dinarides and Pannonian basin based on 2-D seismic and gravity interpretation of the Alp07 profile in the ALP 2002 experiment. Geophys. J. Int. 179, 615-633.

[133] Tackley, P.J. (1998). Self-consistent generation of tectonic plates in three-dimensional mantle convection, Earth Planet. Sci Lett., 157, 9-22.

[134] Tackley, P.J. (2006). Heating Up the Hotspot Debates. Science 313, 1240-1241.

[135] Tesauro, M., Kaban, M.K., Cloetingh, S.A.P.L. (2008). EuCRUST-07: a new reference model for the European crust, Geophys. Res. Lett. 35.

[136] Tondi, R., R. Schivardi, I. Molinari, and A. Morelli (2012). Upper mantle structure below the European continent: constraints from surface wave tomography and GRACE satellite gravity data, J. Geophys. Res., doi:10.1029/2012JB009149

[137] Trampert, J. (1998). Global seismic tomography: the inverse problem and beyond, Inverse Problems, 14, 371-385.

[138] Urban, L., Cichowicz, A., Vaccari, F. (1993). Computation of analytical partial derivatives of phase and group velocities for Rayleigh waves with respect to structural parameters. Stud. Geophys. Geod. 37, 14-36.

[139] Vaccari F., Gregersen S., Furlan M. e Panza G. F. (1989). Synthetic seismograms in laterally heterogeneouos, anelastic media by modal summation of P-SV waves, Geophys. J. Int., 99, 285-295.

[140] Van Keken, P.E. (2003). The structure and dynamics of the mantle wedge. Earth and planetary science letters 215, 323-338.

[141] Wessel P and W.H.F. Smith (1995). New version of Generic Mapping Tools (GMT) version 3.0 released. Eos Trans AGU 76:329

[142] Woodhouse J. H. (1974). Surface Waves in Laterally Varying Layered Structure, Geophys, J. R. astr. Soc., 37, 461-490.

[143] Yanovskaya, T.B. (1997). Resolution estimation in the problems of seismic ray tomography. Izv., Phys. Solid Earth 33 (9), 762-765.

[144] Yanovskaya, T.B. (2001). In: Keilis-Borok, V.I., Molchan, G.M.(Eds.), Development of methods for surface-wave tomography based on Backus-Gilbert approach. Computational Seismology 32, 11-26.